Constraining cavern backgrounds for the LUX-ZEPLIN experiment

Niamh M. Fearon

St Peter's College

University of Oxford

A thesis submitted for the degree of

Doctor of Philosophy

Hilary 2024

Abstract

There is an abundance of evidence, both astrophysical and cosmological, for the existence of non-luminous, gravitationally interacting matter that cannot be accounted for by the current Standard Model - dark matter. It is estimated that dark matter accounts for $\sim 84\%$ of the matter density of the Universe, but has yet to be directly detected.

The LUX-ZEPLIN experiment (LZ) is searching for a popular dark matter particle candidate, weakly interacting massive particles (WIMPs), in the energy range GeV/c^2 – TeV/c^2. The LZ detector consists of a dual-phase time projection chamber filled with a 7 t active target of liquid xenon. Recoil interactions of dark matter contained within the galactic halo are expected to produce signals via charge and scintillation channels on the order of a few keV in the xenon target. Owing to passive and active shielding, fiducialisation and background rejection, LZ has reported the world-leading result for spin-independent WIMP–nucleon interactions with data collected during the first science run.

This thesis presents work characterising and constraining the background produced by the cavern environment, namely from naturally occurring radioactive material contained within the cavern rock. This results in a penetrative gamma-ray background from long-lived isotopes of ^{40}K and ^{238}U and ^{232}Th decay chains. Radiogenic neutrons are also produced via spontaneous fission and (α, n) reactions. A new gamma spectroscopy experiment was conducted in the Davis cavern directly outside of the water tank housing LZ in order to gain long-exposure measurements of the gamma-ray background. Simulations are employed to compare our models with real data. The accuracy of our modelling becomes increasingly important as LZ continues to take science data, adding to the live time of the WIMP search and other rare physics searches, such as for low-energy electron recoils and neutrinoless double-beta decay of ^{136}Xe.

Declaration

I declare that the contents of this thesis are original and my own, except where explicit reference is made to the work of others. This thesis has not been submitted in whole or in part for consideration for any other degree or qualification in this, or any other university.

Author contributions

The following contributions to the analysis presented in this thesis were made by the author:

- **Chapter 4:** The author undertook a long-term attachment to Sanford Underground Research Facility during November 2022 - February 2023. During this period, in parallel to on-site shifting tasks, the long-exposure gamma-ray spectroscopy experiment was set up in the Davis cavern where the LUX-ZEPLIN detector is located. The author was the on-site lead for this project and responsible for all experimental equipment and the creation of a job hazard analysis document. The gamma source calibration campaign was completed by the author with authorisation from the on-site radiation safety lead. The author was solely responsible for the analysis of the calibration and background exposure datasets.

- **Chapter 5:** The LUX-ZEPLIN DD neutron calibration was coordinated by on-site personnel and the Brown University group in October 2023. The author analysed background data taken by the gamma-ray spectroscopy experiment during this calibration.

- **Chapter 6:** The author was responsible for all aspects of the simulation, production and analysis codes. The GEANT4-based simulation is an extension of the BACCARAT framework utilised by the LUX-ZEPLIN Collaboration. The neutron yields were calculated using the publicly available NeuCBOT coded maintained by Shawn Westerdale.

Niamh M. Fearon
Hilary 2024

Acknowledgements

Embarking on my PhD journey at the University of Oxford has been an extraordinary privilege, one for which I am profoundly grateful. This opportunity has been made possible through the unwavering support and love of numerous individuals who have stood by me throughout this endeavour. To my family and friends, I dedicate this work to you.

First, thank you to my supervisor Prof. Hans Kraus for providing sage wisdom and advice throughout the course of my research. His guidance has played a pivotal role in shaping me as a scientist. I extend my thanks to the Oxford group and the LZ Collaboration: Amy, Kevin, Kim, Sally and David, and others, for many useful discussions. To the excellent technical staff at the Sanford Underground Research Facility, thank you all for welcoming me so warmly into the local community during a dark snowy winter. Additionally, I thank Kim Proudfoot and Sue Geddes for their tireless work to make sure the Particle Physics department is always kept in order.

To my colleagues Ciaran, Daniel, Jenny, Karan and Ynyr, both at Manchester and Oxford, thank you for countless hours of camaraderie. I am so grateful we were all offered this opportunity to continue our studies together on such a wide array of brilliant experiments. Your company made all the highs and lows of this journey worthwhile. I extend my gratitude to my larger physics family of Ciara, Nicola, Sol, Gwen, Calum and many others from my undergraduate studies at Manchester. I take this moment to think of Oscar, whom we all loved so much and hold dearly in our hearts.

Special thanks to my friends at St Peter's College, particularly Bethan, Camille, Ceri, Katie, Kim, and Naomi, for the enduring friendships forged during my time here. To the many variations of friends that enjoy Tuesday nights at The Old Bookbinders, thank you for always keeping me in high spirits. To Ellen, your enduring support helped me reach the finish line, for which I am eternally grateful.

Finally, I would like to thank my family. To my parents and sister Caitriona, thank you for always encouraging me to reach for the stars. You continue to inspire me every day.

Contents

List of Figures

List of Tables

List of Acronyms

$0\nu\beta\beta$	Neutrinoless Double-Beta Decay
$2\nu\beta\beta$	Two-Neutrino Double-Beta Decay
ALP	Axion-Like Particle
BAO	Baryon Acoustic Oscillations
BBN	Big Bang Nucleosynthesis
BPE	Borated Polyethylene
BSM	Beyond the Standard Model
CCD	Charge-Coupled Device
CDM	Cold Dark Matter
CEνNS	Coherent Elastic Neutrino–Nucleus Scattering
CL	Confidence Level
CMB	Cosmic Microwave Background
CSD	Calibration Source Deployment
DAQ	Data Acquisition
DD	Deuterium-Deuterium
DEC	Double Electron Capture
DIM	Detector Interface Module
DM	Dark Matter
DSNB	Diffuse Supernova Neutrino Background
EC	Electron Capture
EFT	Effective Field Theory
EMS	Environmental Monitoring Station
ER	Electron Recoil
FV	Fiducial Volume

FWHM	Full Width Half Maximum
G3	Third-Generation
GdLS	Gadolinium-Loaded Liquid Scintillator
GXe	Gaseous Xenon
HPGe	High Purity Germanium
HV	High Voltage
ICV	Inner Cryostat Vessel
iRRS	Inline Radon Reduction System
LHC	Large Hadron Collider
LSP	Lightest Supersymmetric Particle
LUX	Large Underground Experiment
LXe	Liquid Xenon
LZ	LUX-ZEPLIN
MACHO	Massive Astrophysical Compact Halo Object
MC	Monte Carlo
MCA	Multichannel Analyser
mCP	Millicharged Particle
MS	Multiple Scatter
MSSM	Minimal Supersymmetric Standard Model
MWE	Metre Water Equivalent
NaI(Tl)	Thallium-doped Sodium Iodide
NEST	Noble Element Simulation Technique
NORM	Naturally Occurring Radioactive Material
NR	Nuclear Recoil
OCS	Optical Calibration System
OCV	Outer Cryostat Vessel
OD	Outer Detector
PBH	Primordial Black Hole

PCL	Power-Constrained Limit
PDF	Probability Density Function
PE	Photoelectron
PHD	Photons Detected
PLR	Profile Likelihood Ratio
PMT	Photomultiplier Tube
PTFE	Polytetrafluoroethylene
QCD	Quantum Chromodynamics
RFR	Reverse Field Region
ROI	Region Of Interest
RQ	Reduced Quantity
S1	Primary Scintillation Signal
S2	Secondary Scintillation Signal
SD	Spin Dependent
SE	Single Electron
SHM	Standard Halo Model
SI	Spin Independent
SM	Standard Model
SR1	Science Run 1
SS	Single Scatter
SURF	Sanford Underground Research Facility
SUSY	Supersymmetry
TPC	Time Projection Chamber
VUV	Vacuum Ultraviolet
WIMP	Weakly Interacting Massive Particle

Introduction

There is an abundance of evidence on astrophysical and cosmological scales suggesting the existence of a non-baryonic, gravitationally interacting and non-luminous substance - dark matter. Dark matter is expected to account for $\sim 84\%$ of the total matter density of the Universe according to the cosmological ΛCDM theory. Despite its prevalence, the exact nature of dark matter remains unknown. It is theorised that dark matter may be composed of new particles that exist beyond the Standard Model of particle physics. A popular dark matter candidate is the weakly interacting massive particle (WIMP) which has a typical mass range on the order of GeV/c^2. Various detection technologies have been developed to search for dark matter, yet direct detection has remained elusive.

The LUX-ZEPLIN (LZ) experiment is a dark matter direct detection experiment that is located at the Sandford Underground Research Facility, in Lead, South Dakota, USA. LZ aims to search for WIMPs via scattering interactions with target nuclei that generate low-energy recoil signals. The LZ detector utilises a dual-phase time projection chamber (TPC) filled with an active mass of 7 t of liquid xenon instrumented with two arrays of photomultiplier tubes used for optical readout of scintillation and ionisation channels. Analysis of the first science run of the LZ experiment reports the world-leading sensitivity limit for the spin–independent WIMP–nucleon scattering cross-section at 36 GeV/c^2, rejecting cross-sections above $9.2 \times 10^{-48}\,\mathrm{cm}^2$. LZ continues operations with the ultimate goal of WIMP discovery alongside rare-event physics searches such as for neutrinoless double-beta decay, solar neutrinos and solar axions over an estimated 1000 live day campaign.

The focus of the work presented in this thesis is on characterising and constraining backgrounds that originate from the cavern environment that hosts the LUX-ZEPLIN experiment. These backgrounds are key to understand for the primary WIMP search, as well as other rare physics searches that the LZ experiment is sensitive to. A breakdown of the topics included are stated below.

Chapter **1** introduces the astrophysical and cosmological evidence for the existence of dark matter, detailing historic results first reported in the early 20th century up to modern findings in the era of precision cosmology. Theoretical dark matter candidates are explored, including WIMPs and axions. The three major search channels for dark matter detection are introduced and a short review of modern experiments is presented. A summary of the current field of direct dark matter detection experimental results is given.

Chapter **2** then describes the nature of particle interactions in xenon and the advantageous properties of xenon as a direct detection target medium. Dual-phase time projection chamber technology is summarised, which can be utilised to provide excellent event discrimination between electron and nuclear recoil events to set world-leading limits on WIMP–nucleon interactions. Finally, the LUX-ZEPLIN experiment is introduced. The LZ TPC and veto detectors are presented, alongside some key detector subsystems and calibration methods. All relevant sources of backgrounds are covered. Specific details of the analysis techniques and the first dark matter search results from LZ are reported.

Chapter **3** outlines the details of the Davis cavern that surrounds the LZ experiment. This short Chapter aims to summarise details of the immediate environment of the LZ experiment to preface the analysis presented in later material. The layout of the Davis cavern at the Sanford Underground Research Facility is introduced. The geology of the Black Hills region of South Dakota is briefly outlined in order to contextualise the cavern rock composition. Sources of backgrounds and previous gamma-ray preliminary measurement are reported. Finally, the LZ environment monitoring station is introduced, with the aim of measuring radon, neutron and gamma-ray backgrounds during science data-taking for the lifetime of LZ.

Chapter **4** details the first measurements of the high-energy gamma background originating from the laboratory surroundings, the dominant source being the rock composing the Davis cavern walls. High-energy gamma-rays are produced via secondary (α,γ) captures on light nuclei present in the rock composition. These high-energy electron recoil backgrounds are of particular importance to rare physics searches that can be performed with LZ, such as sensitivity to the $0\nu\beta\beta$ decay of ^{134}Xe and ^{136}Xe. A thallium-activated sodium iodide detector was installed on the lower level of the Davis cavern to record a long-exposure measurement of the ambient cavern background. Successful operation of the sodium iodide detector over the course of LZ data-taking has lead to the inception of the LZ environmental monitoring station - a permanent slow-control integrated system used to track cavern gammas, neutrons and airborne radon levels.

Chapter **5** presents measurements taken by the NaI detector during LZ low-energy nuclear recoil calibrations using a DD neutron generator. The DD generator produces neutrons of energy 2.45 MeV and operates in different configurations to select the energy of neutrons entering LZ. The presence of a high-energy neutron source in the Davis cavern causes (n,γ) captures on materials that are abundant in the cavern environment. Analysis of the data collected during the neutron exposure from the DD source is reported.

Chapter **6** presents simulations of cavern backgrounds including neutron yields from (α,n) reactions and cavern gamma-rays. The simulations of the cavern gamma backgrounds are used to perform a study of the naturally occurring radioactive material background: uranium, thorium, radon and potassium decay contributions, including their progeny and secondary capture products. Future work for high-statistics Monte Carlo simulations of the gamma background from the cavern geometry is discussed, including a novel biasing technique needed in order to simulate the statistics required to fully model the cavern gamma background component to compare with measurements.

Finally, Chapter **7** provides a summary of the key findings of the thesis, and concludes with an outlook on possible future extensions for the work presented.

1 Dark matter

The existence of dark matter (DM) has been inferred by both astrophysical and cosmological data from as early as the 1920–1930s. Some early evidence came from observations of the local galactic neighbourhood, where the presence of a “dark” non-luminous gravitationally interacting matter was inferred.

While the astrophysical and cosmological evidence for dark matter has continued to accumulate for a century, physicists are still left with the question of the nature of dark matter. This Chapter covers the wide range of evidence for the existence of dark matter, the current particle candidates for dark matter and the various search methods used in order to detect these particles.

1.1 Evidence for the existence of dark matter

1.1.1 Early evidence

From the 1920s there were many efforts made by astronomers to model the dynamics of stars in our own Milky Way galaxy [1–3]. It was from these observations and calculations that first introduced the idea of “dark matter” being present in our Universe. At the time, this matter was thought to be “dark” stars that were either extinct or too faint to be detected by Earth-based telescopes. The pioneering work by these astronomers led to quantifying the local dark matter density, which is a topic of importance today relating to direct detection experiments [4].

1.1.2 Dynamics of galaxy clusters

Measurements of dispersion velocities of galaxies within galaxy clusters pointed towards evidence of dark matter in these systems. Zwicky published studies of dispersion velocities in the Coma cluster in 1933 [5], using redshift measurements of spectral lines via the Doppler effect for various galaxies from Hubble and Humason [6]. Under the assumption that the Coma cluster was in a stationary stable state, the Virial theorem could be applied, which for a bound system in equilibrium is given by:

$$\langle K \rangle = -\frac{1}{2}\langle U \rangle, \tag{1.1.1}$$

where $\langle K \rangle$ and $\langle U \rangle$ are the time averaged kinetic energy and potential energy of a system, respectively.

He concluded that in order to account for the dispersion velocity values measured, there would have to be significantly more dark matter than luminous matter in the cluster. Zwicky later went on to improve his analysis of the Coma system in 1937 [7], quoting the lower limit of the average mass per galaxy $\overline{M} = 4.5 \times 10^{10} M_{\odot}$, where $M_{\odot}$ represents one solar mass. The luminosity of an average nebula is assumed to be equal to $L = 8.5 \times 10^{7} L_{\odot}$, which resulted in the reported mass-to-light ratio of the galaxy cluster being surprisingly high with a value on the order of $\sim 500\ M_{\odot}/L_{\odot}$. This led Zwicky to conclude that this large discrepancy implies that further analysis of this problem is needed.

At a similar time, Smith reported studies of the Virgo Cluster [8]. The mass reported for the Virgo cluster was also much greater than that calculated considering the mass of the luminous matter contained within the number of galaxies. Smith attributed this mass excess to “internebular material” with low luminosity. Many scientists were sceptical of Zwicky’s and Smith’s findings, causing much discussion about what the missing mass could be attributed to.

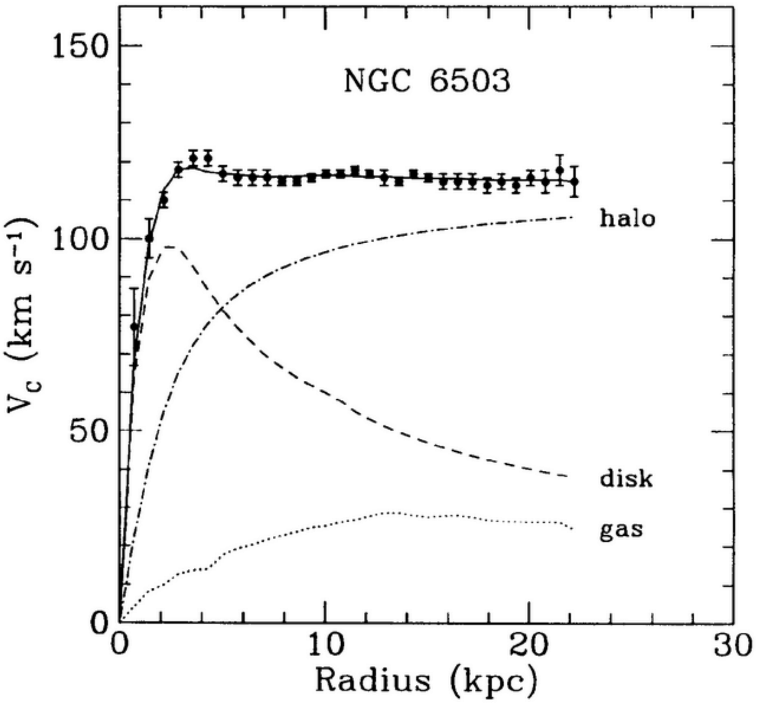

Figure 1.1.1: The rotation curve of lenticular galaxy NGC 6503. Observed data points and their associated error bars are shown with a black solid fit line. The separate components of the rotation curve are shown for the halo (dash-dotted), disk (dashed) and gas (dotted). Figure taken from Ref. [9].

1.1.3 Galactic rotation curves

In 1970, Vera Rubin and Kent Ford measured the rotation curve of nearby spiral galaxy Andromeda (M31) to evaluate the galactic mass distribution [10]. Orbital velocities can be measured via photometric optical data and radio astronomy using the 21 cm spectral line produced by neutral hydrogen (HI). The velocity profile of the stars within the galaxy is given by the Keplerian model, from Newtonian dynamics:

$$v(r) = \sqrt{\frac{GM(r)}{r}}, \tag{1.1.2}$$

where v is the orbital velocity, r is the radius, G is the gravitational constant and $M(r)$ is the mass enclosed within the radius. The expected velocity distribution for a spiral galaxy is analogous to a compact disk, which is linear as a function of distance from the centre of the galaxy, followed by a Keplerian distribution

($v \propto \sqrt{1/r}$) beyond the visible disk.

However, Rubin and Ford measured that the velocity profile became independent of radius beyond the linear relationship associated with the matter contained within the galaxy. An example of a galaxy velocity distribution is shown in Figure 1.1.1. This suggests that a large amount of the mass component of the galaxy extends well beyond the visible disk. This first introduced the idea of spherical dark matter halo structures being present in galaxy structures. Many other spiral galaxy measurements were made in the 1970s that corroborated Rubin and Ford's results which was a major turning-point within the scientific community [11–14].

1.1.4 Gravitational lensing

Gravitational lensing occurs when a massive object in between the line of sight of an astrophysical source and the observer distorts the space-time light path [15]. Strong gravitational lensing can result in the creation of multiple images or arcs of the original source by a large mass acting as a lens. The observer may also see a distorted, stretched and magnified image, as in the case of weak gravitational lensing, when multiple source galaxies contained within a cluster may be affected, e.g. Abell 370 [16].

Gravitational lensing measurements taken of merging cluster 1E 0657–558, known as the Bullet cluster, provide strong evidence for the existence of dark matter [17]. Optical and X-ray images of the cluster merger are shown in Figure 1.1.2. In this particular merger, two galaxy clusters have collided along a horizontal pathway relative to observations. This allowed for three cluster components to be studied: stars, gas and dark matter.

Optical imaging of the cluster (Figure 1.1.2a) shows that the stars contained within the clusters are largely unaffected by the merger. The bright regions shown in Figure 1.1.2b are the X-ray emission from the hot baryonic gas of the colliding fluid components of the cluster merger. The green contours are produced by

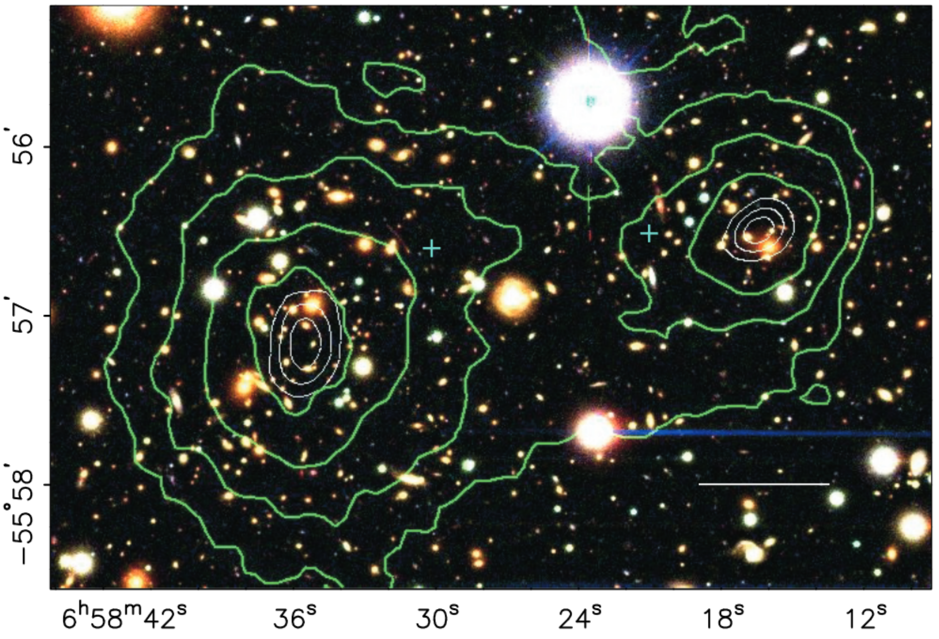

(a) Colour optical image of the merging cluster 1E 0657–558 taken by the Magellan telescope.

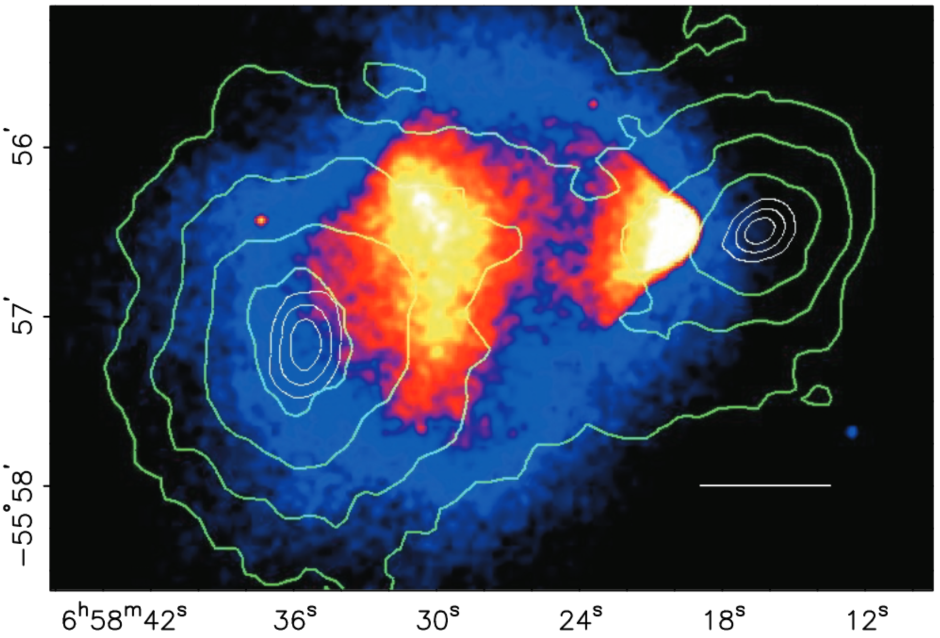

(b) X-ray image of the merging cluster 1E 0657–558 taken by the Chandra X-ray observatory.

Figure 1.1.2: Optical and X-ray images of the merging cluster 1E 0657–558, with the white bar indicating 200 kpc scale at the distance of the cluster. The green contours are the weak lensing reconstructions and the blue crosses represent the centre of mass of the gaseous plasma clouds. Figure taken from Ref. [17].

the weak lensing reconstruction of the mass of the cluster system. This gives us an indirect measure of the mass distribution contained within both galaxy clusters. These gravitational lensing maps show that the gravitational potential of the system does not trace the gaseous plasma distribution, which is the dominant baryonic component. Rather, the mass distribution traces the distribution of the galaxies, as shown in Figure 1.1.2a. The conclusion drawn was that the majority of the mass in the system is therefore dominated by a collisionless dark matter component present in the galaxy clusters.

1.1.5 The ΛCDM model

Dark matter is hypothesised to have been instrumental in the structure formation of the Universe [18]. A well-motivated description of the Universe is based on the ΛCDM model which is the standard model of Big Bang cosmology [19]. Here, Λ is the cosmological constant (arising from Einstein's theory of general relativity [20]) and CDM stands for cold dark matter. This cosmological model formalises the thermal history of the Universe from a hot dense plasma to the isotropic and homogeneous Universe observed today.

The evolution of the Universe can be described by the first Friedmann equation which is obtained considering Einstein's field equations:

$$\left(\frac{\dot{a}}{a}\right)^2 + \frac{kc^2}{a^2} = \frac{8\pi}{3}G\rho, \tag{1.1.3}$$

where $a(t)$ is the dimensionless scale factor and ρ is the total energy density of the Universe. k is the curvature parameter and can be equal to $\{-1, 0, +1\}$ in the cases of an open, flat or closed Universe, respectively.

The critical density is defined as,

$$\rho_{\text{crit}} \equiv \frac{3}{8\pi G}\left(\frac{\dot{a}}{a}\right)^2 \equiv \frac{3H^2}{8\pi G}, \tag{1.1.4}$$

using the relationship between the scale factor and the Hubble constant:

$$H = \frac{\dot{a}}{a}. \tag{1.1.5}$$

We can define the fraction of critical density contributed by each component by:

$$\Omega_i \equiv \frac{\rho_i}{\rho_{\text{crit}}}, \tag{1.1.6}$$

where i denotes each constituent species, either matter, radiation or dark energy Λ.

In the Friedmann–Lemaître–Robertson–Walker cosmology model of a flat Universe where $k = 0$, the Friedmann equation becomes:

$$\rho_{\text{crit}} = \sum_i \rho_i + \rho_\Lambda, \tag{1.1.7}$$

which then simplifies to the final result:

$$\sum_i \Omega_i + \Omega_\Lambda = 1. \tag{1.1.8}$$

The observed properties of the known Universe are then dependent on the values of Ω_i. Observational cosmologists are working to evaluate these parameters in order to robustly test cosmological models. Evidence to support the ΛCDM standard cosmological model include measurements of “standard candle” Type Ia supernovae sources, which provide evidence that the Universe is expanding at an accelerating rate due to dark energy, Λ [21–23]. Other supporting cosmological evidence includes the cosmic microwave background and large scale structure of the Universe, both introduced in the following discussion.

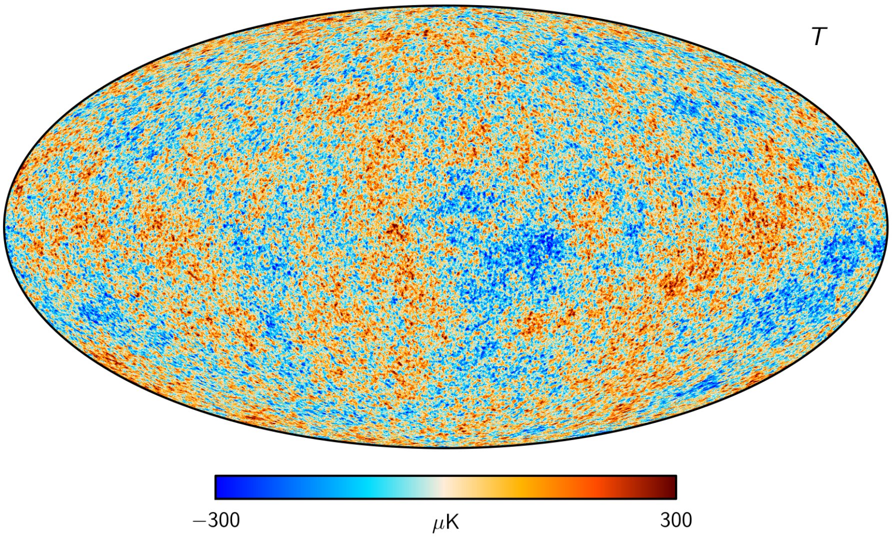

Figure 1.1.3: An all-sky temperature map of the CMB taken by the Planck satellite. The map highlights the CMB temperature anisotropies on a scale of +300 μK to −300 μK. Figure taken from Ref. [26].

1.1.6 The cosmic microwave background

Cosmic microwave background radiation (CMB) was first measured in 1965 by radio astronomers Penzias and Wilson [24], and is relic radiation originating from photons produced in the Big Bang. The CMB originates from the recombination epoch in the history of the Universe, approximately 380,000 years after the Big Bang. As the Universe expanded and cooled, electrons and protons combined to form neutral hydrogen. The Universe then became transparent and photons were able to free stream. The CMB represents the surface of last scattering from which these photons were first able to travel across the Universe. The CMB has the spectrum of a blackbody radiator, with a temperature of approximately $T_{\mathrm{CMB}} = 2.725\,\mathrm{K}$ [25].

Current precision measurements of the cosmic microwave background temperature anisotropies from the 2018 Planck telescope data release are shown in Figure 1.1.3 [26]. Small temperature anisotropies over this map of the Universe are measured on the order of $\delta T \sim 10^{-5}\,\mathrm{K}$. Temperature anisotropies are expressed

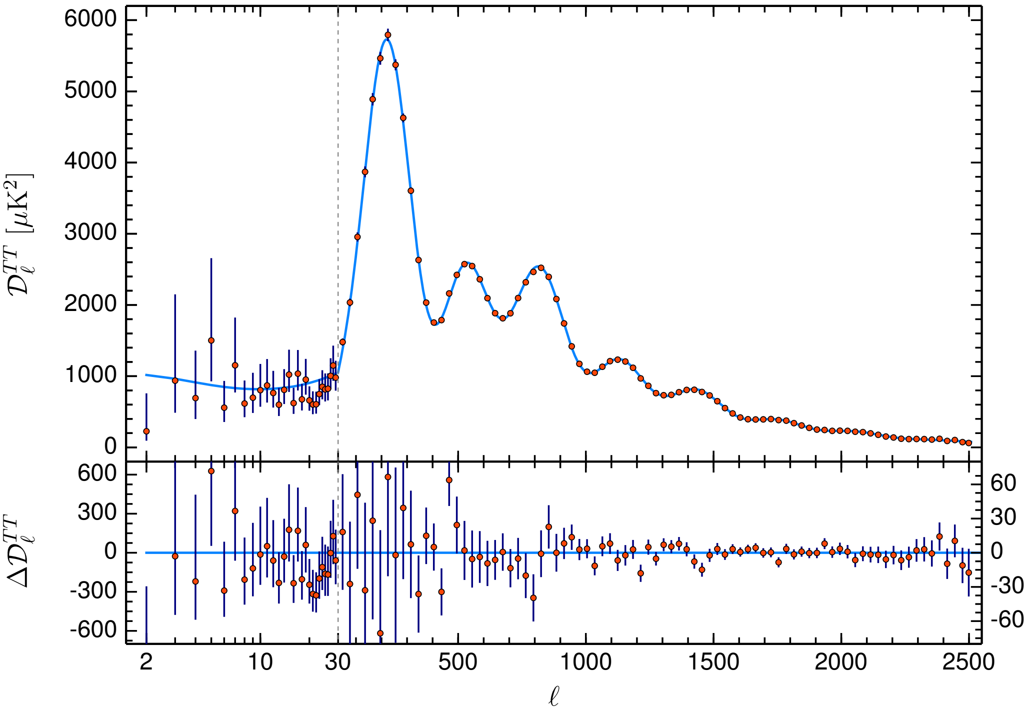

Figure 1.1.4: The angular power spectrum $\mathcal{D}_\ell$ of the temperature anisotropies of the CMB for multipole order $\ell \geq 2$. The best fit of the base-ΛCDM theoretical spectrum to Planck data is shown in light blue in the upper panel. Residuals with respect to this model are shown in the lower panel. Figure taken from Ref. [27].

using a spherical harmonic expansion of the CMB sky:

$$T(\theta, \phi) = \sum_{\ell m} a_{\ell m} Y_{\ell m}(\theta, \phi), \tag{1.1.9}$$

where $a_{\ell m}$ is the strength of the angular oscillation over $Y_{\ell m}(\theta, \phi)$, ℓ is the multipole number and m is the azimuthal index.

Assuming a statistically-isotropic sky distribution implies no azimuthal dependence, i.e. there is no preferred axis and there is dependence only on angular separation, ℓ. The angular power spectrum $\mathcal{D}_\ell$ of the anisotropy of the CMB contains information about the formation of the Universe and its contents. The angular power spectrum is expressed mathematically as:

$$\mathcal{D}_\ell^{TT} = \frac{\ell(\ell+1)\, \mathcal{C}_\ell^{TT}}{2\pi}, \tag{1.1.10}$$

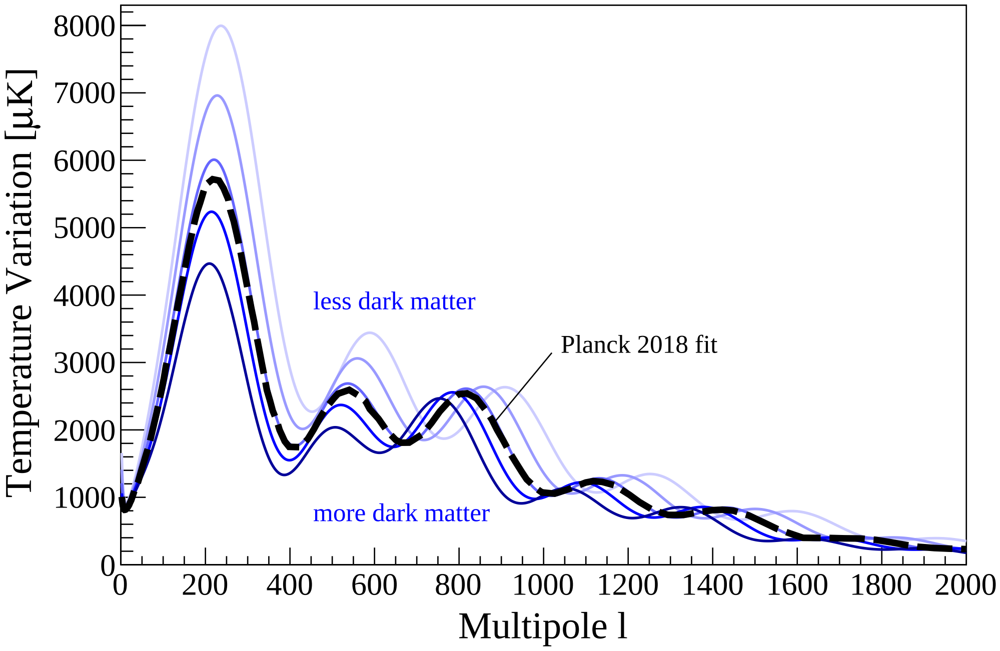

Figure 1.1.5: Temperature power spectrum of the cosmic microwave background (CMB) for a dark matter density contribution Ω_c varying between 0.11 and 0.43 (blue lines). All other input parameters of the model are kept constant. The dashed black line shows the best fit to the Planck data from the 2018 release [26]. Figure taken from Ref. [29].

where $\mathcal{C}_\ell^{TT} = \langle |a_{\ell m}|^2 \rangle$.

Figure 1.1.4 quantifies how temperature fluctuations vary with angular frequency, denoted by the multipole order ℓ. High values of ℓ relate to small angular scales. The peak structures present in the power spectrum are referred to as acoustic peaks. These peaks are associated with the underlying physics of baryon acoustic oscillations (BAO), when baryons were coupled to photons before the epoch of recombination. The oscillations were driven by gravitational potential perturbations of large scale structure in the early Universe. The acoustic peaks are sensitive to the amount of dark matter in the Universe, as shown in Figure 1.1.5. The location of the first acoustic peak is dependent on the value of the total energy density parameter of the Universe Ω, and implies that the curvature of the Universe is flat. The amplitude and position of the third acoustic peak in relation to the second acoustic peak is sensitive to the dark matter density of the Universe [28].

The Planck Collaboration reports the values of the 6-parameter ΛCDM cosmological model constrained using Planck CMB temperature, polarisation and lensing power spectra in combination with BAO data:

$$\begin{aligned} h &= 0.677 \pm 0.004, \\ \Omega_\mathrm{b} h^2 &= 0.0224 \pm 0.0001, \\ \Omega_\mathrm{c} h^2 &= 0.1200 \pm 0.0012, \\ \Omega_\mathrm{m} &= 0.3111 \pm 0.0056, \\ \Omega_\Lambda &= 0.6889 \pm 0.0056, \end{aligned} \tag{1.1.11}$$

where h is a dimensionless quantity related to the Hubble constant by $H_0 = 100h\ \mathrm{km\,s^{-1}\,Mpc^{-1}}$, and Ω_i are the density parameters for the various matter species, Ω_b is the energy density of baryonic matter, Ω_c is the energy density of cold dark matter, Ω_m is the energy density of all matter and Ω_Λ is the energy density parameter of dark energy [27]. Taking these values into account and assuming a flat Universe where $\Omega_\mathrm{tot} \equiv \sum \Omega_i + \Omega_\Lambda = 1$ and a total matter density $\Omega_\mathrm{m} \equiv \sum \Omega_\mathrm{b} + \Omega_\mathrm{c}$, dark matter is estimated to contribute 26.4% of the critical density in the Universe, or 84.4% of the total matter density [30].

1.1.7 Large scale structure

Dark matter is hypothesised to have been instrumental in the structure formation of the Universe [18]. The ΛCDM model of the Universe parameterises the history of the Universe in terms of quantities such as energy densities of the baryonic matter, dark matter and dark energy components. This model is heavily supported when both observing and simulating the large scale structure of the Universe.

Large sky surveys, such as the 6dF Galaxy Survey, Sloan Digital Sky Survey, Dark Energy Survey and Gaia Survey have mapped and characterised celestial objects with precision [31–34]. These surveys allow us to create three-dimensional

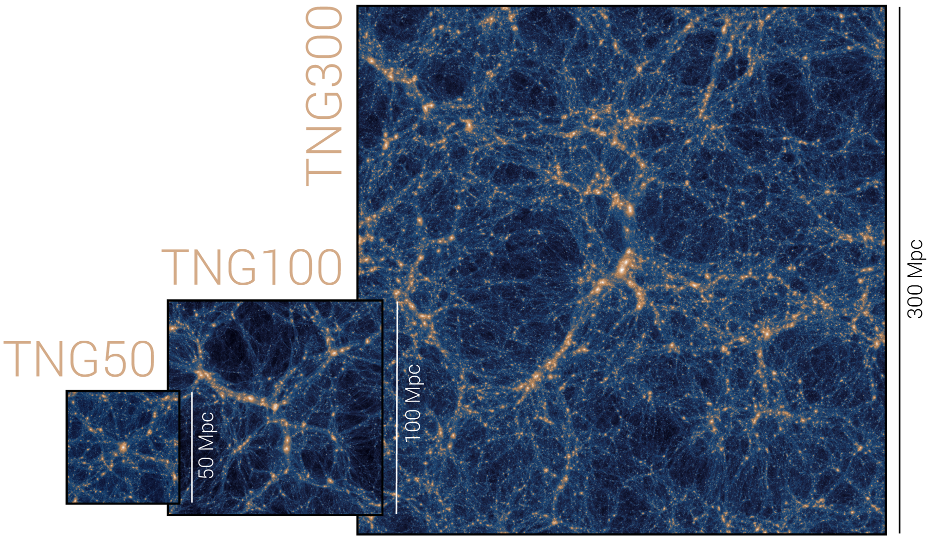

Figure 1.1.6: Comparison of the three TNG simulations: TNG50, TNG100, and TNG300. For each simulation the projected dark matter density is shown. Image credit to the TNG Collaboration.

maps of galaxies to inform us about the spatial distribution of matter in the Universe. The resolution of these maps will improve with new telescope technologies set to conduct surveys, such as the James Webb Space Telescope, the Euclid Telescope and the Legacy Survey for Space and Time (LSST) at the Vera Rubin Observatory [35–37].

Computational N-body simulations of the Universe at different redshift values assuming parameter values from the ΛCDM model create simulated datasets that can be compared to survey observations [38–40]. A comparison of simulations produced by the TNG Collaboration are shown in Figure 1.1.6. These simulations that are dominated by a cold dark matter mass component are able to reproduce the hierarchical structure of galaxies and galaxy clusters at megaparsec scales. This evidence leads to the ΛCDM being widely accepted as the standard model of Big Bang cosmology.

1.1.8 Alternative theories

Over Section 1.1 we have discussed a wide range of evidence that provides a compelling case for the existence of dark matter in the Universe. However, alternative gravity theories that do not involve the introduction of extra matter have also been postulated [41].

In 1983 Milgrom introduced the theory of Modified Newtonian dynamics (MOND) to explain the observed galactic rotation curve independence from r at large radii, without the introduction of a dark matter halo [42–44]. MOND modifies Newton's second law such that,

$$F = ma \;\rightarrow\; F = \frac{ma^2}{a_0}, \tag{1.1.12}$$

below the critical acceleration value a_0, in the limit of very low accelerations $a \ll a_0 \sim 1.2 \times 10^{-10}\,\mathrm{m\,s^{-2}}$. At this limit it is possible to account for the motion of stars and gas within galaxies without the presence of dark matter.

The relevant resulting velocity distributions are:

$$v(r) = \begin{cases} (GM(r)/r)^{1/2} & \text{Newtonian,} \\ (GM(r)a_0)^{1/4} & \text{MOND,} \end{cases} \tag{1.1.13}$$

for each dynamical case, where $M(r)$ is the baryonic mass contained within a sphere of radius r. There is no dark matter resulting from the MOND interpretation.

MOND also provides a solution to the empirical baryonic Tully-Fisher relationship [45], which relates the luminosities and rotation velocity of spiral galaxies by $L \propto V_{\mathrm{rot}}^{\alpha}$ where $\alpha \approx 4$. Assuming a common mass-to-light ratio for all galaxies, MOND is able to predict this relationship with an exact value of $\alpha = 4$ by using the mass-velocity proportionality in Equation 1.1.13.

However, MOND has less success explaining other phenomena such as the acoustic peaks of the CMB, the Bullet cluster, dynamics of galaxies on cluster scales and gravitational lensing. The limitations of MOND in accounting for major aspects of the current ΛCDM model of cosmology lead to a large consensus within the scientific community of the existence of dark matter.

1.2 Dark matter candidates

1.2.1 Dark matter properties

Dark matter particles have yet to be directly detected and the composition of the dark matter is currently unknown. However, astrophysical observations discussed in Section 1.1 give us information about the properties of dark matter. From these observations we can infer the following nature of dark matter:

- **Electromagnetically neutral:** Dark matter does not interact electromagnetically with photons, but is inferred by gravitational astrophysical observations. Limits can be placed on "millicharged" particles (mCP), with $Q = \epsilon e$, constituting dark matter by considering the decoupling from the baryon-photon plasma at the time of recombination [46] and with experimental small charge searches [47]. mCPs may arise from kinetic mixing between dark sector photons with the SM photon [48, 49].

- **Non-baryonic:** Evidence from the fitting of the ΛCDM model to the CMB anisotropies discussed above suggests that dark matter is non-baryonic in nature, contributing $\sim 25\%$ of the energy density of the Universe.

- **Non-relativistic:** The velocity distribution of dark matter is non-relativistic, often referred to as "cold" at the time of decoupling from the hot particle plasma in the early Universe. CDM reproduces the observed large scale structure in N-body simulations.

- **Weakly interacting and collisionless:** Constraints on the self-interactions of dark matter have been placed from observations of galaxy cluster mergers, such as the Bullet cluster [50] and ellipticity measurements of certain galaxies using X-rays telescopes [51].

- **Stable:** The lifetime of dark matter is of the order of the age of the Universe in order to impact large scale structure formation and inform astrophysical observations [52]. Model independent bounds have been set giving the lifetime of cold dark matter $> 160\,\mathrm{Gyr}$.

Dark matter is not accounted for in the current Standard Model (SM) of particle physics and its relation to the other known SM particles is one of the biggest unsolved problems in physics. However, Beyond the Standard Model (BSM) theories provide multiple viable candidates for particle dark matter. Here we will briefly describe some of the leading candidates in the field.

1.2.2 Axions and axion-like particles

Axions are particles that arise from the Peccei-Quinn theory solution to the strong charge-parity (CP) problem [53]. The conservation of CP cannot be explained by quantum chromodynamics (QCD) and requires the addition of a $U(1)_{PQ}$ symmetry as an extension to the Standard Model formalism. The axion QCD Lagrangian term introduced is:

$$\mathcal{L} = \left(\frac{a}{f_a} - \bar{\theta}\right)\frac{\alpha_s}{8\pi} G^{\mu\nu}\tilde{G}_{\mu\nu}, \tag{1.2.1}$$

where a is the axion field, f_a is the axion decay constant, α_s is the strong coupling constant, G is the gluon field strength tensor and $\bar{\theta}$ is the strong-CP violating term. The symmetry is spontaneously broken at scales $\sim f_a$, resulting in the production of a pseudo-Nambu-Goldstone boson: the QCD axion. The mass of the QCD

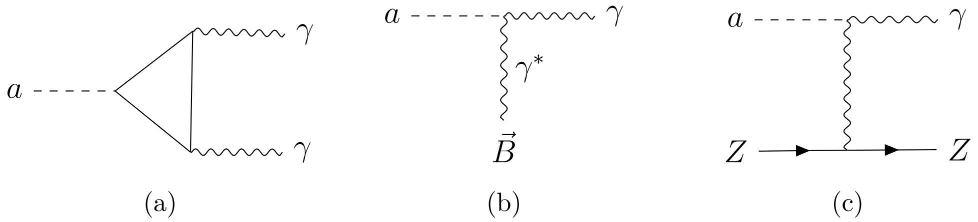

Figure 1.2.1: Feynman diagrams of axion interactions. (a) Conversion of axion to two photons via coupling $g_{a\gamma}$. (b) Axion conversion to photons via virtual photons generated in an applied magnetic field, $\vec{B}$. (c) Inverse Primakoff effect, where the axion scatters coherently with the entire nucleus $Z \equiv (e^-, N)$.

axion is expressed as:

$$m_a \simeq 5.7\left(\frac{10^{12}\,\mathrm{GeV}}{f_a}\right)\mathrm{\mu eV}. \tag{1.2.2}$$

In addition, more generalised axion-like particles (ALPs) resulting from a global $U(1)$ symmetry breaking do not interact and couple the same way with gluons as the QCD axion. Therefore, ALPs are not restricted by QCD effects and cover a broader mass range than the standard QCD axion [54].

The main principle of axion detection involves axion coupling to photons via the Primakoff effect [55]. Three example Feynman diagrams of axion interactions are shown in Figure 1.2.1. Diagrams (a) and (b) show axions decaying to photons, via a virtual loop or via virtual photons γ^* generated in the presence of a strong laboratory magnetic field $\vec{B}$. The final diagram (c) shows the inverse Primakoff effect, where the axion coherently scatters with the entire nucleus Z via $a + Z \to \gamma + Z$.

Experiments looking to detect axions and ALPs are utilising two key detection technologies: haloscopes and helioscopes [56]. Axion haloscopes are sensitive to galactic halo axions with mass $m_a \sim$ µeV that can be converted to microwaves in applied magnetic fields within resonant cavities. Axion helioscopes are searching for solar axions originating from production in the Sun's magnetic field via the Primakoff effect [57]. In the presence of a strong magnetic field, solar axions with energy of order $\mathcal{O}$(keV) can be re-converted to X-rays via $a \to \gamma$. These X-rays

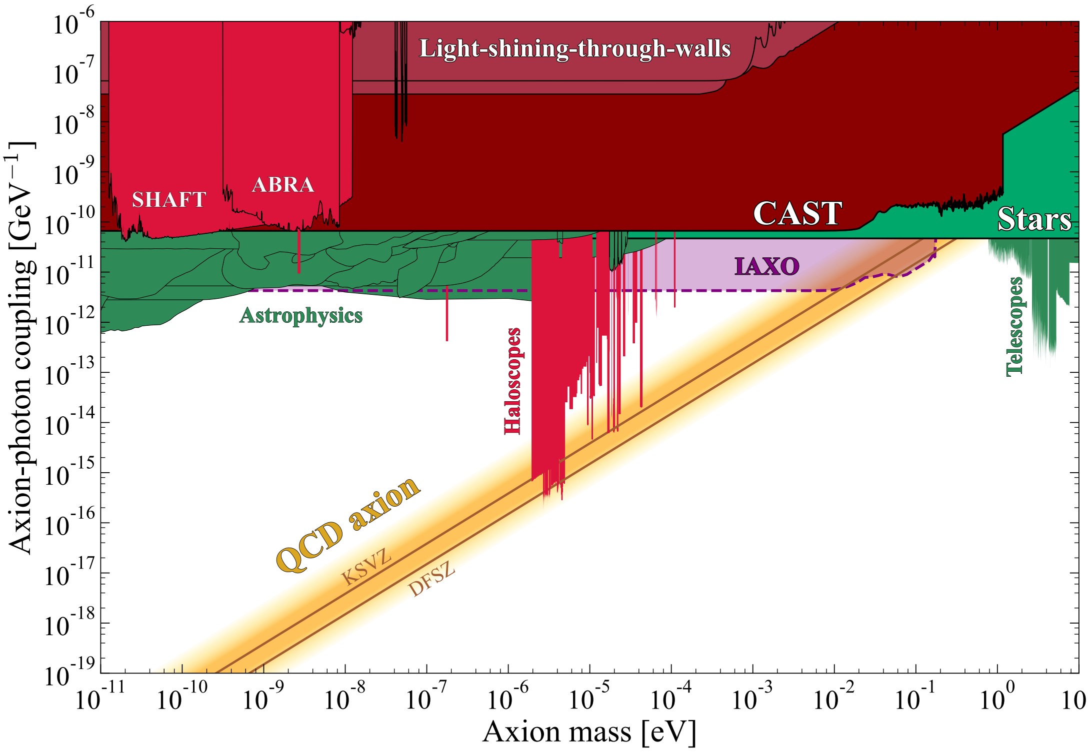

Figure 1.2.2: Axion-photon coupling $g_{a\gamma\gamma}$ constraints with axion mass m_a set by various terrestrial axion experiments and astrophysical observations. The bounds shown are from astrophysics observations (green), haloscope experiments (light red vertical bands) and helioscope experiments including CAST (dark red) and IAXO projections (dashed purple). KSVZ and DFSZ are two theoretical QCD axion models where $g_{a\gamma\gamma} \propto m_a$, with different coefficient values [62]. Figure created using the AxionLimits code [63].

are then recorded and analysed via X-ray telescopes.

The current landscape of measurements of the axion-photon coupling $g_{a\gamma}$ with axion mass m_a are shown in Figure 1.2.2. The current leading axion haloscope experiment is ADMX [58, 59], which is probing the QCD axion model parameter space. The CAST experiment has set the most stringent limits from helioscope experiments, with the larger next-generation IAXO experiment projected to push down further into the axion-photon coupling space, shown via the dashed purple line [60, 61].

1.2.3 Sterile neutrinos

Sterile neutrinos are hypothetical neutral heavy lepton (NHL) particles that could solve three major problems in physics: the neutrino mass scale, the matter-antimatter asymmetry in the Universe and also be a possible dark matter candidate [64, 65]. Sterile neutrinos emerge from considering BSM neutrinos with right-handed chirality that are separate to the three flavours of active left-handed Standard Model $SU(2)_L$ neutrinos $(\nu_e, \nu_\mu, \nu_\tau)$. Sterile neutrinos are named so as "sterile" refers to particles with no coupling to the weak interaction and "neutrinos" as the particles do not couple to the strong and electromagnetic interactions. Sterile neutrinos from this BSM theory emerge with a keV mass range that is suitable for the relic abundance of dark matter and are a viable dark matter candidate with the properties described in Section 1.2.1. Several neutrino physics experiments are looking for signatures of sterile neutrinos, with recent limits set by the MicroBooNe detector [66], CMS at the LHC [67] and the STEREO experiment [68].

1.2.4 Primordial black holes

Primordial black holes (PBHs) are a possible dark matter candidate [69, 70] that are thought to be formed by gravitational collapse in the early Universe [71, 72]. The mass of PBHs respective to the cosmological energy density at early times in the Universe is given by the relation:

$$M \sim \frac{c^3 t}{G} \sim 10^{15} \left(\frac{t}{10^{-23}\,\mathrm{s}} \right) \mathrm{g}, \tag{1.2.3}$$

where M is the PBH mass, t is time since the Big Bang in seconds, and G is the gravitational constant. Therefore, PBHs can span a huge mass range from formation at the Planck time $(10^{-43}\,\mathrm{s})$ with Planck mass $10^{-5}\,\mathrm{g}$ to those formed

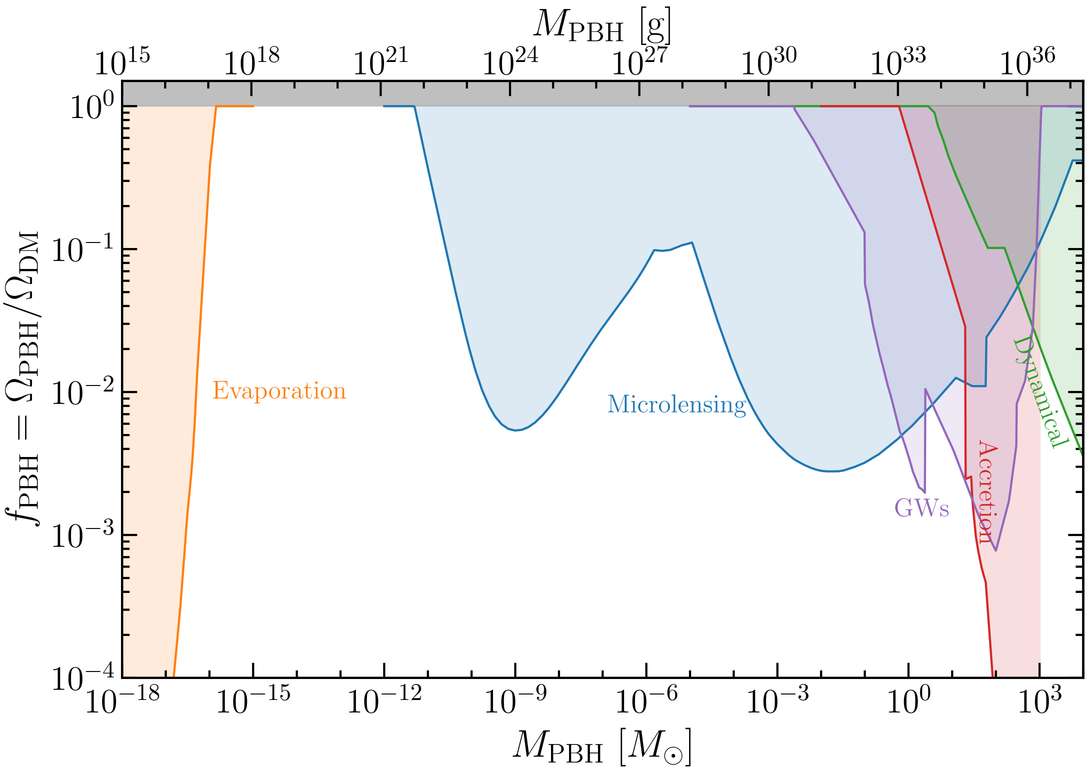

Figure 1.2.3: Constraints on the fraction of dark matter in the form of PBHs, f_{PBH}, as a function of PBH mass. Here, we assume that all PBHs have the same mass, i.e. the PBH mass is a delta function. The bounds shown are from evaporation (orange), microlensing surveys (blue), gravitational waves (purple), accretion (red) and dynamical effects (green). Figure created using the PBHbounds code [74].

1 s after the Big Bang having a mass of 10^5 $M_{\odot}$. Multiple possible formation mechanisms for primordial black holes exist and involve the gravitational collapse of large density fluctuations and inhomogeneities. PBHs are theoretical objects formed in the radiation dominated era of the Universe and therefore do not have as stringent mass limits adhering to black holes produced by stellar core collapse. This category of black holes were formed before Big Bang nucleosynthesis (BBN) and therefore do not contribute to the baryon energy density of the Universe. There is also a distinction that PBHs could account for some composite percentage of all dark matter in the Universe [73].

Hints for the existence of such black holes are provided by microlensing surveys of stars such as the EROS [75], MACHO [76] and OGLE [77] surveys aiming to detect the presence of massive astrophysical compact halo objects (MACHOs). More recently observation of gravitational waves (GWs) produced by black hole binary mergers have suggested the existence of a wide mass range of black hole binaries present in the local Universe [78]. In total 90 gravitational wave events have been observed using highly sensitive laser interferometers with the LIGO-Virgo-KAGRA Collaboration [79] since gravitational waves were first detected in 2015 [80]. Searches for PBH subpopulations within the LIGO-Virgo-KAGRA dataset are currently underway since first studied as a dark matter signature in 2016 [81, 82].

The tightest constraints on the fraction of PBHs as dark matter, $f_{\mathrm{PBH}} = \Omega_{\mathrm{PBH}}/\Omega_{\mathrm{DM}}$, from astrophysical observations including microlensing surveys and GWs are shown in Figure 1.2.3. Currently it appears that planetary, Solar and multi-Solar mass PBHs cannot make up all of dark matter. However, there is a range of masses, $10^{17}\,\mathrm{g} \lesssim M_{\mathrm{PBH}} \lesssim 10^{22}\,\mathrm{g}$, described as the "asteroid mass window" where PBHs could account for all of dark matter ($f_{\mathrm{PBH}} = 1$). Asteroid mass PBHs emit $\mathcal{O}$(MeV) gamma-rays via Hawking radiation [83], which could be directly detected by future MeV gamma-ray telescopes such as AMEGO [84, 85].

1.2.5 Weakly interacting massive particles

The production of dark matter in the early Universe can occur via thermal freeze-out, where a particle species chemically decouples from the hot dense particle plasma [30, 86]. A particle species chemically decouples from the plasma when the particle annihilation rate Γ_{ann} falls below the Hubble parameter, $H(t)$:

$$H(t) \geq \Gamma_{\mathrm{ann}} = n\langle\sigma_{\mathrm{ann}}v\rangle, \tag{1.2.4}$$

where n is the number density, and $\langle\sigma_{\mathrm{ann}}v\rangle$ is the average annihilation cross-section multiplied by the relative velocity. The relic abundance for a particular particle species can then be calculated by estimating the freeze-out temperature, and equating the number density of particles at freeze-out to the physical density of relic particles observed in the Universe today.

Considering weakly interacting massive particles we find that:

$$\Omega_\chi h^2 \simeq \frac{3 \times 10^{-27}\,\mathrm{cm}^3\,\mathrm{s}^{-1}}{\langle \sigma_{\mathrm{ann}} v \rangle}, \tag{1.2.5}$$

which is quoted as the present mass density for a general thermal WIMP, independent of WIMP mass [87].

To match the dark matter energy density observed in the Universe we find that:

$$\langle \sigma_{\mathrm{ann}} v \rangle_f \approx 3 \times 10^{-26}\,\mathrm{cm}^3\,\mathrm{s}^{-1}, \tag{1.2.6}$$

where f denotes value at time of freeze-out. For typical velocity values of $v \approx 0.1c$, the annihilation cross-section σ_{ann} is of order of the weak scale $\sim 10^{-36}\,\mathrm{cm}^2$. The coincidence that a weakly interacting particle can correctly reproduce the dark matter energy density is often referred to as the "WIMP miracle" [88, 89]. The time evolution of the dark matter thermal relic density during the expansion and cooling of the early Universe is shown in Figure 1.2.4. This connection between particle physics and cosmology has motivated and led to many searches for WIMP dark matter.

WIMPs are a highly motivated particle candidate which emerge from a BSM model called supersymmetry (SUSY) that addresses the hierarchy problem [87, 91, 92]. The basics of SUSY involve the introduction of a conserved quantity called R-parity. The introduction of this conserved quantity results in new supersymmetric particles that are paired with each SM particle that differ by half-integer spin. Therefore, each SM fermion now has a boson "supersymmetric partner", and vice versa. The Minimal Supersymmetric Standard Model (MSSM) introduces a minimum number of new particles, with the lightest supersymmetric particle (LSP)

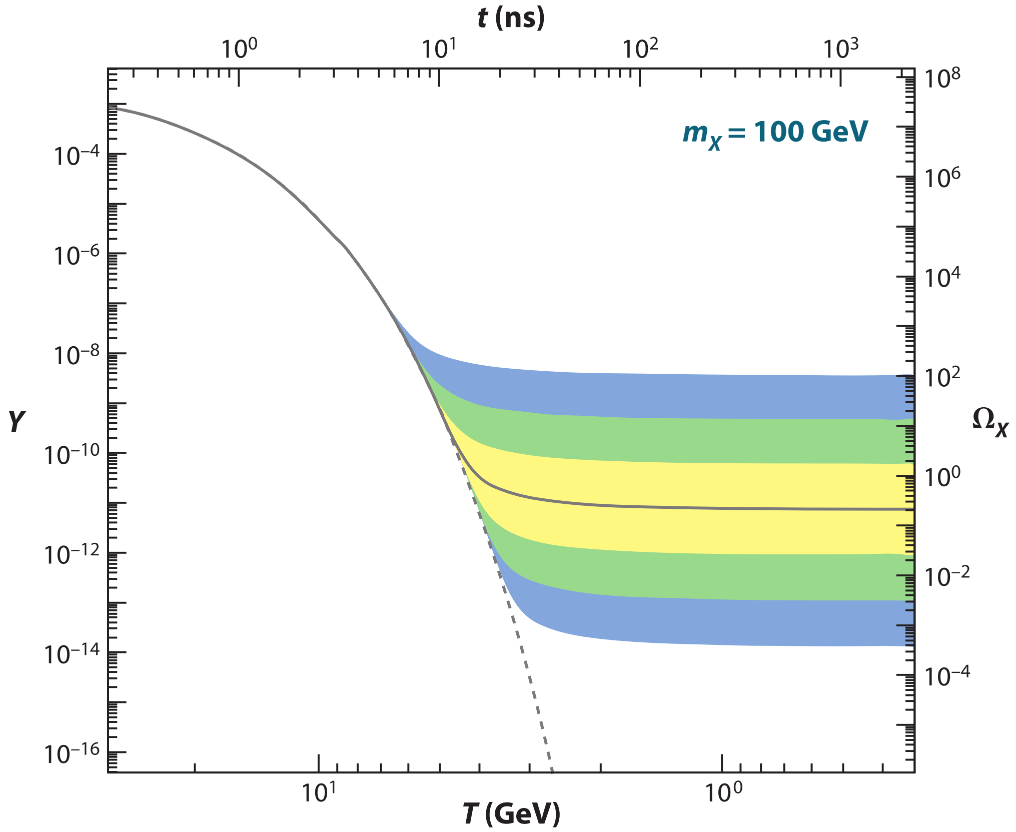

Figure 1.2.4: The WIMP yield Y as a function of temperature T during thermal freeze-out in the Universe for a heavy dark matter particle with mass $m_\chi = 100\,\mathrm{GeV}/c^2$. The solid grey line is for the annihilation cross-section that yields the correct relic density Ω_χ, and the yellow, green and blue contours vary from this value by factors of 10^1, 10^2 and 10^3, respectively. The dashed grey contour is the number density of a particle remaining in equilibrium. Figure taken from Ref. [90].

being stable, electrically neutral and interacting weakly with other SM particles. This makes the LSP an ideal dark matter candidate and is often referred to as the neutralino (denoted by the symbol χ).

1.3 Dark matter searches and experiments

Experimental methods for determining the particle nature of dark matter are grouped into three main categories: direct detection of scatters with nuclei using terrestrial detectors, indirect detection of dark matter annihilation products and production from Standard Model particles in colliders. These three search categories are shown in Figure 1.3.1. Here we will summarise some of the key

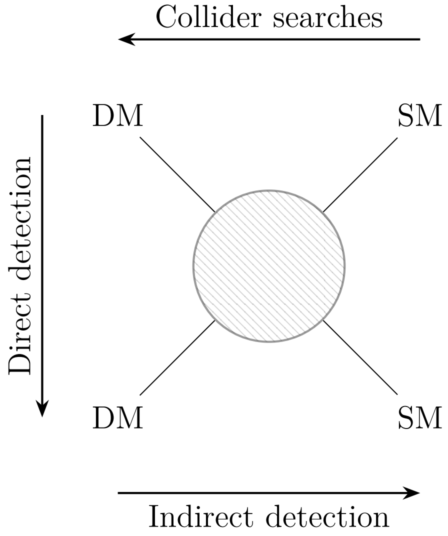

Figure 1.3.1: A schematic showing the three possible dark matter detection channels. The diagram can be read three ways by following the arrows shown for interactions of dark matter with Standard Model particles. These are production at colliders, scattering with a target material (direct detection), and dark matter self-annihilation into SM particles (indirect detection).

experiments that are leading the field of particle dark matter searches, with a particular focus on direct detection experiments.

1.3.1 Collider searches

Collider searches for dark matter are taking place at the Large Hadron Collider (LHC) based at CERN [93]. The LHC is currently the largest collider experiment on Earth, with a beam line ring circumference of 27 km. Two beams of particles are accelerated by a ring of superconducting magnets very close to the speed of light, and collide at four points along the ring corresponding to the locations of four particle detectors: ALICE, ATLAS, CMS and LHCb [94–97]. The LHC is in its third period of data-taking (Run 3), where two proton beams collide to produce pp collisions with a centre-of-mass energy of $\sqrt{s} = 13.6\,\text{TeV}$. By colliding protons at such high energies, the structure of fundamental particles in the Standard Model are studied, as well as possible extensions to this current theory of particle physics.

The production of dark matter particles could result from colliding together

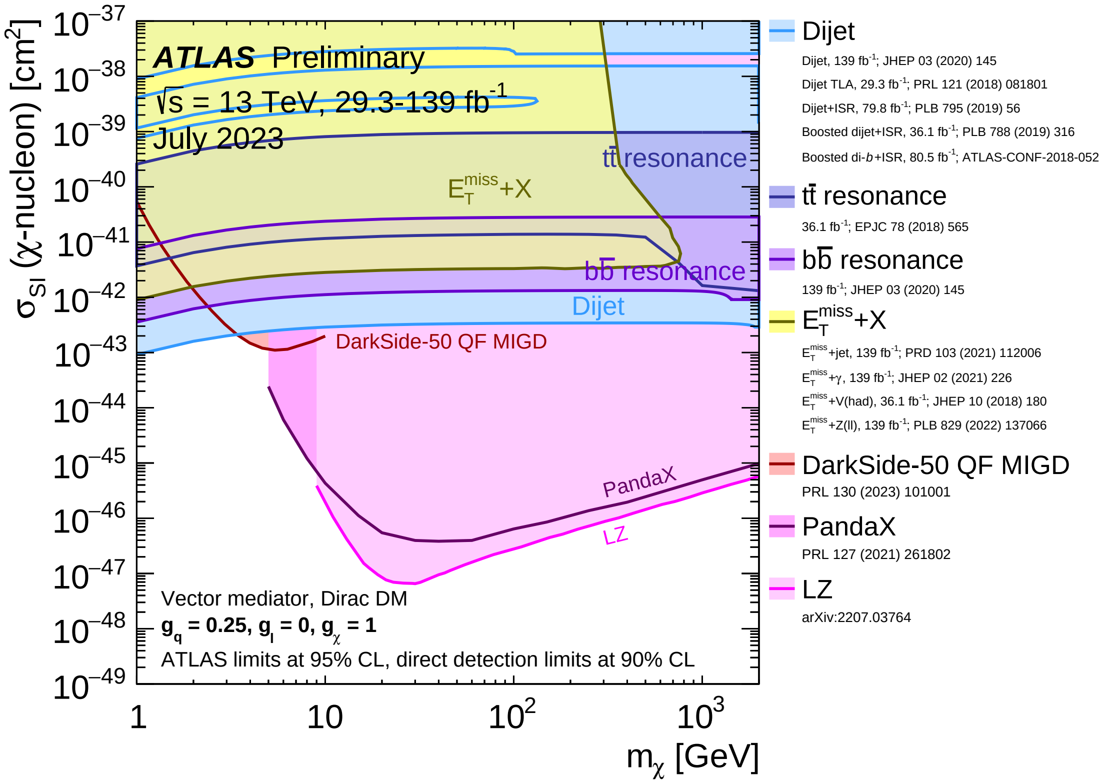

Figure 1.3.2: A comparison of the inferred limits with the constraints from direct-detection experiments on the spin-independent WIMP–nucleon scattering cross-section with ATLAS data in the context of the leptophobic vector mediator simplified model. Figure taken from Ref. [98].

Standard Model particles at these high energies. Collider production implies production of a mediator, i.e. a force carrier that connects the dark sector with the visible sector of the Standard Model. Similar to neutrinos, dark matter particles would pass through the detectors without interacting in trackers or calorimeters, therefore carrying away energy and momentum. For a given event, this is termed as "missing" transverse energy $\not{E}_T$ [99]. There are many possible BSM theories tested with observations at the LHC, such as Higgs and Z boson mediated electroweak interactions and the search for new supersymmetric particles [100].

No significant signatures of new dark matter physics have been seen at the LHC so far. Instead, the LHC has set limits of dark matter candidate masses, couplings and cross-sections. These limits can then be compared to measurements via other search methods such as direct detection limits, as shown in Figure 1.3.2. The

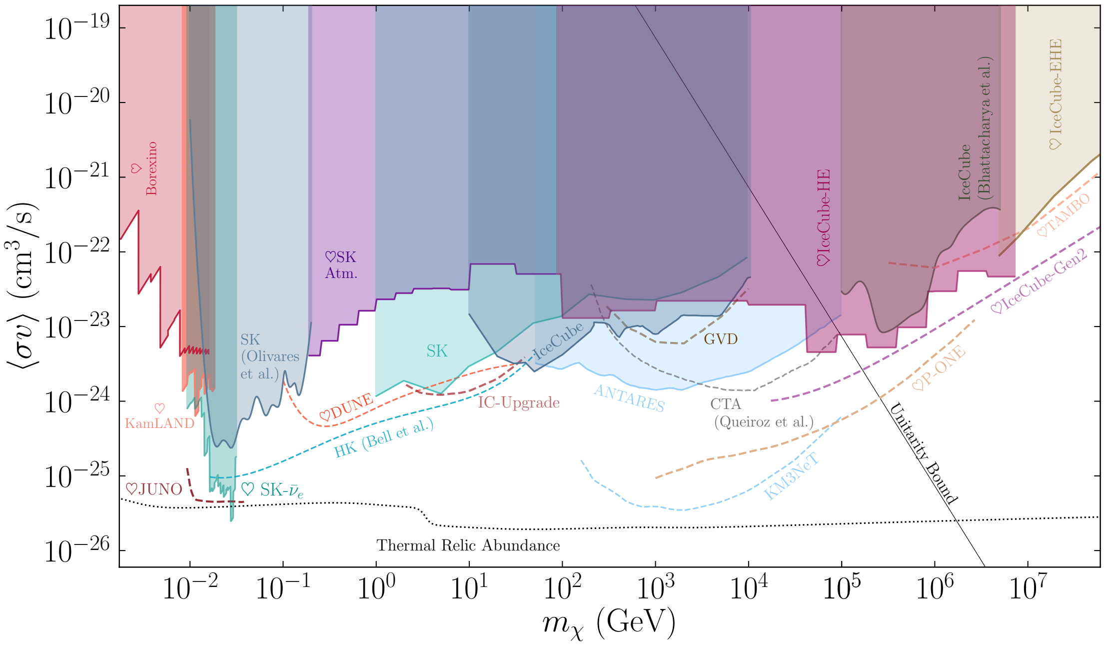

Figure 1.3.3: Limits of dark matter annihilation into neutrinos from 10^{-3} GeV to 10^{8} GeV. Solid and dashed lines represent 90% confidence level limits and sensitivities, respectively. The dotted line corresponds to the value required to explain the observed abundance via thermal freeze-out [89]. The straight diagonal line, labelled "unitarity bound", gives the maximum allowed cross-section for a non-composite DM particle [102, 103]. These results assume that 100% of the dark matter is composed of a given Majorana particle. Figure taken from Ref. [104].

"mono-X" search signature is a jet created from initial state radiation, produced back-to-back with respect to the dark matter. Dijet searches look for visible decays of the mediator and are able to place tight constraints on mediator masses in dark matter searches. Development of the High-Luminosity LHC (HL-LHC) will allow for collider searches to continue with an increased luminosity and therefore higher event rate, increasing our chances of observing rare physics events [101].

1.3.2 Indirect detection

Indirect searches for dark matter annihilation products assume that dark matter particles may annihilate with each other (or decay) into particles from the Standard Model [105]. Experiments that are conducting indirect searches often hunt for unexplained excess sources of neutrinos, antiprotons, positrons and gamma-rays produced by astrophysical sources. Measurements of a significant gamma-ray excess originating from the Galactic Centre at GeV scales are not easily accounted for by known astrophysical models and provide a compelling hint for annihilating dark matter [106–108].

Searches consist of space-based searches for excess radiation originating from the celestial bodies, the Sun, the Galactic Centre and dwarf spheroidal galaxies. Space-based searches include PAMELA [109], AMS-02 [110, 111] and Fermi LAT [112]. Existing ground-based neutrino experiments search for annihilation products via Cherenkov interactions produced when muons or neutrinos travel through water and ice. These experiments take advantage of large target exposure using natural mediums already available to use on Earth, and reconstruct signals using photosensors that can effectively record emission at corresponding wavelengths. Searches include IceCube [113], ANTARES [114] and the KM3NeT observatory [115, 116].

1.3.3 Direct detection

Direct detection aims to measure the scattering of dark matter particles with nuclei and set limits on the dark matter–nucleon cross-section as a function of dark matter masses. Here we will delve deeper into the mathematical formalism of direct detection techniques.

Dark matter is assumed to populate galaxies in dark matter halo structures, as inferred by measurements of spiral galaxy rotation curves discussed in Section 1.1.3. Properties of the Standard Halo Model (SHM) are used to mathematically formulate the WIMP flux on Earth. The galactic-frame velocity distribution is assumed to be a Maxwell-Boltzmann distribution:

$$f(v) \propto \exp\left(-\frac{|v^2|}{2\sigma_0^2} \right) \Theta(v_{\text{esc}} - |v|), \tag{1.3.1}$$

where σ_0 is the isotropic velocity dispersion and $v_0 = \sqrt{2}\,\sigma_0$. The velocity distribution is truncated by the Heaviside function Θ as objects with velocities exceeding the escape velocity $v_{\rm esc}$ are not gravitationally bound. A set of standard conventions are now in use in the direct detection community in order to accurately compare experimental limits, including values of astrophysical parameters in the SHM [117]. These values are: the local dark matter density, $\rho_0 = 0.3\,\mathrm{GeV\,cm^{-3}}$, $v_0 = 238\,\mathrm{km\,s^{-1}}$ and $v_{\rm esc} = 544\,\mathrm{km\,s^{-1}}$ [118–121]. Extensions to the SHM motivated by observations taken by the Gaia satellite also exist, namely the SHM^{++} [122].

Since WIMPs are presumed to carry no electric charge interactions with nuclei occur by elastic scattering off the nucleus [118]. The momentum transfer creates a nuclear recoil (NR) signal which may be detectable. The expected differential WIMP scattering event rate off a target nucleus is given by:

$$\frac{\mathrm{d}R}{\mathrm{d}E_{\rm NR}} = \frac{\rho_0 M}{m_N m_\chi}\int_{v_{\rm min}}^{v_{\rm esc}} v f(v)\frac{\mathrm{d}\sigma}{\mathrm{d}E_{\rm NR}}\mathrm{d}v, \tag{1.3.2}$$

where $E_{\rm NR}$ is the NR energy, m_χ is the WIMP mass, m_N is the target nucleus mass, σ is the scattering cross-section and M is the total target mass of the detector.

Considering scattering kinematics, the minimal velocity required for a WIMP-induced NR of energy $E_{\rm NR}$ to occur is:

$$v_{\rm min} = \sqrt{\frac{E_{\rm NR} m_N}{2}\frac{(m_N + m_\chi)^2}{(m_N m_\chi)^2}} = \sqrt{\frac{E_{\rm NR} m_N}{2}\frac{1}{\mu^2}}, \tag{1.3.3}$$

where μ is the reduced mass of the nucleus–WIMP system. The upper limit of the integral is given by the escape velocity of the galaxy, $v_{\rm esc}$, relating to the halo velocity distribution in Equation 1.3.1.

The WIMP–nucleus differential cross-section given in Equation 1.3.2 consists of two components that detail WIMP interactions with nuclei: the spin-independent (SI) interaction and the spin-dependent (SD) interaction. These components de-

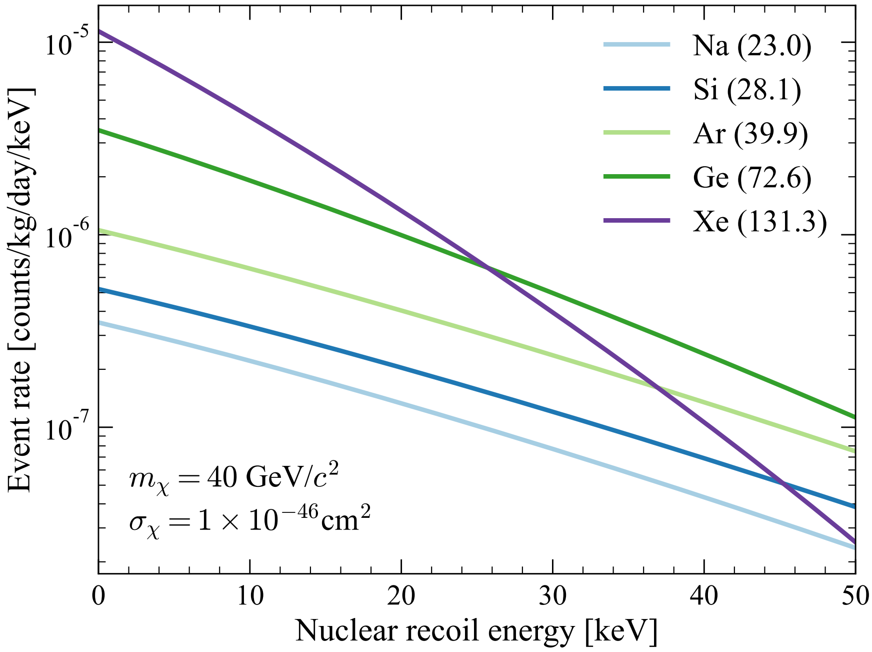

Figure 1.3.4: Event rate for WIMP scattering in several commonly used direct detection materials: sodium, silicon, argon, germanium and xenon. The WIMP mass and WIMP–nucleon cross-section are set to be $40\,\mathrm{GeV}/c^2$ and $1 \times 10^{-46}\,\mathrm{cm}^2$, respectively. Figure created using the wimprates code [123].

scribe WIMP coupling to the mass of the nucleus and coupling to the spin of the nucleus, respectively. Using this generalised effective field theory (EFT), the differential cross-section can be separated into two parts:

$$\frac{\mathrm{d}\sigma}{\mathrm{d}E_{\mathrm{NR}}} = \left(\frac{\mathrm{d}\sigma}{\mathrm{d}E_{\mathrm{NR}}}\right)_{\mathrm{SI}} + \left(\frac{\mathrm{d}\sigma}{\mathrm{d}E_{\mathrm{NR}}}\right)_{\mathrm{SD}} = \frac{m_N}{2v^2\mu^2}\Big(\sigma_{\mathrm{SI}}F^2_{\mathrm{SI}}(E_{\mathrm{NR}}) + \sigma_{\mathrm{SD}}F^2_{\mathrm{SD}}(E_{\mathrm{NR}})\Big), \tag{1.3.4}$$

where F_{SI} and F_{SD} are the SI and SD form factors, respectively. The SI cross-section is given by:

$$\sigma_{\mathrm{SI}} = \frac{\mu^2}{\mu_n^2}\sigma_n A^2, \tag{1.3.5}$$

where the subscript n now refers to the WIMP–nucleon system. Equation 1.3.5 assumes that the WIMP coupling to protons and neutrons are equivalent. This allows direct detection experiments using different targets to directly compare cross-section results. The A^2 dependence on the cross-section leads to heavier target nuclei observing high rates of WIMP interactions, however, recoil energies are smaller which leads to effects on detection thresholds. WIMP scattering rates for various materials are shown in Figure 1.3.4.

1.3.4 Underground research facilities

Direct detection of dark matter particles with detectors based on Earth requires very low background rates. Cosmogenic backgrounds produced in the Earth's atmosphere require additional shielding, which means hosting experiments in facilities located underground (see Figure 1.3.5) [125, 126]. Two types of facilities exist; accessed either by vertical shafts for subterranean sites or by horizontal access for sites located within mountains.

Shielding against cosmogenic muons is vital to reduce the muon-induced neutron background that could mimic a WIMP signal in a direct detection experiment. In Figure 1.3.6 the muon flux at various depths of some underground facilities is shown, where m.w.e. stands for metre water equivalent, which is a standardised unit used to quote attenuation of cosmic rays due to rock overburden. While the depth increases from 1500 m.w.e. to 6720 m.w.e., the muon flux decreases by more

Figure 1.3.5: A map of deep underground laboratories worldwide. The small red circles highlight sites under construction or proposed as of 2020. Figure taken from Ref. [124].

than three orders of magnitude. This plot demonstrates the additional coverage that a flat overburden geometry provides, whereas in mountain ranges we need to account for their particular size and geometry due to additional angular exposure. The information relating to several facilities that host dark matter experiments are shown in Table 1.3.1.

Table 1.3.1: Muon flux values at the locations of various underground research facilities. Values for the integrated total muon flux are taken from Ref. [127–135].

Category	Facility	Location	Overburden [m.w.e.]	Total muon flux [$\mathrm{cm}^{-2}\,\mathrm{s}^{-1}$]
Mountain	Kamioka	Kamioka, Japan	2700	$(1.58 \pm 0.21) \times 10^{-7}$
	LNGS	Gran Sasso, Italy	3800	$(3.432 \pm 0.003) \times 10^{-8}$
	LSM	Modane, France	4800	$(6.25 \pm 0.23) \times 10^{-9}$
	CJPL	Sichuan, China	6720	$(3.53 \pm 0.22) \times 10^{-10}$
Flat	Soudan	Minnesota, USA	1950	$(1.65 \pm 0.10) \times 10^{-7}$
	Boulby	North Yorkshire, UK	2850	$(4.09 \pm 0.15) \times 10^{-8}$
	SURF	South Dakota, USA	4300	$(5.31 \pm 0.17) \times 10^{-9}$
	SNOLAB	Ontario, Canada	5890	$(3.31 \pm 0.09) \times 10^{-10}$

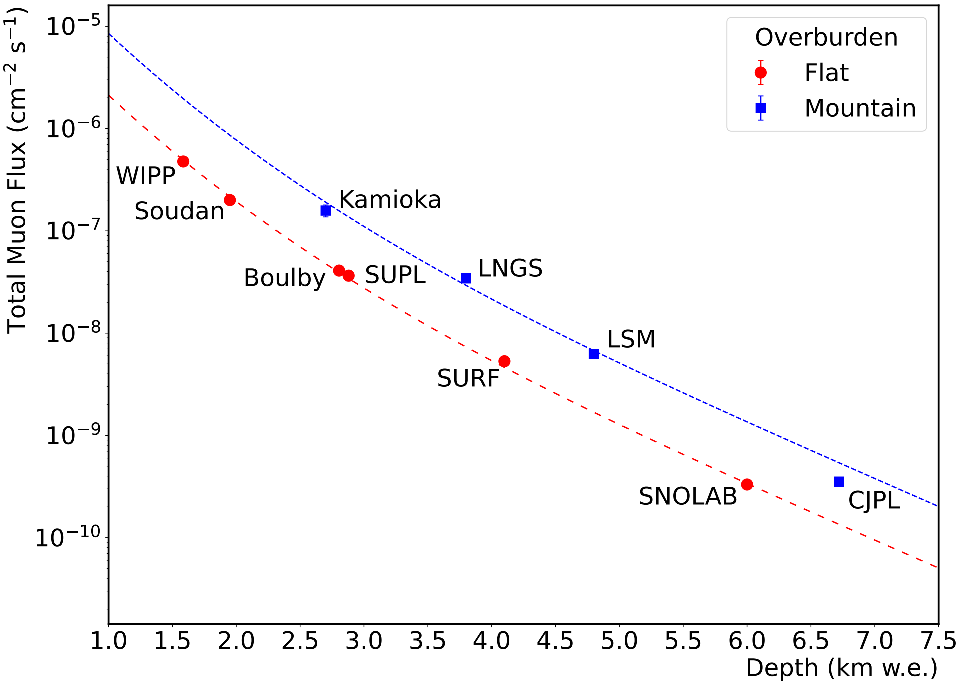

Figure 1.3.6: Muon flux as a function of depth at various underground research facilities. Empirical fits are shown for flux values reported at both flat and mountain range overburdens. Figure taken from Ref. [136].

1.3.5 Direct detection experiments

Direct detection technologies usually exploit scintillation, ionisation or other solid state phenomena, such as the production of phonons, to search for dark matter signals. The most advanced detectors use a combination of two of these primary channels. No one type of detector technology would be able to probe the entire mass range of dark matter candidates, which has led to a huge variety of experimental methods being developed in order to the search for dark matter [88]. Direct detection technologies include (among others):

- **Noble liquid detectors:** Noble liquid detectors utilise scintillation properties of noble liquids to collect light signals from particle interactions in the target material. Single phase detectors measure the primary scintillation signal only. Spherical detectors are surrounded by photomultipliers in 4π to achieve high light yields. Single phase detectors include MiniCLEAN [137], DEAP-3600 [138] and XMASS [139]. Dual-phase time projection chambers (TPCs) collect secondary charge signals by drifting ionisation electrons with applied electric fields, allowing for 3D event reconstruction. Argon detectors include ArDM [140], DarkSide-50 [141–143] and the upcoming DarkSide-20k experiment [144]. Current xenon target experiments include LUX-ZEPLIN [145, 146], XENONnT [147–149] and PandaX-4T [150]. Noble liquid time projection chambers are the technology we will focus on and will be explained in further detail in Chapter 2.

- **Bubble chamber detectors:** Bubble chamber detectors used superheated liquids as the target material for dark matter interactions, that are usually refrigerants such as C_3F_8. Energy deposits in the target volume will lead to a phase transition of the liquid and will begin the formation of a bubble. Detector parameters can be tuned so that only interactions by α particles or neutrons can create bubbles, not radiation from β or γ sources. 3D reconstruction of events is done with multiple imaging cameras. Examples of such bubble chamber experiments include those produced by the PICO Collaboration: PICO-60 and PICO-40L [151–153].

- **Charge-coupled device sensors:** Silicon skipper charge-coupled device (CCD) sensors are sensitive to low-mass dark matter signals on the MeV scale, by exploiting dark matter-electron scattering in semiconductor materials with charge resolutions of 1-2 e^-. Readout of ionisation particle tracks in CCDs allow for 3D event reconstruction and particle identification. Current experiments include DAMIC-SNOLAB and DAMIC-M at Laboratoire Souterrain de Modane (LSM) [154, 155] and SENSEI [156], with development of the large-scale Oscura experiment on the horizon [157].

- **Solid-state cryogenic detectors:** Solid-state targets made from Si and Ge can use applied bias voltages to gain particle discrimination sensitivity. These sensors are sensitive to dark matter masses on the scale of GeV and below, aiming to probe new parameter space with observing dark matter-electron interactions. Collaborations include SuperCDMS [158–160] and EDELWEISS [161, 162] which are developing multiple technologies at small and large target scales. CRESST-III uses a cryogenically cooled $CaWO_4$ scintillating crystal to simultaneously measure a phonon (heat) and a scintillation light signal, setting DM–nucleon cross-section limits in the sub-GeV mass range [163].

- **Inorganic crystal detectors:** Arrays of low-background NaI(Tl) and CsI(Tl) inorganic crystals coupled to PMTs are used to detect scintillation signals. Examples include DAMA/LIBRA [164], COSINE-100 [165, 166] and ANAIS [167]. DAMA/LIBRA now quote an observation of annular modulation to 13.7σ with combined exposure, which is in direct tension with results from other dark matter experiments [168]. The SABRE North and

SABRE South experiments [169–171] aim to disentangle seasonal or site specific effects of modulation signals using twin detectors in the Northern and Southern Hemispheres. The COSINUS experiment was the first to cryogenically cool NaI(Tl) to $\sim$ mK temperatures in order to create a calorimeter that is able to record both scintillation light and phonon signals for particle discrimination [172, 173]. First data-taking for COSINUS is due to start in 2024.

- **Spherical proportional counters:** The NEWS-G Collaboration operates spherical proportional counters (SPCs) that are filled with light noble gases. Previous experiments have been located at LSM, and a new SPC is to be fabricated at SNOLAB [174, 175]. Use of light targets such as H, He and Ne optimises sensitivity to lower mass dark matter particles in the sub-GeV – GeV range. The use of gas mixtures, such as neon and methane (CH_4) allows for further signal discrimination due to the mass dependence of the dark matter interaction cross-section. Advantages of this novel technology include high amplification gain, single-electron detection sensitivity leading to low thresholds and the use of low intrinsic background materials [176]. The physics potential for DarkSPHERE, a proposed 3 m SPC to be built at Boulby Underground Laboratory, has been explored [177].

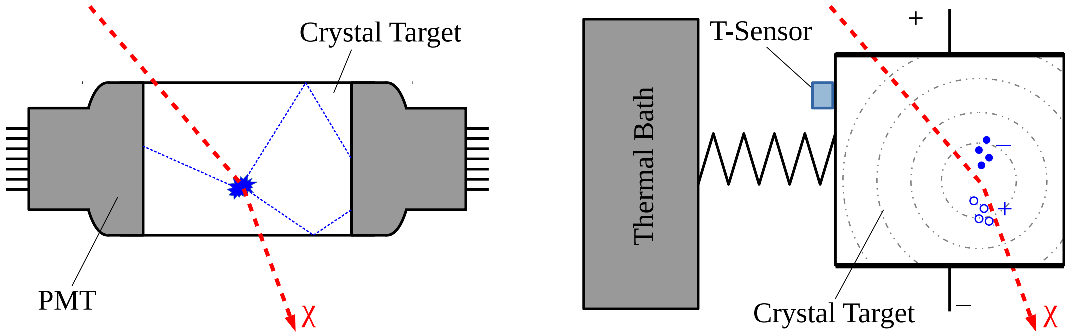

(a) Inorganic crystal detector.

(b) Solid-state cryogenic detector.

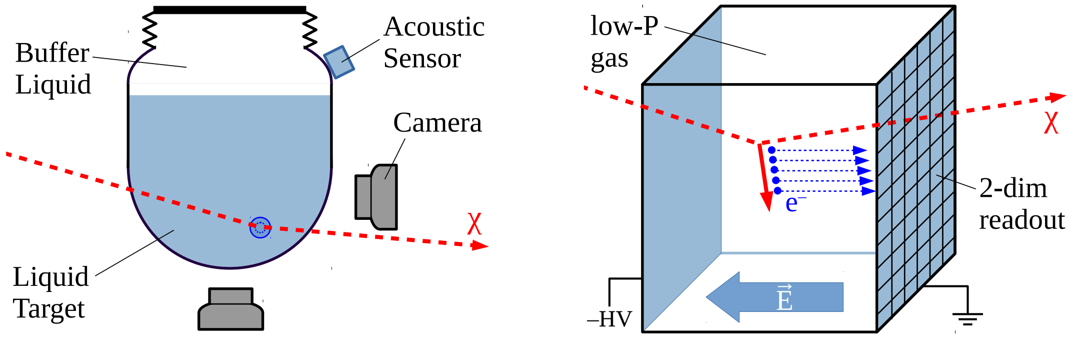

(c) Bubble chamber.

(d) Directional drift detector.

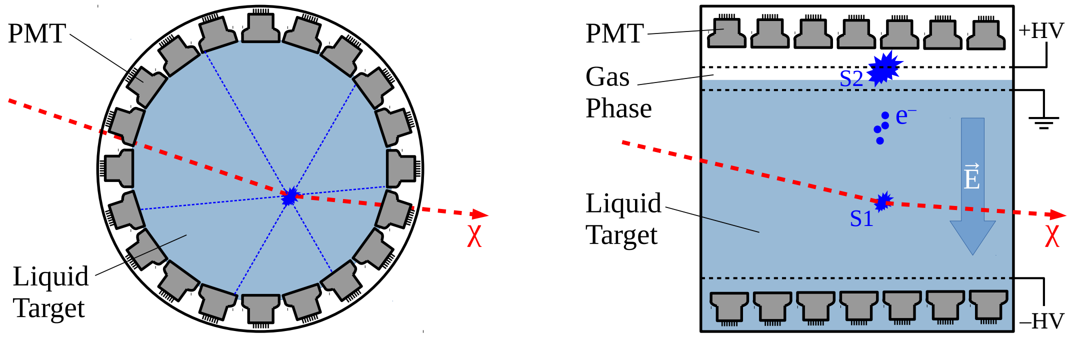

(e) Single-phase noble liquid detector.

(f) Dual-phase time projection chamber.

Figure 1.3.7: Schematics of different direct detection technologies and the respective signal readout systems. For each diagram WIMP interactions are indicated by the red-dashed line. Figures taken from Ref. [29].

1.3.6 Status of the field

The first results from the LUX-ZEPLIN experiment have set the current best limit for spin-independent scattering at 36 GeV/c^2, rejecting cross-sections above $9.2 \times 10^{-48}\,\text{cm}^2$ at 90% confidence level (CL). This result is presented alongside various exclusion curves from other direct detection experiments in Figure 1.3.8. This thesis will focus on the LUX-ZEPLIN experiment discussing the detector technologies, background mitigation techniques and analysis methods used to achieve a world-leading dark matter search result.

Noble liquid detectors stand as the current leading technology for direct detection. Primarily sensitive to WIMP masses ranging from a few GeV/c^2 up to the TeV/c^2 scale, they also excel in probing sub-GeV DM masses through low-threshold searches and the Migdal effect [178]. This versatility renders noble liquid detectors sensitive across a broad spectrum of dark matter masses, positioning them competitively against results from smaller cryogenic experiments.

Current noble liquid searches are beginning to head towards an irreducible neutrino background: the neutrino fog [179, 180]. This is due to coherent elastic neutrino–nucleus scattering (CEνNS) [181], which can mimic a dark matter scatter with the target nuclei. Below the line indicating the edge of the neutrino fog contours are plotted for each source of neutrinos: atmospheric, geothermal, reactor and the diffuse supernova neutrino background (DSNB). Solar neutrinos from nuclear fusion reaction chains in the Sun are also shown: *pp*, *pep*, *hep*, ^{7}Be, ^{8}B and CNO. In Figure 1.3.8, the opacity of the neutrino fog is coloured by the parameter n, which is the gradient of discovery limit. This index is quantified by considering how the discovery limit σ decreases with increasing exposure, and thus the number of background events N. Neutrinos will become a significant background source for large exposure third-generation (G3) detectors as the size and sensitivity of direct detection experiments improves.

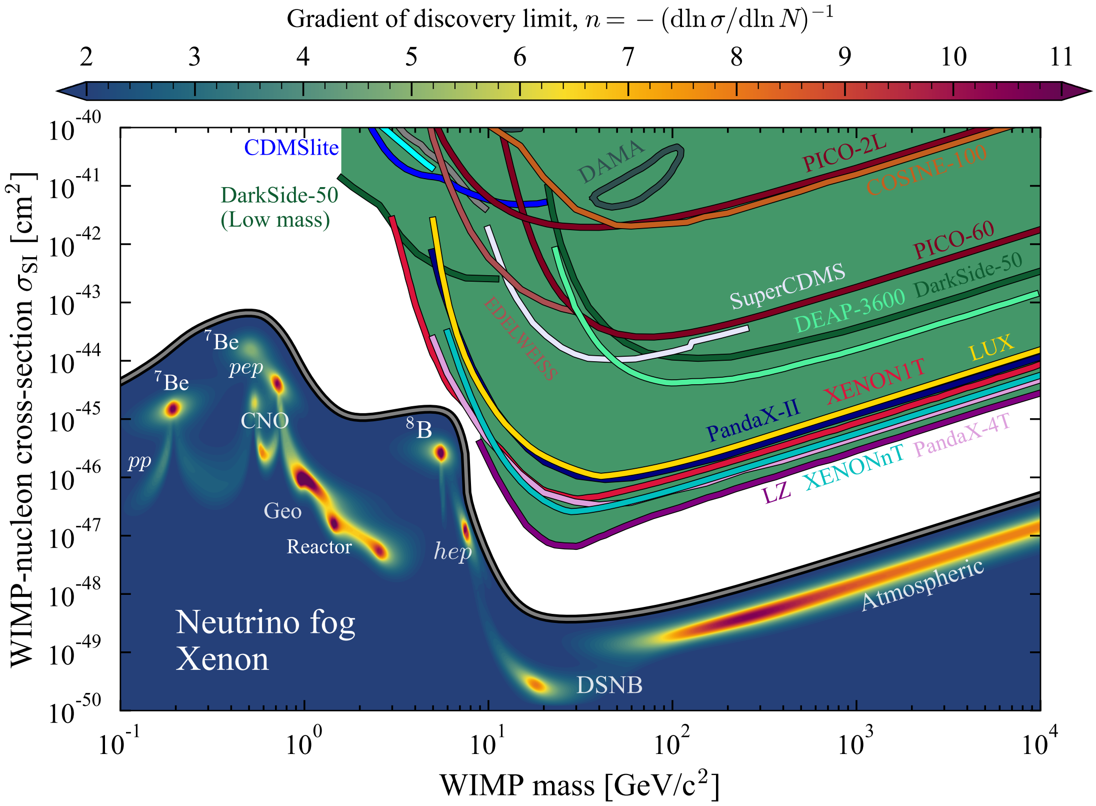

Figure 1.3.8: Spin-independent WIMP–nucleon cross-section limits set by various direct detection experiments. The neutrino fog is shown for coherent scattering of neutrinos with xenon nuclei [179]. Below the line indicating the edge of the neutrino fog contours are plotted for each source of neutrinos: atmospheric, geothermal, reactor, solar and the diffuse supernova neutrino background (DSNB). The gradient of discovery limit $n = 2$, under typical Poisson subtraction where $\sigma \propto 1/\sqrt{N}$. Figure adapted from Ref. [179] to include recent limits published by LZ [123], XENONnT [148] and PandaX-4T [150].

Dark matter remains one of the key unknowns at the cosmic frontier of particle physics. The need for a next-generation dark matter detectors is strongly acknowledged and accepted throughout the international High Energy Physics (HEP) community. Detailed plans to probe the cosmic frontier, including new searches for the classic WIMP via time projection chamber technology, have been outlined in reports such as the Snowmass 2021 cosmic frontier report and the Astro Particle Physics European Consortium (APPEC) dark matter report [88, 182]. Plans for a multi-tonne G3 xenon observatory are in progress within the XLZD Consortium between XENON, LUX-ZEPLIN and DARWIN [183–185].

2 The LUX-ZEPLIN experiment

The LUX-ZEPLIN (LZ) detector is a second-generation dark matter detector that uses a dual-phase xenon time projection chamber with the primary aim of directly detecting WIMPs [186]. It is located in the Davis cavern at the 4850' level (4300 m.w.e.) of the Sanford Underground Research Facility (SURF) in Lead, South Dakota, USA [187].

LZ is an ultra-low background experiment that is not only sensitive to physics signals from WIMP scattering, but will also have sensitivity to other rare physics events. These searches include more generic elastic scattering effective field theories, low-energy electron signals that could be produced from solar axions and ALPs [188, 189] and low-threshold Migdal searches [190]. In addition to dark matter searches, LZ is also a neutrino physics observatory. Neutrino studies possible with LZ include observations of solar neutrinos in addition to the extremely rare processes of two-neutrino and neutrinoless double electron capture (DEC) [191] of ^{124}Xe and ^{126}Xe and two-neutrino and neutrinoless double-beta decay ($0\nu\beta\beta$) of ^{134}Xe and ^{136}Xe isotopes [192, 193].

In this Chapter, the properties of xenon that make it an ideal target for direct detection experiments will be discussed, followed by an outline of particle interaction mechanisms in xenon. Subsequently, an overview of dual-phase time projection chamber detector technologies utilised in direct detection experiments that have been developed over several decades will be presented. Finally, the LUX-ZEPLIN experiment will be introduced in detail, and the results from the first science run of the experiment will be reported.

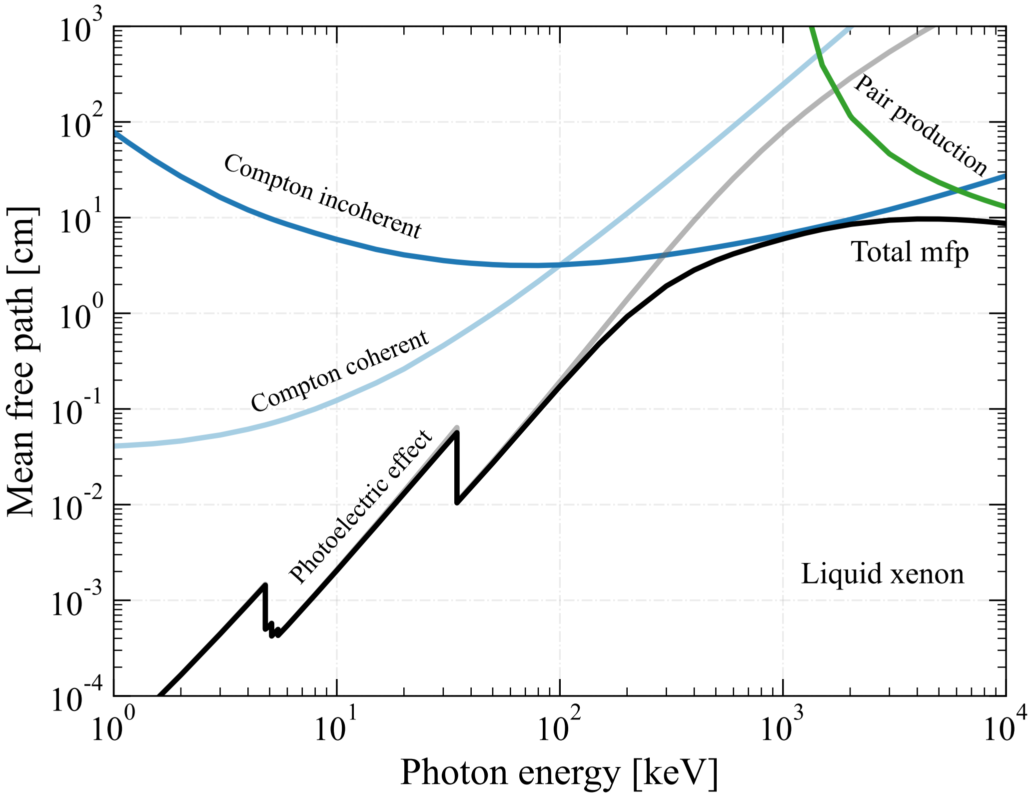

Figure 2.1.1: The mean free path of photons in liquid xenon as a function of incident gamma energy. The total mean free path is shown by the black line, as well as the individual photon interaction processes that contribute. Figure made using data provided by NIST [194].

2.1 Particle interactions in xenon

2.1.1 Properties of xenon

In order to characterise signals from WIMP scattering with nuclei, it is important to consider the properties of the target material used. Xenon has a high mass number (131.3 u), which increases the sensitivity of SI WIMP–nucleon scattering due to the A^2 dependence on the interaction cross-section as described in Equation 1.3.5. Xenon provides a high event rate for low nuclear recoil energies, whilst still offering a sustainable event rate at higher NR energies. The event rates for xenon in comparison to other typical target materials are shown in Figure 1.3.4.

Natural xenon also contains two neutron-odd isotopes: ^{129}Xe and ^{131}Xe, with

26.4% and 21.2% natural abundance, respectively [195]. The presence of an unpaired neutron gives these two isotopes non-zero nuclear spin, therefore searches using xenon as the target material are also sensitive to SD WIMP interactions. This also allows xenon direct detection experiments to report competitive sensitivity limits to WIMP–neutron scattering, as well as WIMP–proton scattering.

Liquid xenon (LXe) is a relatively high density material with $\rho = 2.888\,\mathrm{g\,cm^{-3}}$. This is a desirable physical property when paired with a high-Z element, as it results in the self-shielding property of LXe [196]. Due to the high density, gamma-rays travel distances on order of a few centimetres before being scattered by interactions with xenon nuclei. Figure 2.1.1 shows the mean free path distribution as a function of incident gamma energy for photon interactions in LXe [194]. These interaction lengths are much smaller than the dimensions of the detector and can therefore be rejected when they are scattered multiple times in the liquid xenon volume. This self-shielding property is especially important when considering fiducialisation of the active volume of a LXe TPC and the scalability to build large TPCs whilst maintaining background rejection capability [184].

2.1.2 Xenon microphysics

The following Section details an overview of xenon microphysics, and explains the processes that causes particles scattering with xenon nuclei to produce observable physics signals. This process is analogous for noble elements including He, Ne, Ar and Xe; with argon and xenon being the most commonly used target materials in direct detection experiments. This discussion follows material presented in Ref. [197].

Particles interacting in liquid xenon can scatter off a xenon nucleus or an atomic electron, resulting in either nuclear recoils (NR) or electron recoils (ER), respectively. The dominant background to the WIMP search are ER events caused by scatters of β and γ particles. NR events are produced by scattering of α

particles and neutrons and are problematic as they are indistinguishable from a WIMP signal.

Energy transfer of recoiling nuclei and electrons is split between three primary channels: ionisation, excitation and heat. The proportion of energy split into these channels is different for ER and NR signals, allowing for particle discrimination based on observed ionisation and excitation signatures. It should be noted that for NR events, a significant proportion of energy is attributed to the recoil itself and is dissipated as heat.

The excitation of xenon (Xe^*) caused by the impact of incoming particles results in the formation of a strongly bound diatomic molecule in an excited state, known as excimers (Xe_2^*) [198, 199]. The excimer molecule then dissociates by transitions from excited states to the ground state. This dissociation releases vacuum ultraviolet (VUV) scintillation photons, which are the primary scintillation signal and often referred to as an S1 signal. Primary scintillation light can be produced by both excited and ionised xenon atoms as a result of ER and NR interactions. Here we will describe how excitation and ionisation processes create primary scintillation light.

The excitation process can be displayed by the following steps, considering an electron as the incoming particle:

$$\begin{aligned}
\mathrm{e}^- + \mathrm{Xe} \rightarrow \mathrm{Xe}^* + \mathrm{e}^- &\qquad \text{impact excitation} \\
\mathrm{Xe}^* + \mathrm{Xe} \rightarrow \mathrm{Xe}_2^{*,\nu} &\qquad \text{excimer formation} \\
\mathrm{Xe}_2^{*,\nu} + \mathrm{Xe} \rightarrow \mathrm{Xe}_2^* + \mathrm{Xe} &\qquad \text{relaxation} \\
\mathrm{Xe}_2^* \rightarrow \mathrm{Xe} + \mathrm{Xe} + \gamma &\qquad \text{VUV emission}
\end{aligned}$$

Here the superscript ν is used to distinguish excited states with vibrational excitation ($\mathrm{Xe}_2^{*,\nu}$), from purely electronic excitation where $\nu = 0$ (Xe_2^*). The vibrational relaxation is mainly non-radiative, but it should be noted that emission of infrared photons is also possible by atomic or excimer transitions [200].

The alternative VUV luminescence process to direct excitation is caused by the ionisation and recombination of ionisation electrons and positive xenon ions. The ionisation process is displayed by the following steps, again considering an electron as the incoming particle:

$$\begin{aligned}
\mathrm{e}^- + \mathrm{Xe} &\rightarrow \mathrm{Xe}^+ + 2\mathrm{e}^- && \text{ionisation}\\
\mathrm{Xe}^+ + \mathrm{Xe} + \mathrm{Xe} &\rightarrow \mathrm{Xe}_2^+ + \mathrm{Xe} &&\\
\mathrm{e}^- + \mathrm{Xe}_2^+ &\rightarrow \mathrm{Xe}^{**} + \mathrm{Xe} && \text{recombination}\\
\mathrm{Xe}^{**} + \mathrm{Xe} &\rightarrow \mathrm{Xe}^{*} + \mathrm{Xe} + \text{heat} &&\\
\mathrm{Xe}^{*} + \mathrm{Xe} + \mathrm{Xe} &\rightarrow \mathrm{Xe}_2^{*} + \mathrm{Xe} + \text{heat} &&\\
\mathrm{Xe}_2^{*} &\rightarrow \mathrm{Xe} + \mathrm{Xe} + \gamma && \text{VUV emission}
\end{aligned}$$

The excimer Xe_2^* can relax to the ground state via transitions from one of the two lowest electronic excited states: the singlet state ${}^1\Sigma_u^+$ and the triplet state ${}^3\Sigma_u^+$. Transitions from the singlet and triplet excited state to the ground state, given by ${}^1\Sigma_u^+ \rightarrow^1 \Sigma_g^+$ and ${}^3\Sigma_u^+ \rightarrow^1 \Sigma_g^+$, decay on two different time scales. The singlet lifetime is reported to be 3.1 ns and the triplet lifetime as 24 ns [201]. For liquid argon the difference between the singlet and triplet lifetimes is more pronounced ($\sim$ 7 ns and 1.6 µs, respectively [202]) which allows for pulse shape discrimination (PSD) to be used for particle identification [203]. PSD is harder to achieve for liquid xenon experiments as the time difference between singlet and triplet states is much smaller.

For liquid xenon the VUV scintillation photons have a wavelength centred around 175 nm [204], while some previous measurements also report a value closer to 178 nm [198]. These VUV photons are not reabsorbed by the target material. Therefore, xenon is transparent to its own prompt scintillation light. The light from the S1 signal can be detected by photosensor devices installed in detectors.

Recombination in liquid xenon is measured to be a much longer process, that has a lifetime on the order of several µs [205]. Applied electric fields can be utilised to drift ionisation electrons away from ionisation interaction sites to avoid recombination. Secondary light signals, known as S2 signals, are produced by accelerating the ionisation electrons from the liquid phase into a gaseous phase by using a high voltage extraction field.

2.2 Dual-phase time projection chambers

2.2.1 Conceptual overview

Dual-phase time projection chambers that utilise rare noble liquid and gaseous phases have set competitive limits on WIMP–nucleon interactions for several decades [206–208]. The scalability of dual-phase TPCs has allowed for several collaborations, including DarkSide, LUX, PandaX, ZEPLIN and XENON, to build a successive series of detectors that are able to reject more parameter space due to increased target exposure. The rejection of this parameter space by limits set by several direct detection experiments that use TPCs are shown in Figure 1.3.8.

The LUX-ZEPLIN experiment uses a dual-phase TPC in order to detect WIMP scattering interactions with xenon nuclei. An example of a scattering interaction in a TPC is visualised in Figure 2.2.1. The TPC consists of a volume of liquid xenon (LXe) contained within a cylindrical volume and a smaller gaseous xenon (GXe) region located above the liquid. A vertical electric field is applied across the LXe volume. Photosensor arrays, in this case photomultiplier tubes (PMTs), are located at the top and bottom of the xenon volume.

The initial scatter of incoming particles with xenon nuclei produces scintillation light via the processes outlined in Section 2.1.2. The scatter produces primary scintillation light (S1) and ionisation electrons. The ionisation electrons are drifted away from the interaction site and towards the gaseous layer by the applied electric

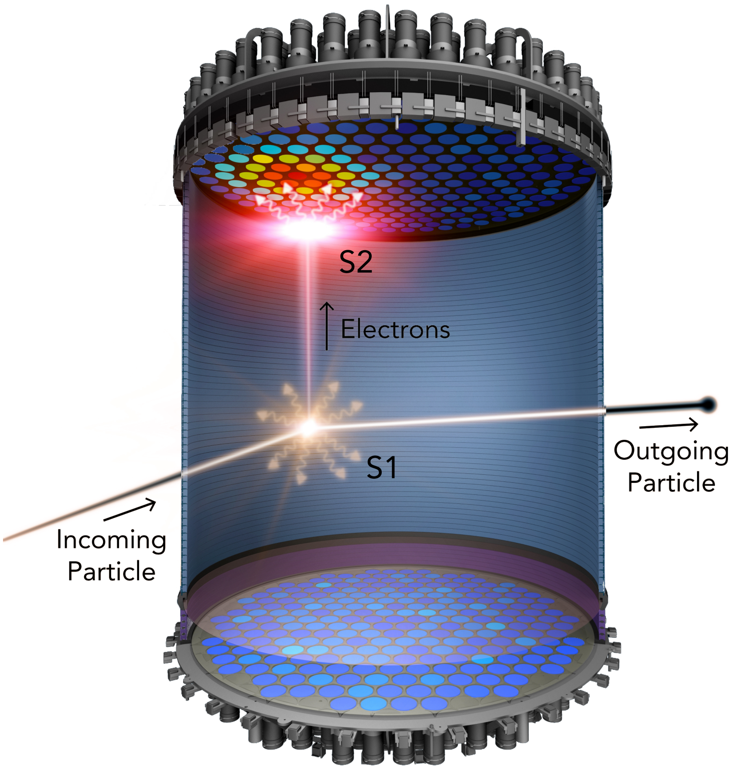

Figure 2.2.1: An illustration of a particle interaction in a dual-phase time projection chamber. The initial scatter produces the primary scintillation signal S1 and the S2 signal is produced by extraction of ionisation electrons via an applied electric field. Photons are detected by photomultiplier tube arrays located on the top and bottom of the detector. Figure adapted from Ref. [186].

field. At the liquid-gas boundary, a strong extraction electric field is applied to extract the electrons from the liquid volume. The acceleration of electrons in the GXe volume produces secondary scintillation signal (S2) via electroluminescence. The VUV photons are recorded by the arrays of photosensors.

Both S1 and S2 signals are used for 3D event reconstruction in dual-phase TPCs. The time delay between the S1 and S2 signal allows for reconstruction of the z coordinate in a known applied electric field. The S2 photon hit pattern as recorded by photosensors in the top arrays allows for reconstruction of the (x,y) position of an event. S1 and S2 signals are also used for energy reconstruction of events, and the partition of energy between S1 and S2 signals for ER and NR events can be used for event discrimination. Signal reconstruction will be discussed in further detail in Section 2.2.2 and Section 2.2.4.

2.2.2 Light and charge yields

We can express the number of emitted VUV photons n_γ and the number of extracted electrons n_e from an interaction as [209]:

$$\begin{aligned} n_\gamma &= N_{ex} + rN_i, \\ n_e &= (1-r)\,N_i, \end{aligned} \tag{2.2.1}$$

where N_{ex} is the number of excited atoms (excitons), N_i is the number of electron-ion pairs and r is the recombination probability.

The energy of an interaction is split linearly between the number of quanta produced by excitation and ionisation by the following equation for electron recoils:

$$E_{\mathrm{ER}} = W\,(N_{ex} + N_i), \tag{2.2.2}$$

where W is the average energy needed to produce a single excited or ionised atom. For liquid xenon, the widely used value of this parameter is $W = (13.7 \pm 0.2)\,\mathrm{eV}$ measured at $\sim 100\,\mathrm{keV}$ by Dahl [210]. This value is in direct contention with more recent results measuring a value of $W = (11.5 \pm 0.1_{\mathrm{stat}} \pm 0.5_{\mathrm{sys}})\,\mathrm{eV}$ using $\mathcal{O}(\mathrm{MeV})$ gamma-ray sources in the EXO-200 detector [211]. The xenon W–value was also measured by Baudis *et al.* using internal calibration sources in the $\mathcal{O}(0\text{–}10\,\mathrm{keV})$ energy range [212]. The numerical result reported is $W = 11.5^{+0.2}_{-0.3}$ (syst.) eV, with negligible statistical uncertainty. The 20% deviation between these values should prompt more independent measurements of the mean excitation energy of xenon.

For nuclear recoils we must modify the above equation by also considering a quenching factor that accounts for energy lost in the atomic collision of the nuclear recoil. This is given by:

$$E_{\mathrm{NR}} = \frac{W}{\mathcal{L}}\,(N_{ex} + N_i), \tag{2.2.3}$$

where $\mathcal{L}$ is the energy-dependent nuclear quenching factor first proposed by Lindhard in the 1960s [213]. Hence, $\mathcal{L}$ is also often referred to as the Lindhard factor. In order to differentiate between E_{ER} and E_{NR} the reconstructed energy values are often quoted in units of $\mathrm{keV_{ee}}$ and $\mathrm{keV_{nr}}$, respectively. Here $\mathrm{keV_{ee}}$ refers to electron-equivalent energy and $\mathrm{keV_{nr}}$ refers to nuclear recoil energy.

From the expressions for n_γ and n_e given in Equation 2.2.1, we find that:

$$n_\gamma + n_e = N_{ex} + N_i. \tag{2.2.4}$$

By substituting Equation 2.2.4 into Equation 2.2.2 we can rewrite the total energy in terms of S1 and S2 signals recorded by the detector as:

$$\begin{aligned} E_{\mathrm{ER}} &= W\left(n_\gamma + n_e\right) \\ &= W\left(\frac{\mathrm{S1}}{g_1} + \frac{\mathrm{S2}}{g_2}\right), \end{aligned} \tag{2.2.5}$$

for electron recoil events. Here, g_1 and g_2 are detector gain parameters with units of phd/quantum, where phd stands for number of photons detected. g_1 represents the total photon detection efficiency for primary scintillation in the liquid and is a product of the average light collection efficiency and the average PMT quantum efficiency. g_2 corresponds to the total photon detection efficiency for secondary scintillation and is a product of the electron extraction efficiency and the average single electron (SE) pulse size in phd.

Similarly, by considering Equation 2.2.3 for nuclear recoils we find:

$$\begin{aligned} E_{\mathrm{NR}} &= \frac{W}{\mathcal{L}}\left(n_\gamma + n_e\right) \\ &= \frac{W}{\mathcal{L}}\left(\frac{\mathrm{S1}}{g_1} + \frac{\mathrm{S2}}{g_2}\right). \end{aligned} \tag{2.2.6}$$

The values of g_1 and g_2 can be extracted by measuring the light yield and

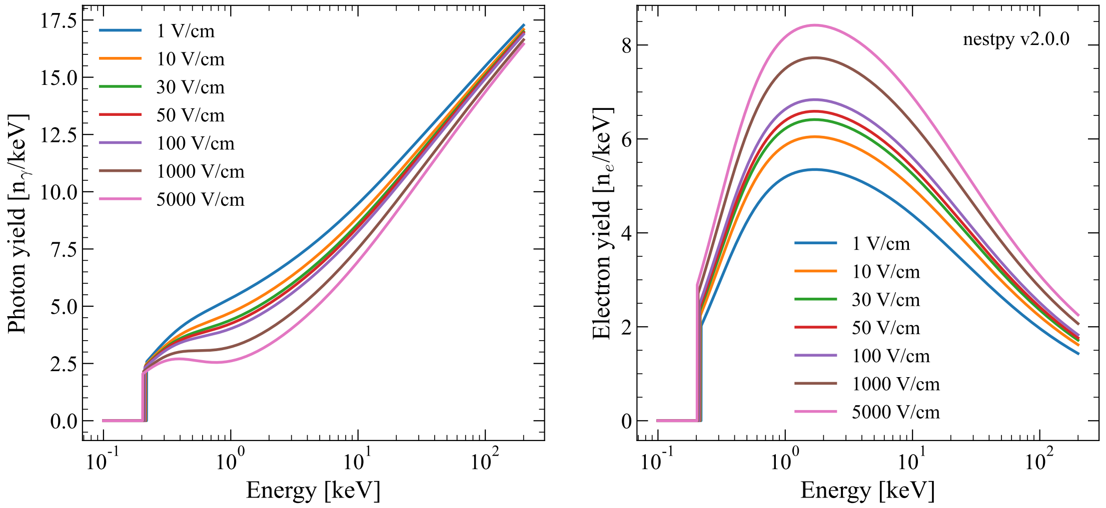

Figure 2.2.2: The light and charge yields for NR events as a function of recoil energy, as modelled in an infinite volume of liquid xenon by NEST. Therefore, this does not account for specific detector effects. Figure created using the nestpy v2.0.0 code [214].

charge yield for monoenergetic lines from internal and external radioactive sources, by rearranging equation 2.2.5 such that:

$$\frac{\mathrm{S2}}{E} = \frac{g_2}{W} - \frac{g_2}{g_1}\frac{\mathrm{S1}}{E}, \tag{2.2.7}$$

where the charge yield $Q_y = \mathrm{S2}/E$ is plotted against the light yield $L_y = \mathrm{S1}/E$. This is commonly referred to as the Doke plot [215], from which we can extract the values of g_1 and g_2 from the slope and intercept of the linear relationship [216].

2.2.3 Field dependence

The light and charge yields for electron recoil and nuclear recoil events are dependent on the electric field strength applied across the liquid xenon in the TPC. These are modelled semi-empirically by the Noble Element Simulation Technique (NEST) Collaboration [217, 218], using data from xenon experiments that operate at different field configurations. The yield distributions for with electric field strength are shown in Figure 2.2.2 for nuclear recoil events, which demonstrates the anti-correlation between photon and electron yields. Similar distributions also

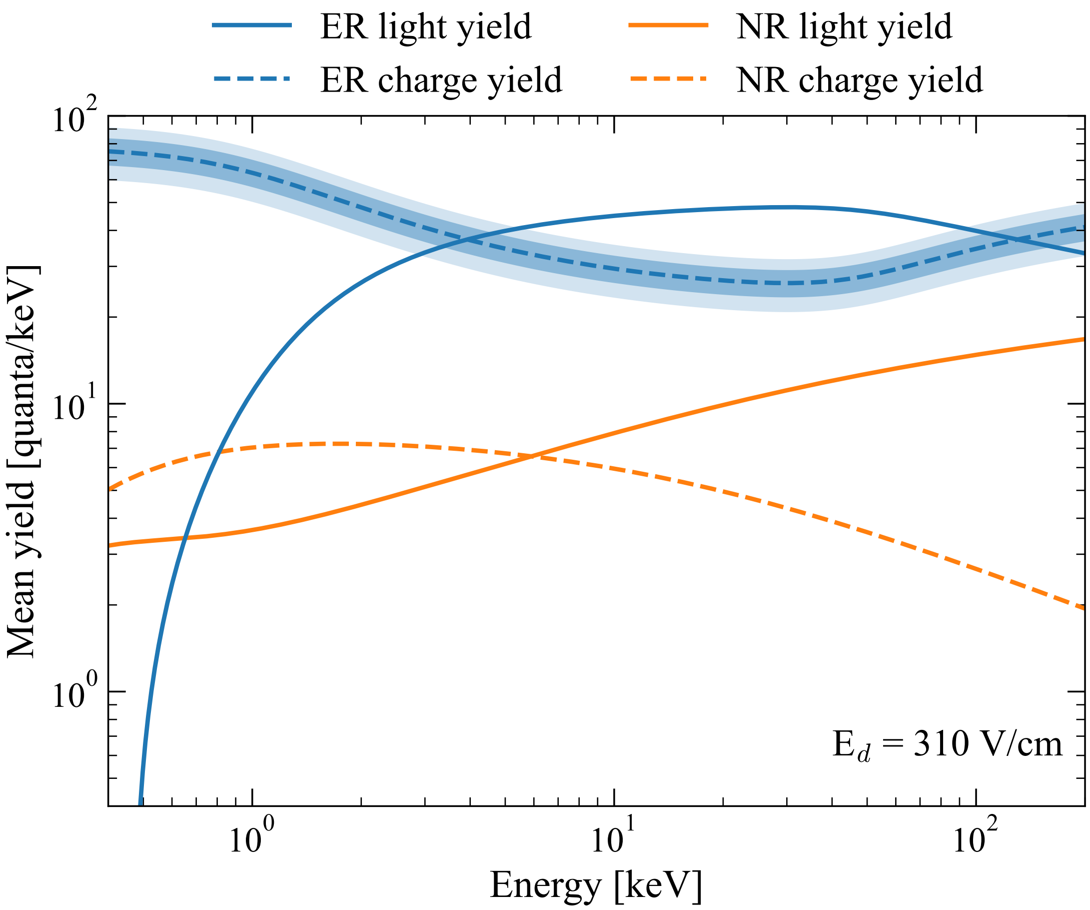

Figure 2.2.3: The light and charge yields for NR and beta ER interactions as a function of recoil energy, at the nominal LZ drift field of $E_d = 310\,\mathrm{V\,cm^{-1}}$ [186]. The coloured bands represent the $\pm 1\sigma$ and $\pm 2\sigma$ error bands. Figure created using the nestpy v2.0.0 code [214].

exist for beta and gamma ER interactions.

The high light and charge yields in LXe lead to sensitivity to recoil energies of $\mathcal{O}$(keV) up to several MeV. The mean yields for NR and beta ER interactions are shown in Figure 2.2.3 for a drift field value of $E_d = 310\,\mathrm{V\,cm^{-1}}$, which is the value of the nominal LZ field from the Technical Design Report [186].

2.2.4 Event discrimination

The ratio between ionisation and excitation differs for ER and NR events, allowing for event discrimination for the WIMP search. As ER events dominate the back-

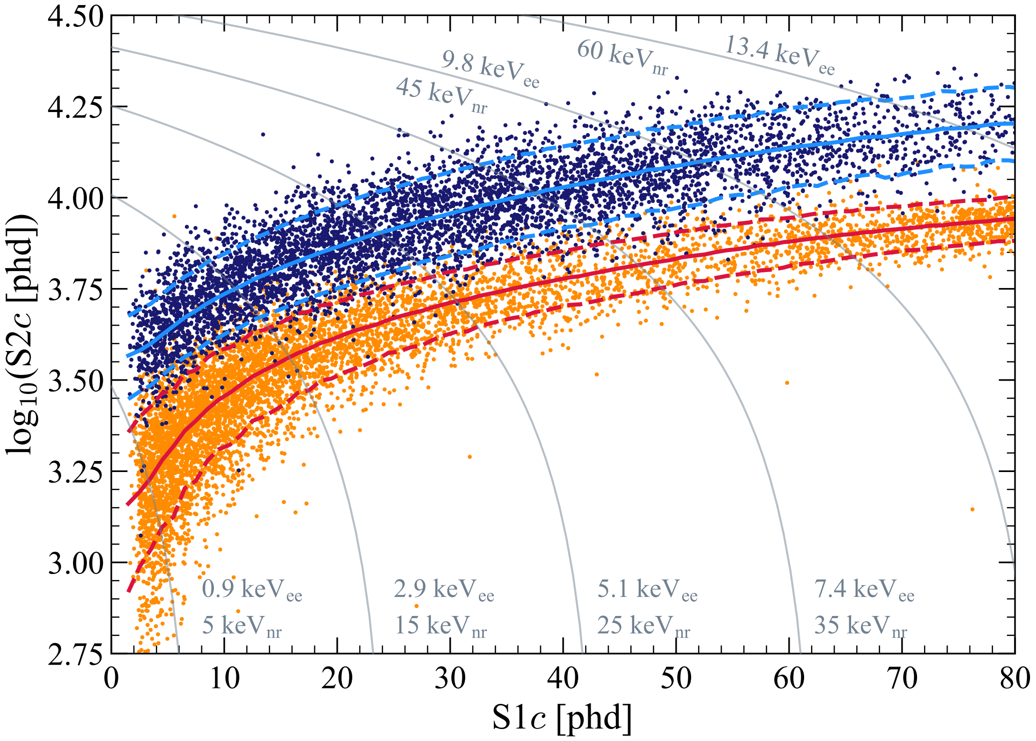

Figure 2.2.4: Calibration events demonstrating the separation of ER and NR signals in (S1c, $\log_{10}$(S2c)) space. ER calibrations were taken using a tritium source and are shown in dark blue. NR calibrations were done using a deuterium-deuterium (DD) neutron source and are shown in orange. The solid light blue and red lines indicate the median of ER and NR simulated distributions, respectively. The dotted lines indicate the 10% and 90% quantiles. The thin grey contours show lines of constant electron-equivalent energy and nuclear recoil energy. Figure taken from Ref. [146].

ground to the WIMP search, it is vital that we can discriminate between these events using S1 and S2 signals. For electron recoils in LXe the ratio of the number of excitons to electron-ion pairs is often quoted to be $N_{ex}/N_i = 0.13$, which is an average between values expected from theory (0.06) and those measured by experiments (0.2) [215]. For nuclear recoils the ratio is given by $N_{ex}/N_i \sim 1$ [219].

Figure 2.2.4 shows ER and NR separation in (S1c, $\log_{10}$(S2c)) parameter space for calibrations used in the first science run of LZ. ER calibration points shown in blue are from a tritiated methane source (CH_3T) dispersed in the TPC, which is used to calibrate the detector low-energy ER response with β decays up to an energy of 18.6 keV [220, 221]. NR calibration points shown in orange are from a deuterium-deuterium (DD) generator that produces monoenergetic neutrons at an energy of 2.45 MeV [222–224]. Visually the ER and NR events populate two distinct bands, termed the ER band and the NR band respectively. Simulations of these calibration sources produced by the NEST package [217, 218] show the median ER and NR response via the solid blue and red lines, respectively.

2.3 The LUX-ZEPLIN detector

2.3.1 Overview of the LZ detector

LZ consists of three separate detection regions with the dual-phase xenon TPC at the centre, surrounded by the Xe skin detector and the outer detector (OD) (see Figure 2.3.1) [225]. The inner cryostat vessel (ICV) holds a total of 10 t of LXe, with 7 t contained within the LXe TPC. Roughly 2 t of LXe are held in the Xe skin volume between the field cage and the ICV. The Xe skin provides dielectric insulation between these two regions. The ICV is suspended inside the outer cryostat vessel (OCV) which is cooled by liquid nitrogen thermosiphons to 175 K and is thermally isolated by an insulating vacuum. Both the ICV and OCV are fabricated from radiopure titanium [226]. The Xe skin detector and OD are used as independent veto detectors and are instrumented with independent light collection systems. All three detectors are housed in a large water tank which is used to shield the detector from external background sources.

The three detectors have been constructed using low-background intrinsically radiopure materials [227], and backgrounds [228] can be mitigated further by observations of interactions in the veto detectors [229]. These three detectors will be detailed in the following Sections, along with some other key detector subsystems that are required for detector operations. Extensive details of the LZ detector are given in Ref. [225].

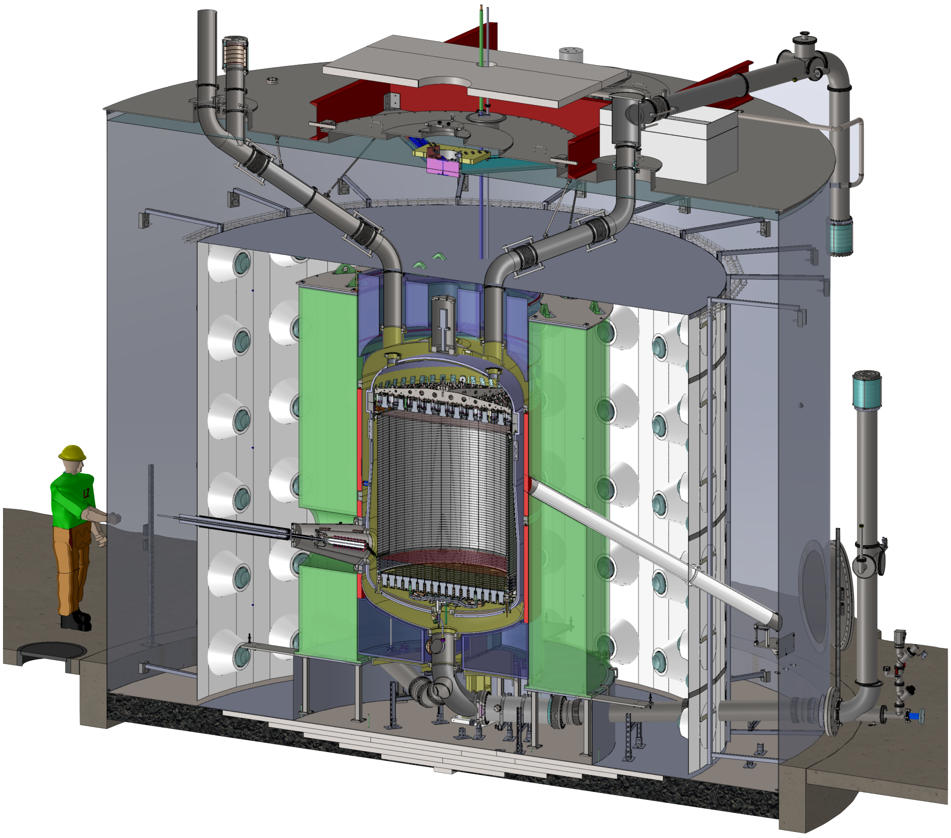

Figure 2.3.1: A rendering of the LZ experiment, showing the main detector subsystems. The cylindrical TPC is contained centrally within a titanium cryostat, which is surrounded by the outer detector tanks (green) and light collection system (white), which are housed in a large water tank (blue-grey). Diagram produced by Joseph Saba (Lawrence Berkeley National Laboratory).

2.3.2 Time projection chamber

The active volume of the TPC is a cylinder with dimensions of diameter and height both equal to 1.46 m. The TPC contains 7 t of LXe. The TPC is viewed by two PMT arrays. The top array is located in the gaseous region of the TPC and the bottom array is located in the liquid xenon phase. Interactions in the liquid phase produce primary S1 signals. The thin layer of gaseous xenon at the top of the detector produces secondary S2 signals by extraction of electrons drifted by an applied electric field. The design of the LZ TPC optimises: (i) the collection of VUV photons produced by both S1 and S2 signals by using carefully considered optical materials and photosensors; and (ii) the detection of ionisation electrons

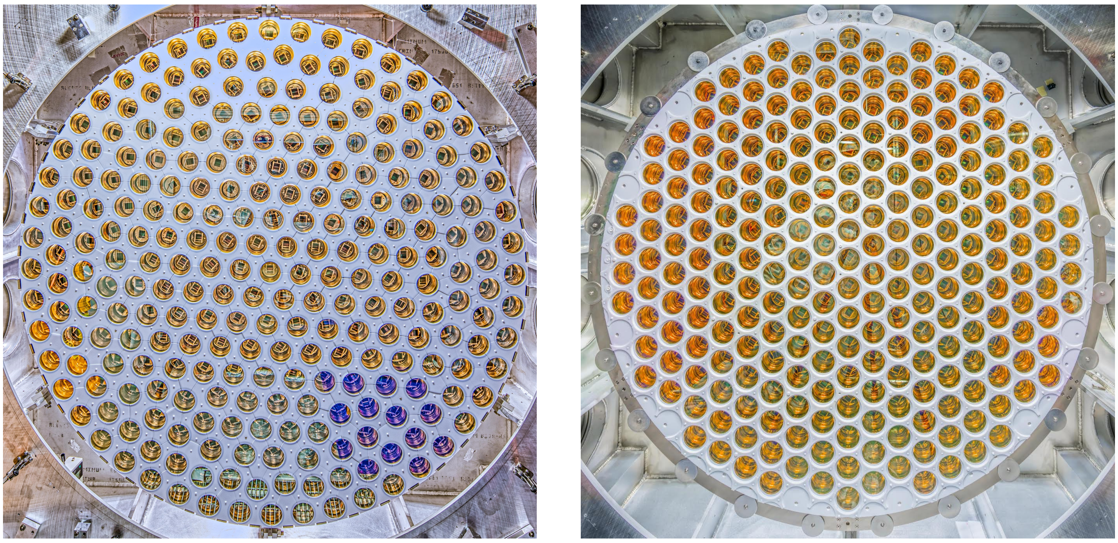

(a) Top PMT array.

(b) Bottom PMT array.

Figure 2.3.2: Arrays of Hamamatsu R11410-22 PMTs viewing the LZ TPC. **Left:** The top PMT array with circular PMT arrangement that transitions to hexagonal at the centre. **Right:** The bottom PMT array in a close-packed hexagonal pattern. The interlocking titanium surfaces are covered in reflective PTFE. Photographs by Matthew Kapust (Sanford Underground Research Facility).

leading to the S2 signal by a series of electric fields applied across regions of the TPC volume.

The TPC PMTs are 3-inch diameter Hamamatsu R11410-22 PMTs that have been developed for operation in cold liquid xenon and optimised for detection of VUV luminescence photons. This PMT variant was designed for LZ operations in particular, by considering the ultra-low radioactivity needs and spurious light emission observed in previous PMT models [230]. Calibrations of Hamamatsu R11410-22 PMTs have reported a quantum efficiency (QE) of $(30.9 \pm 2.5)\,\%$ in cold xenon [205], taking into consideration double photoelectron emission[1] [231, 232].

Two PMT arrays detect VUV luminescence produced by interactions in the LXe TPC. These arrays are shown in Figure 2.3.2. The bottom PMT array (Figure 2.3.2b) contains 241 PMTs arranged in a close-packed hexagonal pattern to

---

[1] For sufficiently energetic short wavelength photons, the primary photoelectron may lead to the emission of a second photoelectron via impact ionisation in the PMT cathode. This results in double photoelectron emission from a single incident photon [205, 231].

maximise the collection efficiency of S1 light. The top PMT array (Figure 2.3.2a) is located in the gaseous phase and contains 253 PMTs arranged in a hybrid pattern that changes from hexagonal near the centre to circular towards the circumference. This arrangement was chosen for the top array in order to optimise the (x,y) position reconstruction of S2 signals near the walls of the TPC. The titanium surfaces of the PMT arrays are covered with reflective polytetrafluoroethylene (PTFE) to optimise light collection.

The effective performance of a dual-phase TPC is dependent on establishing electric fields that are strong enough to remove free electrons from an interaction site, drift the electrons through the liquid, extract these electrons into the gas and then create the electroluminescence signal. It is also important to consider field uniformity and minimise the effects of stray electric fields [233].

The high voltage (HV) electrode configuration for the LZ TPC is shown in Figure 2.3.3. This schematic show the four HV grids that create electric fields over various regions of the TPC next to a photograph of the fully assembled TPC. Baseline operating conditions for LZ are designed to have the cathode set at a voltage of $-50\,\mathrm{kV}$, with the gate grid at a voltage of $-5.75\,\mathrm{kV}$ and the anode grid at a voltage of $5.75\,\mathrm{kV}$. This establishes a nominal drift field of $310\,\mathrm{V\,cm^{-1}}$ in the active region of the TPC, which is desirable for ER/NR event discrimination power [234]. The bottom grid has a voltage of $-1.5\,\mathrm{kV}$ and is responsible for shielding the bottom PMT array from the strong fields in the region below the cathode in the reverse field region (RFR).

During the first science run, the detector achieved stable operating conditions with the cathode biased to a voltage of $-32\,\mathrm{kV}$ and a voltage difference of $\Delta V = 8\,\mathrm{kV}$ was established across the gate and anode grid in the extraction region. The field configuration values achieved in the first science run of LZ are further listed in Section 2.7.1.

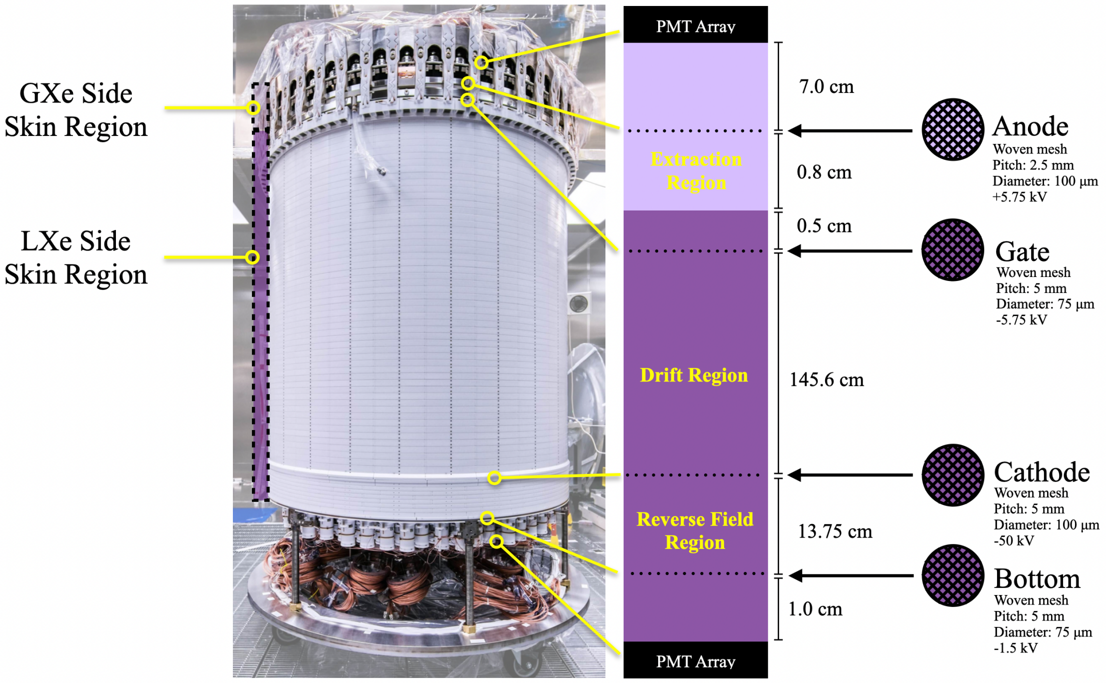

Figure 2.3.3: The HV electrode configuration for the LZ TPC, next to a photograph of the assembled TPC. Light purple corresponds to gaseous xenon and dark purple corresponds to liquid xenon. The extraction field is located between the gate and the liquid surface and the electroluminescence field is located between the liquid surface and the anode. The electric field values quoted are for baseline performance [186]. Figure taken from Ref. [233].

2.3.3 Xenon skin detector

The xenon skin holds $\sim 2\,\mathrm{t}$ of LXe in the region between the TPC field cage and the ICV. The skin provides 4–8 cm of stand-off distance between these two volumes in order to electrically shield the components. The skin is instrumented with its own optical readout system in order to record scintillation-only (i.e. S1 but no S2) events. This allows the skin to be used as a veto detector, able to reject events that have coincident signals in the skin and the TPC. This is particularly efficient for vetoing multiply scattered gamma-ray backgrounds. The field cage is also designed to optically isolate the TPC from the Xe skin, so that light leakage between detectors is minimised.

The side region of the skin is viewed from above by 93 1-inch diameter Hamamatsu R8520-406 PMTs. These are held in a PTFE structure attached to the

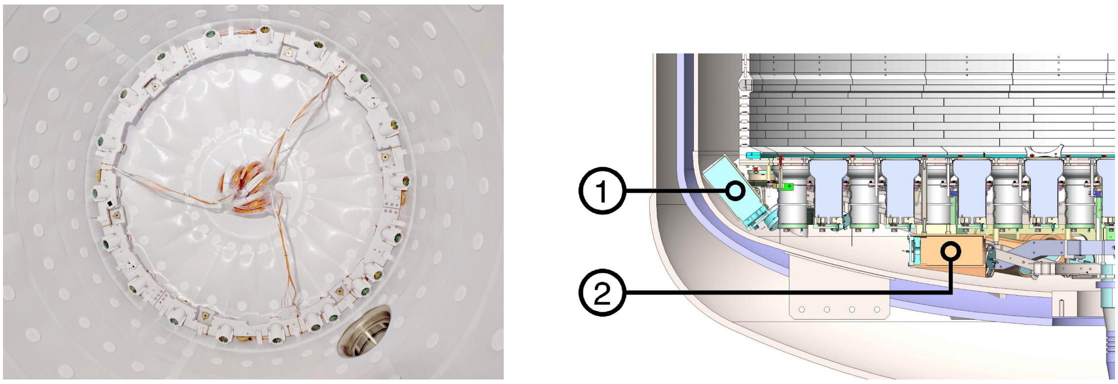

Figure 2.3.4: PMTs in the Xe skin detector. **Left:** Photograph showing the white PTFE panelling attached to the ICV that is used to achieve high reflectance in the skin. The 20 2-inch side skin PMT ring is also shown, which is located at the bottom of the vessel. **Right:** CAD drawing showing the location of the 2-inch side skin PMTs (1) and the dome PMTs (2). Figure taken from Ref. [225].

external side of the field cage. At the bottom of the detector there are a further 20 2-inch Hamamatsu R8778 PMTs viewing upwards into this lateral region. The dome region of the skin is located below the TPC bottom array and has 18 2-inch R8778 PMTs. These are horizontally mounted with 12 PMTs looking radially outward and 6 PMTs facing radially inward to optimise light collection. To enhance light collection in the skin, PMT array structures, sides of the ICV and the bottom dome are covered in PTFE.

2.3.4 Xenon circulation system

The online Xe purification system continuously removes electromagnetic impurities from the Xe while also providing a system for removing problematic radon backgrounds that constantly emanate into the xenon volume. A schematic of the purification system is shown in Figure 2.3.5.

The purity of the LXe is important to ensure that ionisation electrons can drift with a sufficient lifetime to the liquid-gas boundary without being captured on electromagnetic impurities in the TPC. Electronegatives such as oxygen and water limit the free electron lifetime and therefore affect the performance of the TPC [186]. Therefore, a requirement of effective detector operations is that the

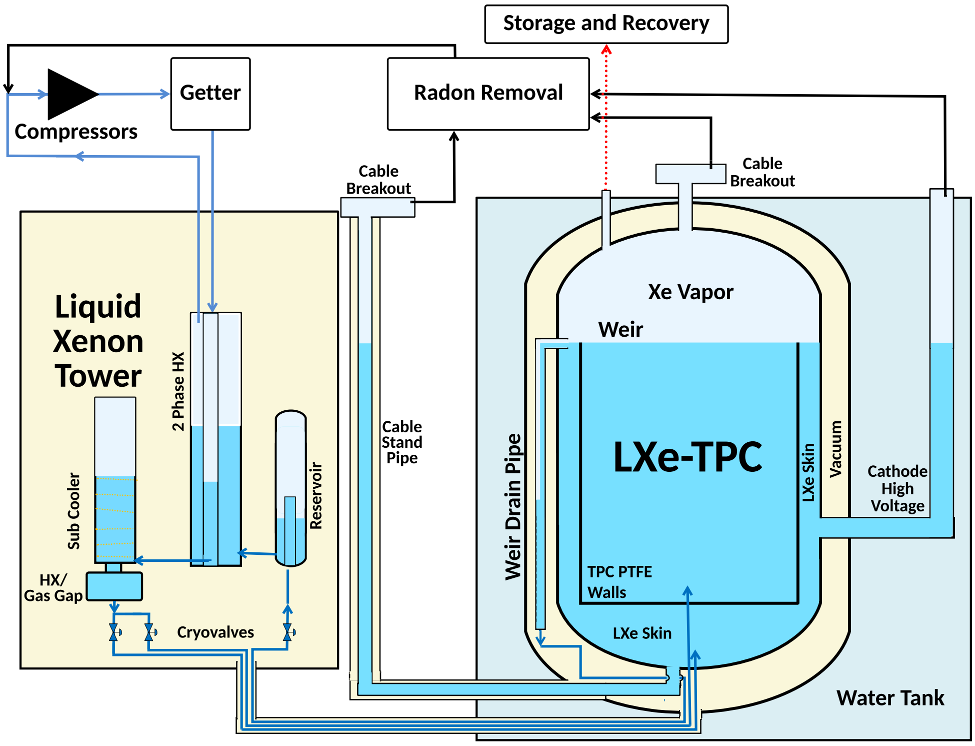

Figure 2.3.5: A schematic overview of the xenon purification system. LXe in the detector (right) spills over a weir drain and flows horizontally to the liquid xenon tower, which stands outside the water tank. The LXe is evaporated in a two-phase heat exchanger, pumped through a hot zirconium getter, and then returned to the detector after condensing. Cryovalves control the flow of the LXe between the LXe tower and the LXe TPC. A radon removal system treats Xe gas before sending it to the compressor inlet. Figure taken from Ref. [225].

charge attenuation length of the LXe should be 1.46 m or larger, which corresponds to the vertical height of the TPC. This translates to an electron lifetime of 806 µs given the nominal field as given above and in the Technical Design Report [186]. These electronegative impurities are removed from the xenon by the hot zirconium getter.

Radioactive noble gases are not removed by the getter and create ER backgrounds that cannot be mitigated with the self-shielding property of Xe. The gases of concern are ^{222}Rn and ^{85}Kr, as well as ^{220}Rn and Ar isotopes. Kr and Ar can be removed from Xe by using gas charcoal chromatography at a facility located at SLAC National Accelerator Laboratory. LZ uses an inline radon reduction system (iRRS) in order to remove radon that continuously emanates into the

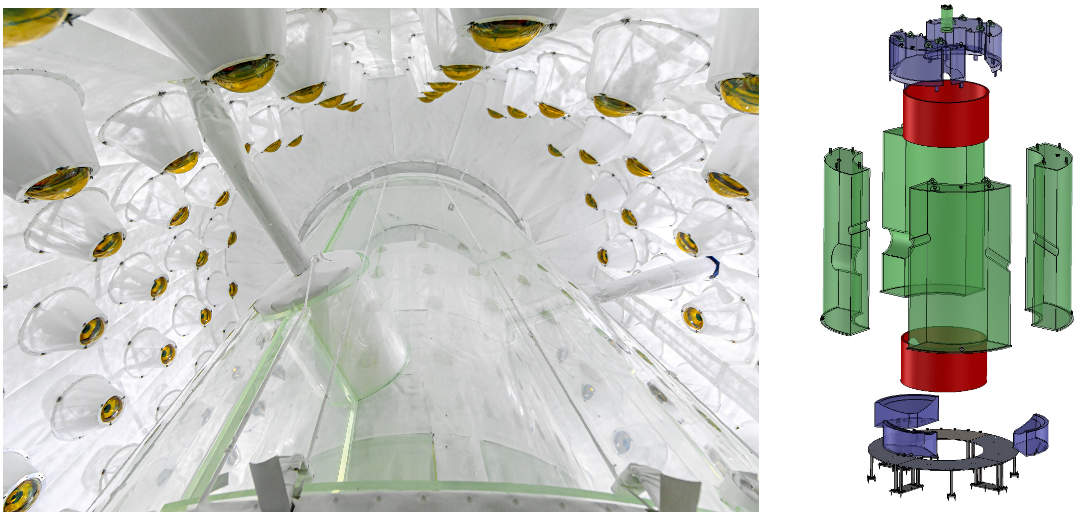

Figure 2.3.6: The outer detector system. **Left:** The OD PMTs viewing the acrylic vessels in the unfilled water tank. Photograph taken by Matt Kapust (Sanford Underground Research Facility). **Right:** The outer detector system in an exploded view. The four large side vessels are shown in green and the fiver smaller top and bottom vessels are shown in blue. The water displacers are shown in red and the stainless steel base is shown in grey. Figure taken from Ref. [225].

LXe target [235]. A charcoal-based adsorption trap [236] is implemented in the LZ circulation system to take radon-rich gaseous xenon from the gas circulation system and return radon-reduced xenon to the main circulation loop. The iRRS is designed to sequester ^{222}Rn for 3 half-lives (12.7 d) allowing for 90% of these atoms to decay [225].

2.3.5 Outer detector

The purpose of the outer detector is to tag neutron scattering events in the TPC. Most neutrons originate from fission of uranium and thorium radioactive impurities in materials adjacent to the TPC. Neutrons may also be produced by (α,n) reactions, with captures on fluorine contained in PTFE being a dominant source. The OD is a liquid scintillator detector that is designed to capture and tag neutrons within a coincident time window that can be correlated to NR events observed in the TPC. An exploded view of the OD is shown in Figure 2.3.6.

The OD uses a 17 t gadolinium-doped liquid scintillator (GdLS) target which is contained within segmented hermetic acrylic vessels that surround the OCV. The addition of Gd to the LS enhances the efficiency of neutron detection due to the high neutron capture cross-section of natural gadolinium. Neutron capture on ^{155}Gd and ^{157}Gd isotopes present in $^{\mathrm{nat}}$Gd produces a total energy of 8.5 MeV and 7.9 MeV, respectively [237]. This energy is released by a gamma cascade, resulting in the production of on average 4.7 gammas. Approximately 10% of neutrons capture of hydrogen, producing a single 2.2 MeV gamma.

These gammas induce scintillation in the LS that is collected by 120 8-inch diameter Hamamatsu R5912 PMTs that view the OD from a support system inside the water tank. These PMTs are situated 115 cm radially away from the outer wall of the acrylic vessels and are immersed in 238 t of ultrapure water [146]. A photograph of the OD PMTs taken when the water tank was empty is shown in Figure 2.3.6.

The veto performance of the OD is dependent on the event rate observed in the outer detector. Events can be attributed to internal and external backgrounds sources, including contaminants present in the GdLS, radioactivity from LZ detector components and radioactivity originating from the Davis cavern itself. Measurements of radioactive contaminants in the GdLS have been conducted with a LS Screener, which is a small liquid scintillator detector containing 23 kg of GdLS used in the OD. Contaminants include products from radioactive decay chains of ^{238}U, ^{235}U and ^{232}Th as well as ^{40}K and ^{14}C. For full details of the LS Screener results see Ref. [229]. The biggest contribution to the rate in the OD is from radioactivity produced by the rock formations that constitute the cavern walls of the Davis cavern. This background will be presented in detail in Chapter 4.

2.4 Calibration

Many attributes of the LZ detector response require *in situ* calibration. Goals of detector calibrations range from low-level quantities such as PMT gains and timings to high-level quantities such as the models of the detector electron recoil and nuclear recoil response. Xe PMTs are calibrated using a total of 78 LEDs that are installed in the TPC and Xe skin, while OD PMTs are calibrated using the optical calibration system (OCS) [238]. The LEDs are used to calibrate PMT gains and the timing response of the detector. The OSC is designed for PMT monitoring and measurements of the optical properties of the GdLS and acrylic.

The LZ calibration strategy is designed to accurately model the detector response using a wide range of calibration sources available (shown in Table 2.4.1). Due to the variation of physical size, form and production mechanisms of calibration sources, different hardware and deployment methods are required. There are four calibration source deployment methods used in LZ:

1. **Internal source injection:** Gaseous sources are mixed with the LXe volume in the TPC in order to calibrate the ER response in the active volume. Self-shielding limits calibrations via external gamma sources in this case. The gaseous sources are released via a source injection panel into the xenon circulation system which is carried into the TPC. Gaseous sources include short-lived sources ($^{83\text{m}}$Kr, $^{131\text{m}}$Xe, ^{220}Rn) stored in the form of their parent nuclide and long-lived sources (CH_3T) stored as pressurised gas.

2. **Calibration source deployment (CSD):** External calibration sources are lowered into the space between the ICV and the OCV by three conduits which are capped by calibration source deployment (CSD) system. The CSD raises and lowers sources with a final position accuracy of ±5 mm, which is measured using a laser ranger. The external sources are a set of

commercial gamma sources (Eckert & Ziegler [239]), with custom AmLi [240] and AmBe [241] (α,n) sources fabricated to be compatible with the CSD system.

3. **Photoneutron sources**: A selection of photoneutron (γ,n) sources, including ^{88}YBe, are available to calibrate the NR energy range from below 1 keV up to $\sim$ 4.6 keV. This energy range corresponds to the expected energy deposits from ^{8}B solar neutrino scattering via CEνNS. The ratio of neutron to gamma production is on order of 10^4, so a significant amount of gamma shielding is required. A 140 kg tungsten shielding block containing photoneutron sources is designed to be lowered into LZ via a crane through a custom hole in the OD acrylic vessels.

4. **DD generator**: NR calibration events are created using a DD generator that emits monoenergetic neutrons at an energy of 2.45 MeV at a rate of up to 10^9 neutrons per second [242]. These neutrons are directed into the LXe volume via two sets of conduits, one horizontal and one inclined at 20° to the horizontal. The DD beam can also be reflected using a D_2O target (D-reflector) and a H target (H-reflector) to obtain quasi monoenergetic neutrons with a minimum energy of $\sim$ 270 keV and 10 keV, respectively [186]. This allows for the low-energy NR response to be calibrated with decreased uncertainty.

Using the dispersed sources, the S1 signal is normalised to the geometric centre of the detector, using a correction in x, y and drift time. The corrected S1 signal is called S1c. The S2 signal is normalised to a signal at the radial centre and the top of the detector; this normalised quantity is called S2c. The scale of these S1 corrections depends primarily on the light collection efficiency and PMT quantum efficiency. S2 (x,y) corrections are dependent on any non-operational PMTs and non-uniformity caused by electrostatic deflection of the gate and anode electrodes,

Table 2.4.1: A summary of radioactive sources used for the LZ calibration strategy [243].

Deployment	Nuclide	Type	Purpose	Energy [keV]	Half-life, $t_{1/2}$
Internal	CH_3T	β	ER response	$\rightarrow$ 18.6	12.3 y
	^{83m}Kr	β, γ	TPC (x,y,z)	9.4, 32.1	1.83 h
	^{131m}Xe	γ	TPC (x,y,z)	164	11.8 d
	^{220}Rn	α, β, γ	LXe flow, Xe skin	various	10.6 h
CSD	^{22}Na	γ	TPC and OD coincidence	511, 1275	2.61 y
	^{54}Mn	γ	^{134}Xe $\beta\beta$ studies	835	312 d
	^{57}Co	γ	Xe skin threshold	122	0.74 y
	^{228}Th	γ	OD threshold	2615	1.91 y
	^{241}AmLi	$(\alpha$,n)	NR response	$\rightarrow$ 1500	432 y
	^{241}AmBe	$(\alpha$,n)	NR response	$\rightarrow$ 11000	432 y
	^{252}Cf	n	NR efficiency	Watt spectrum	2.65 y
Photoneutron	YBe	$(\gamma$,n)	NR response	152	107 d
DD	DD	n	NR response	2450	-
	D-reflector	n	NR response	270 $\rightarrow$ 420	-
	H-reflector	n	NR response	10 $\rightarrow$ 160	-

while the correction in z is due to electron attachment on impurities. A full report of LZ calibrations are presented in Ref. [243].

2.5 Backgrounds

In order to ensure confidence in any claim of detection of new physics it is essential to understand and minimise potential sources of background. The design and construction of LZ have been heavily influenced with this priority. Here the main sources of background for the LUX-ZEPLIN experiment are described.

2.5.1 Trace radioactivity

Gamma backgrounds are produced by naturally occurring radioactive materials (NORMs) within detector components. NORMs include gamma emitting ^{40}K, ^{60}Co and ^{137}Cs isotopes, as well as ^{238}U, ^{235}U, ^{232}Th and their progeny, which decay by emission of α, β, γ particles eventually reaching stable lead isotopes. The ^{232}Th and ^{238}U decay chains are shown in Figure 2.5.1 and Figure 2.5.2, respectively. Detector materials used to construct LZ were selected according to radiopurity and cleanliness requirements, with materials being radioassayed using high-purity germanium detectors (HPGe) alongside an assembly program inline with strict cleanliness protocols in order to reduce surface backgrounds [227]. Trace radioactivity is not expected to be a leading contributor to the experiment backgrounds, owing to the comprehensive radioassay program and the self-shielding properties of LXe.

2.5.2 Surface contamination

Surface contamination can occur due to radon progeny plate-out on detector surfaces due to exposure to air [244, 245]. ^{222}Rn decays through α, β and γ emission to reach long-lived isotope ^{210}Pb with a half-life $t_{1/2} = 22.3\,$years. Therefore, radon is an ever-present background for rare event searches. Dust contamination also contains NORMs that release gamma-rays and can in turn induce neutron emission.

Radon plate-out probability on the PTFE surface exposed to the active xenon volume is significant due to the PTFE carrying negative charges [246] and the high probability that the radon daughters are positively charged [247]. Ions from the ^{210}Po subchain present at the edge of the TPC may be misreconstructed as NR events due to charge loss near the wall. This is dependent on the performance of event reconstruction and drives the radial fiducial volume cut for the active volume. Additionally, α decays of ^{210}Po produce a recoiling ^{206}Pb which can create problematic event topologies at the detector walls. Neutrons can also be produced via (α,n) processes on the fluorine present in PTFE due to this decay [248].

In order to ensure radon surface and generic dust contamination do not exceed the required limits all components that are xenon-wetted were cleaned adhering to strict protocols. Detector assembly occurred in a radon-reduced clean room built at the Surface Assembly Laboratory at SURF.

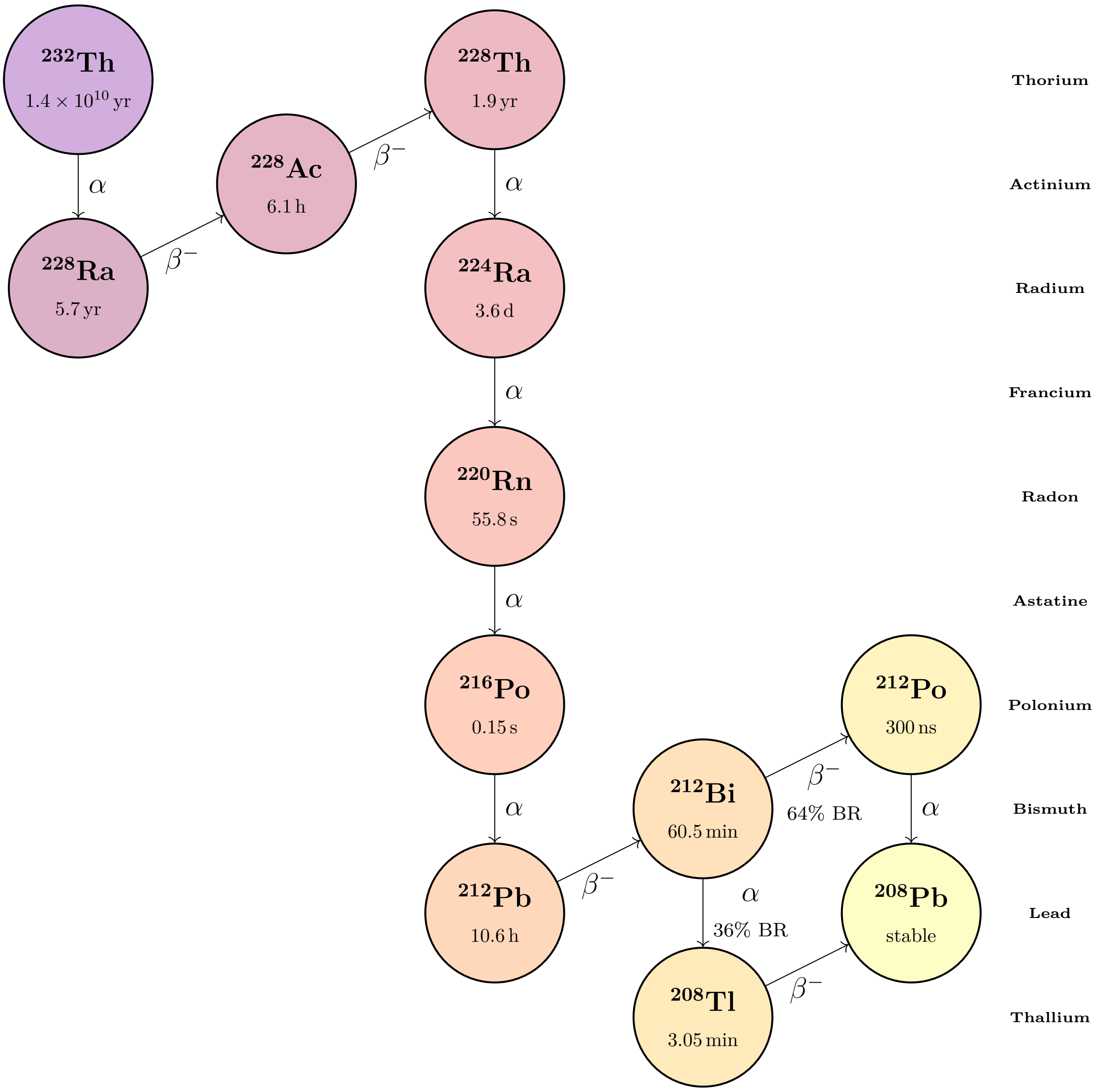

Figure 2.5.1: Decay chain of ^{232}Th. The half-life of each decay is listed below the relevant isotope.

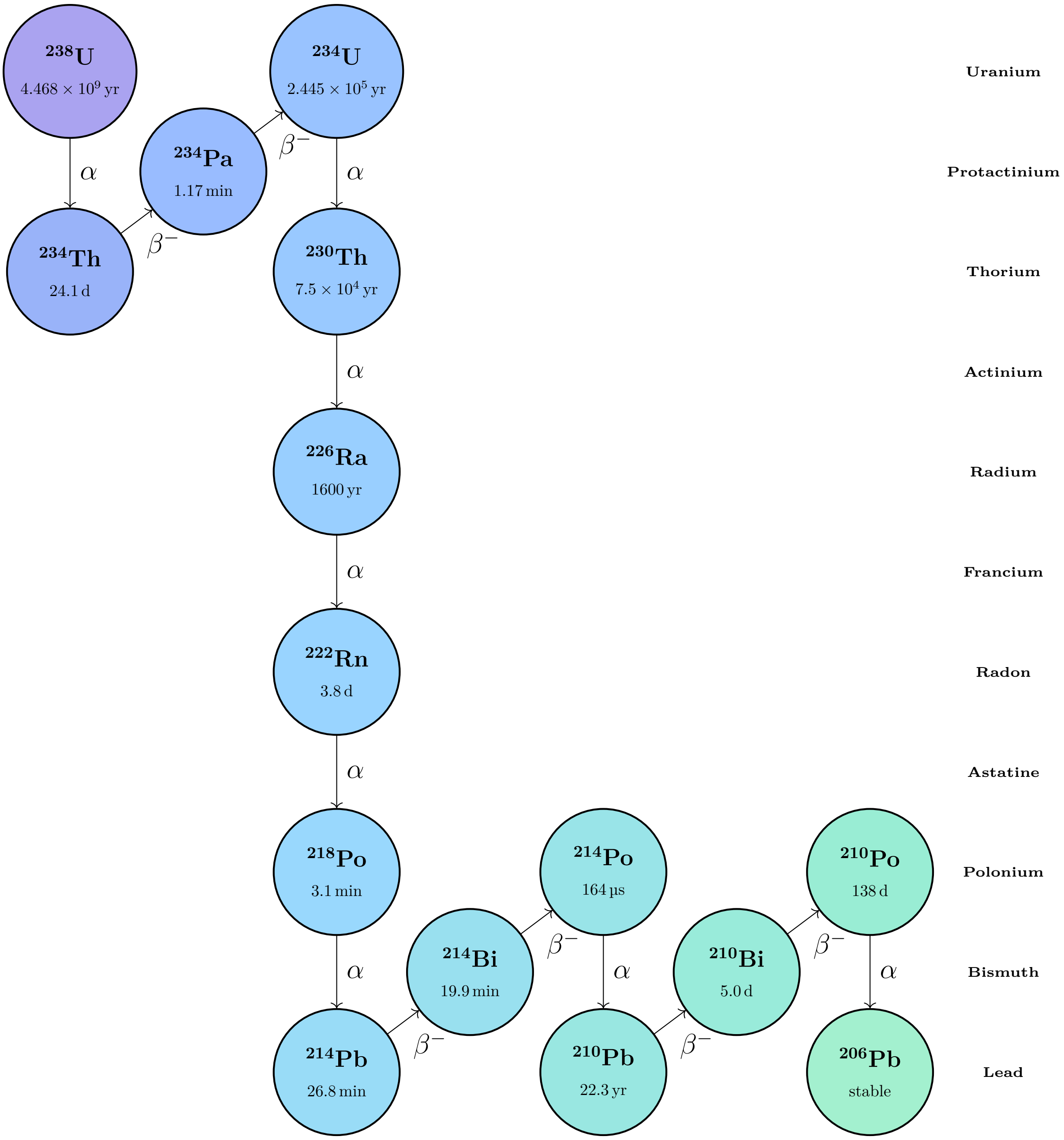

Figure 2.5.2: Decay chain of ^{238}U. This schematic shows decays with branching ratios >1%.

2.5.3 Dispersed xenon contaminants

Radioisotopes that are dispersed throughout the xenon bulk cannot be mitigated by the self-shielding properties of liquid xenon. Radon emanation from detector materials and dust is the largest source of background for the LUX-ZEPLIN experiment. This is due to “naked-beta” emission - a beta particle emitted with no accompanying gamma-rays - which is a decay mode of ^{214}Pb and ^{212}Pb that originate from the ^{222}Rn and ^{220}Rn decay chains, respectively. The branching ratio for the naked decay of ^{214}Pb and ^{212}Pb to the ground-state of the relevant Bi isotope is 9.2% and 13.3%, respectively [249, 250]. This beta decay mode is difficult to veto for the WIMP search. There is also the possibility of a “semi-naked” decay occurring, where the gamma produced in an event escapes outside of the active volume. Direct measurements of radon emanation from xenon wetted materials have been performed to inform rates [251] and the gas handling system uses an inline radon reduction system to continuously remove radon that emanates into the LXe target [235].

Natural xenon also includes trace levels of ^{85}Kr and ^{39}Ar that are dispersed in the xenon liquid. Both isotopes are beta-emitters that lead to low-energy ER events that contribute to the WIMP search background. Gas charcoal chromatography was used in a dedicated purification campaign carried out at SLAC National Accelerator Laboratory in order to reduce the amount of trace krypton present in 10 tonnes of xenon utilised in LZ [252, 253].

2.5.4 Cosmogenic and laboratory backgrounds

The 4300 m.w.e. of rock overburden above the Davis cavern at SURF heavily reduces the muon flux by a factor of $\sim 1 \times 10^6$ with respect to the surface [254]. Muon events are vetoed by detecting Cherenkov signals recorded in the water tank and liquid scintillator and along with any time-coincident signals within the xenon

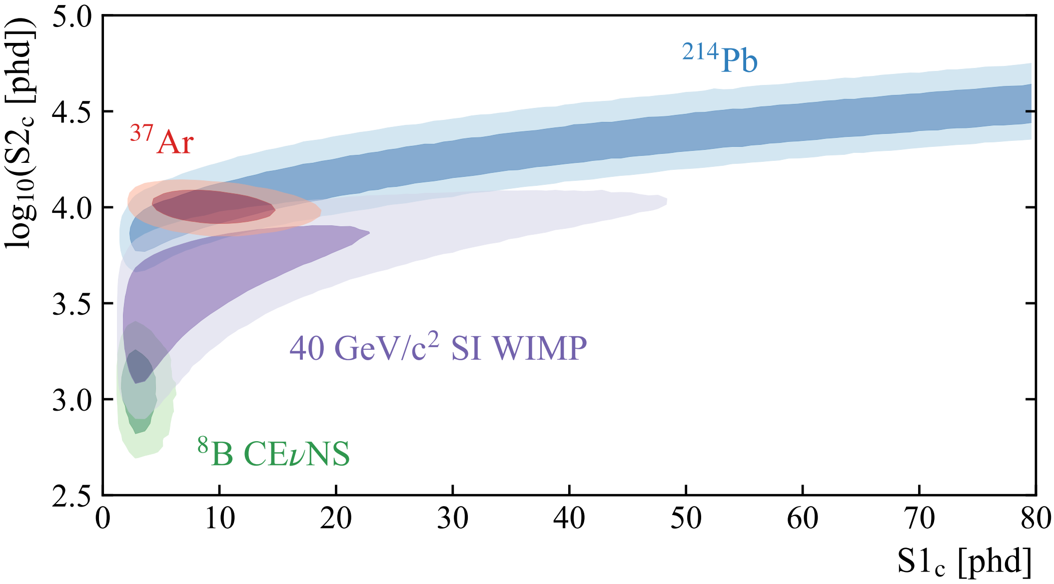

Figure 2.5.3: The distributions of various signal and background components in (S1c, $\log_{10}$(S2c)) parameter space expected in LZ, assuming operating conditions described in Ref. [145]. The ER contribution from the 2.82 keV K-shell decay of ^{37}Ar is shown in red and the β-decay of ^{214}Pb is shown by the blue contour and populates the ER band. NR events from a 40 GeV/c^2 WIMP and CEνNS interactions of ^{8}B neutrinos are shown by the purple and green contours, respectively. For each population the dark and light contours represent the 1σ and 2σ regions. Figure taken from Ref. [257].

detectors. The muon-induced neutron background has been quantified by conducting simulations of muon transport through the surrounding rock [255, 256]. These neutrons are effectively attenuated by the water and liquid scintillator contained within the OD.

However, cosmogenic activation of xenon during storage and transport on the Earth's surface leads to the production of ^{127}Xe, $^{129\mathrm{m}}$Xe, $^{131\mathrm{m}}$Xe, $^{133\mathrm{m}}$Xe and ^{37}Ar via cosmic-ray-induced spallation [257–259]. The longest lived of the Xe isotopes is ^{127}Xe with a half-life of $t_{1/2} = 36.3$ d and will be a key background that will reduce during detector commissioning and the beginning of data-taking [260]. ^{37}Ar decays to the ground state of ^{37}Cl via electron capture (EC) with a half-life of $t_{1/2} = 35.02$ d [261]. The subsequent atomic relaxation of ^{37}Cl results in energy deposits via X-ray emission up to the K-shell energy of 2.82 keV. In Figure 2.5.3 the ^{37}Ar has finite overlap with the signal contour for a WIMP mass of 40 GeV/c^2, indicating this background can weaken the experimental sensitivity in this region. Additionally, neutrons from calibration sources are expected to further contribute to the activation of the xenon target. It is expected that the most significant background from cosmogenic activation of detector materials is ^{46}Sc due to activation of titanium.

The dominant environmental background from outside of the LZ detector is produced by U/Th/K decays originating from the cavern rock. The gamma-ray flux from the Davis cavern has been measured using inorganic crystal scintillator detectors [262], and has also been measured in the TPC during commissioning of the LZ detector [228]. However, these studies did not consider high-energy gammas that can be produced by (α,γ) or $(\alpha$,n) reactions that contribute to the background above the upper limit of the 2.6 MeV ^{208}Tl gamma-ray. A study of characterising and constraining ER backgrounds originating cavern surroundings is presented in Chapter 4.

2.5.5 Physics backgrounds

There are sources of backgrounds that present interesting physics in their own right that can mimic a WIMP signal: two-neutrino double electron capture (DEC) of ^{124}Xe, two-neutrino double-beta decay of ^{136}Xe and solar and atmospheric neutrino interactions. Each of these events can result in single scatter events uniformly distributed in the TPC with no corresponding veto signal.

^{124}Xe 2νDEC can occur via a combination of captures on the K, L, M and N-shell, resulting in low-energy ER signals. The first observation of ^{124}Xe 2νDEC was reported by the XENON1T experiment [191], with further measurements these results were later improved upon reporting a half-life value of $T_{1/2}^{2\nu\text{DEC}} = (1.1 \pm 0.2_{\text{stat}} \pm 0.1_{\text{sys}}) \times 10^{22}$ years [263].

^{136}Xe is known to decay via $2\nu\beta\beta$ and is a physics background which has been observed by enriched ^{136}Xe experiments searching for $0\nu\beta\beta$ signals to determine

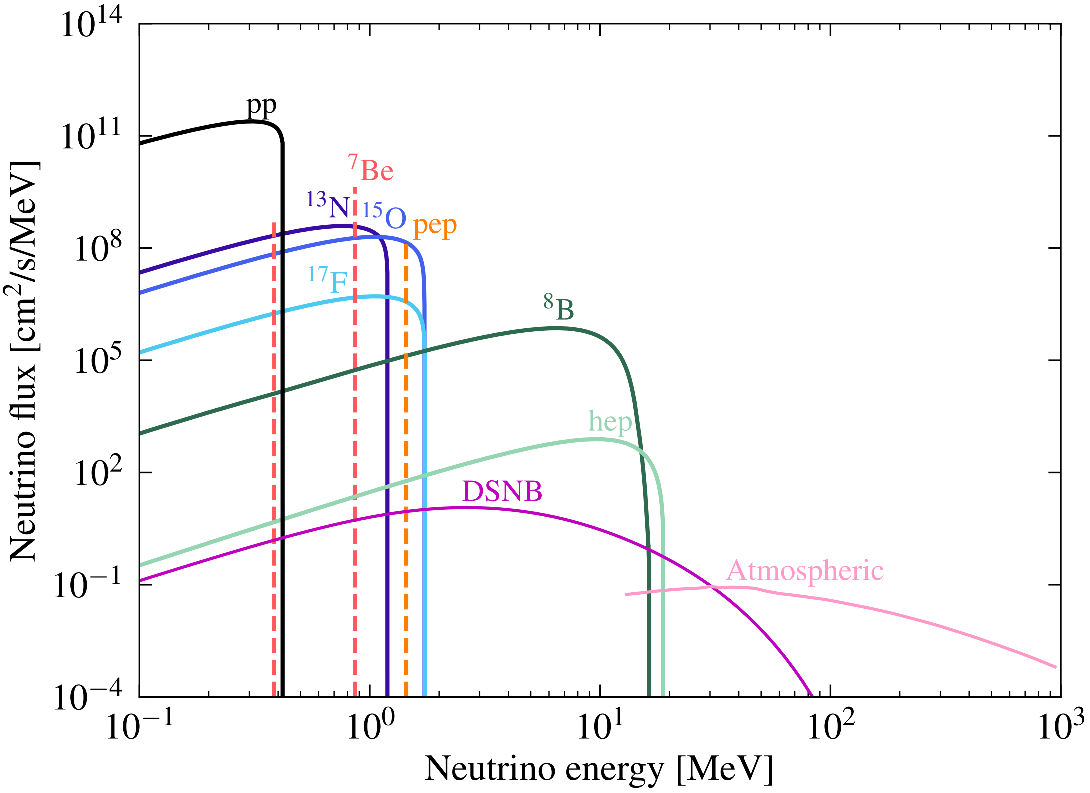

Figure 2.5.4: The dominant neutrino fluxes that contribute background to direct detection experiments: solar, atmospheric and DSNB. Each contribution to the solar neutrino flux is labelled explicitly. Figure taken from Ref. [117].

the nature of neutrinos [264, 265]. ^{136}Xe is also present in experiments using xenon targets with natural abundance [263, 266], where the isotopic abundance of ^{136}Xe in $^{\mathrm{nat}}$Xe is 8.9% [195]. The half-life of ^{136}Xe $2\nu\beta\beta$ is reported by the EXO-200 experiment to be $T_{1/2}^{2\nu\beta\beta} = (2.165 \pm 0.016_{\mathrm{stat}} \pm 0.059_{\mathrm{sys}}) \times 10^{21}$ years. The ^{136}Xe $Q_{\beta\beta}$ value is listed as (2457.83 ± 0.37) keV [267]. For LZ analysis the beta energy spectrum has been updated following results from Ref. [268].

Figure 2.5.4 shows the flux-normalised energy spectra of neutrinos that contribute to the background of direct detection experiments from solar, atmospheric and diffuse supernova neutrino background (DSNB) sources. The solar neutrino ER background is dominated by *pp* neutrinos, with smaller contributions from ^{7}Be and CNO cycle processes in the Sun. Solar models are used to inform the flux and spectra of each source of neutrinos to calculate solar neutrino rates [269]. Nuclear recoils can be induced by neutrinos undergoing coherent elastic neutrino–nucleus scattering with the xenon nucleus. ^{8}B and *hep* neutrinos result in lower energy NR events, whereas atmospheric neutrinos and the DSNB produce much higher energy NR events.

2.5.6 Non-standard backgrounds

A set of non-standard backgrounds may arise due to irregular event topologies in the detector. For example, multiple scattering gamma-rays may interact at a site that has limited charge collection in the detector, such as the reverse field region. This may cause the events to have a lower S1/S2 ratio than typical ER events and cause leakage into the NR band. It is also possible that uncorrelated S1-S2 pairs may end in the same event window due to accidental coincidence. These events can be accounted for by a sophisticated selection of cuts that exploit typical properties of S1s and S2s [228].

2.6 Simulations and data analysis

LZ employs a suite of custom data analysis software that is used to process low-level detector instrument data to high-level event reconstruction. Monte Carlo (MC) simulations of particle interactions in materials are performed using GEANT4 based software [270–272] in order to model backgrounds to physics searches. BACCARAT serves as the simulation framework for LZ that models particle interactions in the LZ geometry and records energy depositions [273].

Following this, the Noble Element Simulation Technique (NEST) package [217, 218] is used to convert energy deposits into corrected S1 and S2 signals. This is done via models of xenon physics that quantify the detector response using ionisation models, light and charge yield models and electric field maps. These models are informed by measurements taken by previous and current noble liquid detec-

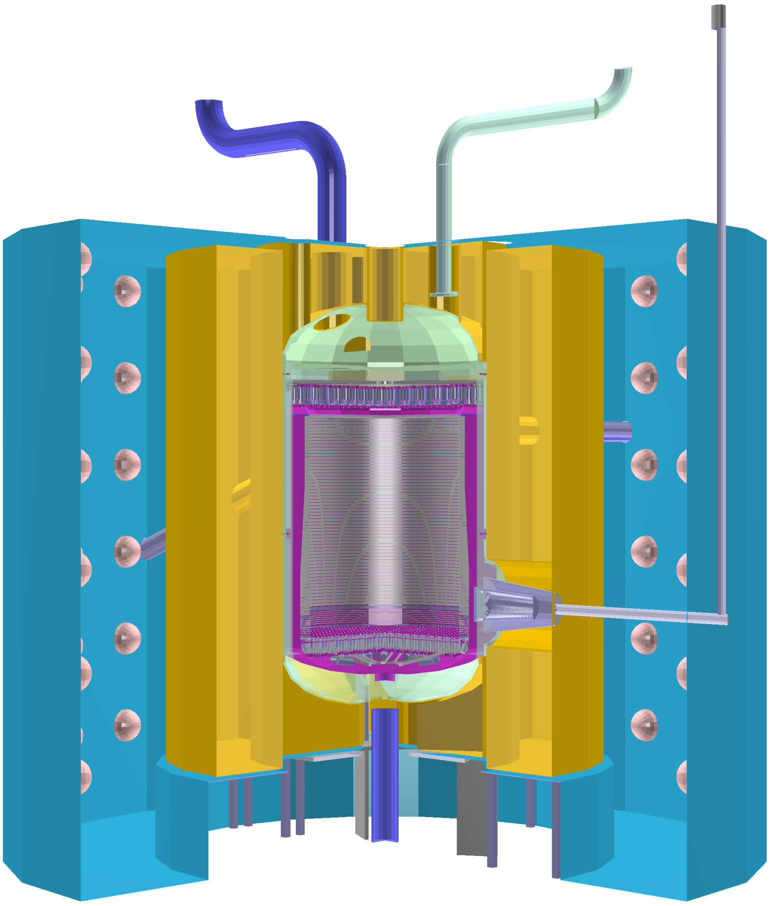

Figure 2.6.1: Visualisation of the LZ geometry in the Geant4-based software framework Baccarat. The TPC (magenta) is contained within the cryostat (light green), and is surrounded by the GdLS in the acrylic vessels (yellow). The system is contained within the water tank and the OD PMT structure is shown in blue. Figure taken from Ref. [273].

tors and are frequently updated to reflect recently published data. The following section will briefly cover the details of LZ software packages and data analysis tools.

2.6.1 BACCARAT

Baccarat is the LZ simulation package built on a Geant4 framework. The LZ geometry is constructed by creating a series of nested volumes with specific material properties to model particle interactions in detector volumes. A visualisation of the geometry is shown in Figure 2.6.1. Custom physics lists are used to model particle interactions at low energies for both ER and NR interactions. The prominent modules including in Baccarat are:

- **G4EMLivermorePhysics:** This module uses Livermore models for gamma and electron cross-sections [274, 275], which are valid down to low-energy processes occurring at 10 eV. This model has a particular focus on Rayleigh and Compton scattering, bremsstrahlung and the photoelectric effect.
- **G4HadronPhysicsQGSP_BIC_HP_Gd:** Employs the binary cascade (BIC) intra-nuclear model for certain low-energy inelastic interactions. Modifications to the nuclear capture and subsequent gammas cascade of excitation states of ^{155}Gd and ^{157}Gd isotopes are improved using the DICE-BOX neutron capture model [276]. This is vital for correctly simulating OD physics.
- **G4S1Light and G4S2Light:** Developed by LZ collaborators to integrate NEST physics into Baccarat, to accurately generate light and charge quanta in xenon.

2.6.2 Parametric chain and full chain

From Baccarat there are two separate chains that process the information output: the parametric chain and the full chain. Both simulation chains are outlined in Figure 2.6.2.

The parametric chain records energy depositions in detector volumes and passes them to a secondary package Lzlama (LZ Light Analysis Montecarlo Application). Lzlama models the LZ detector response using Nest to convert energy deposits to observables such as S1 and S2 signals, and provides timing and event location reconstruction. This enables the generation of large statistics datasets, which can be analysed to assess background rates and sensitivity analysis. Probability density functions (PDFs) of (S1c, $\log_{10}$(S2c)) distributions for signal and background simulations are used to produce the sensitivity limits of LZ using a Profile Likelihood Ratio analysis (PLR).

The full chain enables a full optical simulation of the VUV photons and ionisation electrons produced by interactions in the LXe, as well as scintillation in the OD. Custom models have been added into BACCARAT to correctly model these physics processes. NEST is used to calculate the raw photons and electrons as a result of an interaction. PMT hits recorded by BACCARAT are then processed through the Detector Electronics Response (DER) software package, which translates quanta into PMT waveforms by modelling the front-end electronics. While the optical processing chain is more computationally intensive, it allows for realistic, event-by-event analysis.

The output from LZ simulations is designed to be in a format such that it can be analysed analogous to real data collected by the detector systems. Therefore, the same data quality cuts and analysis methods can be used to both MC generated data and real data.

2.6.3 LZap

The LZ Analysis Package (LZap) is the data processing and reconstruction software used by LZ. LZap extracts the PMT charge and time information from digitised signals. Calibrations are then applied to convert ADC signals to physical quantities, and the pulse finder and pulse classifier identify S1 and S2 events above a certain electronic noise threshold. For LZ we require a 3-fold coincidence, i.e. record signals above threshold in at least three PMTs. Time-ordering of S1 and S2 pulses is then used to identify single scatter (SS) events where one S1 precedes one S2. Multiple scatter (MS) events have one S1 preceding multiple S2 signals.

Raw data containing S1 and S2 pulses summed over the signals collected by the TPC, Xe skin and OD PMT arrays can be visualised using the LZ Event Viewer. The Event Viewer can apply LZap processing to raw event files or can

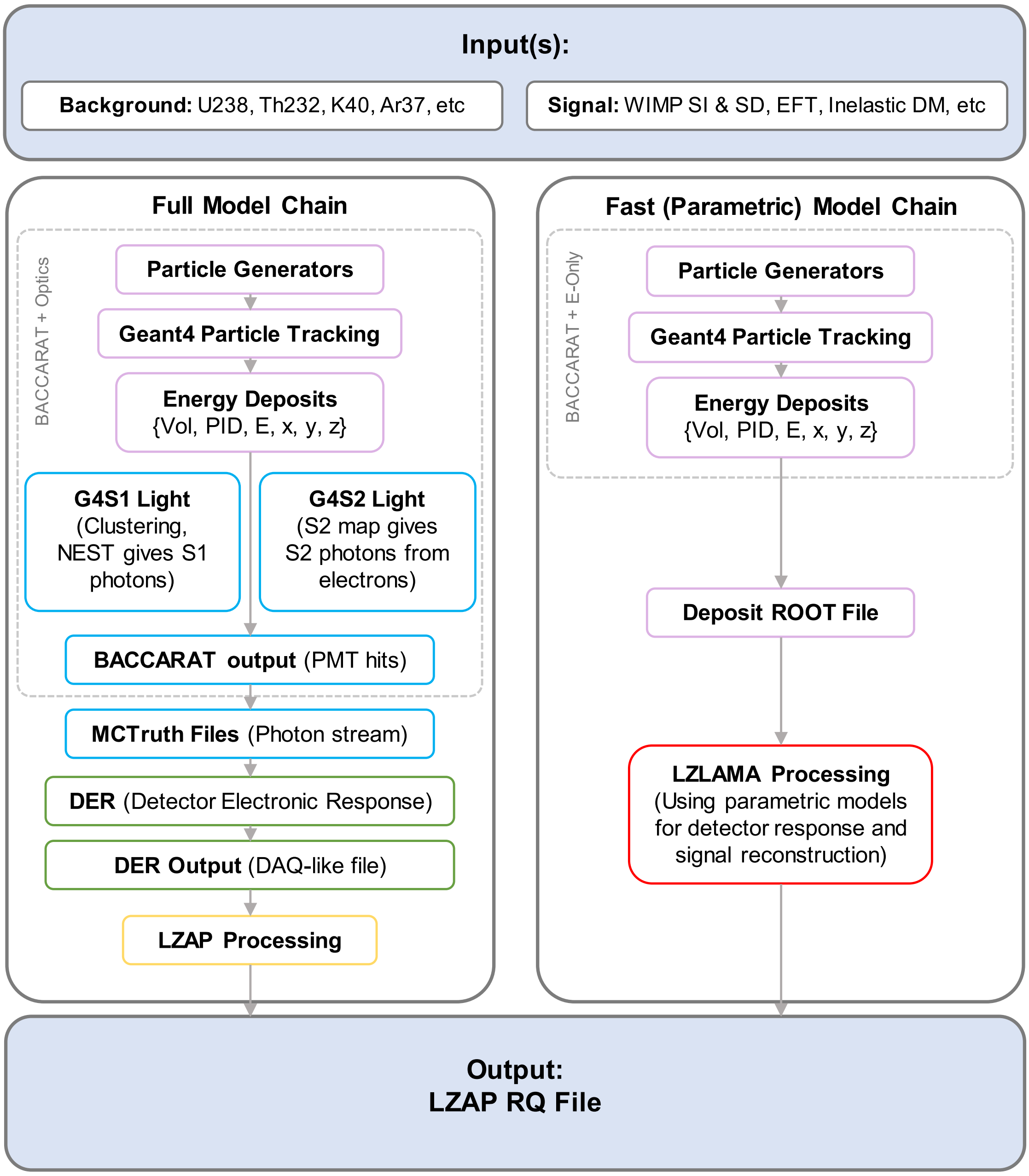

Figure 2.6.2: The LZ simulation framework for both the optical chain (full chain model) and the energy-only chain (parametric model chain). Diagram adapted from previous version produced by Alissa Monte (University of California, Santa Barbara).

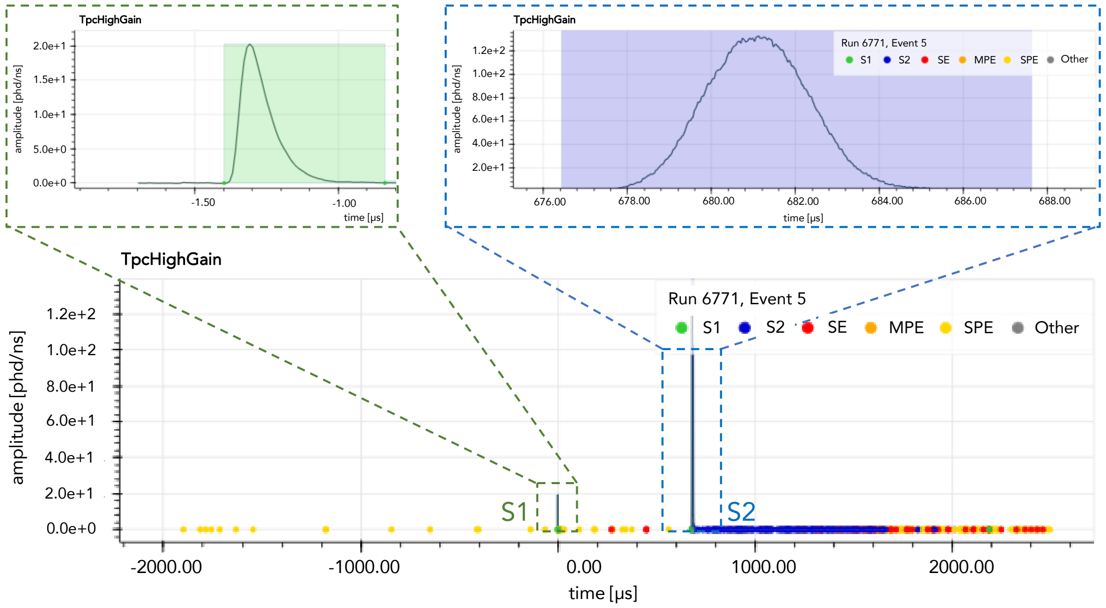

Figure 2.6.3: An example of an SR1 event displayed in the LZ event viewer, processed with LZap version 5.4.6. This is a single scatter event with one S1 pulse followed by one S2 pulse. The S1 pulse is shaded green and is highlighted by the dashed green box. The S2 pulse is shaded blue and highlighted by the dashed blue box.

load pre-processed waveform files. It is particularly useful for checking properties of irregular events, as well as providing event classification, event trigger information and PMT hit map data. An example SS event recorded in the first science run (SR1) of LZ is shown in Figure 2.6.3.

The outputs of LZap processing are called reduced quantities (RQs), which are the high-level variables that are used in LZ physics analysis. LZap RQs are stored in ROOT files [277] that can be analysed using either C++ frameworks or Python libraries, e.g. Uproot [278].

2.7 Science Run 1

2.7.1 Data collection and calibrations

LZ's first Science Run (SR1) commenced after commissioning and preliminary *in situ* calibrations of the detector. The SR1 data-taking period ran from 23rd

December 2021 to 11th May 2022 under stable detector conditions. SR1 had the primary goal of being the first search for WIMP dark matter with LZ, setting new limits for spin-independent and spin-dependent interactions. A new world-leading limit was set on the spin-independent WIMP–nucleon cross-section at a sensitivity of $9.2 \times 10^{-48}\,\mathrm{cm}^2$ at the 90% CL for a WIMP mass of $36\,\mathrm{GeV}/c^2$. The following discussion will outline the details of the LZ SR1 WIMP search result presented in Ref. [146].

SR1 also served as an engineering run, testing stable operating conditions of the detector. A drift field of $193\,\mathrm{V\,cm^{-1}}$ was established between the cathode and gate electrodes. A field of $7.3\,\mathrm{kV\,cm^{-1}}$ was established over the gas extraction region. The 10 t of xenon used in LZ was continuously purified throughout data-taking, at a rate of $3.3\,\mathrm{t\,d^{-1}}$ through the zirconium getter system described in Section 2.3.4. The observed electron lifetime was between 5000 μs and 8000 μs, which is significantly longer than the maximum drift time of 951 μs in the TPC at this field configuration. Twelve TPC PMTs and two Xe skin PMTs developed malfunctioning connections or displayed excessive noise during detector commissioning and were disabled prior to the run.

The (x,y) location of events is determined by the PMT hit pattern of S2 light from the extracted ionisation electrons, using the MERCURY algorithm [279]. The algorithm was tuned using uniformly distributed radioactive sources in the TPC. A 1σ resolution of 4 mm is reported for S2 signals of 3000 phd. This resolution worsens by a factor of ~ 2 near the TPC wall due to asymmetric light collection at the edge of the TPC. In the z direction, a 1σ resolution of 0.7 mm is reported for events near the cathode electrode.

LZ uses radioactive sources to calibrate the detector response to ER and NR events. ER calibration events were obtained by using $^{83\mathrm{m}}$Kr and $^{131\mathrm{m}}$Xe before and during the WIMP search and CH_3T post-search. NR calibration events were produced by the DD-generator directed to the TPC by a conduit and an

AmLi source deployed between the walls of the cryostat vessels in three azimuthal positions and three z positions, giving a total of nine positions overall. The NEST ER model is tuned to match the median and widths of the ER response in (S1c, $\log_{10}$(S2c)) using tritium data at low ER energies. The model is also tuned to match the reconstructed energies of $^{83\text{m}}$Kr (41.5 keV), $^{129\text{m}}$Xe (236 keV) and $^{131\text{m}}$Xe (164 keV) photopeaks. The photon detection efficiency g_1 is determined to be (0.114 ± 0.002) phd/photon and the ionisation gain g_2 to be (47.1 ± 11.0) phd/electron. Figure 2.2.4 shows the tritium and DD neutron data compared to the calibrated model.

2.7.2 Data analysis

The WIMP signal considered in the SR1 analysis is expected to produce low-energy ($\sim$ keV), single scatter NR events uniformly distributed in the TPC, with no coincident signals in the TPC, Xe skin or OD. The following analysis strategy is used to isolate the WIMP population:

- Exclude time periods of excessive TPC activity and electronics interference
- Remove multiple scatter interactions in the TPC
- Remove events outside of the energy region of interest (ROI)
- Remove events due to accidental coincidence of S1 and S2 pulses
- Remove events with coincident signals in the TPC and Xe skin or the OD
- Remove events near the TPC active volume boundaries

For SR1, forms of bias mitigation such as blinding the signal region or adding fake events (“salting”), were avoided to control systematic errors present in any new detector. Instead, all analysis cuts were tested, developed and optimised using sideband and calibration datasets.

The SR1 dataset totals 89 live days of exposure after accounting for detector maintenance, calibration runs, periods of high-rate and 3% loss due to data acquisition (DAQ) dead-time. A further time hold-off was applied to remove periods of elevated rates observed in the TPC following events with large S2 pulses and cosmic-ray muons. The final search live time after these cuts is $(60 \pm 1)\,\mathrm{d}$ where a WIMP interaction could be reconstructed.

Multiple scatters are removed from the dataset using the event classification provided by LZap processing of raw data. The ROI is defined in terms of S1 and S2 signals, where S1c is in the range of 3–80 phd, uncorrected S2 is greater than 600 phd and S2c is less than 10^5 phd.

A set of analysis cuts were applied to remove accidental coincidence of S1 and S2 signals, called "accidentals". Accidental events occur when an unpaired S1 and unpaired S2 are accidentally paired to mimic a single scatter event. Cuts to remove these events target sources of isolated S1 and S2 signals by the expected behaviour of S1 and S2 pulses with respect to other detector quantities, e.g. drift time, pulse width. A more throughout discussion of accidental events can be found in Ref. [228].

Events with coincident signals recorded in the TPC and Xe skin or OD are removed to reduce backgrounds produced by gamma-rays and neutrons. Gamma backgrounds are mitigated by removing events with prompt signals in the OD and Xe skin within $\pm 0.3\,\mu\mathrm{s}$ and $\pm 0.5\,\mu\mathrm{s}$ of the TPC S1 pulse, respectively. Neutron captures on Gd or H in the OD can be tagged by an OD pulse of greater than $\sim 200\,\mathrm{keV}$ within $1200\,\mu\mathrm{s}$ after the TPC S1. Large skin pulses also recorded within this timeframe reject gammas that are directed towards the TPC from an OD capture reaction.

Events outside of a central fiducial volume (FV) are removed to disregard external and wall backgrounds that concentrate near the TPC boundaries. These are shown in Figure 2.7.1. Events at high radius values have worse position reconstruction resolution due to the reduced S2 light collection efficiency and charge-loss effects due to the PTFE covered TPC wall. The FV is defined at a radial distance

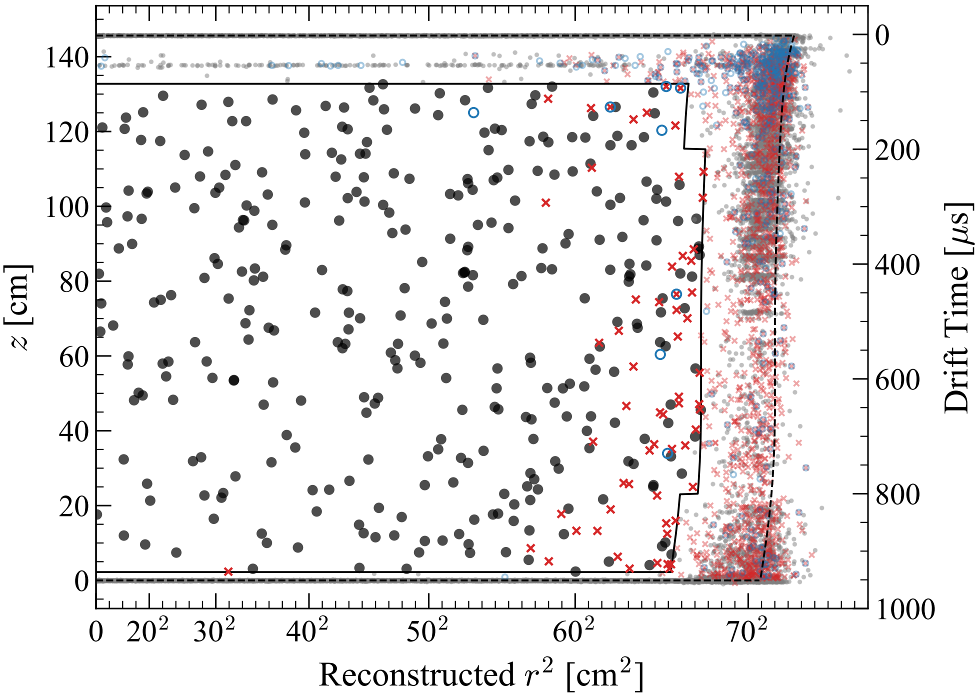

Figure 2.7.1: SR1 data in reconstructed r^2 and z after all analysis cuts. Black data points show the data inside the fiducial volume (FV). Red crosses and blue circles show events that have been vetoed by coincident interactions in the skin and OD, respectively. The solid line shows the definition of the FV and the dashed line defines the active region of the TPC. Figure taken from Ref. [146].

of 4.0 cm away from the active volume edge in reconstructed r. Additional small volumes are removed from the top and bottom corners of the FV to account for increased rate of events in these locations. The stand-off distances are 5.2 cm for drift time $< 200\,\mu\text{s}$ and 5.0 cm for drift time values $> 800\,\mu\text{s}$. Events with drift time values $< 86\,\mu\text{s}$ and $> 936.5\,\mu\text{s}$ established by the grid locations are excluded. The mass of xenon in the FV is estimated to be (5.5 ± 0.2) t using tritium data and confirmed by geometric calculations.

Figure 2.7.2 shows the 335 events passing all data quality cuts outlined above, in (S1c, $\log_{10}$(S2c)) parameter space. Contours representing a 30 GeV/c^2 WIMP, a flat NR distribution and the background model are also shown. The WIMP model assumes spin-independent scattering with an isotropic Maxwell-Boltzmann velocity distribution (see Section 1.3.3).

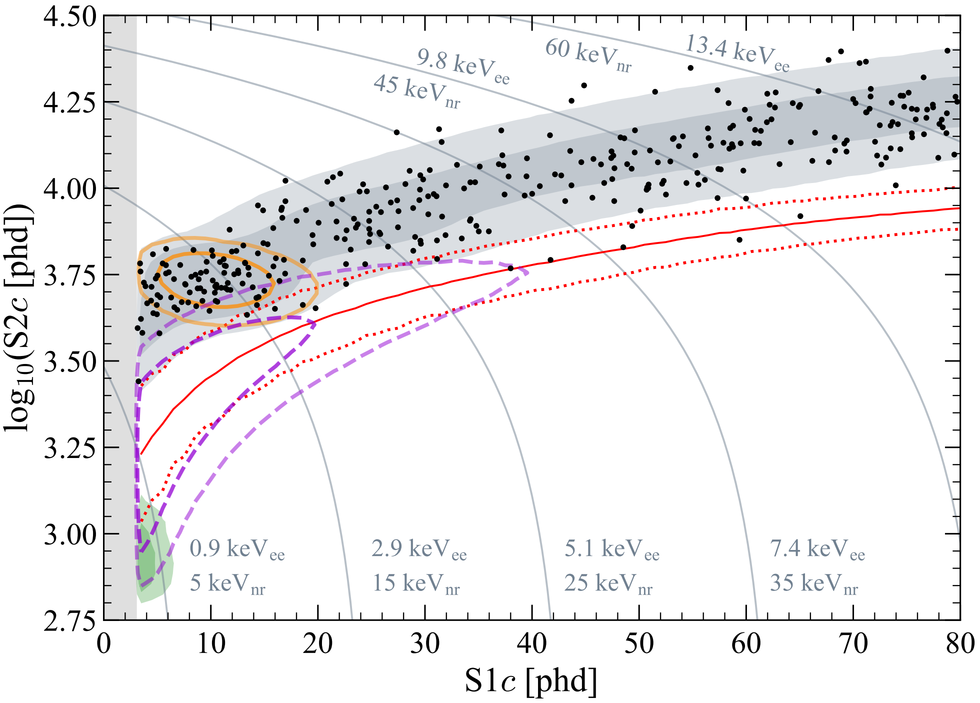

Figure 2.7.2: WIMP search data after all data quality cuts in (S1c, $\log_{10}$(S2c)) parameter space. 1σ and 2σ contours are shown for a 30 GeV/c^2 WIMP (purple), the ^{37}Ar component (orange), ^{8}B neutrinos (shaded green) and the best-fit background model (grey). The solid red line indicates the NR median, and the dotted red lines are the 10% and 90% quantiles. Figure taken from Ref. [146].

2.7.3 Background model

The background model for the WIMP search consists of nine components that are grouped based on their spectra in the ROI or the uncertainty on their rate. Table 2.7.1 lists the expected number of events for each component [146]. A comprehensive summary of all backgrounds relevant to the WIMP search and upcoming physics analyses can be found in Ref. [228].

From Table 2.7.1 it can be seen that the dominant source of background to the WIMP search is ER events originating from radioactive decays of impurities dispersed in the LXe volume. ^{214}Pb from the ^{222}Rn decay chain, ^{212}Pb from the ^{220}Rn decay chain and ^{85}Kr have broad energy spectra that are flat in energy across the WIMP ROI and are summed into an overall β background. The concentrations of ^{214}Pb and ^{212}Pb are determined by fitting peaks in reconstructed energy spectra

Table 2.7.1: Number of events from various sources in the SR1 60 d × 5.5 t exposure [228]. The middle column shows the expected number of events with uncertainties. These uncertainties are used as constraints in the combined fit of the background model plus the model for a 30 GeV/c^2 WIMP. The results from the fit are shown in the final column.

Source	Expected events	Fit results
^{214}Pb	164 ± 35	...
^{212}Pb	18 ± 5	...
^{85}Kr	32 ± 5	...
Detector ER	1.4 ± 0.4	...
β decays + Detector ER	215 ± 36	222 ± 16
ν ER	27.1 ± 1.6	27.2 ± 1.6
^{127}Xe	9.2 ± 0.8	9.3 ± 0.8
^{124}Xe	5.0 ± 1.4	5.2 ± 1.4
^{136}Xe	15.1 ± 2.4	15.2 ± 2.4
^{8}B CEνNS	0.14 ± 0.01	0.15 ± 0.01
Accidentals	1.2 ± 0.3	1.2 ± 0.3
Subtotal	273 ± 36	280 ± 16
^{37}Ar	[0, 288]	$52.5^{+9.6}_{-8.9}$
Detector neutrons	$0.0^{+0.2}$	$0.0^{+0.2}$
30 GeV/c^2 WIMP	...	$0.0^{+0.6}$
Total	...	333 ± 17

above the WIMP ROI. The amount of ^{85}Kr present in the xenon was informed by measurements of $^{\mathrm{nat}}$Kr/$^{\mathrm{nat}}$Xe (g/g) from gas chromatography and *in situ* mass spectroscopy. The β background is also combined with ER contributions ($< 1\%$) from NORM gamma backgrounds from detector materials [227] and the cavern walls [262].

Solar neutrinos are expected to contribute to the flat ER background in the WIMP ROI, with rates calculated from neutrino flux values [117]. As these predictions are precise, neutrinos are kept separate from the β background in this model. The amount of background from ^{124}Xe DEC and ^{136}Xe $2\nu\beta\beta$ are derived from isotopic abundances, lifetimes and decay schemes. Cosmogenic activation of xenon stored above ground before deployment at SURF produces unstable isotopes that decay in the WIMP ROI. Two key components which are present in SR1 are

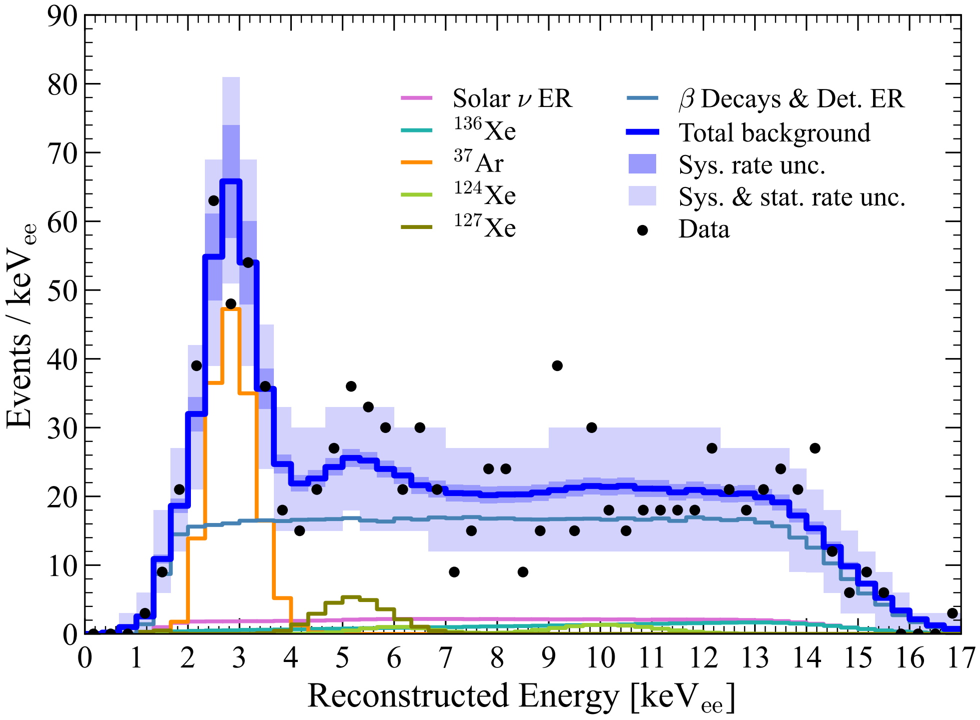

Figure 2.7.3: Reconstructed energy spectrum of the SR1 best-fit model. The blue line shows that total summed background. The model uncertainty and the combined model and statistical uncertainty are shown by the dark blue and light blue bands, respectively. Background components are shown via colours given in the legend. It should be noted that contributions from ^{8}B and accidentals are included in this fit model but are too small to be visible in this plot. Figure taken from Ref. [146].

^{127}Xe and ^{37}Ar, which have half-life values of 36.3 d and 35.0 d, respectively [260, 261].

The NR background includes solar neutrinos that interact with xenon nuclei via CEνNS and radiogenic neutrons. The rate of ^{8}B CEνNS events is small due to the S2 threshold cut. Detector neutrons are informed by the ability to veto events using coincident signals in the OD, the efficiency of which is assessed via AmLi calibration sources. This leads to zero expected neutron events from detector sources after data quality cuts.

Finally, the number of accidental events is estimated using a specialist simulation of unphysical S1-S2 pairings and applying WIMP analysis cuts. Selection efficiency is applied to the remaining events to constrain the final accidental rate.

Events remaining in the WIMP search ROI after all data quality and physics cuts are fitted using an extended, unbinned likelihood containing both signal and background components:

$$\begin{aligned}\mathcal{L}(\mu_s, \boldsymbol{\theta}) = &\ \mathrm{Pois}(N_0|\mu_{\mathrm{tot}}) \\ &\times \prod_{e=1}^{N_0} \frac{1}{\mu_{\mathrm{tot}}} \left(\mu_s f_s(\boldsymbol{x_e}) + \sum_{b=1}^{N_b} \mu_b f_b(\boldsymbol{x_e}) \right) \\ &\times \prod_{b=1}^{N_b} f_b(\mu_b|\nu_b),\end{aligned} \tag{2.7.1}$$

where $\mu_{\mathrm{tot}} = \mu_s + \sum_{b=1}^{N_b} \mu_b$ is the sum of signal and background and e is the index of which runs to the total number of observed events N_0. Signal (f_s) and background (f_b) PDFs are functions of given analysis parameters $\boldsymbol{x_e} = (\mathrm{S1}c, \log_{10}(\mathrm{S2}c))$ which exploits ER-NR discrimination capabilities. The set of nuisance parameters $\boldsymbol{\theta}$ is the set of counts for each background component $\{\mu_b\}$. A constraint function $f_b(\mu_b|\nu_b)$ is used to limit the value of each nuisance parameter based on some prior expectation of each background (ν_b).

For all components, except ^{37}Ar and neutron backgrounds, Gaussian constraints were applied with standard deviations corresponding to the systematic uncertainty on the expectation of each background source. The results of the fitting procedure are listed in right-hand column of Table 2.7.1. The background model and data as a function of reconstructed energy are shown in Figure 2.7.3, with data consistent with a background-only model.

It can be seen from Table 2.7.1 that the likelihood fit does not provide better constraints for the background components than the prefit assessments in the vast majority of cases (excluding ^{37}Ar). In other words, the background model determined without using the WIMP search data is consistent with the fit to the WIMP search data, with better precision than the WIMP search data alone can provide.

The observed background rate for WIMP search criteria outlined above is $(6.3 \pm 0.5) \times 10^{-5}$ events/keV$_{\mathrm{ee}}$/kg/day in the low-energy region, which is approximately 60 times lower than the equivalent rate of $(3.6 \pm 0.4) \times 10^{-3}$ events/keV$_{\mathrm{ee}}$/kg/day reported by the LUX predecessor experiment [228, 280]. The background rate in LZ is likely to improve further over time as cosmogenically-activated xenon isotopes and ^{37}Ar components will decay to subdominant levels.

2.7.4 WIMP sensitivity

Frequentist hypothesis testing is the method commonly used for direct detection experiments to place constraints on regions of parameter space [117]. Statistical inference is performed by employing a two-sided profile likelihood ratio (PLR) test statistic [281]. A scan of signal cross-section values over a range of possible WIMP masses produces the sensitivity limit, typically reported at the 90% confidence level. Detailed discussions of statistical methods, including frequentist and Bayesian philosophies, relating to dark matter searches can be found in Ref. [282].

Figure 2.7.4 shows the LZ SR1 exclusion curve in $(m_\chi,\ \sigma_{\mathrm{SI}})$ parameter space, along with limits reported by DEAP-3600, LUX, XENON1T, XENONnT and PandaX-4T. Above the smallest tested WIMP mass of $9\,\mathrm{GeV}/c^2$, the best-fit number of WIMP events is zero and the data are in agreement with the background-only hypothesis. For the SR1 dataset, LZ reports a minimum limit of $9.2 \times 10^{-48}\,\mathrm{cm}^2$ for the spin-independent WIMP–nucleon cross-section at a WIMP mass of $36\,\mathrm{GeV}/c^2$, rejecting values above this value at the 90% CL [146]. A power constraint was applied in the mass range of 13–$36\,\mathrm{GeV}/c^2$ in order to account for an under-fluctuation of observed data events.

At low WIMP masses sensitivity is limited by the energy threshold of the detector and the minimum of the exclusion curve is related to the mass of the target nuclei. At larger WIMP mass the event rate is suppressed by a factor of $1/m_\chi$ due to the reduced WIMP flux as a result of the conservation of the local

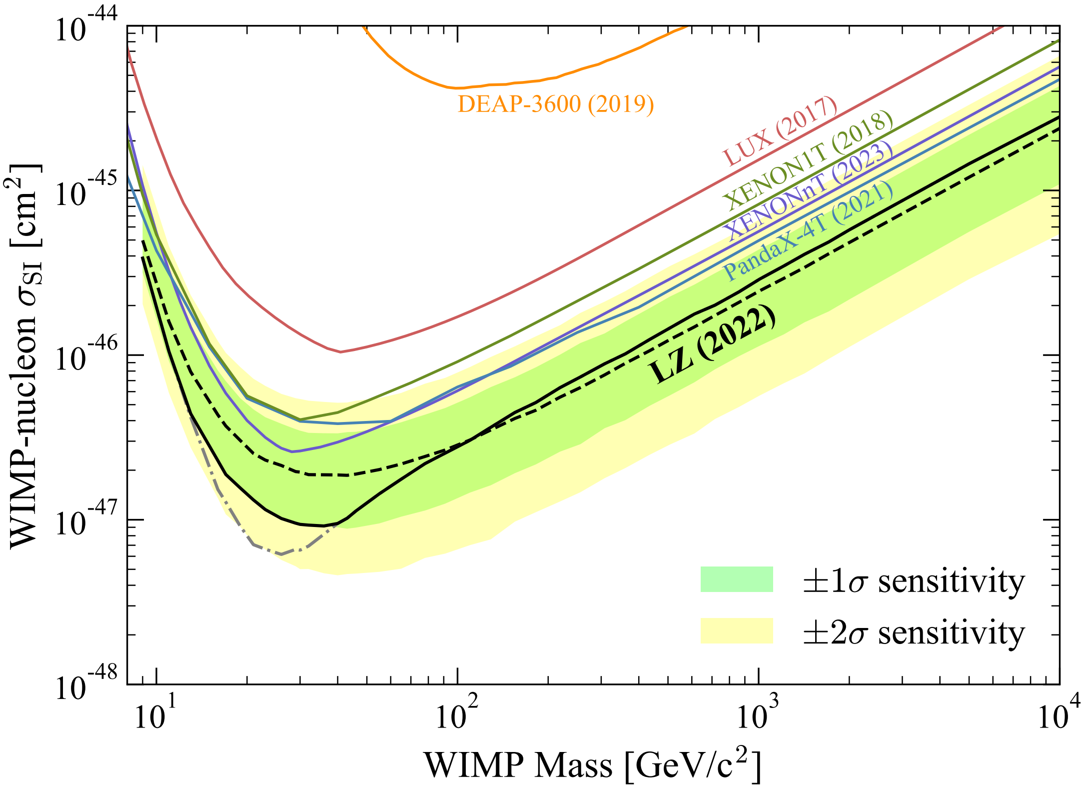

Figure 2.7.4: The 90% confidence limit (black line) for the spin-independent WIMP–nucleon cross-section as a function of WIMP mass for the LZ SR1 exposure. In green and yellow are the $\pm 1\sigma$ and $\pm 2\sigma$ sensitivity bands. Also plotted are sensitivity results from previous dark matter experiments DEAP-3600 [138], LUX [283], XENON1T [284], XENONnT [148] and PandaX-4T [150]. Figure updated from Ref. [146].

dark matter density. The overall sensitivity of an experiment is dominated by the mass of the target and the duration of the experiment, which is also called the exposure, coupled with the ability to reduce background events [285].

In summary, the LZ experiment has achieved the most sensitive measurement of the spin-independent WIMP–nucleon cross-section for WIMP masses greater than 9 GeV/c^2. This can be attributed to successful detector operations over the duration of the SR1 campaign with the largest xenon target TPC currently existing. LZ operations continue in the Davis cavern at SURF, with a planned 1000 live day exposure to reach a projected sensitivity of 1.4×10^{-48} cm^2 for a 40 GeV/c^2 mass WIMP within a 5.6 t fiducial volume [145]. LZ will also take advantage of the low-background environment to search for several other rare physics signals that can be observed with this detector technology, such as axions, solar neutrinos and rare nuclear decays.

3 The Davis cavern environment

The monitoring of environmental backgrounds for experiments that search for rare physics is vital in order to potentially claim discovery of significant new signal. Muon flux, radon emanation and cavern backgrounds from radioactivity all contribute to the events recorded by such experiments. Therefore, it is of great importance to fully characterise the environment surrounding dark matter detection experiments. This Chapter introduces the relevant science facilities at SURF and how they are suited to house low-background experiments, including LZ. A short summary of the geology of the Black Hills region of South Dakota is presented to contextualise the cavern rock composition. The layout of the Davis cavern is shown and radioassay results from samples of laboratory materials are quoted. Following, sources of backgrounds originating from the cavern are described and preliminary measurements of the gamma-ray background from the 2017 gamma spectroscopy campaign are detailed. Finally, the LZ environmental monitoring station is introduced which aims to monitor in real time radon, neutron and gamma-ray backgrounds in the lower level of the Davis cavern.

3.1 Overview of site geology

SURF is situated in the Black Hills region of South Dakota, which is made up of a variety of geological rock formations. Surveys of the rock formations present at SURF shows that there are six rock formations that contribute to the geology of the area: Grizzly, Flagrock, Northwestern, Ellison, Homestake and Poorman [286]. Geological surveys taken at the Homestake mine show that most of the rock present on the 4850’ level is of the Homestake formation, which is made of amphibolite, a metamorphic rock with relatively low U and Th content. Additionally, the Davis cavern rock also contains a rhyolite intrusion, which is an igneous volcanic rock that is silica-rich and has a much higher natural radioactivity.

The chemical composition of the Homestake amphibolite rock has been measured using an array of samples taken from the surface at SURF. The chemical composition adopted for this material is shown in Table 3.1.1, which has been used for models in previous simulation studies [254, 256, 262].

A 3D geological model of the rock situated above the Davis campus is shown in Figure 3.1.1. Models of the local topology and geology are essential to accurately calculate the rock overburden throughout the underground laboratory space, as both the surface topology and the internal rock formations vary for different laboratory spaces at SURF [287].

Table 3.1.1: Radioassay results of a Homestake amphibolite rock sample 278-2. The compounds found in the rock are shown with their corresponding percentage weight fractions.

Homestake rock sample 278–2	
Rock component	Composition [% weight]
Al_2O_3	13.6 ± 0.1
CaO	7.9 ± 0.1
FeO	12.7 ± 0.1
H_2O	10.7 ± 0.01
K_2O	0.21 ± 0.002
MgO	7.0 ± 0.1
MnO	0.13 ± 0.01
Na_2O	2.87 ± 0.03
P_2O_5	0.07 ± 0.001
SiO_2	43.7 ± 0.4
TiO_2	1.22 ± 0.01

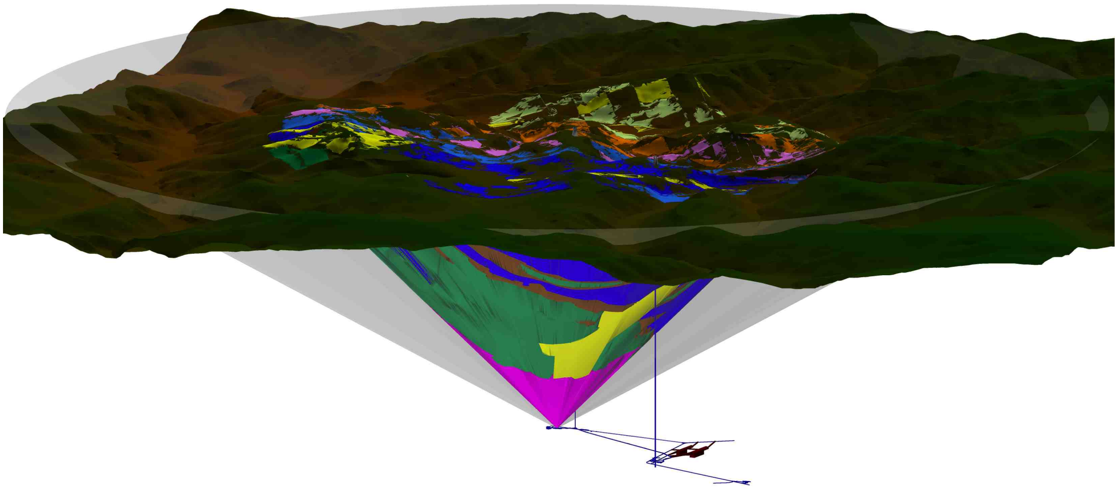

Figure 3.1.1: 3D geological model showing rock cone above the 4850' level centred on the Davis campus [287]. The coloured section represents different rock formations in the 45-degree cone; the gray outline represents the extent of a 60-degree cone. The vertical lines show the locations of the Ross and Yates shafts. Figure taken from Ref. [187].

3.2 The Davis cavern

The Davis campus is a state-of-the-art laboratory space in close proximity to the Yates access shaft at the 4850' level at SURF. A diagram of the space is shown in Figure 3.2.1. Two main experiments are housed in the Davis campus: the MAJORANA DEMONSTRATOR experiment [288] and the LZ experiment, highlighted in blue and red, respectively.

LZ is located within the Davis cavern at the end of the "common corridor" which is shared between the two science collaborations. The dimensions of the Davis cavern are (17 m L × 10 m W × 12 m H; 2089 m^3), which are average values based on laser-scan data taken after the laboratory outfitting was completed. The Davis cavern is divided over two floors, termed the upper and lower levels. Figure 3.2.2a shows a SolidWorks CAD model of the LZ experiment contained in the Davis cavern, with all detector subsystems included.

A layer of sprayed concrete (shotcrete) coats the walls and ceiling of the Davis cavern, with an average thickness of 12.7 cm. This outermost layer coating the laboratory walls is the white material in Figure 3.2.2b. The thickness of the

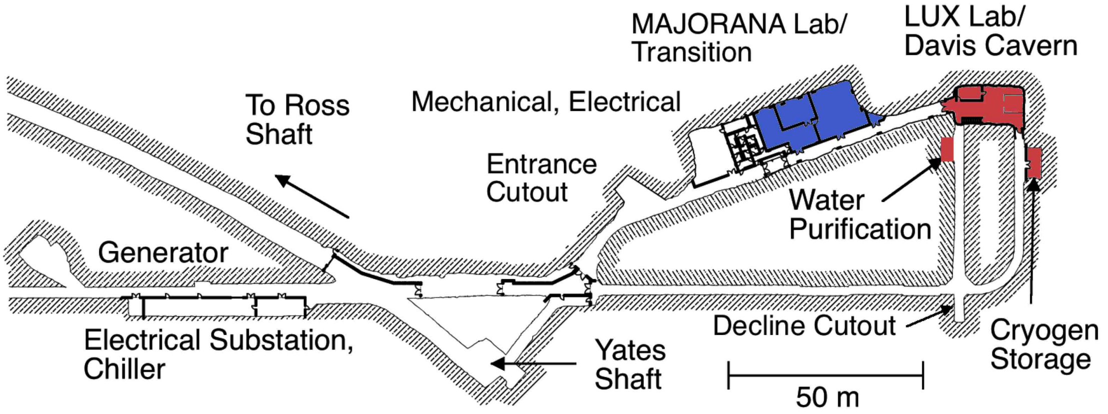

Figure 3.2.1: The floor plan of the Davis campus on the 4850' level showing the main laboratory spaces. The LZ (formerly LUX) lab space in the Davis cavern is highlighted in red. Figure taken from Ref. [187].

shotcrete is known to vary by a factor of two. The floor of the Davis cavern is made of 15 cm of low-radioactivity concrete composed of a rock aggregate selected to lower the typical U/Th concentration by a factor of ~ 2 [289]. The floor in the compressor room towards the north side of the Davis cavern is 30 cm thick.

A map showing the expected locations of the rhyolite intrusions in the Davis cavern walls is shown in Figure 3.2.3. The relevant percentage contribution from each wall is shown, highlighting that the contributions from the floor (64%), west wall (42%) and north wall (36%) are the most dominant, where the intrusion is known to pass diagonally through the cavern.

Radioassays of samples of rock, concrete, shotcrete and gravel have been performed using HPGe screening to assess the U/Th/K concentrations in each material, and are shown in Table 3.2.1. Variations of radioactivity from all samples were observed, so both average values and ranges are given [262]. These assays show that U/Th contributions from the rhyolite intrusions can be 30–40× higher than that from the Homestake amphibolite formation.

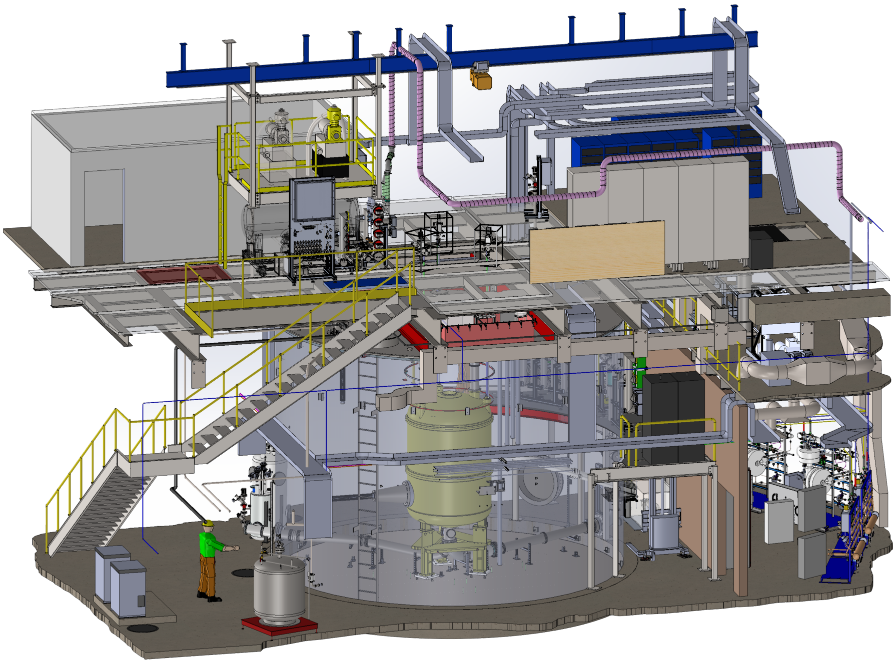

(a) SolidWorks CAD drawing of the LZ experiment in the Davis cavern.

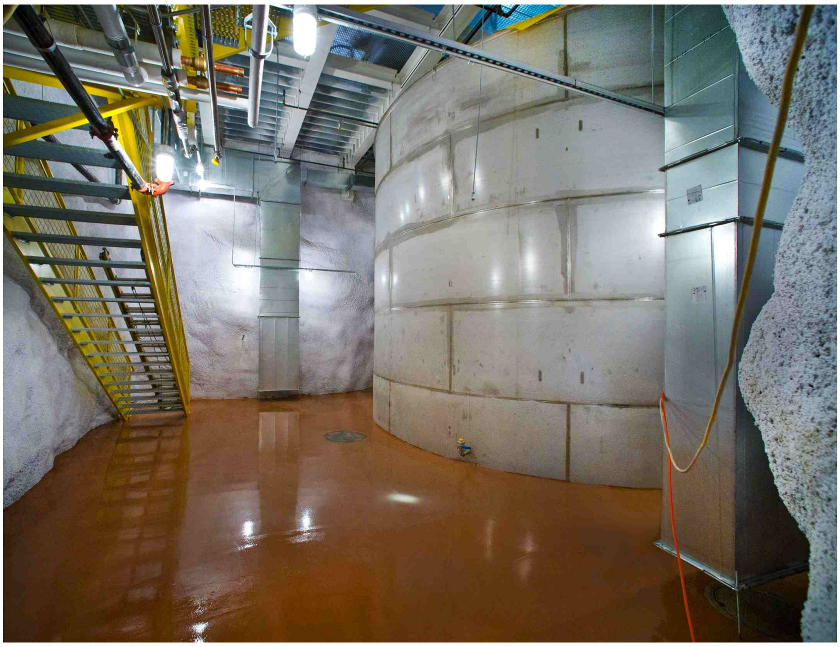

(b) Photograph of the Davis cavern in May 2012 after outfitting had finished showing the water tank from the lower Davis.

Figure 3.2.2: The Davis cavern. **Top:** SolidWorks CAD drawing of the LZ experiment in the Davis cavern. This diagram shows the upper and lower levels of the Davis cavern that each house LZ specific subsystems. Diagram produced by Joseph Saba (Lawrence Berkeley National Laboratory). **Bottom:** Photograph of the Davis cavern in May 2012 after outfitting had finished showing the water tank from the lower Davis. The white coating on the laboratory walls is the layer of shotcrete. Figure taken from Ref. [187].

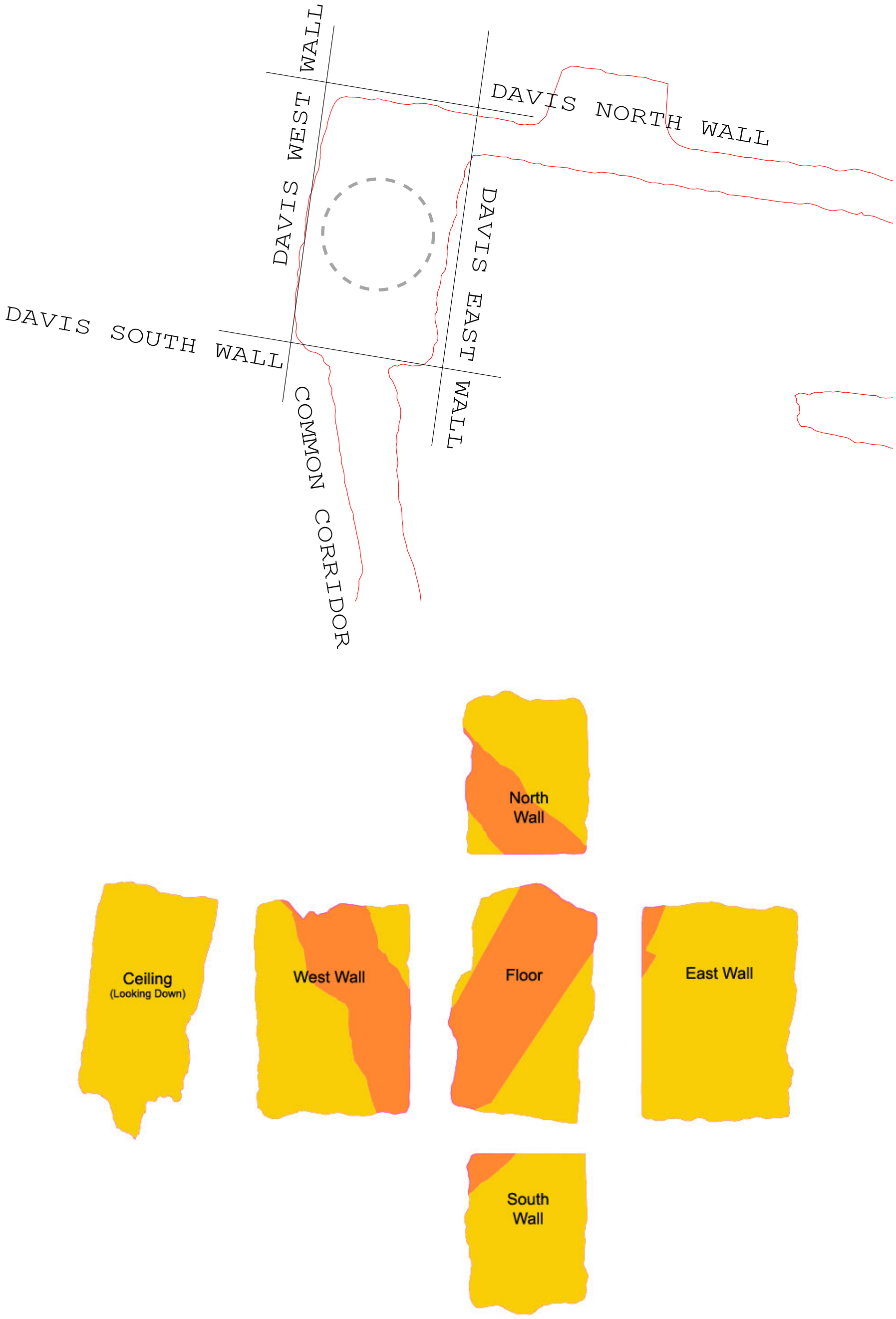

Figure 3.2.3: Maps of the Davis cavern walls. **Top:** A schematic of the Davis campus and the common corridor. The approximate location and size of the water tank is shown by the dashed grey circle. **Bottom:** A map of the expected locations of the rhyolite intrusions on each face of the Davis cavern walls. The rhyolite sections are highlighted in orange, while the amphibolite is shown in yellow. Figure adapted from Ref. [262].

Table 3.2.1: Values of measured activities from radioassays of rock, concrete and shotcrete samples taken during the construction of the Davis cavern [289]. The average and the range of activity measurements are given. When not stated, overall uncertainties are taken to be 10–20%. The final two samples are shotcrete and gravel extracted from the Davis cavern at the time of measurements from the preliminary gamma-ray background campaign [262].

Sample		^{40}K [Bq/kg]	^{238}U [Bq/kg]	^{232}Th [Bq/kg]
Homestake	Avg.	297	2.7	1.3
	Range	31-601	0.7-9.5	1.0-6.5
Rhyolite	Avg.	1291	108	44
	Range	523-2127	99-135	7.7-61
Concrete	Avg.	381	27	13
	Range	368-393	22-27	13-14
Shotcrete	Avg.	272	23	12
	Range	127-393	22-28	8.1-14
Shotcrete	–	220 ± 30	21 ± 1	11.4 ± 0.4
Gravel	–	35.0 ± 0.6	26.3 ± 0.1	1.7 ± 0.8

3.3 Cavern backgrounds

Many rare event physics search experiments are situated in underground laboratories at various locations around the world to take advantage of ultra-low background environments [126]. The cosmogenic muon flux is heavily reduced due to passive shielding provided by rock overburden, which is at a vertical depth of 1470 m (4300 m.w.e.) for the 4850' level at SURF [290]. However, radiogenic backgrounds originating from the intrinsic radioactivity in the cavern environment must also be considered.

3.3.1 Radon emanation

Long-term airborne radon measurements have been taken throughout the SURF laboratory space to track seasonal dependencies in radon concentration levels [187, 289]. Ventilation is provided by the Oro Hondo fan and #5 shaft fan, which brings airflow through the Ross and Yates access shafts. Averages from the Davis cam-

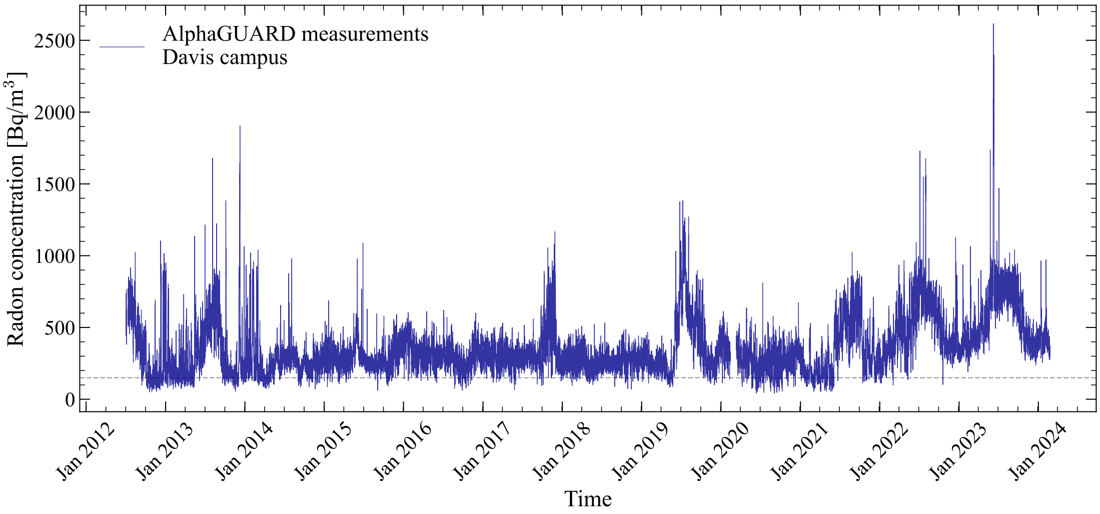

Figure 3.3.1: The radon concentration levels recorded at the Davis campus from July 2012 to February 2024. The baseline at 150 Bq m^{-3} is shown via the dashed grey line.

pus indicate higher radon concentrations over summer months with an average of approximately 300 Bq m^{-3} and a low baseline concentration of 150 Bq m^{-3} during the winter months. High rates above 1000 Bq m^{-3} have been observed, and are usually correlated with known events such as ventilation fan maintenance or covering of the Ross and Yates shafts. Radon trends at the Davis campus are shown in Figure 3.3.1, which have been collected since completion of the cavern in July 2012. Recent increases in trends at the Davis can be attributed to changes in underground ventilation to aid excavation occurring near the Ross access shaft.

3.3.2 Cosmogenic and radiogenic neutrons

Neutrons are produced by three main sources:

1. Muon-induced spallation interactions
2. Spontaneous fission of heavy elements
3. (α,n) reactions caused by α particles produced by ^{238}U and ^{232}Th

Highly energetic cosmic muons have sufficient energy to penetrate through the Earth's surface and cause interactions producing neutrons in detector materials and the environmental surroundings [129, 291]. The first measurement of the muon flux at the Davis campus was reported with the muon veto system of the MAJORANA DEMONSTRATOR experiment with a value of $(5.31 \pm 0.17) \times 10^{-9}$ μ $\mathrm{cm}^{-2}\,\mathrm{s}^{-1}$ [135]. Models of the muon flux used for LZ calculated using muon transport codes [255] indicate a total muon flux of 6.16×10^{-9} μ $\mathrm{cm}^{-2}\,\mathrm{s}^{-1}$, slightly higher than measurements. The accuracy of the muon model is estimated to be roughly 20%, primarily due to uncertainty in the rock density [273].

Neutrons from fission and (α,n) originate from detector materials and surroundings. In order to minimise this source of NR backgrounds, material selection and radioassay campaigns are vital. The thermal neutron background at the 4850' level was measured with ^{3}He proportional counters outside the entrance to the clean space of the Davis campus and in the MAJORANA clean space [292]. The thermal neutron flux is reported as $(1.7 \pm 0.1) \times 10^{-6}$ neutrons $\mathrm{cm}^{-2}\,\mathrm{s}^{-1}$.

3.3.3 Gamma-ray background

Gamma-rays produced by U/Th/K produce an energy spectrum with four prominent photopeak features above 1 MeV. These are:

- **^{40}K:** ^{40}K ($t_{1/2} = 1.25 \times 10^9$ years) decays via two prominent channels - beta-decay to ^{40}Ca or by electron capture to the first excited level of ^{40}Ar, with branching ratios of 89.2% and 10.5%, respectively [250]. A gamma-ray of energy 1460.8 keV is emitted from the excited ^{40}Ar nucleus decaying to the ground state.

- **^{238}U:** ^{214}Bi decays to ^{214}Po by β^- decay, emitting gamma-rays with energies of 1764.5 keV (15.4%) and 2204.2 keV (4.9%). The relevant branching ratios are given in brackets. Depending on the detector energy resolution, the lower intensity 2118.6 MeV (1.1%) peak may also be resolved (see Ref. [293]

for details of energy resolution for high-energy ER events in LZ).

- **^{232}Th:** ^{208}Tl decays by β^- emission to ^{208}Pb, decaying from the first excited state and emitting a gamma-ray of energy 2614.5 keV with branching ratio close to 100%. This is the highest energy gamma-ray produced directly by the uranium and thorium chains and is considered to be the maximum of the primary gamma background produced by NORMs.

The gamma-ray flux at SURF has been measured at the surface administration building and underground at the 800', 2000' and 4550' levels [254], and at the 4850' level in the Davis cavern using a HPGe detector [294] and a sodium iodide detector [262]. Measurements of the gamma-ray background from the Davis cavern rock from the 2017 campaign are further explored in Section 3.4.

3.4 Preliminary measurements of the cavern gamma-ray background

Gamma spectroscopy measurements of the gamma-ray background flux from cavern rocks and construction materials are standard measurements that have been taken in locations such as the Gran Sasso National Laboratory [295, 296], the Modane Underground Laboratory [297, 298], the Boulby Underground Laboratory [299, 300], the SNO cavity [301] and the China Jinping Underground Laboratory [302].

A two-week gamma-ray measurement campaign occurred in October 2017 before the start of LZ detector commissioning. Measurements of the gamma-ray flux originating from the Davis cavern rock were performed by taking *in situ* gamma-ray spectroscopy measurements at nine different locations in the Davis cavern using a thallium-doped sodium iodide detector (NaI(Tl), or simply NaI) [262]. During this time, the water tank was empty, and the nine measurements aimed to mea-

Table 3.4.1: Measurement dates, live times, radon concentrations and integrated count rates for the gamma-ray spectroscopy campaign in October 2017 [262]. Here, “looking down (up)” refers to the shielding configuration where only the underside (topside) of the detector is not shielded by lead. Uncertainties on rates are Poisson counting errors only.

Measurement position	Label	Start date	Live time	Avg. radon	Integrated rate [Hz]	
			[h]	[Bq/m^3]	Total	> 200 keV
Centre of water tank, unshielded	a	24/10/17	4.0	422 ± 34	595.7 ± 0.2	386.0 ± 0.2
Upper Davis, unshielded	b	26/10/17	3.6	868 ± 222	794.4 ± 0.2	512.0 ± 0.2
East Counting Room, unshielded	c	26/10/17	2.1	929 ± 70	1355.0 ± 0.4	750.9 ± 0.3
Edge of tank, looking down	d	16/10/17	18.2	358 ± 80	94.17 ± 0.04	64.40 ± 0.03
Halfway to edge of tank, looking down	e	17/10/17	17.9	336 ± 55	17.15 ± 0.02	10.70 ± 0.01
Centre of tank, looking down	f	19/10/17	117.0	500 ± 155	16.715 ± 0.006	10.427 ± 0.005
Centre of tank, looking up	g	18/10/17	20.2	372 ± 76	203.57 ± 0.05	139.00 ± 0.04
Centre of tank, looking west	h	24/10/17	17.3	359 ± 37	95.11 ± 0.04	51.77 ± 0.03
Centre of tank, looking east	i	25/10/17	22.3	316 ± 46	106.33 ± 0.40	59.14 ± 0.03

sure any asymmetry in rates due to the rhyolite intrusions in the cavern. This was done using different lead shielding configurations in order to expose the detector to different areas of the cavern. The detector was calibrated using ^{60}Co, ^{137}Cs and ^{228}Th sources to measure the energy response and resolution of the NaI crystal. Further details about the equipment setup and calibration results can be found in Ref. [262].

The background spectra for the nine measurements are shown in Figure 3.4.1. Table 3.4.1 shows the integrated rates for the total spectra and also specifically in the energy range 200–3300 keV. The differing live times for each exposure were dictated by time available underground at SURF, with shielded measurements given priority for overnight data-taking to account for the lower rate. The overall measured rates were highest in the east counting room, followed by the upper level of the Davis cavern and the centre of the water tank. Differences in rate can be attributed to shielding, the proximity to the steel pyramid shielding located under the water tank (see Figure 2.3.1) and differences in the structure and material of the floor.

For the measurements facing downwards at the steel shielding pyramid, the total rate measured above 30 cm of steel in the centre was within 3% of the rate in

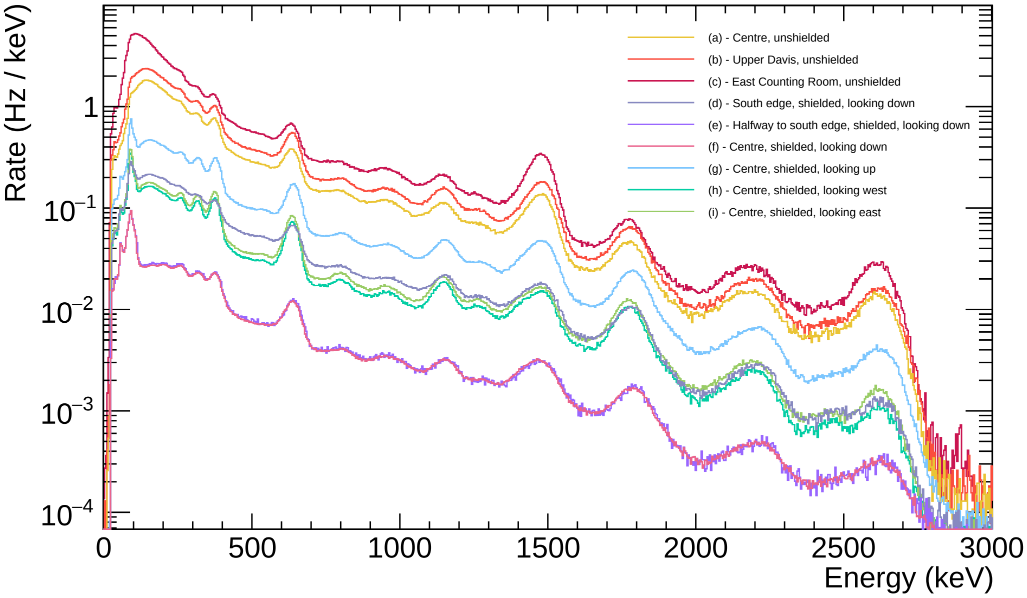

Figure 3.4.1: The energy spectra for the nine measurements taken in the Davis cavern in the range 0–3000 keV. Figure taken from Ref. [262].

the position at half of the tank radius, where the detector was shielded by 15 cm of steel. This is demonstrated by the two lowest rate histograms overlapping in Figure 3.4.1. The measurement at the edge of the tank (d) had a higher rate, with no steel shielding beneath. The gravel under the water tank is known to have low radioactivity, therefore it was assumed that the lowest rates measured in (e) and (f) correspond to the intrinsic background of the experimental setup. NaI(Tl) crystals are known to have intrinsic ^{40}K, ^{238}U and ^{232}Th contamination [303] and PMTs are also known sources of radioactivity [227, 304, 305].

Gaussian fits to the four high-energy peaks present in the background spectra are used to quantify the activities of ^{40}K, ^{232}Th and ^{238}U. The fitted energy spectrum for an unshielded measurement at the centre of the water tank (a) is shown in Figure 3.4.2. The two low-rate measurements are excluded from the fit results. The averaged gamma flux activities over seven background exposure measurements are (220 ± 60) Bq/kg of ^{40}K, (29 ± 15) Bq/kg of ^{238}U and (13 ± 3) Bq/kg of ^{232}Th. These results of consistent with assays of the shotcrete material that covers the

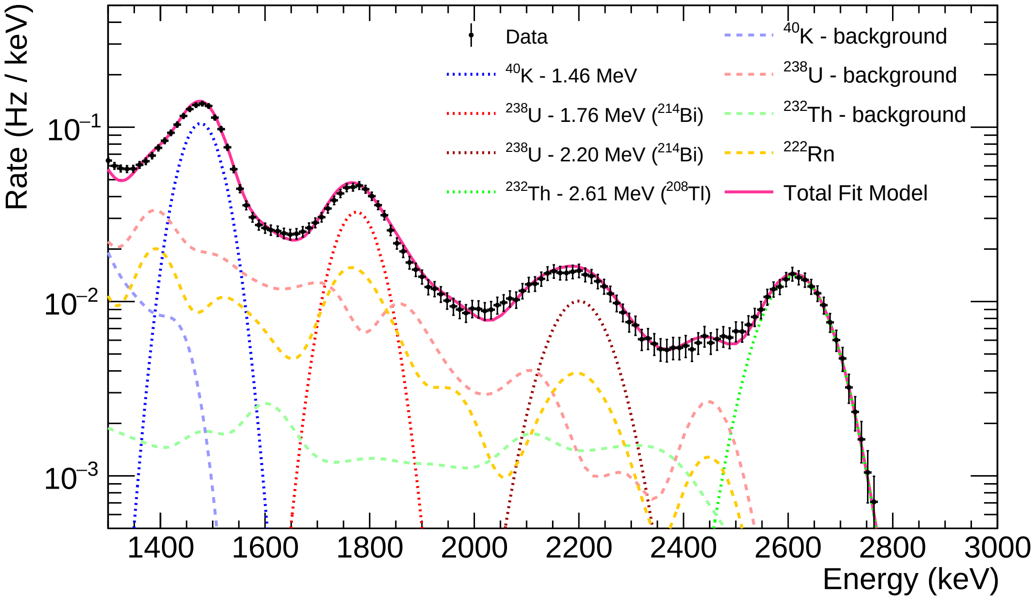

Figure 3.4.2: Fitted energy spectrum for background measurements taken at the centre of the unfilled water tank (a) in the preliminary gamma background campaign. The spectrum shows the 1461 keV ^{40}K line, the 1764 keV and 2204 keV lines originating from the ^{238}U chain and the 2614 keV line from the ^{232}Th chain. Contributions from sub-dominant lines, Compton scattering and airborne radon are also shown. Figure taken from Ref. [262].

cavern walls. The total integrated flux in the Davis cavern from radioactive contamination within the cavern walls is quoted to be 1.9 ± 0.4 γ cm^{-2} s^{-1} in the range 0–3000 keV.

This is consistent with the upper limit of 2.19 γ cm^{-2} s^{-1} set by a previous gamma-flux measurement in the east counting room using a HPGe detector [294]. This preliminary campaign added another complimentary measurement of the gamma-ray flux at SURF, which has also been measured at the surface administration building and underground at the 800’, 2000’ and 4550’ levels [254].

3.5 The LZ environmental monitoring station

As data-taking operations continue for LZ, rare physics searches for WIMPs and ^{8}B neutrinos continue to push closer to detector thresholds. Any claims of discovery

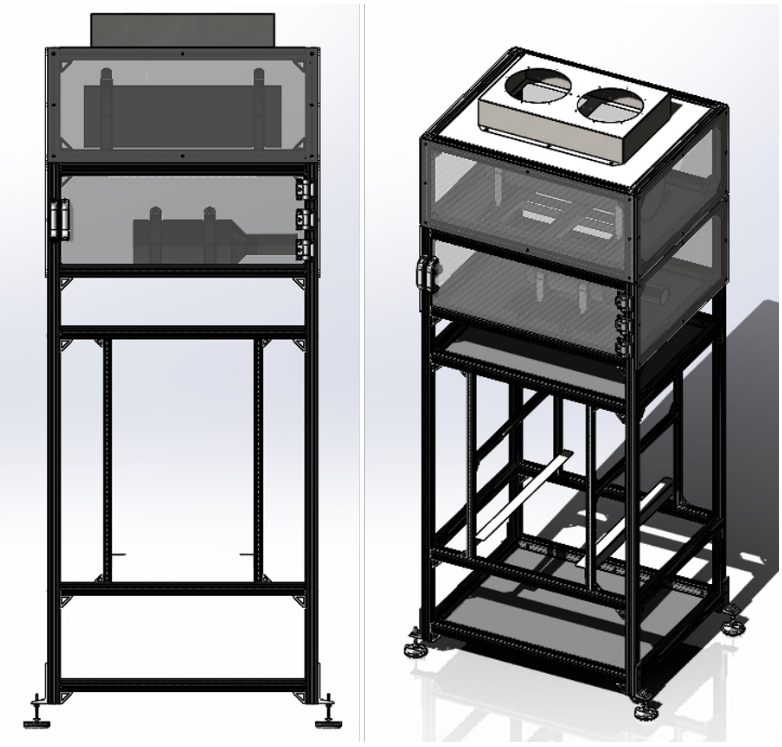

Figure 3.5.1: CAD diagrams of the LZ environmental monitoring station, which will hold three independent background detectors: Rad7 radon counter, BF_3 neutron proportional counter and a NaI gamma-ray detector. The BF_3 neutron proportional counter and a NaI gamma-ray detector are shown on the top shelves of the rack. Diagrams produced by Charles Maupin (South Dakota Science and Technology Authority).

will require excellent understanding of all background sources. Comprehensive environmental monitoring *in situ* of the Davis cavern is necessary to support any future physics results.

Plans are in place for the LZ environmental monitoring station (EMS), which is a series of slow-control integrated background detectors measuring cavern backgrounds. This suite of detectors includes a DURRIDGE Rad7 radon counter, a BF_3 neutron proportional counter and a NaI gamma-ray detector. CAD diagrams of the physical EMS rack are shown in Figure 3.5.1, which will house these three detectors and the relevant electronics. The individual detectors are provided by Kevin Lesko (Lawrence Berkeley National Laboratory) and the design of the slow-control integrated DAQ system is headed by collaborators at the University of Rochester.

Once functional, tracking trends from these monitors will be added to the checklist of tasks to be completed during daily online shifting duties for LZ operations. Any excursions from nominal background levels will be flagged and correlations with data from other LZ detector systems can then be further investigated.

4 Measurements of high-energy cavern gammas

Physics searches such as two-neutrino and neutrinoless double-beta decay of ^{134}Xe and ^{136}Xe require a good understanding of the high-energy ER background. First measurements of high-energy gamma-rays originating from the Davis cavern are presented in this Chapter. Preliminary studies of the cavern gamma background originating from naturally occurring radioactive material contained within the cavern rock have previously been quantified up to an energy of 2.6 MeV. However, high-energy gammas with energies up to 10 MeV can be produced via (α,γ) interactions on light nuclei present in the cavern rock. The goal of this work is to characterise the high-energy background using new measurements of the gamma-ray flux in the Davis cavern taken with a NaI(Tl) detector. The measurements from this work will set a foundation for background models relevant for upcoming high-energy searches.

4.1 Motivation

4.1.1 Overview

In order to perform any rare physics searches with LZ, we must first characterise and model backgrounds that are present due to environmental radioactive sources. This includes modelling backgrounds that originate from the detector surroundings, such as those arising from the cavern rock that surrounds the LZ experiment.

LZ is shielded from environmental backgrounds originating from the cavern

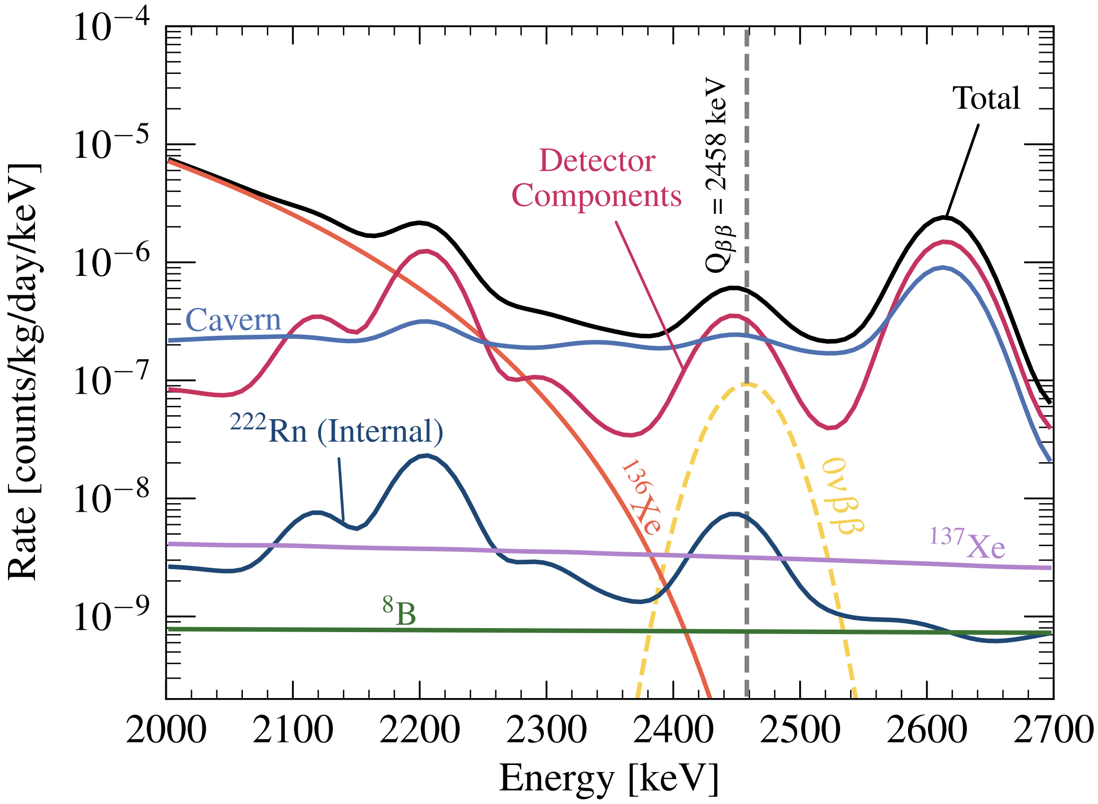

Figure 4.1.1: Background energy spectrum for an inner 967 kg volume used to analyse the projected LZ sensitivity to the $0\nu\beta\beta$ decay of ^{136}Xe. The contribution from the cavern gamma background is shown via the solid blue line, showing a significant contribution for $0\nu\beta\beta$ searches. Figure taken from Ref. [193].

rock by a water tank of diameter 7.62 m and height 5.91 m. Further shielding is provided by six octagonal steel plates with a thickness of 5 cm each that are inlaid in the floor beneath the water tank. This shield has the shape of an inverted pyramid, centred on the bottom of the water tank directly below where the LZ xenon target is positioned (refer to Figure 2.3.1). The tank and the pyramid sit on top of a layer of gravel that extends to the end of the pyramid and the radius of the water tank. Finally, an additional 8 cm of steel shielding was implemented above the water tank to enable competitive double-beta decay analysis [193].

The OD, as described in Section 2.3.5, is contained within the water tank and has the primary goal of vetoing neutrons. Neutron capture on Gd isotopes present in the GdLS produces optical signals up to ~ 8.6 MeV as bursts of several gamma-rays (γ). These higher energies allow discrimination of gamma-rays produced by naturally occurring radioactive material from U/Th/K decays, which have a maximum energy at the ^{208}Tl shoulder. Therefore, the energy range from the ^{208}Tl shoulder at 2.6 MeV up to 8.6 MeV is particularly useful for tagging neutron backgrounds. Maintaining a low background rate inside the OD from sources external to the detector, such as the gamma-rays from cavern NORMs, is essential for its role as an effective veto detector.

Quantifying the cavern background is not only important for the WIMP dark matter search, but also informing high-energy ER physics searches which include sensitivity studies of two-neutrino and neutrinoless double-beta decay of ^{134}Xe and ^{136}Xe isotopes [192, 193]. The sensitivity to the half-life of ^{136}Xe $0\nu\beta\beta$ after 1000 live days of LZ exposure is projected at $T_{1/2}^{0\nu\beta\beta} = 1.06 \times 10^{26}$ years for 90% CL. For comparison, the recent limit published by the KamLAND-Zen experiment reported a half-life value of $T_{1/2}^{0\nu\beta\beta} > 3.8 \times 10^{26}$ years [306], using enriched xenon with $\sim 90\%$ isotopic abundance of ^{136}Xe.

Figure 4.1.1 shows the energy spectrum of background sources considered for the LZ sensitivity to the $0\nu\beta\beta$ decay of ^{136}Xe. This plot highlights a dominant contribution from the Davis cavern background, with two problematic gamma lines near the endpoint value $Q_{\beta\beta} = (2457.83 \pm 0.37)$ keV [267]. The gamma decay of ^{208}Tl from the ^{232}Th$_l$ chain produces a photopeak of energy 2614.5 keV with a branching ratio of 100% [261]. The gamma decay of ^{214}Bi from the ^{238}U$_l$ chain with an energy of 2447.86 keV is in close proximity to $Q_{\beta\beta}$ with a branching ratio of 1.5% [249]. The separation of these background peaks from potential physics signals is dependent on the energy resolution (σ/E) achieved by the LZ experiment [293].

4.1.2 Motivation for a high-energy gamma measurements

Preliminary studies of the cavern background in the Davis cavern focussed on quantifying the primary gamma backgrounds produced by ^{40}K and the ^{232}Th and

^{238}U primordial decay chains up to the ^{208}Tl shoulder at an energy of 2.6 MeV.

High-energy gammas of energies up to $\sim$ 10 MeV can be produced by secondary (α,γ) captures that occur on light-Z nuclei, such as aluminium, oxygen and silicon present in cavern rock [307–312]. α particles of energies up to a value of 8.8 MeV originate from ^{232}Th and ^{238}U which decay to stable Pb isotopes via a series of α and β decays (see Figure 2.5.1 and Figure 2.5.2). It is also important to consider (n,γ) reactions that can occur due to neutrons produced by spontaneous fission of U and Th, as well as neutrons produced via (α,n) captures in the rock [313, 314].

The setup of a dedicated high-energy gamma spectroscopy experiment was completed in January 2023 with the goal of taking long-exposure measurements of the gamma-ray flux in the Davis cavern using a larger sodium iodide crystal (see Figure 4.2.2). Given that LZ is highly sensitive to an array of signal and background signatures, the long-exposure is necessary in order to gain more precise measurements of the high-energy flux as well as to characterise the energy spectrum beyond 2.6 MeV. Since the 2017 gamma spectroscopy campaign, the LZ detector and detector subsystems have been installed and the layout of the Davis cavern has changed, motivating a new, up-to-date campaign with more relevance to present and future data-taking.

As part of a suite of background monitors to support additional physics analyses, the NaI detector used to take the measurements presented in this Chapter will be integrated into the LZ EMS, alongside a DURRIDGE Rad7 radon counter and a BF_3 neutron proportional counter. The goal of the EMS is to continuously monitor environmental backgrounds present in the vicinity of the LZ experiment to inform background rates observed in the TPC and the OD. The inclusion of a long-term gamma spectroscopy experiment at the 4850' level of SURF will give the LZ Collaboration the ability to monitor the gamma-ray flux over the experiment lifetime now that detector operations are stable and science data-taking is ongoing.

This Chapter presents the equipment utilised for collecting high-energy gamma spectroscopy measurements. Following this, detector calibrations that are essential for understanding the response of the NaI detector are discussed. Validation of these calibrations are explored using BACCARAT simulations. Subsequently, the methods for data collection are outlined. The Chapter concludes with a presentation of the results from the long-exposure gamma spectroscopy campaign and a discussion of future work, emphasising the importance of integrating the NaI detector into the LZ EMS.

4.2 Experimental setup

4.2.1 Gamma spectroscopy and properties of NaI(Tl)

Gamma-ray (γ-ray) spectroscopy is a widely used analytical technique to identify radioactive isotopes present in a sample or environment and to classify the energy spectra of gamma-ray sources [315, 316]. X-ray or gamma-ray photons are uncharged particles that create no direct ionisation or excitation of the material through which they travel. The detection of gamma-rays in materials is therefore dependent on the interactions that the photons undergo with electrons in the absorbing material. Detailed discussion of photon interaction mechanisms in matter can be found in Ref. [315].

Thallium-activated sodium iodide was first demonstrated to have desirable scintillation properties by Robert Hofstadter in 1948 [317]. This technology remains at the forefront of modern gamma spectroscopy. The main advantage of NaI detectors relates to their high detection efficiency capabilities, sharp linear response and good energy resolution. The high light yield of 38 photons/keV is the most notable property of NaI. Scintillator activators are normally chosen so that the emission wavelength is in the visible or near-UV range, where photomultiplier tubes are most sensitive. Thallium-activated sodium iodide crystals exhibit

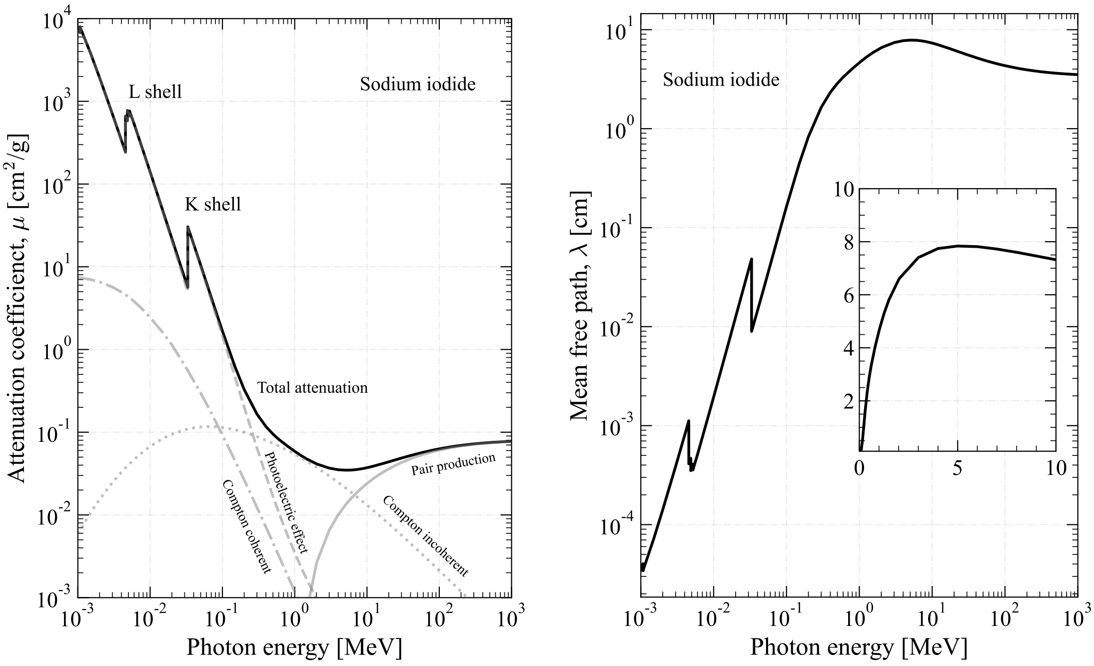

Figure 4.2.1: Photon interactions in sodium iodide. The mass attenuation coefficient (left) and mean free path (right) of gamma-rays interacting in NaI as a function of incident photon energy. Figure made using data provided by NIST [194].

a wavelength of maximum emission of 415 nm and the scintillation pulses have a primary decay time of 250 ns as measured at room temperature [318]. Newer HPGe detectors offer superior energy resolution to that of NaI [319], and so are often used for high-precision isotope identification applications, such as the material assay measurements previously discussed for LZ. A disadvantage of NaI is that it is a hygroscopic material, and therefore must be enclosed in an airtight container (usually aluminium).

NaI crystals are optically coupled to a photomultiplier tube connected to an external high voltage supply. Interactions of incident gamma-ray photons in the crystal cause ionisation of the atoms in sodium iodide. This creates excited states that then decay via the emission of scintillation light. The number of scintillation photons produced is proportional to the amount of energy deposited in the crystal by the incident gamma-ray. At the photocathode, the scintillation photons produce photoelectrons via the photoelectric effect. The number of photoelectrons is then

Table 4.2.1: Key properties of NaI(Tl) [318].

Material	Density $[\mathrm{g\,cm^{-3}}]$	Wavelength of maximum emission [nm]	Primary decay constant [ns]	Light yield [photons/keV]	Hygroscopic
NaI(Tl)	3.67	415	250	38	yes

amplified by a series of dynodes.

The charge output of the PMT is then passed through a signal-processing chain consisting of amplifier systems and is finally presented as a voltage pulse. The height of this pulse is proportional to the energy deposited in the scintillator. A multichannel analyser (MCA) is connected to this amplifier chain and is able to store pulse heights into a histogram to record the energy spectrum observed in the NaI detector. This process is known as pulse height analysis (PHA). The width of each channel bin corresponds to a range of energies. Calibration sources of known energy are used to relate channel number to energy.

Figure 4.2.1 shows the mass attenuation coefficient of gamma-rays in NaI as a function of incident gamma energy. The total attenuation curve is broken down into different photon processes in the material, including coherent and incoherent Compton scattering, the photoelectric effect and pair production. These distributions highlight how each process contributes as a function of energy, and allow identification of the dominant process for each energy or range.

The interaction of gamma-rays can also be defined by their mean free path λ, which is the average distance travelled in the material before an interaction takes place. Figure 4.2.1 shows the mean free path of photons in NaI, by converting the attenuation curve in using the relation $\lambda = 1/\rho\mu$. Here we assume a standard density $\rho = 3.67\,\mathrm{g\,cm^{-3}}$ for NaI crystals [318]. The distribution shows that over the energy range 0–10 MeV the value of the mean free path for photons in NaI is $\sim$ 10 cm. A summary of the key properties of NaI(Tl) is shown in Table 4.2.1.

4.2.2 Experimental equipment

In order to measure the gamma-ray flux in the Davis cavern, a coaxial ⌀ 6-inch × 6-inch thallium-doped sodium iodide scintillation crystal optically coupled to a 5-inch PMT manufactured by Solon Technologies, Inc., Harshaw/QS Crystal and Dosimetry Products was used. The PMT was connected to a TENNELEC TC 952 high voltage (HV) power supply, and all calibration and background measurements were taken with the PMT biased to a voltage of +1200 V. The PMT signal output was connected to a series of ORTEC subsystems [320], including a detector interface module (DIM) which feeds into a digiDART multichannel analyser. The spectra were visualised by connecting the MCA to a Windows 7 laptop loaded with the MAESTRO MCA emulation software [321]. A lower level discriminator was set to 5 to establish a lower-level cut-off point by channel number for ADC conversions. A photograph of the equipment and a diagram of the electronics setup is shown in Figure 4.2.2.

The NaI experiment was set up in the lower Davis cavern. Figure 4.2.3 shows the location of the experiment in relation to other LZ subsystems, such as the water tank and the xenon tower. The components shown in Figure 4.2.2 were housed within a Pelican 1660 equipment case in order to minimise the footprint of the experiment while located in a working laboratory space. The Pelican case was modified to provide suitable airflow using a small electric fan to minimise the chance of overheating of electronic equipment. Housing the equipment in the Pelican case allows for easy transportation of the equipment if necessary and also allowed us to safely secure radioactive sources to comply with radiation safety requirements at SURF.

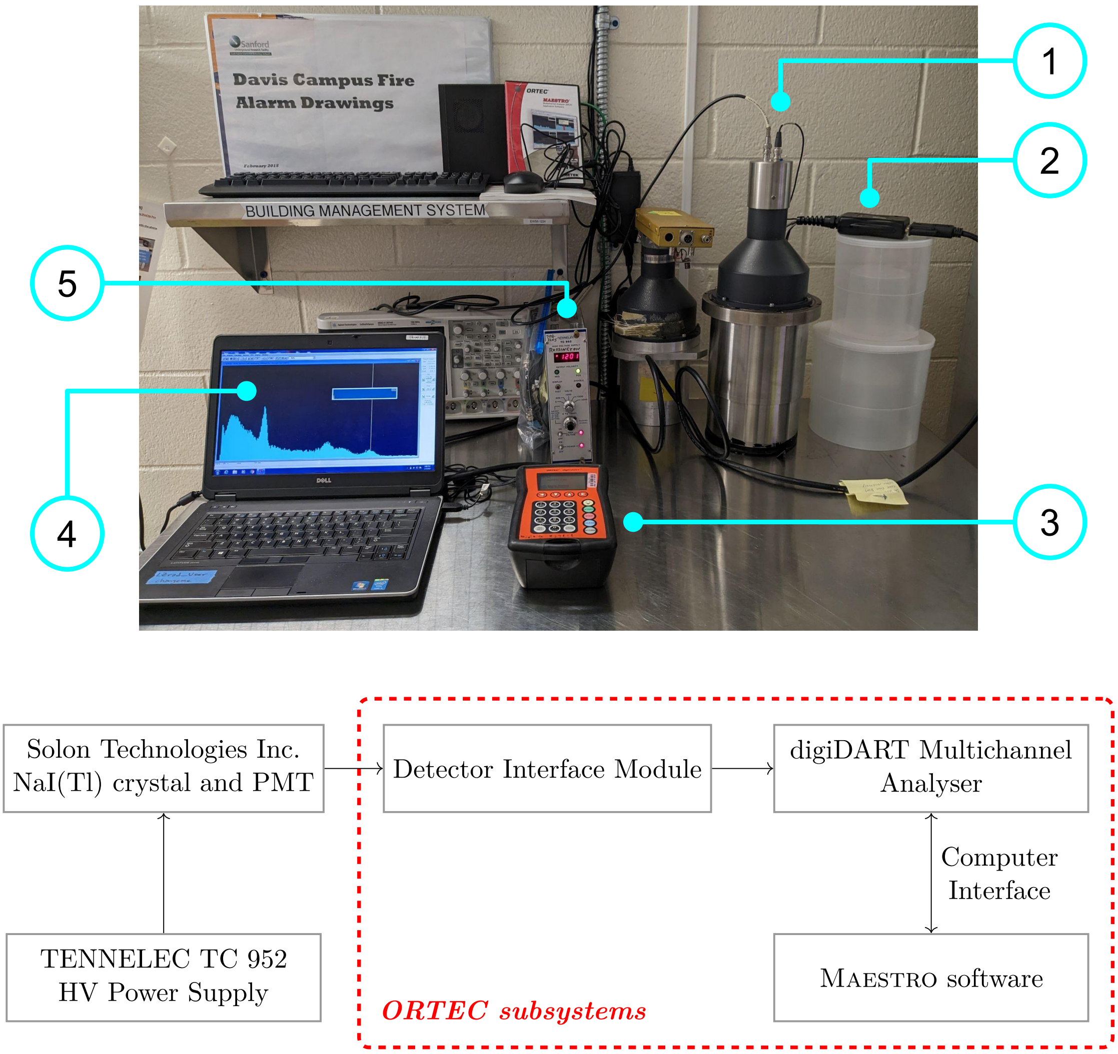

Figure 4.2.2: The gamma spectroscopy experimental equipment. **Top:** A labelled photograph of the equipment setup in the common corridor shows the NaI crystal coupled to a PMT (1), the DIM (2), the digiDART MCA (3), the laptop running the MAESTRO software (4) and the TENNELEC HV power supply (5). **Bottom:** A schematic diagram of the setup of the equipment used to perform the gamma spectroscopy measurements. The ORTEC subsystems are contained within the dashed red rectangle. The schematic shows the equipment connections.

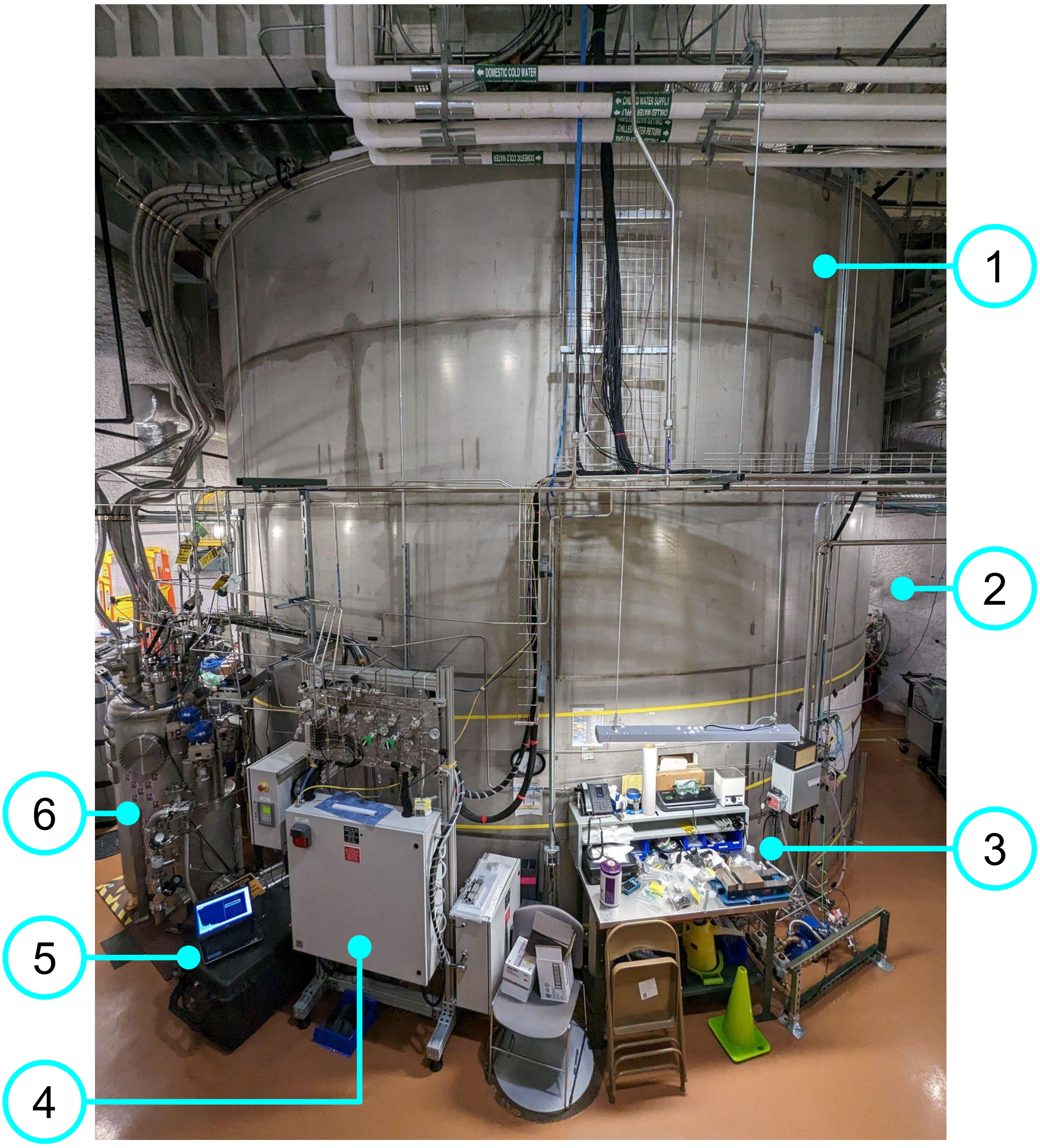

(a) Photograph of the view of the lower Davis cavern, taken from the stairs leading from the upper to the lower level.

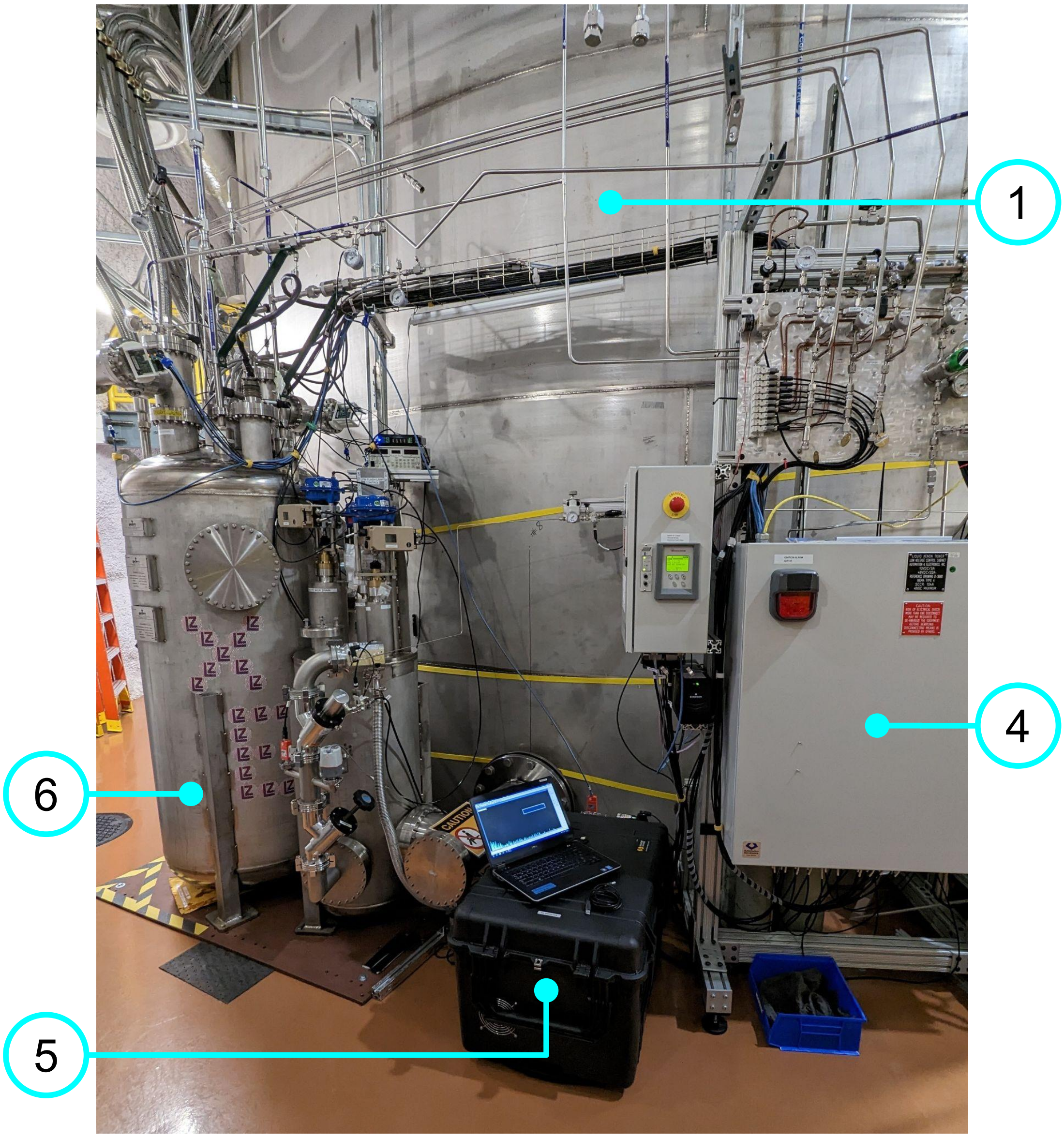

(b) Photograph of the systems in the vicinity of the gamma spectroscopy experiment.

Figure 4.2.3: Photographs of the lower Davis cavern. The water tank (1) is located centrally in the cavern, surrounded by the cavern walls coated in a white shotcrete layer (2). Outside the water tank, there is a workstation (3) used for detector maintenance. The gamma spectroscopy experiment (5) is housed in the black Pelican 1660 case, in between the xenon tower slow-control system (4) and the xenon tower (6).

4.2.3 Initial testing

Testing of any hardware system is necessary to ensure that all components of the system function as required. Environmental monitoring systems must be able to achieve stable operational conditions to be effective as monitoring tools over a series of long-exposure measurements that supplement science data for the LZ experiment.

Initial background measurements were taken in the common corridor and the lower Davis cavern. Figure 4.2.4 shows a comparison between the rates recorded with the NaI detector placed in the common corridor and the lower Davis cavern as shown in Figure 4.2.2 and Figure 4.2.3, respectively. These initial short exposures confirmed that the NaI detector operated as a functional gamma spectroscopy experiment, with no concerns about the dead time of measurements. The dead

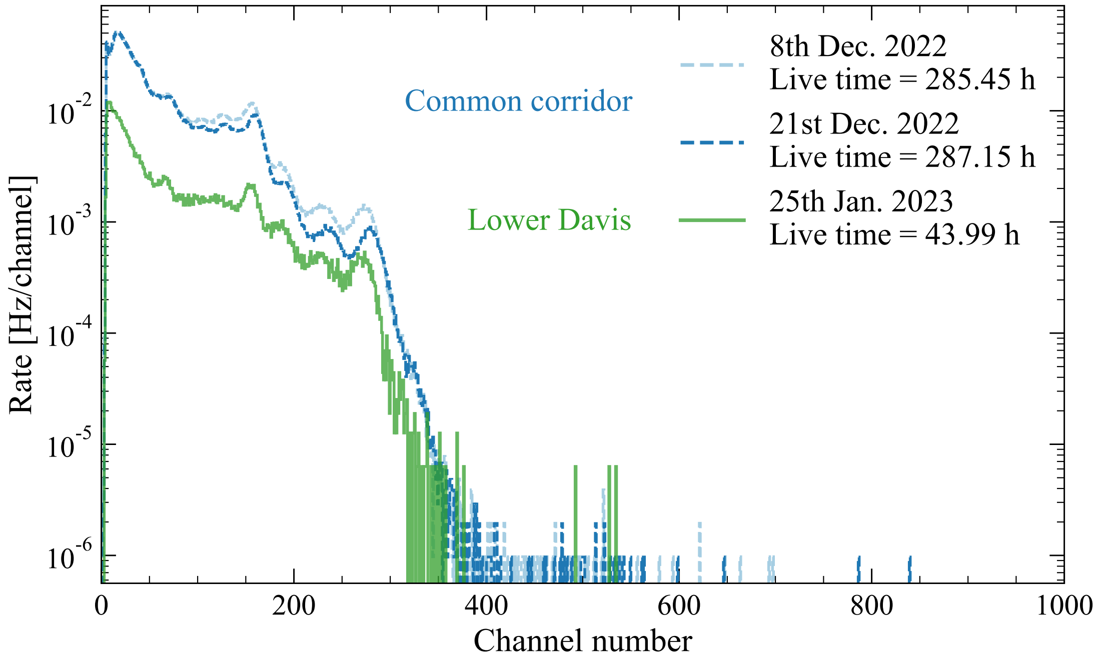

Figure 4.2.4: Raw spectra for initial test background measurements taken at the common corridor (dashed blue lines) and the lower Davis cavern (solid green line). The NaI detector has no shielding for measurements taken at the common corridor. Spectra collected using the MAESTRO software.

Table 4.2.2: Parameters for initial background measurements situated in the common corridor and the lower Davis cavern, including shielding configuration, live time, percentage dead time and integrated rates. Uncertainties quoted on rates are Poisson counting errors only.

Location	Type of shield	Start date	Live time [h]	Dead time [%]	Integrated rate [Hz]
Common corridor	No shielding	08/12/2022	285.4	6.84	2.93 ± 0.03
	No shielding	21/12/2022	287.1	6.76	2.76 ± 0.02
Lower Davis cavern	Pelican case	25/01/2023	43.9	3.15	0.56 ± 0.03

time percentages quoted in Table 4.2.2 are calculated by:

$$\text{dead time [\%]} = \left(\frac{\text{real time - live time}}{\text{real time}}\right) \times 100\% = \left(1 - \frac{\text{live time}}{\text{real time}}\right) \times 100\%. \tag{4.2.1}$$

Basic analysis of the background spectra shows a factor ~ 5 reduction in total integrated rate of counts recorded in the NaI detector when located in the lower Davis cavern. The highest rate recorded over the exposure in the common corridor is (2.93 ± 0.03) Hz, compared to (0.56 ± 0.03) Hz. The differences in rate may arise from two sources: changes in gain or threshold settings of the hardware and the additional shielding provided by the Pelican casing required for safety protocol in the laboratory space. Statistical errors are calculated assuming Poisson errors on the number of counts contained within each channel bin and scaled by the live time of each exposure. Relevant values for each measurement are reported in Table 4.2.2.

4.3 Calibration

4.3.1 Calibration timeline

In order to evaluate the response of the NaI detector, calibration measurements were performed. The initial set of calibration data were collected from 27th January 2023 to 7th February 2023, with two additional calibrations taken on 15th March 2023 and 17th November 2023. A variety of gamma sources held at SURF were utilised to calibrate the NaI detector over a suitable energy range. The calibration timeline is shown in Figure 4.3.1.

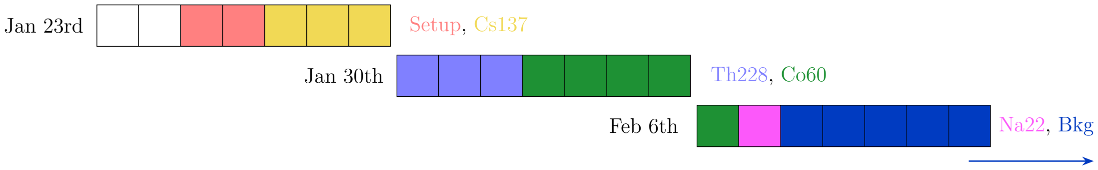

Figure 4.3.1: The calibration timeline of the initial calibration campaign completed between 27th January and 7th February 2023. Here each square represents one day and the colour of each square is associated with a different gamma source. The first background exposure commenced on the 8th February.

4.3.2 Gamma sources

The initial calibration used a total of four external radioactive gamma sources: ^{22}Na, ^{60}Co, ^{137}Cs and ^{228}Th. Calibration data were taken with the NaI crystal exposed to one source at a time, with the order of calibrations shown in Figure 4.3.1. The calibration timeline was constructed to maximise the exposure of each calibration source, prioritising the ^{60}Co measurement which took place over the 4-day weekend in the week beginning 30th January 2023.

The ^{22}Na and ^{228}Th rod sources were manufactured by Eckert & Ziegler Isotope Products [239]. The rod sources have dimensions of $\varnothing$ 15.9 mm × 74.9 mm. The ^{60}Co and ^{137}Cs disk sources were manufactured by Spectrum Techniques [322]. The disks have dimensions of $\varnothing$ 25.4 mm × 3.2 mm. Both rod sources and disk sources are made from acrylic Plexiglas. Information pertaining to calibration quantities for each radioactive source is shown in Table 4.3.1.

The raw spectra collected using the Maestro software are shown in Figure 4.3.2. These spectra show the distinct features of each calibration source: the 511 keV annihilation peak and 1275 keV photopeak for ^{22}Na, the 1173 keV and 1332 keV photopeaks for ^{60}Co, the 662 keV peak for ^{137}Cs and the 2614 keV peak

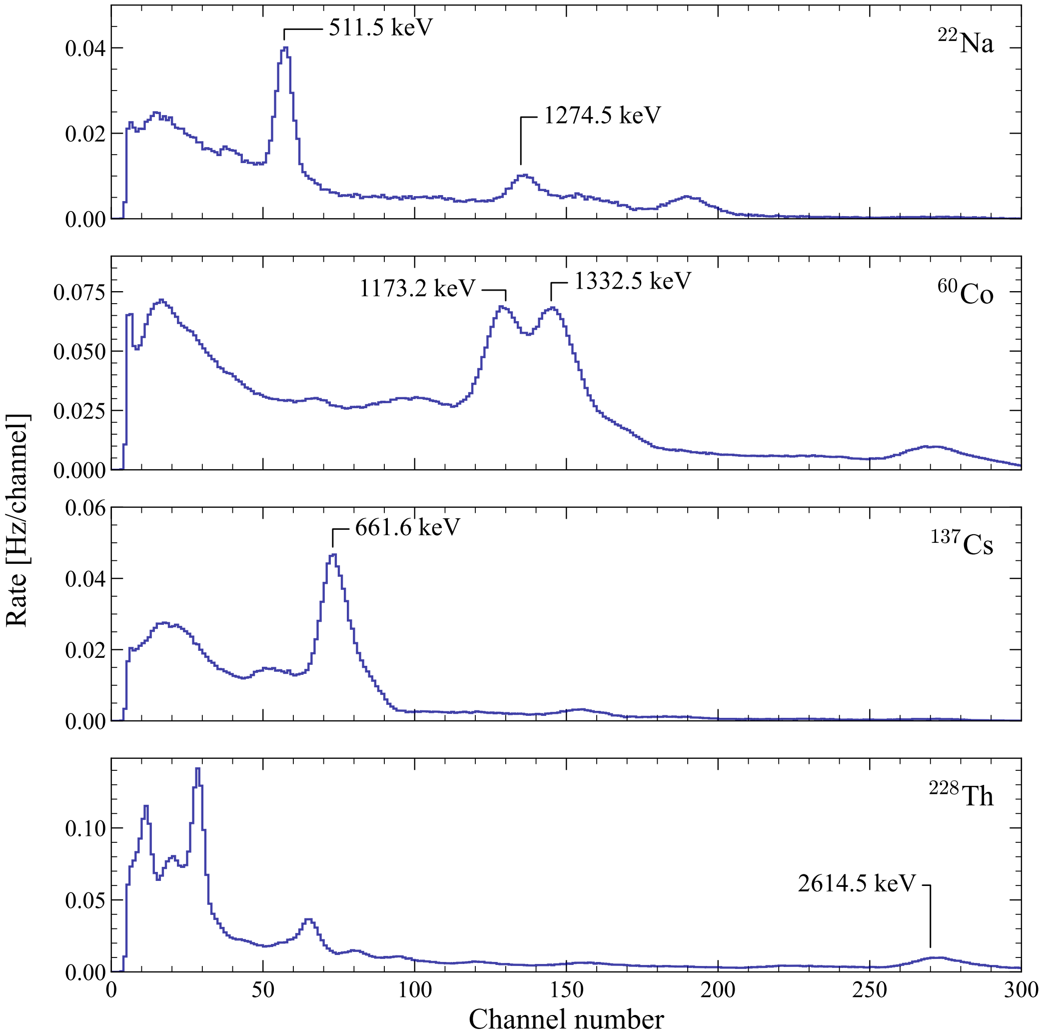

Figure 4.3.2: Raw calibration spectra for the gamma sources: ^{22}Na, ^{60}Co, ^{137}Cs and ^{228}Th. The energies of prominent photopeaks are labelled. Each plot shows the rate of counts in each channel bin, accounting for the live time of each calibration exposure. Spectra collected using the Maestro software.

from ^{208}Tl (which originates from the decay of ^{228}Th decay) [250, 261, 323].

The 511 keV annihilation peak is prominent in the ^{22}Na spectrum as this radionuclide undergoes β^+ emission [316]. This results in the emission of a position which will undergo annihilation with atomic electrons. Two photons are produced each with energy of the rest mass of the electron, $m_e = 511\,\text{keV}$. These photons are known as annihilation radiation and are emitted in opposite directions due to conservation of momentum. Additionally, pair production within the detector surrounding caused by high-energy photons ($E_\gamma > 1022\,\text{keV}$ threshold) followed by

Table 4.3.1: Photopeak energy, measurement dates, live time and calibration parameters for each of the radioactive sources used for calibration of the NaI detector. The source distance is the horizontal distance with respect to the centre of the detector end cap. When not stated, the reference calibration day is assumed to be the first of the month.

Source	Type	Energy [keV]	Activity [kBq]	Half-life [yrs]	Ref. date	Start date	Live time [h]	Dead time [%]	Distance [cm]
^{22}Na	β^+, γ	511, 1274.5	1.899	2.6	01/03/2021	07/02/23	20.8	5.8	0
^{60}Co	β^-, γ	1173.2, 1332.5	37	5.27	10/2002	02/02/23	110.2	8.1	0
^{137}Cs	β^-, γ	661.6	37	30.07	11/2011	27/01/23	65.1	7.2	18
^{228}Th	α, β, γ	2614.5	7.548	1.9	01/08/2020	30/01/23	62.3	8.4	0
AmBe	(α,n),γ	4438.9	4.81×10^3	432.2	12/01/2023	15/03/23	19.1	6.9	2.5
						17/11/23	90.2	5.0	3.5

the escape of an annihilation photon in the direction of the detector will also contribute to the annihilation peak. It should be noted that the 511 keV annihilation peak will be broader than nuclear photopeaks due to Doppler broadening.

The calibrations were performed by placing each calibration source at a set distance from the end cap of the NaI detector so that the dead time of the measurements were of the order of 1–10%. The activity of the ^{22}Na, ^{60}Co and ^{228}Th sources are on the order of ~ 1 kBq at the time of calibration and could be taped directly to the face of the end cap at a distance of 0 cm in order to achieve the desired live time fraction. The ^{137}Cs source has an activity an order of magnitude greater than the other gamma sources due to its much longer half-life and so was not secured directly to the face of the NaI crystal. Instead, the ^{137}Cs source was placed directly opposite the centre of the detector end cap at a distance of 18 cm.

4.3.3 AmBe neutron source

The additional calibrations utilised an americium-beryllium (AmBe) neutron source manufactured by Eckert & Ziegler Cesio for LZ high-energy NR calibrations. This source is a compacted mixture of ^{214}Am and ^{9}Be powders, with dimensions $\varnothing$ 7.8 mm × 10 mm double encapsulated inside a stainless steel casing. The AmBe capsule is embedded inside a stainless steel rod with the same dimensions as the gamma rod sources in order to be used by the CSD system. The stainless

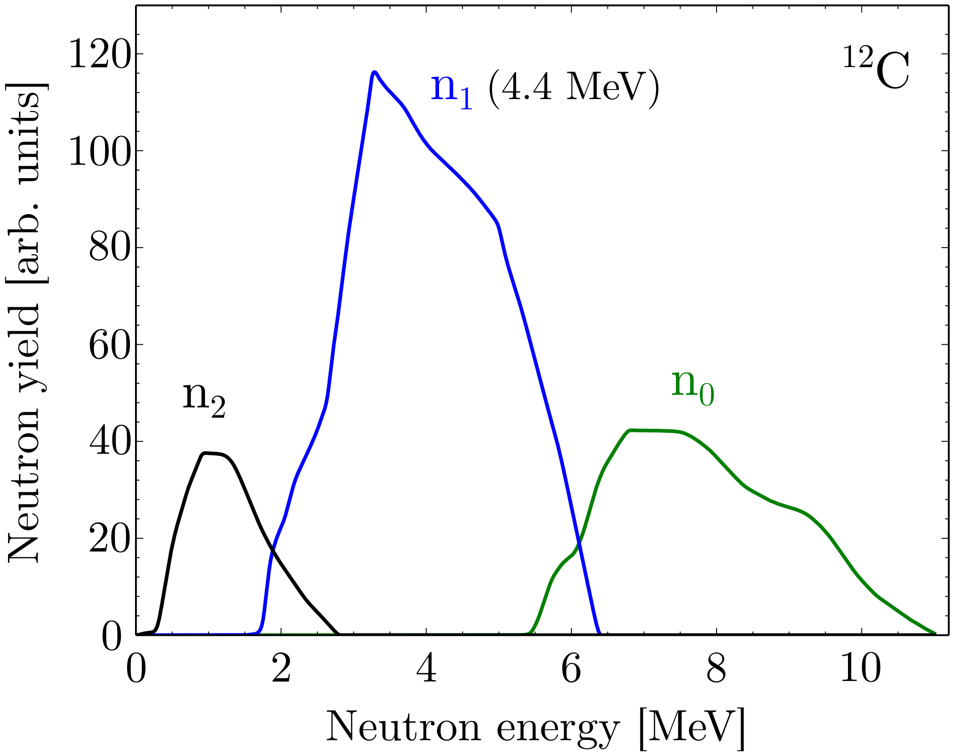

Figure 4.3.3: The neutron energy spectra of the ^{12}C n_0, n_1 and n_2 neutron groups produced by an AmBe alpha neutron source. These spectra were produced by the SOURCES4A code, which determines neutron production rates and spectra from (α,n) reactions [324]. Figure adapted from Ref. [325].

steel shielding is used to reduce the rate of low-energy gammas produced by ^{241}Am entering the TPC, Xe skin and OD veto detectors for NR efficiency studies. Reference calibrations from Eckert & Ziegler Cesio report the activity of ^{214}Am to be 4.81 MBq, with a neutron emission rate of 327 s^{-1}.

^{214}Am is an alpha emitter, which causes (α,n) reactions on ^{9}Be that leads to the production of neutrons. This is demonstrated in Equation 4.3.1:

$$\alpha + {}^{9}\mathrm{Be} \rightarrow {}^{13}\mathrm{C}^{*} \rightarrow {}^{12}\mathrm{C}^{*} + \mathrm{n} \rightarrow {}^{12}\mathrm{C} + \gamma, \tag{4.3.1}$$

where the asterisk denotes the excited state of carbon. The neutron energy spectra of the n_0, n_1 and n_2 neutron groups generated by SOURCES4A are shown in Figure 4.3.3, where the majority of neutrons are in the range 2–6 MeV [324]. The de-excitation of the first excited state of ^{12}C* produces a prompt gamma of energy 4438.9 keV accompanying the neutron emission with a branching ratio of $\sim 60\%$ [241, 326, 327]. This data point is particularly valuable as it lies in the energy range of interest for high-energy gamma backgrounds and allows us to model the detector response at this energy. Furthermore, this energy range is relatively background-free as it extends well beyond the NORM ^{208}Tl endpoint at 2.6 MeV.

The AmBe calibrations were performed by David Woodward (Pennsylvania State University), Kevin Lesko (Lawrence Berkeley National Laboratory) and Julia Delgaudio (South Dakota Science and Technology Authority) on 15th March 2023 and 17th November 2023. Careful planning and use of the AmBe source was considered due to the possibility of neutron activation of both the xenon used in LZ, and the NaI crystal itself by high-energy neutrons. In order to cause minimal disruption to LZ operations, these calibrations were performed at a time when LZ was not taking science data.

For the calibration taken in March, the experimental setup was moved from the original location on the south side of the water tank next to the xenon tower (a), to a location on the north side of the water tank (b). At location b the AmBe source was shielded using borated polyethylene (BPE) which is a widely used effective neutron shield. The AmBe source was also contained within a BPE-lined Pelican 1150 case when this calibration was performed. This calibration was limited to one shift day's worth of exposure due to radiation safety protocols in place at SURF when working with sources of ionising radiation, such as high-energy neutron sources.

The calibration taken in November occurred during a power outage at SURF and shortly after a DD calibration campaign of the LZ experiment when significant activation of the xenon target is expected. The additional activation due to the presence of the AmBe source is sub-dominant. Therefore, the measurement was taken at location a, with a longer exposure possible due to the absence of staff working in the Davis cavern during the source deployment. The specific details

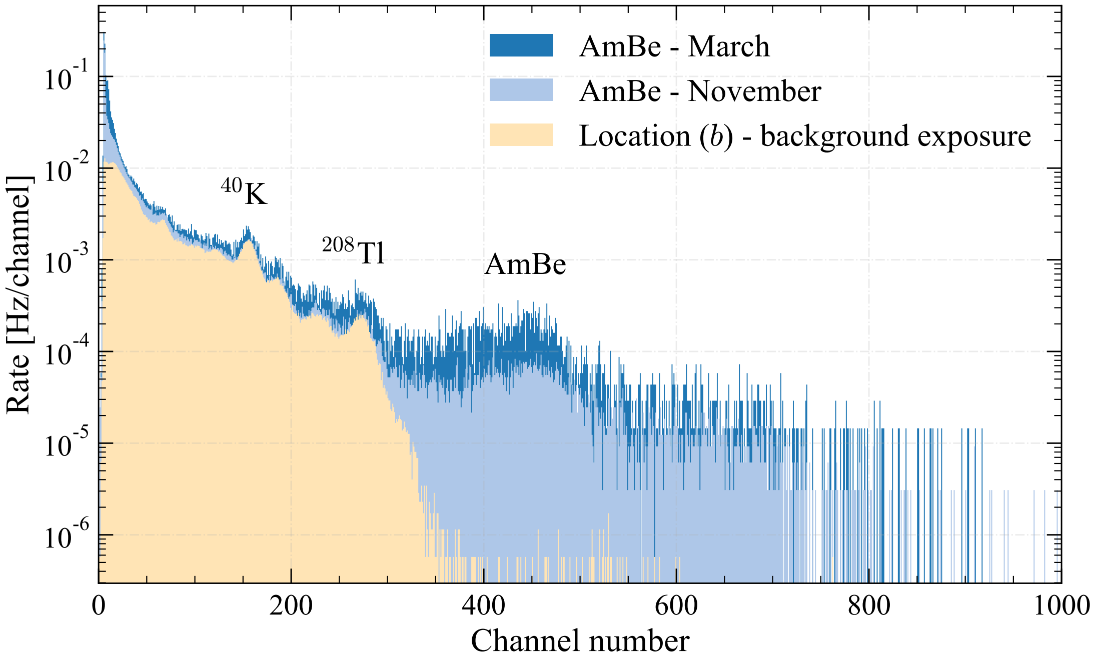

Figure 4.3.4: Raw AmBe calibration spectra taken using the MAESTRO software. The AmBe spectra for exposure in March and November and the background spectrum taken post-AmBe calibration at location *b* are shown by the dark blue, light blue and cream histograms, respectively. Four prominent background peaks from ^{40}K, ^{232}Th and ^{238}U are present in the background spectrum, here the ^{40}K and ^{208}Tl peaks are labelled.

relating to both AmBe calibrations are shown in Table 4.3.1.

The AmBe calibration and background spectra taken at location *b* are shown in Figure 4.3.4. This plot demonstrates that the NaI detector is able to record high-energy gammas that are produced beyond the ^{208}Tl shoulder, most notably the prominent 4.4 MeV photopeak from the AmBe source. Additionally, photon interactions in NaI above the pair production threshold (1.022 MeV) can result in single escape peak and double escape peak spectral features. These occur when one or two annihilation photons of energy 0.511 MeV escape the detector without depositing energy [315]. The single escape peak at an energy of 3.927 MeV is observed in the spectrum, and can be used as an additional data point for characterising the detector response. The difference in rate between the two AmBe calibrations is attributed to the distance of the source with respect to the NaI detector end cap.

It should also be noted that exposure to the AmBe source did not result in significant long-lived neutron activation of the NaI crystal. The background spectra taken directly after the AmBe calibration shows no additional prominent photopeaks associated with possible radioactive isotopes that would result from neutron activation of target isotopes present in the crystal (^{23}Na and ^{127}I).

4.3.4 Energy calibration and resolution

In order to calculate the calibration constants and energy resolution of the NaI detector, each calibration energy spectrum must be analysed. The centroid values, standard deviations and total peak area of the photopeaks associated with each calibration source can be extracted by performing a peak fitting procedure.

A long-exposure background measurement taken at location *a* was subtracted from each gamma source calibration spectrum to remove NORM background counts. The Run 0 background exposure equated to 777.92 hours of live time,

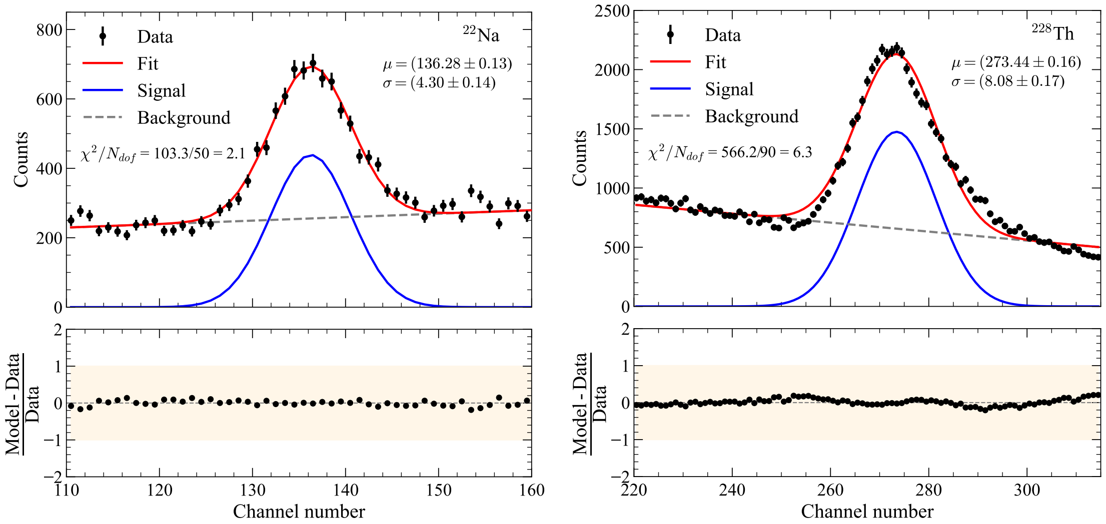

Figure 4.3.5: Example fit results from raw calibration spectra. The black points are the calibration data, the red line is the fit result, the blue line is the extracted Gaussian signal(s) and the grey dashed line is the background which is modelled as the sum of a linear (or exponential) term and independent constant. Reduced chi-squared (χ^2) values for each plot are also shown, where N_{dof} is the number of data points minus the number of fit parameters. Fit results are shown for 1274 keV of ^{22}Na (left) and 2614 keV of ^{228}Th (right), respectively. Error bars account for Poisson counting statistics only.

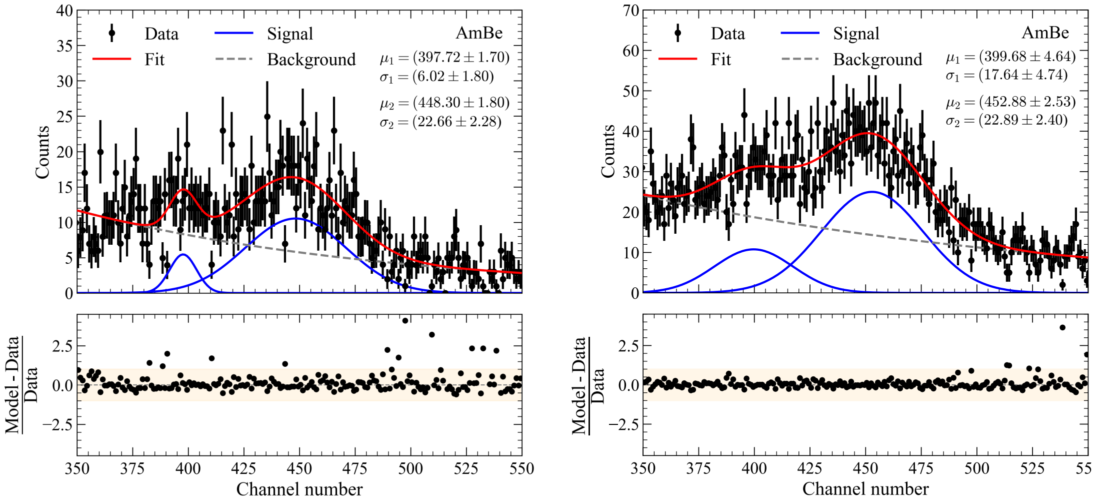

Figure 4.3.6: Fit results from raw AmBe calibration spectra. The black points are the calibration data, the red line is the fit result, the blue line is the extracted Gaussian signal(s) and the grey dashed line is the background which is modelled as the sum of a linear (or exponential) term and independent constant. Both the March calibration (left) and the combined AmBe dataset (right) are shown, with fits to the 3.927 MeV and 4.438 MeV AmBe first escape peak and photopeak. Error bars account for Poisson counting statistics only. Reduced chi-squared values are equal to $236.39/192 = 1.2$ and $193.98/192 = 1.0$, respectively.

and was normalised to the live time of each calibration measurement before the subtraction.

In order to extract a signal from the obtained spectrum, fitting was performed under the assumption that the signal and background comprised of Gaussian, exponential, linear, and constant components. Due to the proximity of the peaks in the ^{60}Co and AmBe spectra, the sum of two Gaussian functions were used to improve precision. Examples of fits to calibration photopeaks for ^{22}Na and ^{228}Th are shown in Figure 4.3.5, where the values and errors of the Gaussian signal μ and σ values are listed.

The AmBe datasets taken in March and November were combined to increase statistics for the 4.4 MeV photopeak in order to reduce the uncertainty on the fit parameters. The fit for the combined AmBe dataset is shown in Figure 4.3.6, with the spectrum from the March AmBe calibration and the combined AmBe calibration both shown. Due to the low rate of high-energy gammas produced

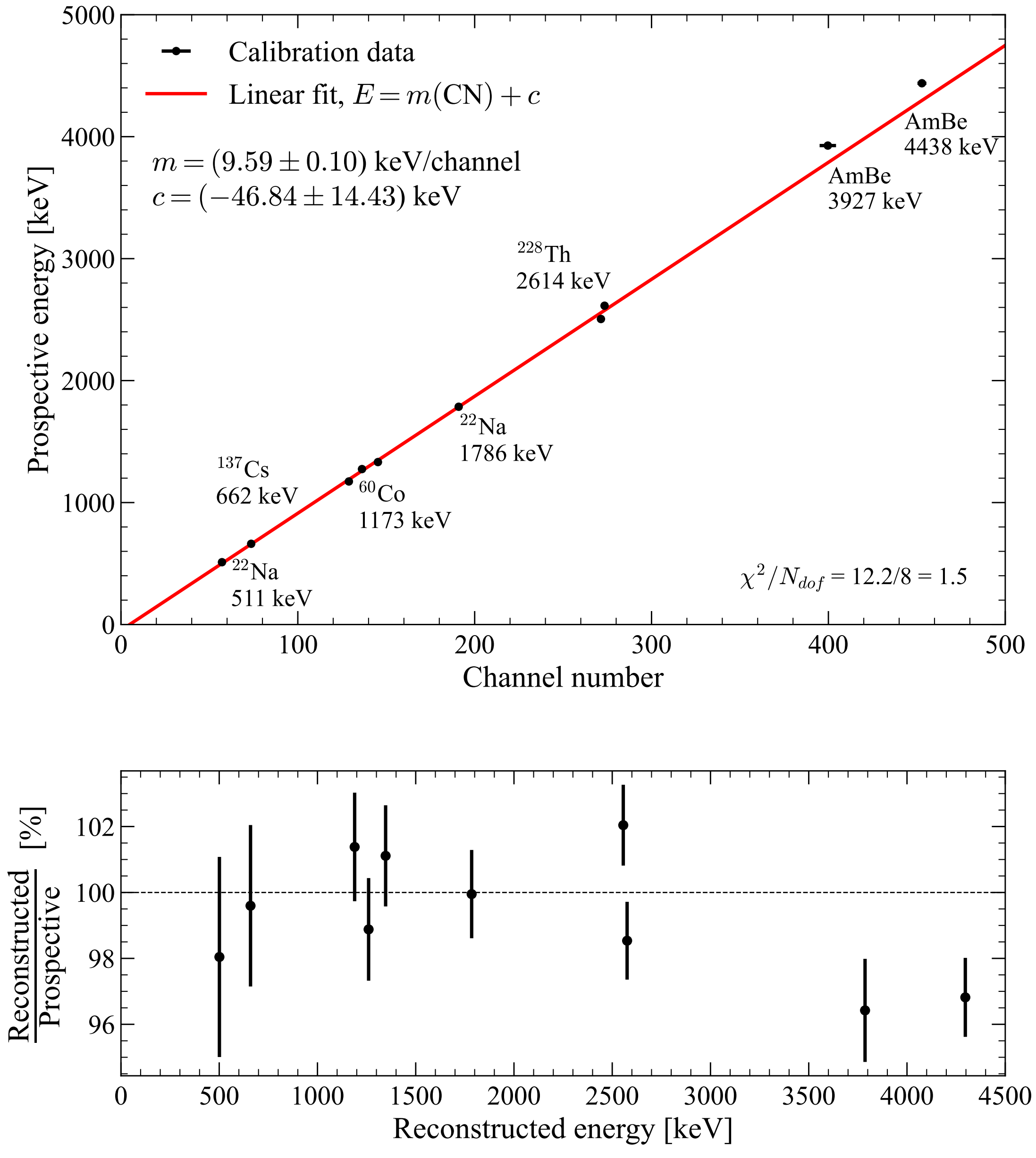

Figure 4.3.7: The linear energy response of the NaI detector as measured for photopeaks from ^{22}Na, ^{60}Co, ^{137}Cs, ^{228}Th and AmBe sources. **Top:** Prospective energy as a function of channel number. The fit is shown by the solid red line and the fit function equation is shown in the legend. The reduced chi-squared for this fit is equal to $\chi^2/N_{dof} = 12.2/8 = 1.5$. **Bottom:** The energy deviation as a function of reconstructed energy. Error bars indicate statistical errors only.

by the AmBe source and additional shielding, the statistics for the 4.438 MeV photopeak and 3.927 MeV first escape peak are limited and susceptible to large parameter fluctuations under fitting with the double Gaussian function. This results in the large statistical error bars associated with the detector resolution at these energies in comparison to the gamma source calibrations.

The location of each calibration source photopeak(s) was used to convert from channel number to energy using a linear scaling factor given by,

$$E = m(\mathrm{CN}) + c, \tag{4.3.2}$$

where CN is the channel number resulting from the centroid of the Gaussian fit μ, m is the linear scaling factor and c is the intercept offset. The result of this fit is shown in Figure 4.3.7, where $m = (9.59 \pm 0.10)\,\mathrm{keV/channel}$ and $c = (-46.84 \pm 14.43)\,\mathrm{keV}$. This result confirms good linearity is observed over the energy range of the calibration data points.

The full-width half-maximum (FWHM) of a Gaussian is given by the formula:

$$\mathrm{FWHM} = 2\sqrt{2\ln 2}\,\sigma, \tag{4.3.3}$$

where σ is the standard deviation of the Gaussian. The resolution R of each photopeak was determined by calculating the FWHM of the Gaussian signal fits and the known energy of the peak E using:

$$R = \frac{\Delta E}{E} = \frac{\mathrm{FWHM}}{E} = \frac{2\sqrt{2\ln 2}\,\sigma}{E}. \tag{4.3.4}$$

The resolution of the NaI detector was quantified by fitting the detector resolution model to this data, which follows the empirical relationship:

$$R = \frac{\Delta E}{E} = \sqrt{\alpha^2 + \frac{\beta^2}{E} + \frac{\gamma^2}{E^2}}, \tag{4.3.5}$$

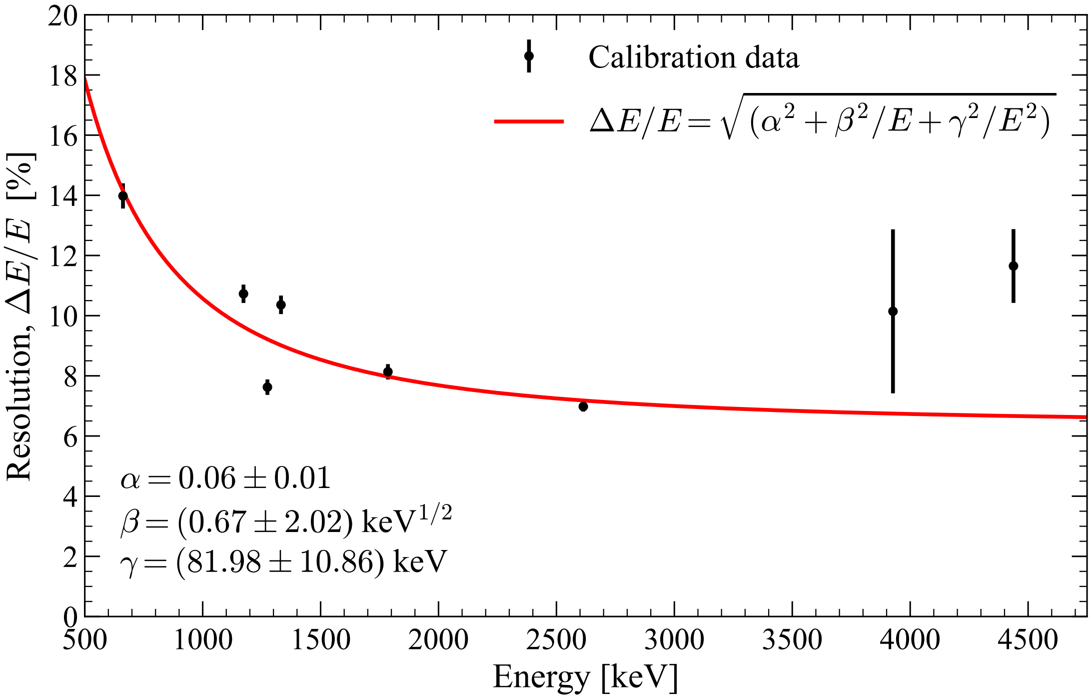

Figure 4.3.8: The energy resolution of the NaI detector as measured for photopeaks from ^{22}Na, ^{60}Co, ^{137}Cs, ^{228}Th and AmBe sources. The fit is shown by the solid red line and the fit function is shown in the legend. Error bars show only statistical errors.

where each term corresponds to sources of uncertainty from charge production, charge collection and electronic noise. α quantifies the light transmission from the scintillator to the photocathode, β represents the statistical fluctuations of photons, and γ is the electronic noise contribution [328]. The result of fitting to this model is shown in Figure 4.3.8, where values and errors of α, β and γ from the fitting to Equation 4.3.5 are listed. This resolution model is used to compare the true energy deposits from simulated cavern gamma flux events to the data collected with the NaI crystal.

4.3.5 Detection efficiency

The detector counting efficiency relates the amount of radiation emitted by a radioactive source to the amount measured by a detector [315, 316]. The detection efficiency can therefore be calculated by using radioactive sources of known activity and recording the detector response. The absolute detection efficiency of a detector, ε_{abs}, is defined as:

$$\varepsilon_{\text{abs}} = \frac{\text{number of pulses recorded}}{\text{number of radiation quanta emitted by source}}, \tag{4.3.6}$$

and is dependent on the geometric acceptance, the conversion of incident γ-rays in the NaI crystal and the light collection efficiency of the detector. The efficiency can be calculated by considering radioactive decays that deposit their full-energy in the detector, i.e. events that contribute to the photopeak in the energy spectrum. The absolute peak efficiency $\varepsilon_{\text{abs}}(E)$, is related to the observed calibration gamma spectrum by:

$$\varepsilon_{\text{abs}}(E) = \frac{N(E)}{A\,T\,P_{\gamma}(E)}, \tag{4.3.7}$$

where $N(E)$ is the number of counts in a photopeak of energy E, A is the activity of the source, T is the live time of the exposure and P_{γ} is the branching ratio probability of a single decay producing a photon of energy E.

The source activity must be corrected to account for radioactive decay processes using the original calibration information:

$$A = A_0 e^{-\lambda t} = A_0 e^{\frac{-\ln(2)t}{t_{1/2}}}, \tag{4.3.8}$$

where A_0 is the activity of the source at the time of the original reference calibration, t is the time elapsed since the reference date for the calibration (shown for each source in Table 4.3.1), λ is the decay constant and $t_{1/2}$ is the half-life of the source.

Values of A_0, A, T and P_{γ} for each gamma energy are collated in Table 4.3.2. Using Equation 4.3.7, the detection efficiency was calculated considering sources attached to the end cap of the NaI detector: ^{22}Na, ^{60}Co and ^{228}Th. The number of counts in each photopeak is calculated by integrating between $\pm3\sigma$ of the value of the mean parameter produced by fits.

Table 4.3.2: Values used to calculate the absolute detection efficiency of the NaI detector. Branching ratio values taken from Ref. [329].

Source	Source type	Reference activity A_0 [kBq]	Activity A [kBq]	Live time T [s]	Energy [keV]	Branching ratio P_γ
^{22}Na	Rod	1.899	1.13	7.48×10^4	511 1274.5	1.8 1.0
^{60}Co	Disk	37.0	2.55	3.97×10^5	1173.2 1332.5 2505.7	1.0 1.0 2.0
^{137}Cs	Disk	37.0	28.44	2.34×10^5	661.6	0.85
^{228}Th	Rod	7.548	3.03	2.24×10^5	2614.5	0.36

Figure 4.3.9 shows the absolute efficiency of the NaI detector from calibration sources. Error bars for each source are related to systematics errors. The error on the source activity A is taken to be 20%, which is quoted as the maximum deviation of the delivered activity from the nominal values by Spectrum Techniques [322]. A 20% error is also used for the time since the original reference calibration t. Error of the calibration live time measurements is set at 5%. Statistical error on the number of counts in each photopeak due to Poisson counting is subdominant in comparison to systematic errors.

Immediately we note that the values of the ^{60}Co photopeaks are outliers with respect to the other sources. Error bars associated with the two primary photopeaks of ^{60}Co are prominent due to the age of the source, which has undergone decays over several half-lives. The energy spectrum for ^{60}Co shows severe overlap between the peaks at 1173 keV and 1332 keV, which causes degeneracy when performing the double Gaussian fitting to the photopeaks.

NaI detectors are known to exhibit a clear decrease of efficiency with increasing energy due to the decreased probability of photon interactions in the detector [315, 316]. However, the calibration data presented here does not show this trend clearly. Therefore, it would be prudent to reassess detection efficiency with repeated calibrations, using a wider range of gamma-ray sources that are available at SURF.

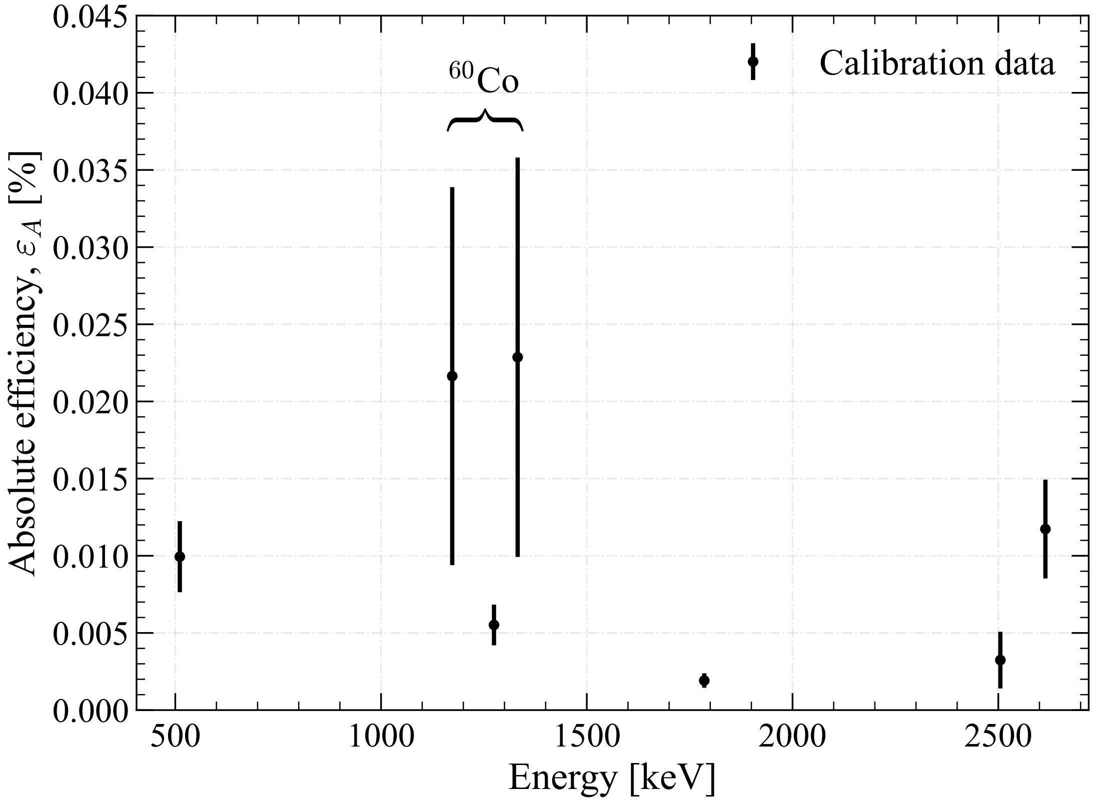

Figure 4.3.9: The absolute efficiency of the NaI detector as measured with photopeaks from ^{22}Na, ^{60}Co and ^{228}Th sources. Each of these sources was attached directly to the end cap of the detector, at an effective distance of 0 cm. Error bars are associated with combined statistical and systematic uncertainty, with 5% error attributed to live time and 20% error to both source activity and time since the original reference calibration.

4.4 Simulations of calibration data

4.4.1 Simulation overview

Simulations of the calibrations were performed using the BACCARAT simulation package (version 6.3.3) primarily used to simulate backgrounds for the LZ experiment, that is built using GEANT4 framework. The GEANT4 version used to generate all simulated data discussed is version 10.03.p02. BACCARAT uses a "component-centric" approach to simulating and recording events. The user is able to define a particle source within any component of the detector geometry with a specified activity. This can be illustrated by the following macro command used to set up a particle generator:

```
/Bacc/source/set A B C D E
```

where `A` is the volume name where the source is located, `B` is the source generator, `C` and `D` are the source activity and the units of activity. `E` is the secular equilibrium Boolean variable which is useful when simulating radioactive decay chains.

The user is able to set record levels for the components created in the geometry. Record levels determine how much information is saved when a particle passes through a volume. In order to optimise the simulation of events, we chose to record deposits in the NaI crystal volume only.

4.4.2 Geometry construction

The components created to simulate the calibration datasets include:

- **Sodium iodide crystal within aluminium casing:** A ⌀ 6-inch × 6-inch sodium iodide scintillation crystal contained within aluminium casing with a thickness of 0.02-inch. Thallium is not included in the definition of the Geant4 material used to simulate the NaI, as informed by the Geant4 NIST material database [272] and private communications with the COSINE Collaboration [330]. The aluminium shielding is necessary to provide hermetic sealing and to attenuate β radiation.
- **Generic PMT:** The custom PMT is modelled very simply as a PMT body constructed from Kovar material, containing a quartz photocathode window and steel dynode. The PMT is placed at one end of the sodium iodide crystal in a coaxial geometry.
- **Pelican 1660 equipment case:** The NaI crystal coupled to the PMT is placed inside a model of the Pelican equipment case, which is a shell made from polypropylene. The exterior dimensions of the box are

80.2 cm × 58.4 cm × 49.5 cm and the interior dimensions of the box are 74 cm × 52.2 cm × 44.6 cm.

- **Calibration sources:** There are two geometry options included to simulate gamma calibration sources contained within either a Spectrum Techniques disk source or an Eckert & Ziegler rod source as described in Section 4.3.2. The source geometry and source distance from the NaI end cap are configurable via commands in the GEANT4 macro used for simulations.

Custom macro commands added to the BACCARAT code to recreate the setup for each calibration include:

```
/NaI/useSource true
/NaI/useSourceType 1 # 0:disk or 1:rod
/NaI/setSourceDistance 5 cm
/Bacc/source/set CalibrationSource G4Decay_228_90 3 kBq
EQUILIBRIUM
```

which places a 3 kBq ^{228}Th source in secular equilibrium inside a rod source 5 cm away from the face of the NaI crystal, for example. Examples of the simulation geometry outlined above are shown in Figure 4.4.1 and have been visualised by taking the GEANT4 VRML file output and rendered using *view3dscence*, a 3D model viewing software [331].

4.4.3 Validations

The simulations of 1×10^7 primary events of ^{22}Na, ^{60}Co, ^{137}Cs and ^{228}Th were completed using computing facilities available to LZ via the National Energy Research Scientific Computing Centre (NERSC). The simulation information for each calibration is shown in Table 4.4.1, where the number of expected decays is equal to the source activity multiplied by the live time.

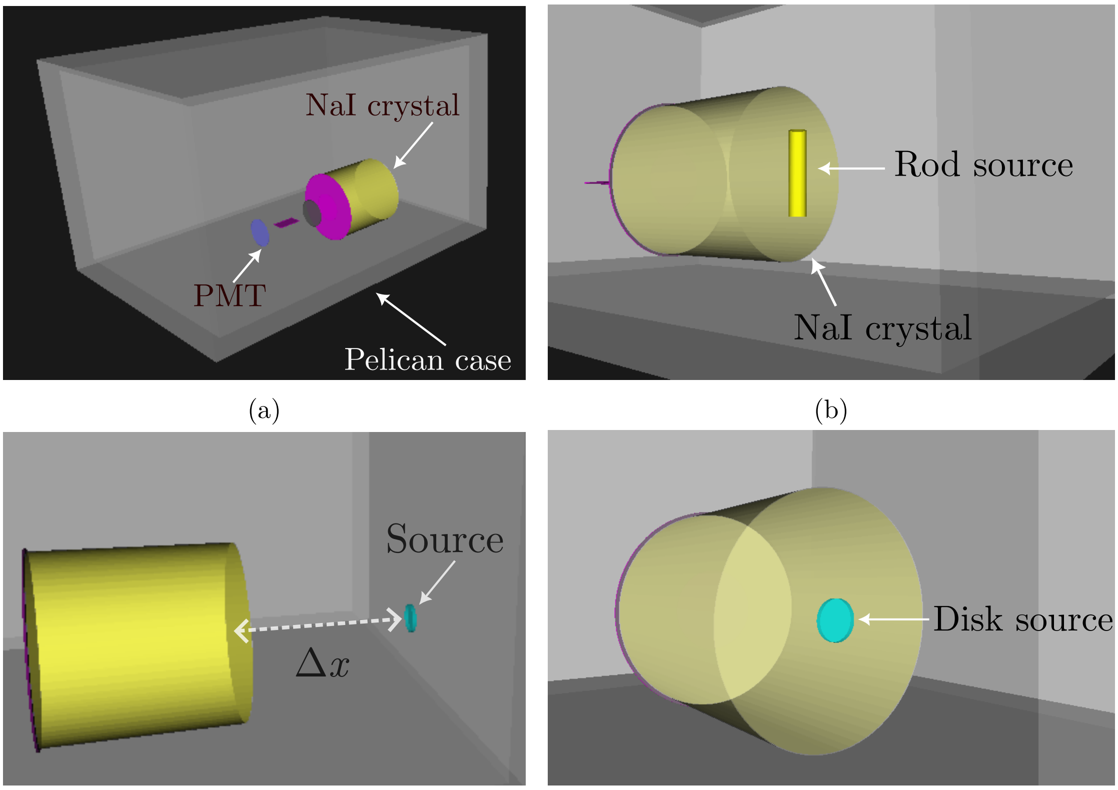

(a) (b)

(c) (d)

Figure 4.4.1: Visualisation of the GEANT4 calibration geometry viewed using *view3dscence* [331]. A view of the NaI detector, consisting of the NaI crystal coupled to a PMT contained within a Pelican case is shown in panel (a). The relative sizes of the rod source (b) and disk source (d) are also shown. Each source type can be set a distance Δx from the detector end cap (c), where in this example $\Delta x = 15\,\text{cm}$.

The analysis of simulations considers true energy deposits only, as no light collection effects or modelling of the PMT signal processing are included. Therefore, simulated energy depositions from gamma-ray interactions in the sodium iodide

Table 4.4.1: The number of expected decays for each gamma calibration source, correcting the source activity accounting for radioactive decay of the source. The deviation from the source reference activity is assumed to be ±20% as quoted by Spectrum Techniques [322].

Source	Activity A [kBq]	Live time [s]	Expected decays	Simulated events
^{22}Na	1.13	7.48×10^4	8.47×10^7	1×10^7
^{60}Co	2.55	3.97×10^5	1.01×10^9	1×10^7
^{137}Cs	28.44	2.34×10^5	6.66×10^9	1×10^7
^{228}Th	3.03	2.24×10^5	6.80×10^8	1×10^7

must be smeared to account for the detector response. The resolution model outlined in Equation 4.3.5 can be combined with Equation 4.3.4 in order to model the energy-dependent resolution of the NaI detector:

$$\sigma(E) = \frac{E}{2\sqrt{2\ln 2}}\sqrt{\alpha^2 + \frac{\beta^2}{E} + \frac{\gamma^2}{E^2}}, \tag{4.4.1}$$

where $\sigma(E)$ is the energy-dependent resolution. The histogram of the simulated data of true energy deposits in the NaI crystal is smeared by convolving with a normal distribution probability density function (PDF) that takes the $\sigma(E)$ function as a parameter.

While GEANT4 is capable of modelling the energy deposits from radioactive isotopes in NaI, the scintillation light yield is known to be a non-linear function of the energy deposit from Birks' law [332]. This non-linearity is dependent on the microphysics of the particle interaction, so cannot be corrected for the total energy deposited per event [333], but can be applied at each simulation step. Non-linearity is increases with decreasing energy [334], so is prominent in the low-energy range of the simulated data sets if uncorrected for in GEANT4.

Figure 4.4.2 shows the simulated energy spectrum of ^{22}Na, ^{60}Co, ^{137}Cs and ^{228}Th decays before and after Gaussian smearing, using the parameters from Equation 4.3.5 to calibration data shown in Figure 4.3.8. The black solid lines show the true energy depositions, while the red solid lines indicate the smeared distributions accounting for detector energy resolution. Events that deposit zero energy in the crystal have been removed from the datasets to more accurately model the spectra at low energies.

To determine the live time of simulated datasets t_s, the following equation can be used:

$$t_s = \frac{N_{\text{primary}}}{A_s} \tag{4.4.2}$$

where N_{primary} is the number of primary decays simulated and A_s is the source

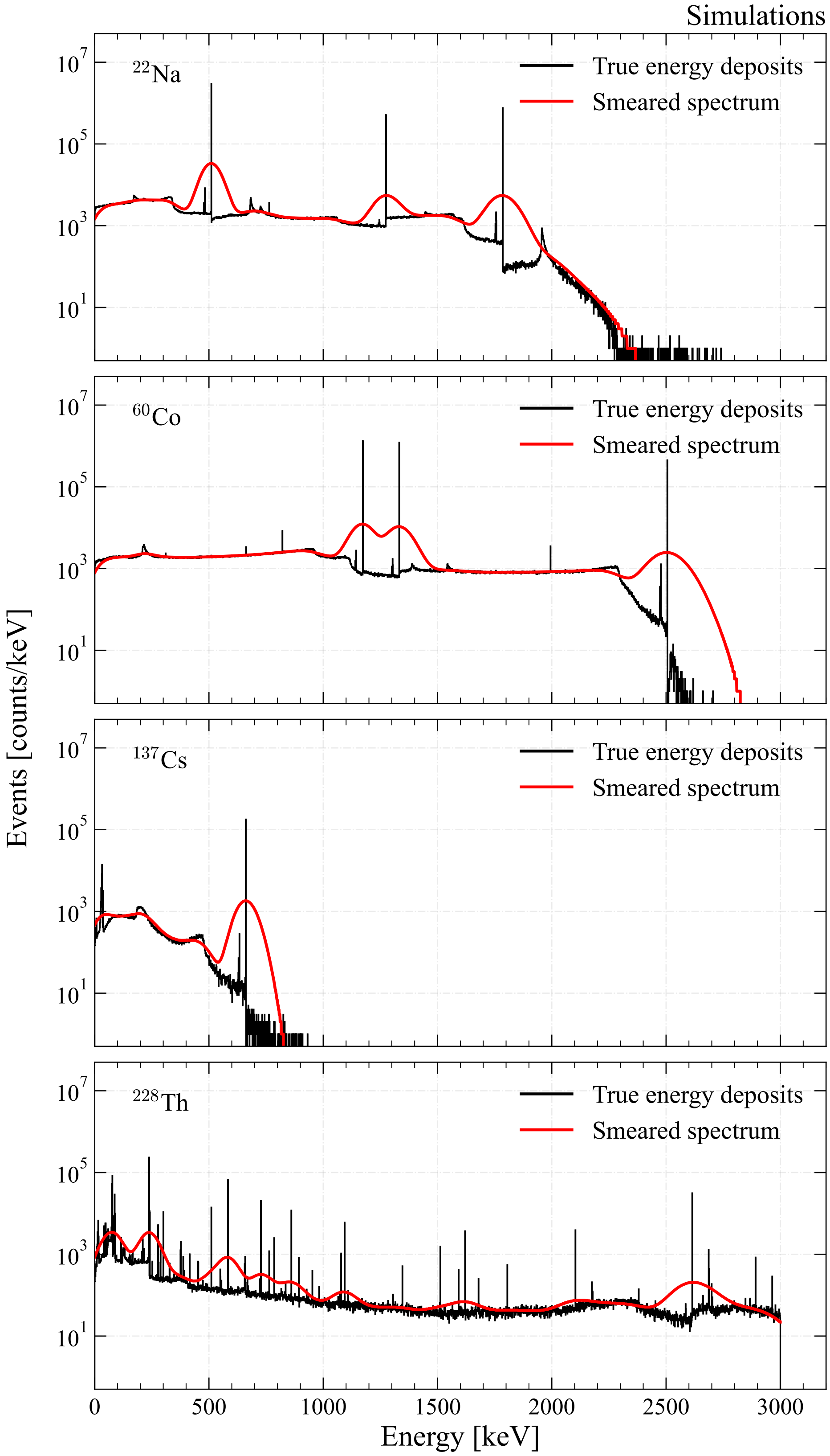

Figure 4.4.2: Application of the detector resolution model to the simulated calibration dataset. The black line shows the true energy deposits from simulation, whereas the red line shows the smeared spectrum using Equation 4.3.5.

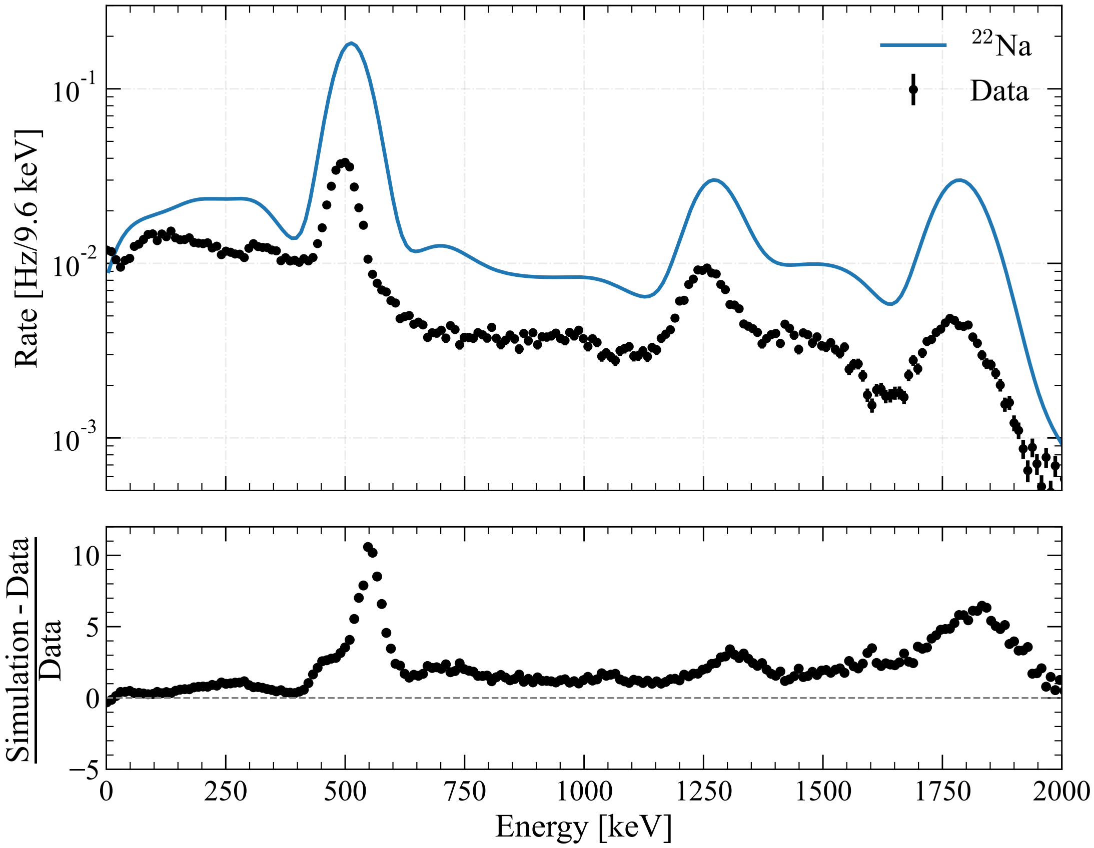

Figure 4.4.3: Comparison of the simulation of ^{22}Na decays (blue line) to calibration data (black data points). A flat absolute efficiency of $\varepsilon_{\mathrm{abs}} = 0.005$ has been applied to the simulated data set. The residuals between the two distributions are shown in the bottom panel, highlighting which energy ranges of the spectrum are not in agreement with the calibration data.

activity in Bq. This scaling can be used to compare rates in calibration data and simulations, as shown in Figure 4.4.3 for ^{22}Na. A flat efficiency of $\varepsilon_{\mathrm{abs}} = 0.005$ has been applied to the simulation, to account for the detector efficiency observed during gamma-source calibrations (see Figure 4.3.9). From the residuals plotted in the bottom panel of Figure 4.4.3, it can be seen that the simulation overestimates the rate of events recorded in the NaI detector up to a factor 10×. This overestimation was also observed for the other gamma sources datasets. This overestimation must be accounted for to compare future background simulations to detector measurements. This could be achieved by doing further calibration measurements in order to apply an energy-dependent efficiency correction.

4.5 Cavern background measurements

4.5.1 Data collection method

All data was collected using the equipment outlined in Section 4.2. The MAESTRO software allows for automated data-taking functionality via a “Job Control” service [321]. This is done by submitting a `.JOB` file containing specific run parameters set by the user. The specific `.JOB` file used during the background exposure sets the real time of each acquisition to be 10 800 s, so that an output file is saved every three hours. The `.JOB` file also specifies how many files to create via a loop statement, and can be stopped at any time during the run. A real time of three hours was chosen so that any time-dependent variations to the background spectra can be monitored, such as small changes in temperature and the bias voltage that may vary over time.

The off-line data files produced by the MAESTRO software are in `.SPE` file format and contain the measurement data and time, live time and real time values and two arrays of channel number and channel counts. The `.SPE` files are stored locally on the Windows 7 laptop. These files are then manually transferred to the LZ US data centre (NERSC), for storage and further analysis.

4.5.2 Auxiliary cavern radon measurement

Radon in the cavern air that results from radon emanation is a background to be considered, as decays below ^{222}Rn contribute the majority of gamma-rays in the ^{238}U chain. Radon emanation rates in the Davis campus are measured hourly by an AlphaGUARD detector [335] located in the common corridor. It should be noted that the common corridor is located outside the Davis cavern (see Figure 3.2.3), so there may be discrepancies between the radon rates recorded and the emanation rate in the cavern itself. Measurements of radon activity are used as a general

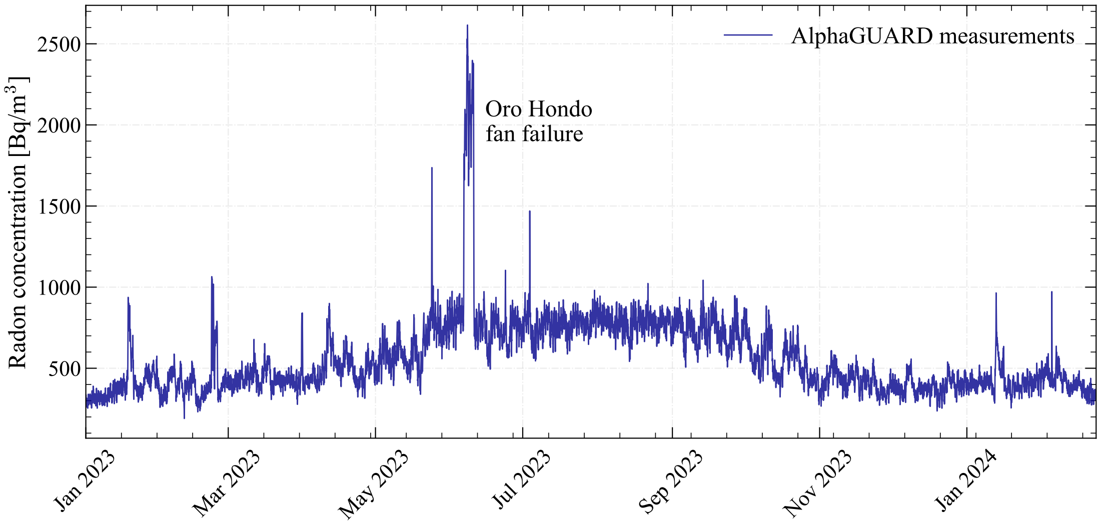

Figure 4.5.1: Radon concentration recorded by the AlphaGUARD detector located in the common corridor of the Davis campus during operation of the NaI detector. All timestamps are given in Mountain Time.

environmental background monitor in the Davis campus.

The radon concentration recorded in the Davis campus over 2023 is shown in Figure 4.5.1. The large spike in radon concentration recorded from 6th to 10th of June was caused by a failure of the Oro Hondo fan, which provides essential underground ventilation [187]. The smaller spikes in January and February relate to the covering of the Yates underground access shaft to prevent against freezing. The general upward trend of radon concentration is due to the airflow needed to support excavation work underway on the 4850' level for the DUNE experiment [336]. Average radon concentration values for each background run are listed in Table 4.5.1. These concentrations are on the order of $\mathcal{O}(100\,\mathrm{Bq\,m^{-3}})$ and are significant enough that the ^{222}Rn contribution must be included in further analysis of these background measurements.

4.5.3 Analysis of cavern background measurements

A total of six background measurements were taken in the Davis cavern. Measurements were taken at two locations: location *a* and location *b*, shown in Figure 4.5.2.

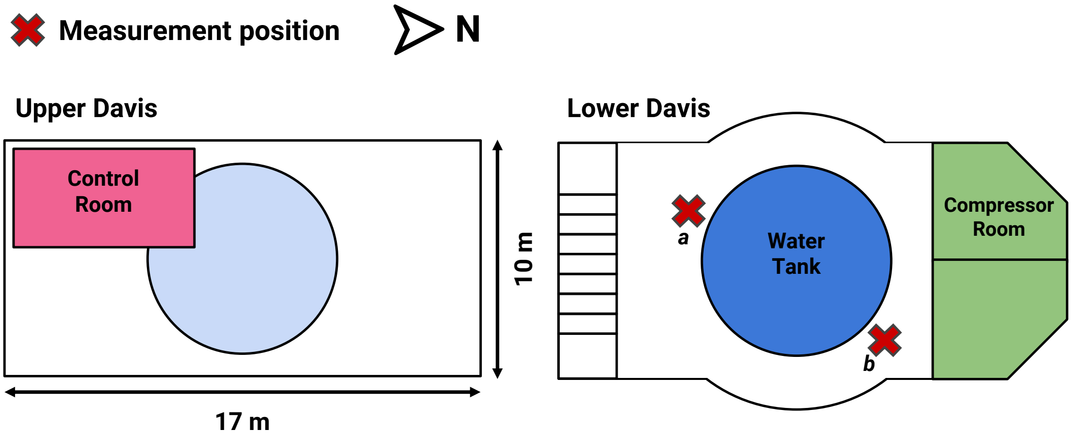

Figure 4.5.2: A schematic of the layout of the Davis cavern at the time at which calibrations and background measurements were taken. Measurement positions are denoted with red crosses. Figure adapted from Ref. [262].

The background exposure at location a commenced on 8th February 2023, after the initial calibration campaign was complete (see Figure 4.3.1). The background exposure at location b commenced on 16th March 2023, after the AmBe calibration measurement was taken. This background measurement ended on 6th April 2023, after which the detector was moved back to location a.

The measurements taken at location a are split into separate continuous runs and information relating to each background exposure is outlined in Table 4.5.1. While the current data acquisition run is ongoing, here we will present all data collected up until 12:00 Mountain Time 21st February 2024. A total of live time exposure of ~ 347.1 days is available to analyse out of a total real time of 360.75 days. The cumulative run time of background measurements as a function of time is shown in Figure 4.5.3.

The large dataset acquired allows for analysis of the rate of events recorded by the NaI detector over time. Figure 4.5.4 shows the event rate for the NaI detector spanning the background data acquisition period. The number of events recorded is dependent on the detector location and presence of calibration sources. The rate of events during the post-AmBe background measurement at location b is consis-

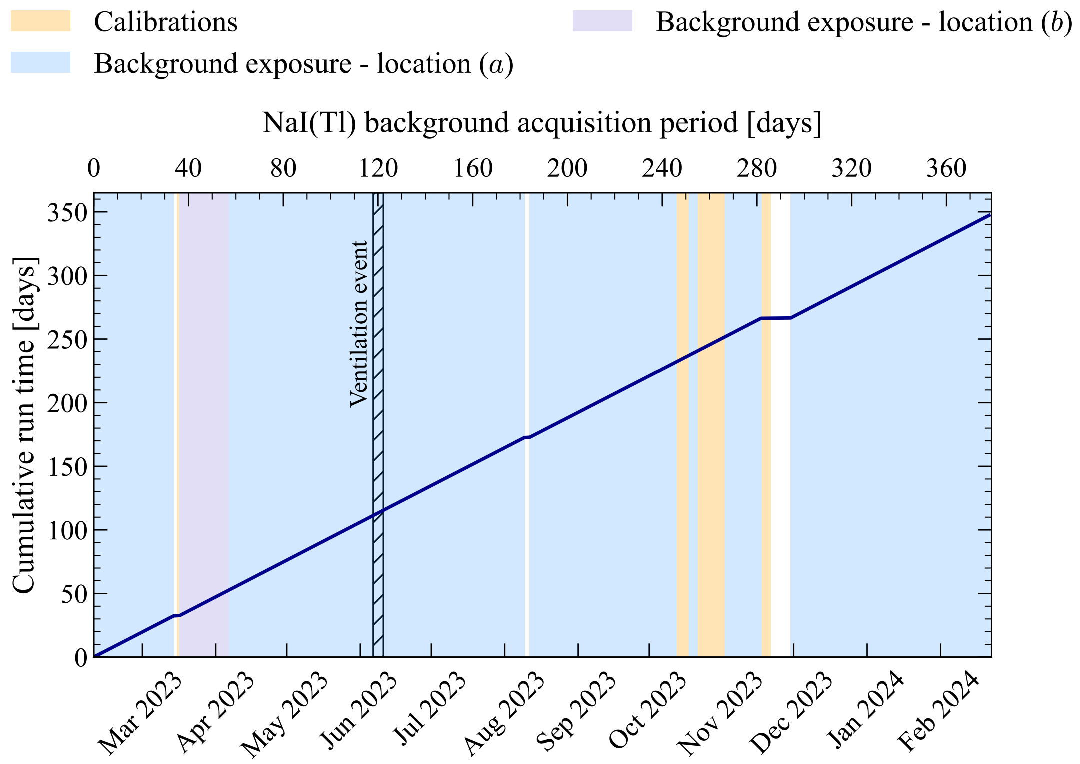

Figure 4.5.3: The cumulative run time of NaI background acquisitions as a function of calendar time.

tently higher than the baseline for other background runs acquired at location a. We attribute this increase to the detector proximity to the compressor room walls and eastern cavern wall and the rhyolite intrusion located in this region. Spikes in the number of events acquired are correlated and align with the Oro Hondo fan failure which affects ventilation in the cavern, AmBe calibrations, and both LZ DD direct and H-reflector mode calibrations. This examination of background data over time demonstrates the sensitivity of the NaI detector to environmental background changes that occur within the Davis cavern.

Identifying these abnormalities allows us to apply appropriate data quality cuts. The entirety of Run 1 is included in the overall dataset to maximise exposure. The higher rate is due to increased radon concentration and therefore ^{222}Rn and its progeny. Comparing the reconstructed energy spectra for Run 1 with and without the ventilation events files shows an increase in the energy range below

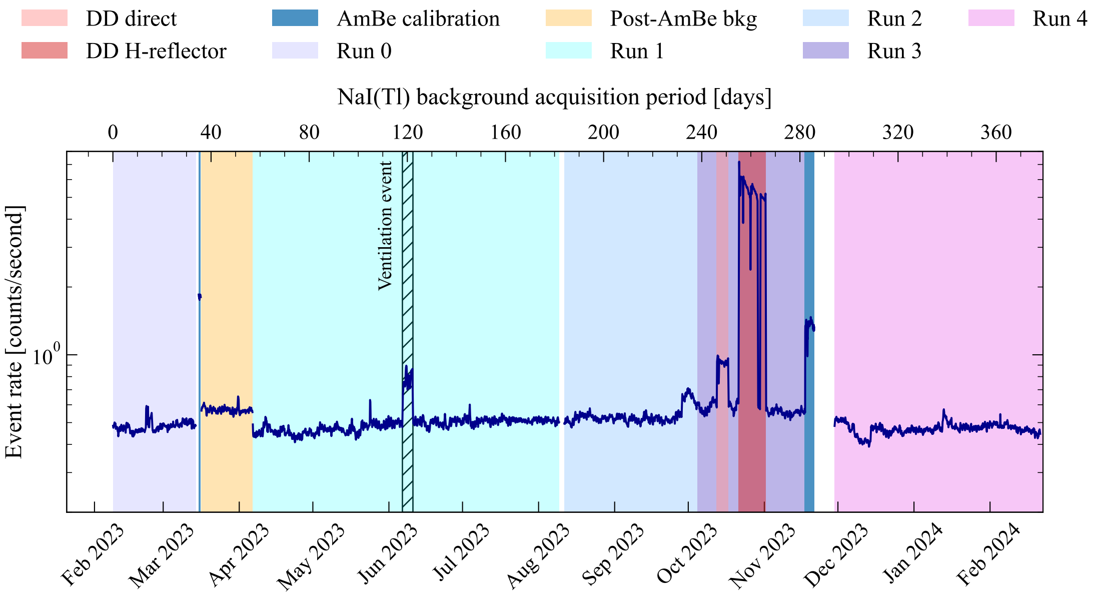

Figure 4.5.4: The rate of events recorded by the NaI detector. The shaded regions correspond to specific calibration and background exposures of the NaI detector, given in the legend. All timestamps are given in Mountain Time. The lower x-axis shows calendar time and the upper x-axis shows the time in days since background acquisitions began.

2 MeV. This is attributed to ^{214}Bi decays from the ^{222}Rn chain that contribute to prominent photopeaks and the Compton continuum. The reconstructed energy spectra for Run 1 are shown in Figure 4.5.5. Increased rates are also observed during LZ detector calibrations. Due to the elevated event rate and high-energy (n,γ) captures recorded by the NaI detector during the DD calibrations (see Chapter 5) this data has been omitted from the Run 3 exposure. After removing the DD calibration exposure from the total dataset, the total live time is reduced from 347 days to 328 days.

It is also important to note that the NaI crystal itself will have intrinsic ^{40}K, ^{238}U and ^{232}Th contamination due to radioactive impurities introduced during crystal growth. The intrinsic radiation could be measured in the future by creating an appropriate γ-ray shielding configuration using the virgin lead (direct from ore) bricks at SURF obtained from the Doe Run Mining Company. The optically coupled PMT is also an additional source of radiation [303, 337]. The surrounding

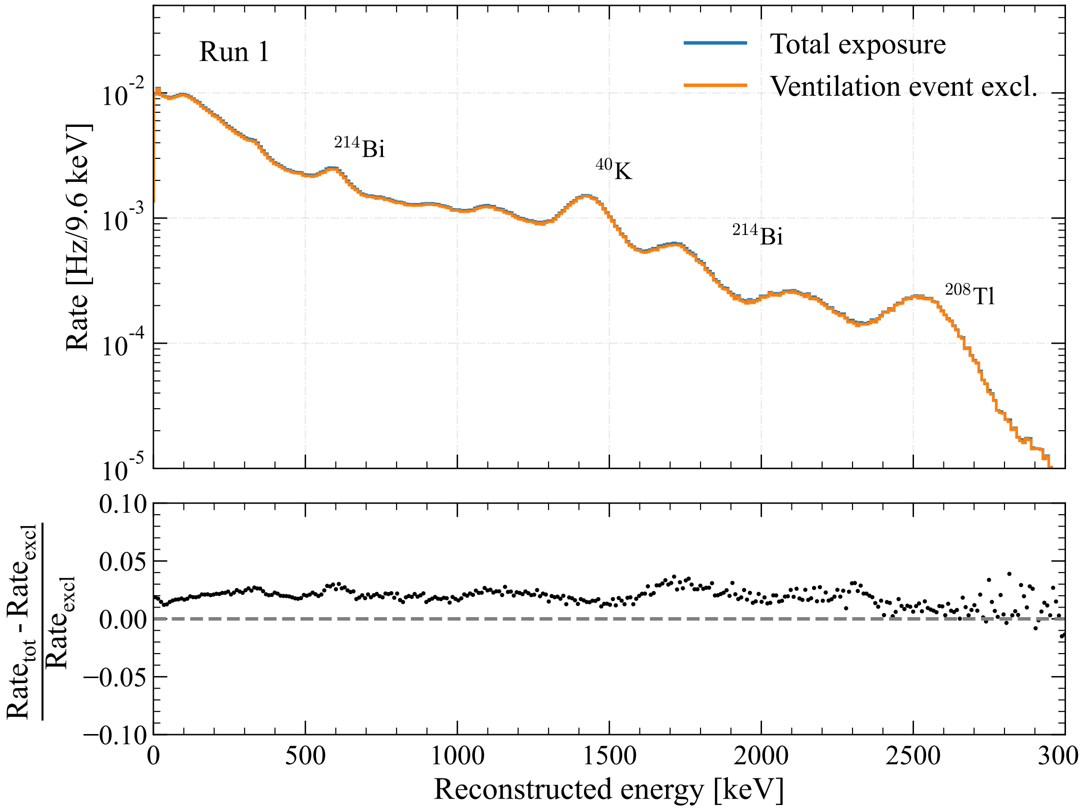

Figure 4.5.5: Comparison of the reconstructed energy spectra for Run 1, considering the total exposure and the exclusion of the ventilation event shown by the blue and orange lines, respectively. The two spectra largely coincide within the 0–3000 keV energy region. In order to highlight the difference between the two distributions, the relative difference in rate with respect to the excluded data is shown in the bottom panel.

electronics and casing may also contribute to the recorded background.

The reconstructed energy spectra for the six background measurements are shown in Figure 4.5.6. Energy values have been reconstructed using the scaling values obtained from calibrations discussed in Section 4.3.4 resulting in a bin width of 9.6 keV.

Key information relating to the analysis of these spectra is presented in Table 4.5.1. The lowest total rate measured during Run 4 at location *a* is within 17.5% of both Run 3 and the measurement at the north side of the water tank (location *b*). The increased rate of counts above 3500 keV during Run 3 (see last column in Table 4.5.1) may be attributed to residual neutrons in the Davis cavern post-DD calibrations. This was checked by examining the spectra split over

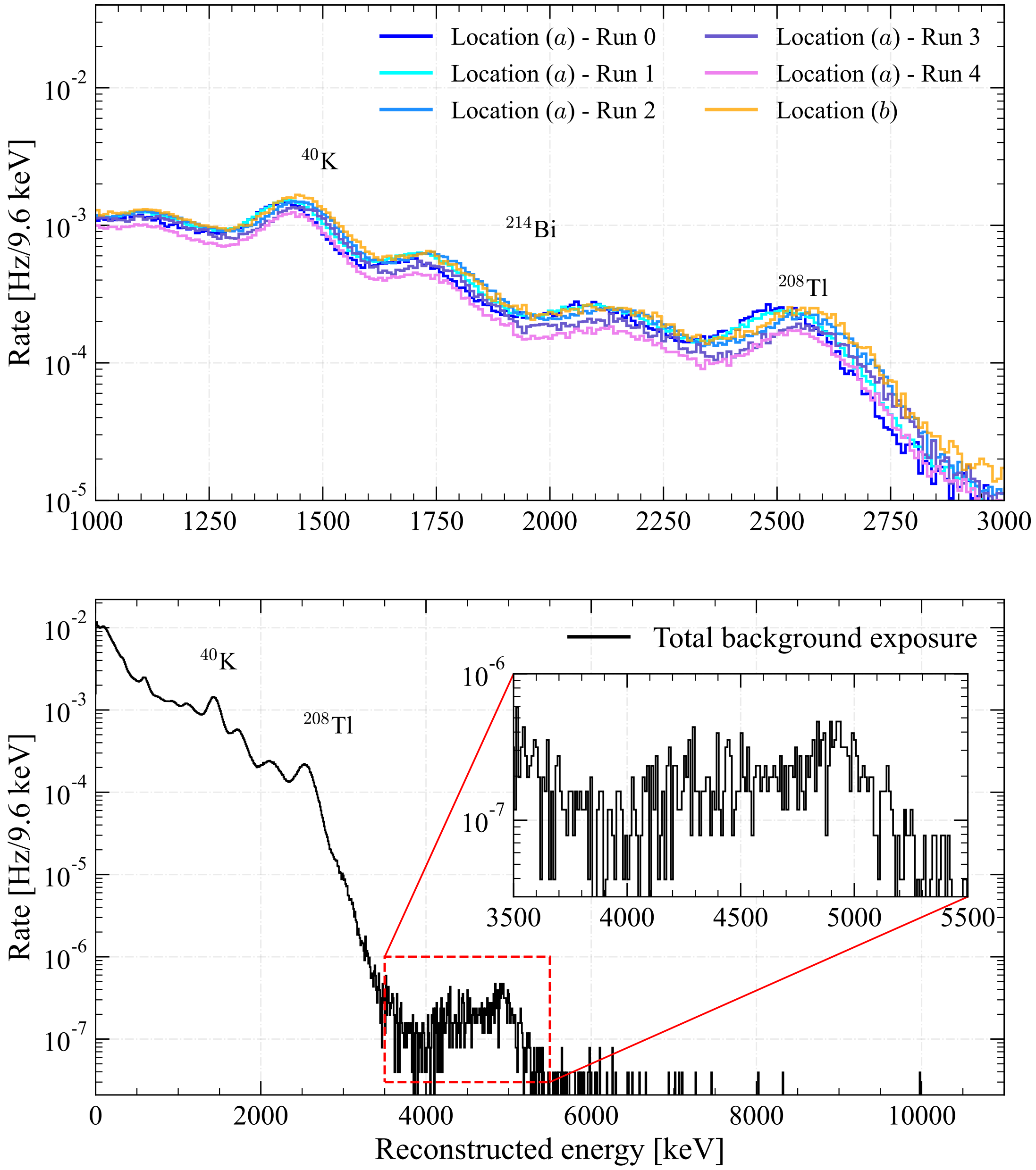

Figure 4.5.6: The reconstructed energy spectra for the six background measurements taken in the Davis cavern. **Top:** Focus on the NORM photopeaks in the energy range 1000–3000 keV. The prominent gamma peaks from ^{40}K, ^{214}Bi and ^{208}Tl are labelled. **Bottom:** The combined energy spectrum in the range 0–11 MeV, highlighting the high-energy counts recorded in the range 3.5–5.5 MeV.

Table 4.5.1: Run numbers, measurement dates, live time, average radon concentrations and integrated count rates for each background measurement taken in the Davis cavern. Uncertainties on the average radon concentration values are given by $\pm 1\sigma$. Uncertainties quoted on rates are Poisson counting errors only.

Meausurement	Label	Run number	Start date	Live time	Dead time	Avg. radon	Integrated rate [Hz]	
position				[h]	[%]	[Bq/m^3]	Total	> 3500 keV
South side	*a*	Run 0	08/02/23	777.9	3.60	422.8 ± 113.3	0.482 ± 0.006	$(2.93 \pm 2.59) \times 10^{-5}$
North side	*b*	n/a	16/03/23	484.4	3.31	436.8 ± 71.1	0.570 ± 0.008	$(4.24 \pm 3.90) \times 10^{-5}$
South side	*a*	Run 1	06/04/23	2880.51	3.89	728.4 ± 290.6	0.497 ± 0.003	$(3.52 \pm 2.37) \times 10^{-5}$
South side	*a*	Run 2	11/08/23	1243.14	3.86	744.8 ± 88.0	0.536 ± 0.005	$(3.93 \pm 3.00) \times 10^{-5}$
South side	*a*	Run 3	04/10/23	542.96	3.73	519.1 ± 99.9	0.566 ± 0.008	$(5.73 \pm 4.96) \times 10^{-5}$
South side	*a*	Run 4	29/11/23	1939.8	3.64	408.3 ± 69.0	0.471 ± 0.004	$(3.79 \pm 2.76) \times 10^{-5}$
Total exposure	-	-	-	**7868.7**	**3.75**	-	$\mathbf{0.500 \pm 0.002}$	$\mathbf{(3.79 \pm 1.76) \times 10^{-5}}$

pre-DD and post-DD acquisitions. Overall, there is no significant difference in the reported integrated rate for each background run.

The six spectra are combined and shown in the bottom panel of Figure 4.5.6, where the statistics for the region above the ^{208}Tl shoulder are shown alongside the dominant NORM background. There is evidence of some substructure in the counts shown, with peaks emerging at approximately 4.1 MeV and 4.9 MeV associated with neutron capture on ^{16}O and ^{28}Si, respectively. It should be noted that these incident gamma-rays are also of energies large enough to produce escape peak features in the energy spectra. The integrated rate of events above 3.5 MeV is $(3.79 \pm 1.76) \times 10^{-5}$ Hz.

4.6 Conclusion

A long-exposure gamma spectroscopy experiment has been deployed in the lower Davis cavern in order to characterise the high-energy cavern background originating from the cavern walls. Understanding this source of ER background is important for the WIMP search sensitivity - along with searches for rare physics signals such as $0\nu\beta\beta$, for which the cavern background contributes in the $Q_{\beta\beta}$ energy region of ^{136}Xe decays. This new high-energy measurement campaign built upon preliminary measurements of cavern background, this time utilising a larger $\varnothing$ 6-inch × 6-inch sodium iodide crystal with longer live times to increase the overall exposure.

The NaI crystal was successfully calibrated using a variety of gamma sources available at SURF, including a newly manufactured AmBe (α,n) source which is a source of high-energy gammas. This allowed for the detector response to be fully characterised; quantifying the energy linear scaling relationship, energy resolution and detection efficiency which are utilised to compare GEANT4 simulations to data.

The work presented in this Chapter demonstrates that the sodium iodide detector can record proof of principle cavern background measurements with stable detector operating conditions over the course of 2023. A total of 6 long-exposure ambient background measurements were taken at a location situated close to the outer edge of the water tank. The integrated rates for each measurement fall within the same order of magnitude with no significant deviations reported. Therefore, the counts for each exposure have been combined to accumulate statistics in the high-energy region above the ^{208}Tl shoulder of the NORM background beyond 2.6 MeV. This has provided the first direct measurement of the high-energy gamma flux in LZ detector surroundings produced by the cavern rocks.

The main body of this study prefaces the integration of the NaI detector into the LZ environmental monitoring station, and highlights that capability of the NaI detector to monitor gamma backgrounds in the Davis cavern. This is a necessity to ensure confidence in future science results reported for rare physics searches by the LZ experiment. The NaI detector will continue to collect background data in the lower Davis cavern until its inclusion in the EMS later in 2024.

5 DD neutron exposure

LZ uses a DD neutron source in order to calibrate the detector response of low-energy NR events. This is a crucial calibration needed to ensure that the NR response is accurately modelled in (S1c, $\log_{10}$(S2c)) parameter space in the region of interest for $\mathcal{O}(10\,\mathrm{GeV}/c^2)$ mass WIMPs and ^{8}B neutrino CEνNS signals. Monoenergetic neutrons of energy 2.45 MeV may be directed into the LZ detector via two conduits: one angled and one horizontal. In October 2023, LZ conducted two DD calibrations using the horizontal conduit during the Run 3 background exposure of the NaI detector. The first calibration was in direct mode and second in H-reflector mode. Analysis of the data collected during the neutron exposure from the DD source is presented in this Chapter.

5.1 DD neutron calibration

There was an opportunity to analyse data collected by the NaI detector during a DD calibration of the LZ detector. Direct DD calibration commenced on 12th October 2023 and ended on 17th October 2023. This was followed by a DD H-reflector calibration which started on the 21st October and finished on the 1st November 2023. During calibration the DD generator is positioned outside the water tank and neutrons are directed into LZ using the horizontal conduit (also referred to as the East conduit), which is located 90° off axis with respect to the angled conduit shown in Figure 5.1.1.

The DD direct and reflector modes each use a custom neutron shielding castle surrounding the generator which is made of BPE, with 5% boron by weight. This is the same shielding that was employed for the AmBe calibration. The direct

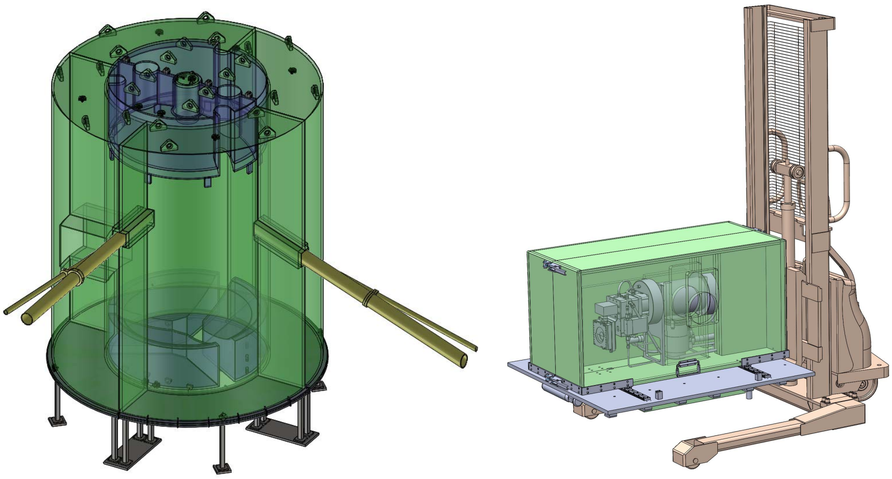

Figure 5.1.1: CAD drawings of DD calibration systems. **Left:** The OD assembly with horizontal and angled DD conduits. **Right:** The Adelphi Technology DD generator enclosed within shielding (green) mounted on a portable lift to position the DD source.

mode shielding is used to reduce neutron entry into the cavern. The reflector mode shielding is additionally designed to mitigate secondary-scattered neutrons from entering the TPC via the conduit.

The DD generator can produce up to 1×10^9 monoenergetic 2.45 MeV neutrons per second into 4π via a DD fusion reaction:

$$\mathrm{D} + \mathrm{D} \rightarrow {}^{3}\mathrm{He} + \mathrm{n}. \tag{5.1.1}$$

The fraction of neutrons that do not enter LZ via the DD conduit and are not captured by the BPE shield may lead to subsequent neutron captures that occur on abundant materials near the detector. These materials include the cavern rock, stainless steel water tank and the NaI crystal target.

5.2 Thermal neutron capture

Subsequent (n,γ) capture reactions will lead to the production of gammas of energies up to ~ 10 MeV [340, 341]. Thermal neutron capture cross-section values [338] for elements contained within the shotcrete, cavern rock and stainless steel are

Table 5.2.1: Elemental abundance of the Homestake rock formation, shotcrete layer and stainless steel water tank used in GEANT4 simulations of the Davis cavern. The corresponding thermal neutron capture cross-sections are given in barn [338]. Shotcrete abundances provided by Kevin Lesko from previous assay measurements for Deep Underground Science and Engineering Laboratory (DUSEL) studies [289, 339].

Element	Homestake [%]	Shotcrete [%]	Stainless steel [%]	σ_{capture} [b]
H	1.19	-	-	0.3326
C	-	-	0.04	0.00351
O	48.4	44.32	-	0.00019
Na	2.13	2.86	-	0.530
Mg	4.22	0.67	-	0.0666
Al	7.20	9.09	-	0.231
Si	20.44	30.08	0.37	0.172
P	0.03	-	-	0.172
S	-	-	0.015	0.534
K	0.17	4.69	-	2.06
Ca	5.65	2.59	-	0.431
Ti	0.73	-	-	6.08
Cr	-	-	19.0	3.07
Mn	0.10	0.25	-	13.36
Fe	9.87	5.4	70.53	2.56
Ni	-	-	10.0	4.39

shown in Table 5.2.1. Due to the proximity of neutrons produced by the DD generator to the stainless steel water tank, we expect that neutron capture on Fe, Cr and Ni will be the dominant contributor to background observed by the NaI detector. Capture on O, Si and Fe in the cavern rock materials may contribute a secondary source of high-energy counts. Neutron capture cross-sections are dependent on the energy of the incident neutron and often have complex resonance structures which are measured via nuclear physics experiments. The neutron capture cross-section for ^{16}O, ^{28}Si and ^{56}Fe as a function of incident of neutron energy are shown in Figure 5.2.1, with data taken from the ENDF/B-VIII.0 nuclear data library [342].

^{16}O, ^{28}Si and ^{56}Fe are the most abundant isotopes present in $^{\text{nat}}$Fe and $^{\text{nat}}$Si, with fractions of 99.8%, 92.2% and 91.7%, respectively. The ^{16}O(n,γ), ^{28}Si(n,γ)

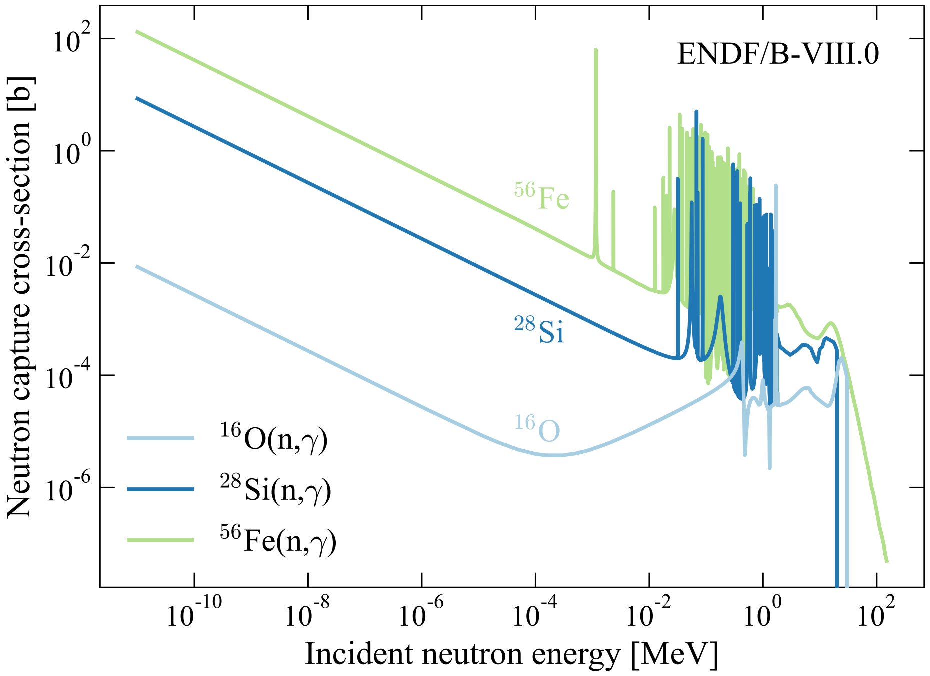

Figure 5.2.1: Neutron capture cross-sections for ^{16}O, ^{28}Si and ^{56}Fe as a function of incident neutron energy. Figure made using data from the ENDF/B-VIII.0 nuclear data library [342].

and ^{56}Fe(n,γ) neutron capture reactions produce high-energy gammas via:

$$\begin{aligned} n + {}^{16}\mathrm{O} &\rightarrow {}^{17}\mathrm{O} + \gamma \qquad (3.272\,\mathrm{MeV}, 4.142\,\mathrm{MeV}), \\ n + {}^{28}\mathrm{Si} &\rightarrow {}^{29}\mathrm{Si} + \gamma \qquad (3.539\,\mathrm{MeV}, 4.934\,\mathrm{MeV}), \\ n + {}^{56}\mathrm{Fe} &\rightarrow {}^{57}\mathrm{Fe} + \gamma \qquad (7.631\,\mathrm{MeV}, 7.645\,\mathrm{MeV}), \end{aligned} \tag{5.2.1}$$

where the energy of the high-intensity prominent gamma-rays are also listed in brackets [343–345]. (n,γ) capture on Ni and Cr isotopes contained within the stainless steel can yield gammas in the region of 8–9 MeV [346, 347].

5.3 Activation of sodium iodide

The incident neutron flux may also result in activation of the NaI crystal target [348]. Neutron activation of the NaI crystal can occur during transportation and storage of the crystal on the Earth's surface due to exposure to the cosmo-

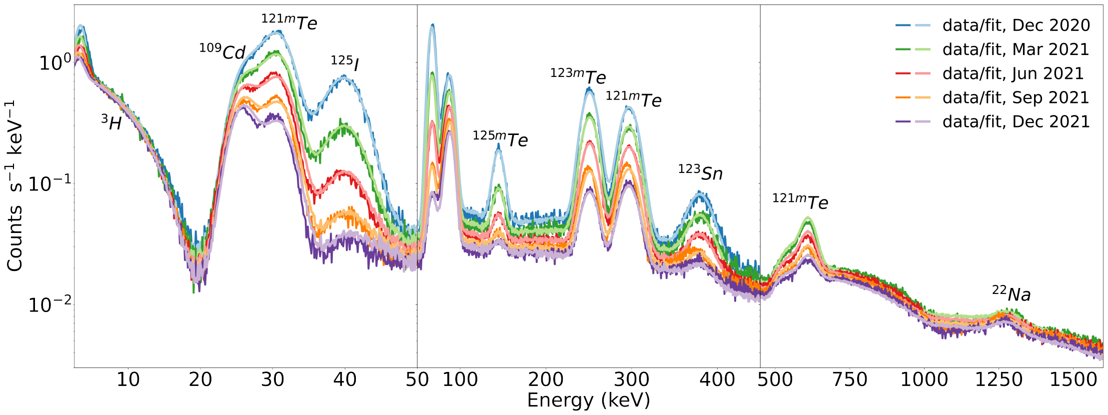

Figure 5.3.1: The decay of activation products resulting from neutron beam irradiation of NaI crystals at Los Alamos Neutron Science Center. The spectral features are labelled with the identity of the isotope primarily responsible for each feature. Figure taken from Ref. [348].

genic neutron flux, or in the presence of a neutron source when underground where cosmogenic backgrounds are sufficiently attenuated. Activation may result in the production of ^{3}H, ^{22}Na, ^{125}I and its progeny. Activation products are a key background for dark matter searches that use arrays of inorganic scintillator targets, so have been extensively studied by other collaborations including ANAIS-112, COSINE-100 and SABRE [349–353]. Information relating to observed activation products in other studies are listed in Table 5.3.1.

A neutron beam facility at Los Alamos Neutron Science Center performed a dedicated study of the production rate of long-lived activation products using NaI crystals [348]. The crystals were irradiated in a controlled environment in order to reproduce the cosmic-ray neutron spectrum. The energy spectra post-exposure are shown in Figure 5.3.1, where prominent activation products are labelled. This test will help inform background estimates for dark matter searches and determine the maximum time that next-generation NaI-based detectors can remain unshielded above ground before impacting sensitivity.

^{3}H is a spallation product produced via the ^{23}Na(n,x)^{3}H interactions [354], whereas ^{22}Na and ^{125}I are products of ^{23}Na(n,2n)^{22}Na and ^{127}I(n,3n)^{125}I processes, respectively. The decays of each are summarised below:

Table 5.3.1: List of radioisotopes that can be produced by activation of NaI, along with their progeny. Each isotope half-life, primary decay mode, main γ emission and Q-values are also provided. EC and IT refer to electron capture and isomeric transition, respectively. Specific energies of cascade X-rays and Auger electrons are not listed.

Isotope	Half-life [d]	Decay mode	Main γ emission [keV]	Q-value [keV]
^{3}H	4500	β^-	-	18.6
^{22}Na	950.4	β^+	511, 1274.6	2842.2
^{109}Cd	461.9	EC	88.03	215.1
^{113}Sn	115.09	EC	391.70	1039
^{125}I	59.4	EC	35.49	185.8
^{121}Te	19.16	EC	507.6, 573.1	1056
$^{121\mathrm{m}}$Te	164.4	IT	294.0	293.97
$^{123\mathrm{m}}$Te	119.3	IT	247.6	247
$^{125\mathrm{m}}$Te	57.4	IT	144.8	247
$^{127\mathrm{m}}$Te	107	IT	88.3	88.3

- **^{3}H:** Tritium is a pure beta emitter and has a low Q-value endpoint of 18.6 keV. This makes it a particularly dangerous background for dark matter searches which focus on the low-energy $\mathcal{O}(10\,\mathrm{keV})$ scale.

- **^{22}Na:** ^{22}Na decays primarily by positron (β^+) emission (90.3%) or by electron capture (9.6%) to the 1275 keV excited state of ^{22}Ne. This result in two prominent peaks at the 511 keV positron-annihilation energy and the 1275 keV photopeak, with can also occur in coincidence to result in the sum peak emerging at 1786 keV (see Figure 4.3.2).

- **^{125}I:** ^{125}I decays by electron capture to the 35.5 keV excited state of ^{125}Te, which then decays to the ground-state via gamma emission. Atomic de-excitation of ^{125}Te occurs through a gamma cascade from atomic shell that the electron capture occurred. For electron capture on the K-shell, an X-ray of energy 31.8 keV will also be emitted. The nuclear and atomic de-excitations of ^{127}I can be treated as prompt signals which will result in a combined peak at 67.3 keV.

5.4 Measurements with the NaI detector

The reconstructed energy spectra for DD direct (light red) and H-reflector (dark red) modes are shown in Figure 5.4.1. For comparison, the total ambient cavern background is also shown by the cream histogram. The NORM background to 2.6 MeV is consistent with ambient background exposure. The energy spectra extending out to a maximum of ~ 10 MeV well beyond the 2.6 MeV shoulder during DD calibrations. Considering the baseline background exposure above an energy of 3.5 MeV, the rate of high-energy gamma events in the flat continuum increased by a factor of $\sim 100\times$ and $\sim 1000\times$ during DD direct and H-reflector modes, respectively. A sharp spike in the rate of events recorded in the NaI detector was also demonstrated in Figure 4.5.4. The total integrated rate for the DD direct and H-reflector modes are (0.91 ± 0.02) Hz and (4.820 ± 0.028) Hz, respectively.

Neutron captures on Fe, Ni and Cr contained within the stainless steel water

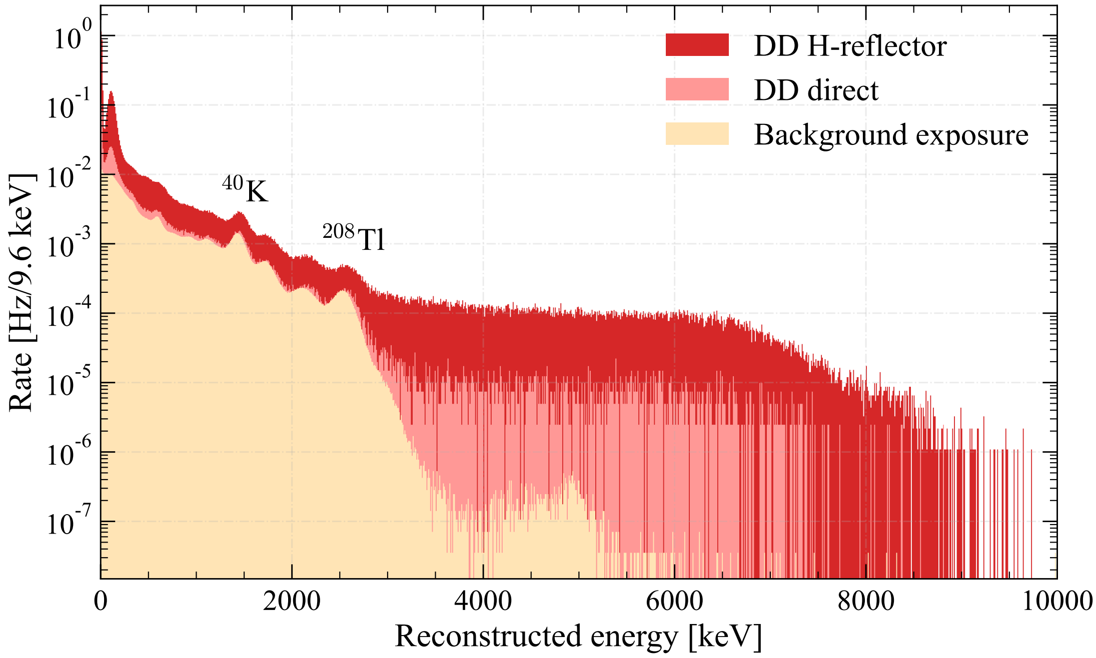

Figure 5.4.1: The reconstructed energy spectra for the total background exposure and the LZ DD calibration exposure in the energy range 0–10 MeV. The DD direct and H-reflector modes are shown separately by the light red and dark red histograms, respectively. The cavern background is shown by the cream histogram.

tank dominate the continuum high-energy region up to 10 MeV. The reconstructed energy spectra shows no clear evidence of photopeaks associated with (n,γ) capture on ^{28}Si (4.9 MeV) or ^{56}Fe (7.6 MeV) in the high-energy range beyond 3 MeV, therefore we assume that gammas produced by neutron captures undergo secondary Compton scattering and attenuation before depositing energy in the crystal volume and recorded by the NaI detector.

During exposure to the neutron source, distinct features appear in the low-energy region of the energy spectra. These peaks could be attributed to the detection of low-energy X-rays produced by photoelectric absorption on surrounding materials in the cavern environment. Figure 5.4.2 shows this low-energy region in channel space. Channel space was chosen as it is known that the NaI light yield non-linearity increases with decreasing energy, therefore accurate energy reconstruction cannot be assumed at low energies [334]. Tailored low-energy calibrations and the need for the application of correction factors may be needed for more accurate reconstruction.

The top panel shows the data split over data taken during DD calibrations and the background data acquired pre-DD and post-DD. The bottom panel shows the spectra from data files immediately before and after H-reflector calibration, which ended at approximately 14:00 Mountain Time on the 1st November 2023 when the DD generator was switched off. Inspecting the data files collected post-DD calibration, both immediately before and after and for the total remaining Run 3 exposure, shows that the low-energy features soon disappear after the DD source is powered down.

This is further supported by Figure 5.4.3 which shows an immediate return to nominal ambient baseline levels of background with no sign of exponential decay. Therefore, as many activation products have half-lives on the order of several days (refer to Table 5.3.1), we can assume there is no significant activation of the crystal resulting from LZ DD calibrations.

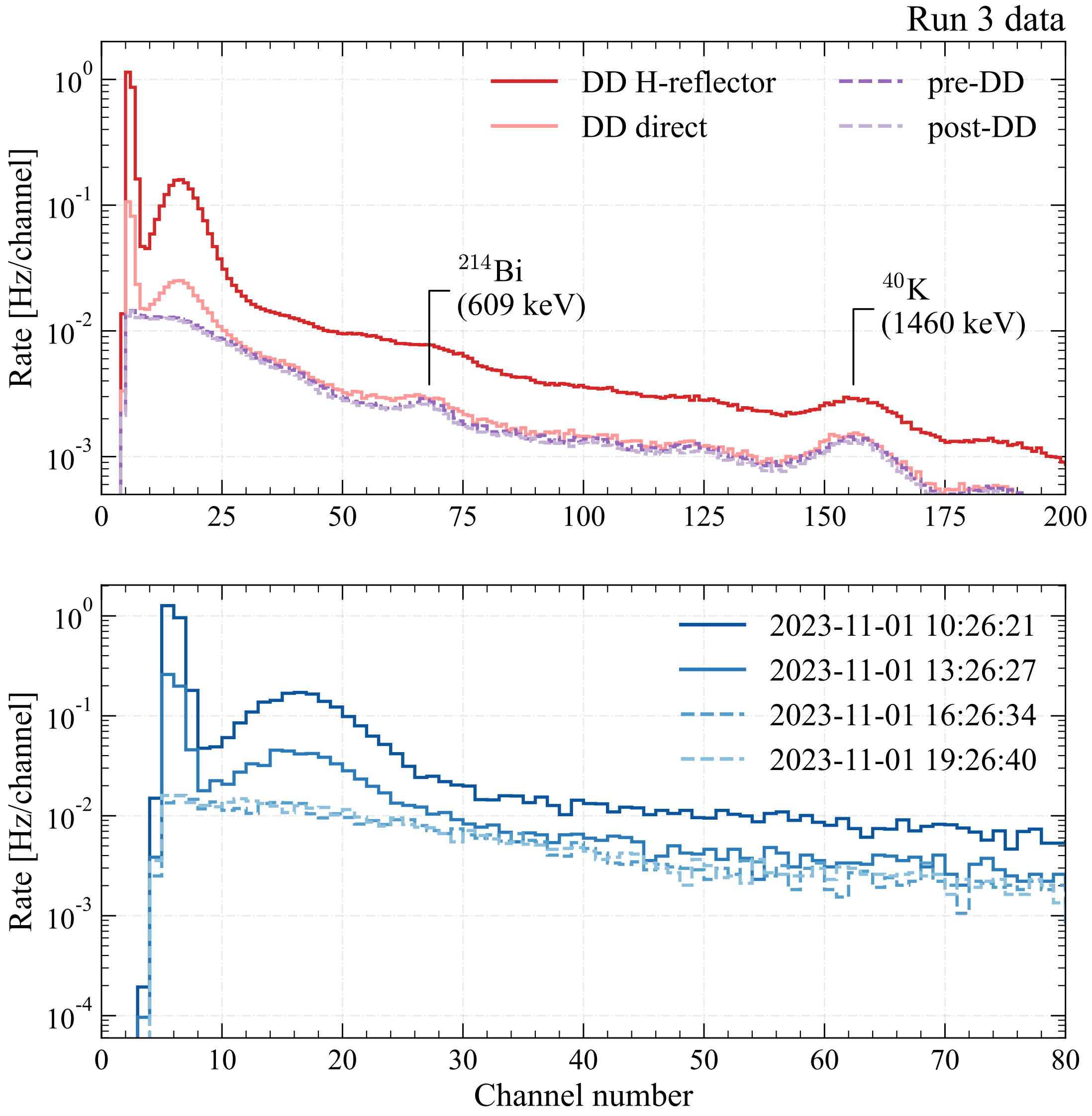

Figure 5.4.2: The raw spectra collected during the Run 3 background acquisition. **Top:** The spectra split into DD calibrations (solid red), pre-DD and post-DD subsets (dashed purple). The 609.3 keV ^{214}Bi and 1460.8 keV ^{40}K photopeaks are labelled for reference. **Bottom:** The spectra collected immediately before (solid) and immediately following (dashed) end of DD H-reflector calibrations, when the DD generator was switched off at approximately 14:00 Mountain Time.

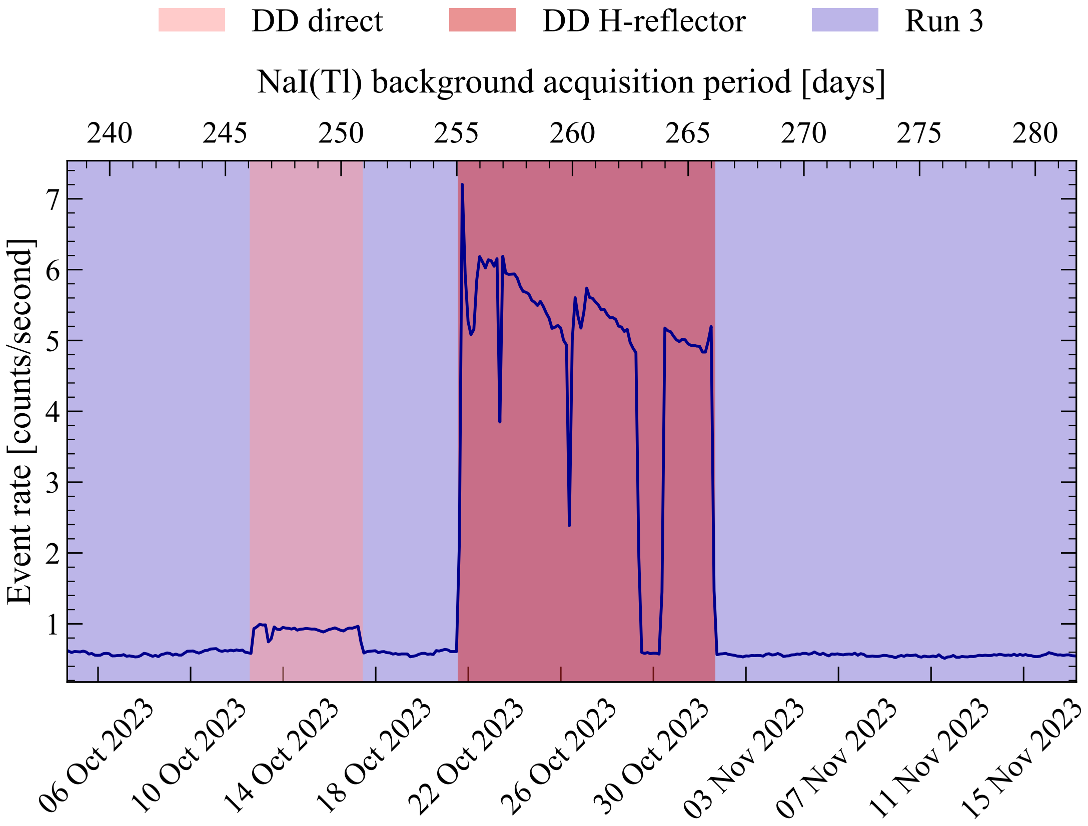

Figure 5.4.3: The event rate during the Run 3 background acquisition, during which LZ DD direct and H-reflector calibrations were conducted in the Davis cavern. The temporary sharp decrease and return to the baseline during the H-reflector calibration was due to the switch off of the DD source as a precaution to prevent damage to the equipment due to low coolant levels.

5.5 Conclusion

LZ performs routine ER and NR calibrations during science data-taking in order to quantify the highly sensitive detector response over time. A DD neutron generator is utilised to record low-energy NR events in the TPC directed via conduits. DD direct and H-reflector calibrations occurred in October 2023, during background measurements of the NaI detector. This allowed for a unique opportunity to measure changes to the Davis cavern background produced by the source *ex situ* of LZ detectors nested within the water tank.

The highest rate was recorded during H-reflector calibrations, where the neutrons are scattered from a H-loaded target at a specific angle to direct neutrons with energy less than 200 keV into the conduit. The presence of nuclei with high thermal neutron capture cross-sections in materials found within the cavern, such as the stainless steel water tank and rock, leads to the production of a significant high-energy (n,γ) background up to 10 MeV.

Exposure of NaI to neutrons may cause activation of the crystal, which can result in the production of ^{3}H, ^{22}Na, ^{125}I and their progeny. These isotopes typically have half-lives greater than order $\mathcal{O}(10\,\mathrm{d})$ and generate problematic low-energy backgrounds. There is no evidence of activation of the NaI crystal due to LZ DD calibrations.

This neutron exposure measurement demonstrates the capability of the NaI detector to monitor the presence of calibration sources in the Davis cavern - a key goal of the LZ environmental monitoring station. Therefore, this work emphasises the importance of the integration of the NaI detector into the EMS to accurately measure the cavern environment over the lifetime of LZ.

6 Simulations of cavern backgrounds

Radiogenic neutrons and high-energy gamma-rays may be produced by α particle interactions in the cavern rock surrounding the LZ experiment. These α particles are products of the ^{238}U and ^{232}Th decay chains and are of sufficient energy to cause nuclear reactions on light nuclei present in the Homestake rock and shotcrete. This Chapter outlines simulations of the backgrounds originating from Davis cavern rock. A comparison study of rock models is presented, which includes neutron yields from statistical model codes and Baccarat test geometry simulation studies. Computational needs for a high-statistics simulation of the Davis cavern are discussed and avenues for future work in order to compare simulations to existing measurements are presented.

6.1 Motivation

Decays of ^{238}U and ^{232}Th contained within the rock walls of the Davis cavern contributes to both the ER and NR background for LZ physics searches. These decays may produce radiogenic neutrons from (α,n) reactions or gamma-rays from primary decays of NORMs and secondary (α,γ) captures on light nuclei. The contributions from both can be assessed using Monte Carlo simulation methods.

Simulations of these backgrounds from Homestake rock have been conducted, but the contribution from shotcrete material has not been previously considered. This Chapter details a comparison of backgrounds originating from Homes-

Table 6.2.1: The elemental abundance values for the Homestake cavern rock [256] and shotcrete materials [339] as defined in the BACCARAT code.

	GEANT4 material	
Element	Homestake [%]	Shotcrete [%]
Al	7.20	9.09
Ca	5.65	2.59
Fe	9.87	5.4
H	1.19	-
K	0.17	4.69
Mg	4.22	0.67
Mn	0.10	0.25
Na	2.13	2.86
P	0.03	-
Si	20.44	30.08
Ti	0.73	-
O	48.4	44.32
Total	**100.0**	**99.95**

take rock and shotcrete, focussing on simulations of backgrounds from (α,n) and gamma-ray emitting NORMs from within the cavern rock.

6.2 Rock models

Current BACCARAT simulations assume a cavern rock composite of homogenous Homestake amphibolite rock, with the chemical composition informed by material assays conducted on a Homestake rock sample from near the surface [254]. Additional improvements to the original cavern geometry simulated in previous studies include the addition of a shotcrete material definition in order to simulate an alternative rock model [339]. Homestake rock and shotcrete are defined with density values of $\rho = 2.70\,\mathrm{g\,cm^{-3}}$ and $\rho = 2.30\,\mathrm{g\,cm^{-3}}$, respectively. The elemental abundance values used to simulate each material in GEANT4 are shown in Table 6.2.1, with the Homestake rock values converted from Table 3.1.1.

Previous simulations have modelled the cavern shell volume using Homestake material definitions, whereas in reality shotcrete is the outermost material coating the cavern walls. Furthermore, the results of the preliminary campaign concluded the activities of U/Th/K in the Davis cavern to be consistent with radioassay measurements of shotcrete material. Differences between radioactive decays originating from two different rock models can be assessed via simulation.

6.3 Yields from (α,n) captures

6.3.1 Overview

The alpha particles produced by the primordial decay chains ^{238}U and ^{232}Th are able to capture on isotopes present in the rock material, producing secondary particles. These alpha particles can induce (α,n) and (α,γ) reactions which contribute to the NR and ER background of dark matter searches, respectively. The energy threshold of these reactions is determined by the Q-value of these reactions and the Coulomb energy barrier of the target nucleus, which is proportional to the target nucleus atomic number Z [248]. Therefore, light- and medium-Z nuclei are most likely to undergo alpha capture. The energies of alpha particles produced by the uranium (^{238}U) and thorium (^{232}Th) chains are on the order of a few MeV, as shown in Table 6.3.1 where the ground state decay energies are listed.

This background can be suppressed by selecting radiopure materials for detector construction to limit the neutron yield produced by uranium and thorium impurities. However, the background originating from the cavern environment cannot be reduced. Therefore, it is essential to model the yields and energy spectra of α-induced captures.

Table 6.3.1: The ground state energies of alpha particles produced by the uranium (^{238}U) and thorium (^{232}Th) decay chains, split into early and late parts denoted by the subscripts e and l, respectively [249, 250, 261, 323, 355].

Decay chain	Decay	E_α [MeV]	BR [%]
$^{238}\mathrm{U}_e$	$^{238}\mathrm{U} \rightarrow {}^{234}\mathrm{Th}$	4.198	100
	$^{234}\mathrm{U} \rightarrow {}^{230}\mathrm{Th}$	4.774	100
	$^{230}\mathrm{Th} \rightarrow {}^{226}\mathrm{Ra}$	4.687	100
$^{238}\mathrm{U}_l$	$^{226}\mathrm{Ra} \rightarrow {}^{222}\mathrm{Rn}$	4.784	100
	$^{222}\mathrm{Rn} \rightarrow {}^{218}\mathrm{Po}$	5.489	100
	$^{218}\mathrm{Po} \rightarrow {}^{214}\mathrm{Pb}$	6.002	100
	$^{214}\mathrm{Po} \rightarrow {}^{210}\mathrm{Pb}$	7.686	100
	$^{210}\mathrm{Po} \rightarrow {}^{206}\mathrm{Pb}$	5.304	100
$^{232}\mathrm{Th}_e$	$^{232}\mathrm{Th} \rightarrow {}^{228}\mathrm{Ra}$	4.011	100
	$^{228}\mathrm{Th} \rightarrow {}^{224}\mathrm{Ra}$	5.423	100
$^{232}\mathrm{Th}_l$	$^{224}\mathrm{Ra} \rightarrow {}^{220}\mathrm{Rn}$	5.685	100
	$^{220}\mathrm{Rn} \rightarrow {}^{216}\mathrm{Po}$	6.288	100
	$^{216}\mathrm{Po} \rightarrow {}^{212}\mathrm{Pb}$	6.778	100
	$^{212}\mathrm{Bi} \rightarrow {}^{208}\mathrm{Tl}$	6.090	36
	$^{212}\mathrm{Po} \rightarrow {}^{208}\mathrm{Pb}$	8.785	64

6.3.2 Theory

The theory describing alpha captures is outlined briefly in the following discussion. The slowing and stopping of alpha particles in a material with density ρ is described by the mass stopping power:

$$S^m(E) = -\frac{1}{\rho}\frac{\mathrm{d}E}{\mathrm{d}x}, \tag{6.3.1}$$

which describes the energy loss of alpha particles of energy E over a distance x.

Yields of neutrons from alpha-induced captures, $Y_i(E_\alpha, E_n)$, can be described by the following relationship:

$$Y_i(E_\alpha, E_n) = \int_0^R n_i \sigma_i(E_\alpha, E_n)\,\mathrm{d}x, \tag{6.3.2}$$

where n_i is the number density of isotope i, $\sigma_i(E_\alpha, E_n)$ is the capture cross-section and R is the range of the alpha particle. Here we assume a thick target where the alpha particle is captured in the same material in which it was produced.

This equation can be converted into an integral over alpha energy via change of variables giving:

$$\begin{aligned} Y_i(E_\alpha, E_n) &= \int_0^{E_\alpha} \frac{n_i \sigma_i(E'_\alpha, E_n)}{-\frac{\mathrm{d}E'_\alpha}{\mathrm{d}x}} \mathrm{d}E'_\alpha \\ &= \frac{n_i}{\rho} \int_0^{E_\alpha} \frac{\sigma_i(E'_\alpha, E_n)}{S_i^m(E'_\alpha)} \mathrm{d}E'_\alpha \\ &= \frac{N_A C_i}{A_i} \int_0^{E_\alpha} \frac{\sigma_i(E'_\alpha, E_n)}{S_i^m(E'_\alpha)} \mathrm{d}E'_\alpha, \end{aligned} \tag{6.3.3}$$

where E_α is the incident alpha energy, $S_i^m(E)$ is the mass stopping power of isotope i, A_i is the mass number of isotope i, C_i is the mass fraction of isotope i in the material and N_A is Avogadro's number [313].

The total yield of neutrons of energy E_n is given by:

$$Y(E_\alpha, E_n) = \sum_i Y_i(E_\alpha, E_n), \tag{6.3.4}$$

obtained by summing over each target isotope present in the material.

Now considering a decay chain producing several alpha particles, we define P_α to be the probability of an alpha decay occurring in the decay chain, based on the branching ratio for the parent isotope and the branching ratio for decay with alpha energy E_α. The total yield of neutrons of energy E_n is then given by:

$$Y(E_n) = \sum_\alpha P_\alpha Y(E_\alpha, E_n). \tag{6.3.5}$$

Thick-target gamma yields, $Y_i(E_\alpha, E_\gamma)$, can be described by an equivalent equation to that shown in Equation 6.3.3, by replacing the capture cross-section $\sigma_i(E_\alpha, E_n)$ with $\sigma_i(E_\alpha, E_\gamma)$. Extensions of this simplified yield in a target consisting of one homogenous single element material can be applied to materials with a more complex elemental and isotopic composition [356].

6.3.3 Experimental measurements

Accurate estimates of (α,n) neutron production rates, energy spectra and correlated gamma cascades are fundamental to understanding backgrounds for future rare-event searches, such as with dark matter and neutrino experiments [357, 358]. The production of radiogenic neutrons due to trace radioactive impurities in detector materials results in strict radiopurity requirements, often informed by modelling (α,n) yields. The ability to accurately model these reactions is key to multiple scientific communities in addition to low-background experiments, including nuclear physics, nuclear astrophysics and nuclear energy applications.

Measurements of (α,n) and (α,γ) yields have been performed experimentally by many researchers utilising alpha beam facilities from the era of emerging nuclear physics during the mid-20th century and into modern day. Beams are often configurable in energy and produce alpha particles of energies up to around 10 MeV to model the highest energy alphas produced in the primordial decay chains. Targets of light elements and composite materials are sufficiently thick to completely stop the highest energy alpha particle within the material. The emitted neutrons and gamma-rays may then be detected by particle detectors, such as ^{3}He proportional neutron counters and HPGe gamma spectroscopy detectors, respectively. Examples of such experiments may be found in Ref. [313, 359–363]. An extensive compilation of experimental nuclear reaction data is provided by the EXFOR library [364, 365].

Due to data limitations, there is a pressing need for new experimental measurements within the community. These updated measurements aim to resolve conflicts in current data (often deviate by $\mathcal{O}(10\%)$ or more), enhance precision, and provide results for relevant materials and isotopes used in rare-event searches [357]. For example, recent high-precision cross-section measurements of ^{13}C(α,n)^{16}O have benefitted backgrounds studies for neutrino oscillation experiments and stellar nucleosynthesis, and exposed differences between previous measurements and evaluations [366]. A list of high-priority isotopes is currently under development, with plans for measurements of (α,n) cross-sections on these targets.

6.3.4 Codes and nuclear data libraries

Codes that exist for calculating neutron yields and energy spectra include NeuCBOT [367, 368], NEDIS [369], SaG4n [370, 371], SOURCES [324, 372] and the USD calculator [314]. These codes perform the yield calculations as outlined in Section 6.3.2. They combine stopping power calculations from SRIM [373] or the ICRU 49 report [374] with (α,n) cross-sections from measurement or theoretical nuclear model codes such as EMPIRE [375] or TALYS [376, 377]. For many isotopes, significant difference exists between measurements, evaluated cross-section libraries, and calculations performed by these codes [248, 378, 379]. Figure 6.3.1 shows a recent comparison of yields on light nuclei with different software codes [368]. The data points are normalised in order to compare theoretical calculations with experimental results.

The main evaluated nuclear data libraries in the world include BROND (Russia) [380], CENDL (China) [381], ENDF/B (USA) [342], JEFF (Nuclear Energy Agency) [382], JENDL (Japan) [383] and TENDL (Europe) [384]. Routine adoption of data or of complete files between different nuclear data projects is common, and can be described as indirectly collaborative. The Collaborative International Evaluated Library Organization (CIELO) pilot project aims to facilitate active collaboration between the agencies that maintain these nuclear data libraries [385].

These libraries are integrated into GEANT4 via the G4ParticleHP package [386], to simulate non-elastic nuclear interactions of incident neutrons, protons, deuterons, tritium, ^{3}He and α particles with kinetic energies up to 200 MeV (up to 20 MeV for neutrons [387]), and elastic scattering of incident neutrons. Valida-

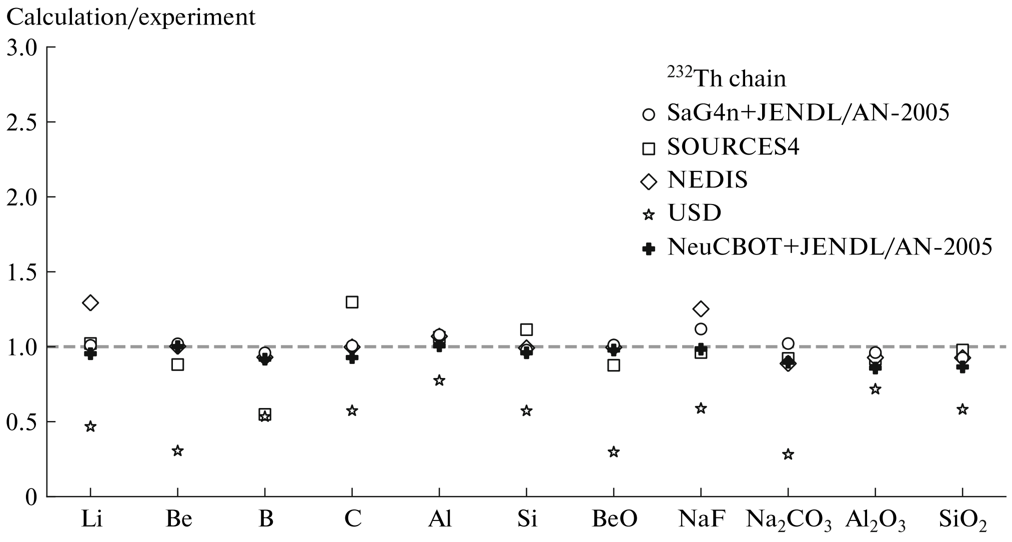

Figure 6.3.1: Comparison of neutron yields for light nuclei with different software codes. The calculated values are normalised to experimental results to assess the level of agreement between theory and measurements. Here, alphas produced by the ^{232}Th chain are considered. Figure taken from Ref. [368].

tions for (α,n) reactions in GEANT4 between the JENDL/AN-2005 library [388] and versions of the TENDL libraries are reported in Ref. [370].

6.3.5 Spectra of neutrons from rock

The spectra and yield of neutrons from (α,n) captures may be calculated with the NeuCBOT (Neutron Calculator Based On TALYS) code (version 2.0), which is publicly available and can be cloned from the NeuCBOT GitHub repository [389]. The advantages of this code include fast calculation speeds, flexibility, minimal dependencies and ease-of-use. NeuCBOT utilises the TALYS-1.95 nuclear reaction database, stopping powers from SRIM, natural isotopic abundances from Ref. [390] and nuclear decay information from NuDat [391] to perform calculations.

The user provides a material data file containing the abundances of elements contained within the target, alongside either an alpha energy data file or a decay chain data file. The ^{232}Th and ^{238}U files are provided by default within the code. NeuCBOT assumes a homogenous material composition and does not allow for more complex material structures or geometries that contain layers of different

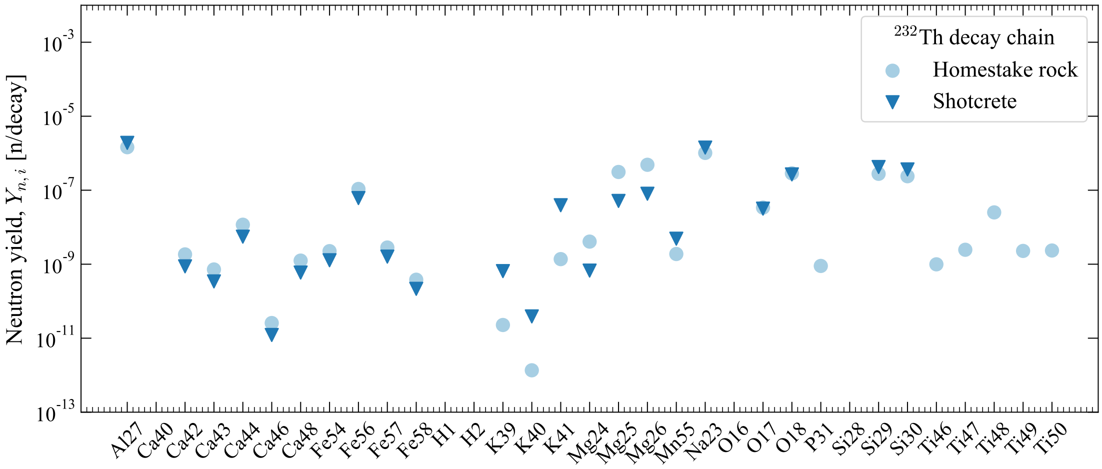

Figure 6.3.2: The individual neutron yields $Y_{n,i}$ for isotopes present in Homestake rock (light blue circles) and shotcrete (dark blue triangles) for the ^{232}Th decay chain. There is no contribution to the yield from ^{40}Ca, H isotopes, ^{16}O and ^{28}Si.

materials. The output file contains the total neutron yield resulting from the calculation outlined in Section 6.3.2 along with the yield resulting from capture on specific isotopes. The contribution from each isotope present in the material is also given. The neutron energy spectrum is binned into 100 keV bins and the total integral of the spectrum is printed to be compared with the total yield with differences typically on the order of $\sim 1\%$.

NeuCBOT was used to compare neutron yields for Homestake rock and shotcrete. The material definitions were taken from Table 6.2.1 and natural isotopic abundance is assumed for all species. The contributions to the neutron yield for each isotope are compared for the thorium chain in Figure 6.3.2. Significant yield contributions arise from capture on ^{27}Al and ^{23}Na. Note that there is no contribution to the neutron yield from ^{16}O, ^{28}Si or ^{40}Ca. This is because the most energetic alpha particle (8.8 MeV from the thorium chain) cannot overcome the energy threshold for (α,n) production for these isotopes [125].

The neutron energy spectra produced are shown in Figure 6.3.3. The contributions from the early and late chains of ^{238}U have been summed together to account for the total yield from the ^{238}U chain, under the assumption that the chain is in

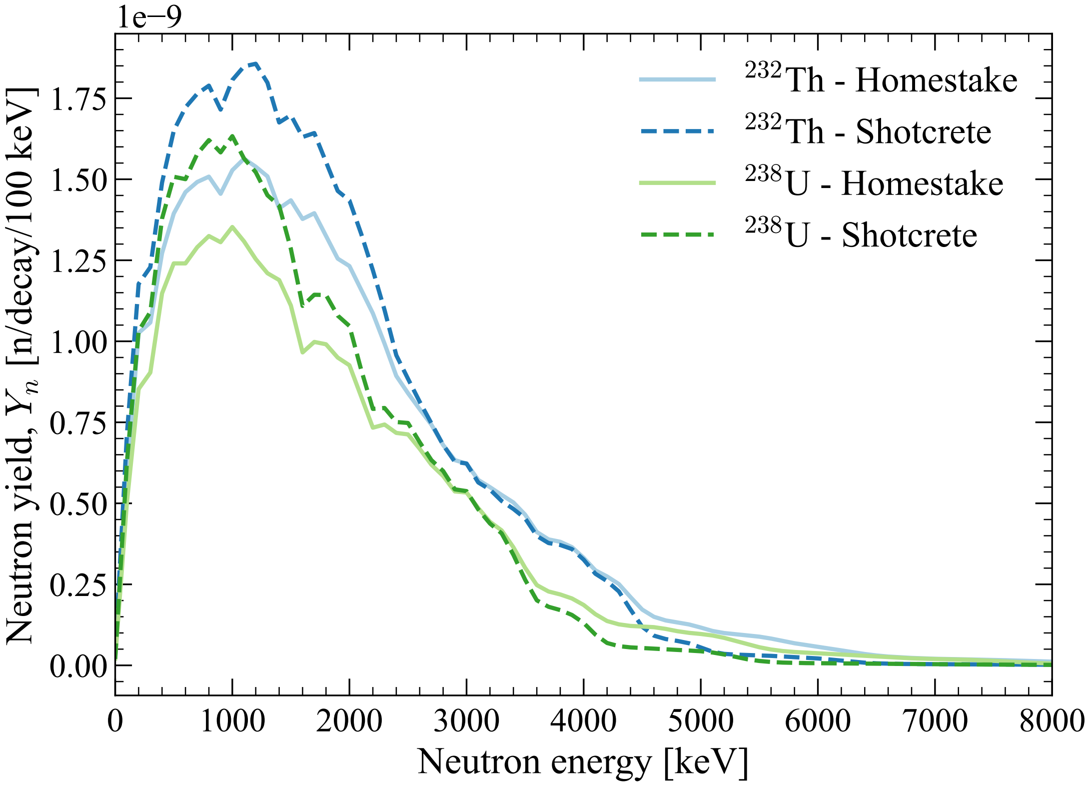

Figure 6.3.3: Spectra of neutrons from the cavern rock models due to (α,n) reactions from ^{232}Th and ^{238}U chains, produced by the NeuCBOT code [367]. The yields for the Homestake rock and shotcrete are shown by the solid and dashed lines, respectively.

secular equilibrium. The neutron yields (neutrons per decay) for each material are presented in Table 6.3.2, quoted for ^{232}Th and ^{238}U, with the latter split into early and late contributions. The decay chain of ^{235}U also contributes to the neutron production, but this contribution is small relative to ^{238}U due to low abundance of ^{235}U present in natural uranium (0.72%) [248].

These yield values are in agreement with those previously calculated using the SOURCES4A code when assessing the uranium and thorium neutron spectra for Homestake rock [256], which quoted $Y_{n,\mathrm{Th}} = 4.15 \times 10^{-6}$ n/decay and $Y_{n,\mathrm{U}} = 3.95 \times 10^{-6}$ n/decay for the combined contribution of ^{235}U and the early chain of ^{238}U.

These calculations do not incorporate the JENDL/AN-2005 library which is known to improve the results produced by NeuCBOT with respect to experimental

Table 6.3.2: The total neutron yield Y_n due to (α,n) reactions from ^{232}Th and ^{238}U chains, produced by the NeuCBOT code [367]. Contributions are broken down into the yields from the ^{232}Th chain, the early and late parts of the ^{238}U chain and the resulting ^{238}U total.

Material	Neutron yield, Y_n [n/decay]			
	^{232}Th	^{238}U	^{238}U$_e$	^{238}U$_l$
Homestake	4.28×10^{-6}	3.38×10^{-6}	7.01×10^{-7}	2.68×10^{-6}
Shotcrete	4.66×10^{-6}	3.64×10^{-6}	7.38×10^{-7}	2.92×10^{-6}

values. The NeuCBOT code is also under beta phase development (version 3.0) to include the gamma yields and spectra produced by (α,γ) reactions with typical gamma yields on the order of 10^{-8} [368].

6.4 BACCARAT studies

6.4.1 Test geometry

A small BACCARAT test geometry can be used to assess the differences in outputs of the two rock models. A cylindrical sodium iodide volume with dimensions ⌀ 0.25 m × 0.5 m enclosed in a 0.05 cm thick aluminium case was placed at the

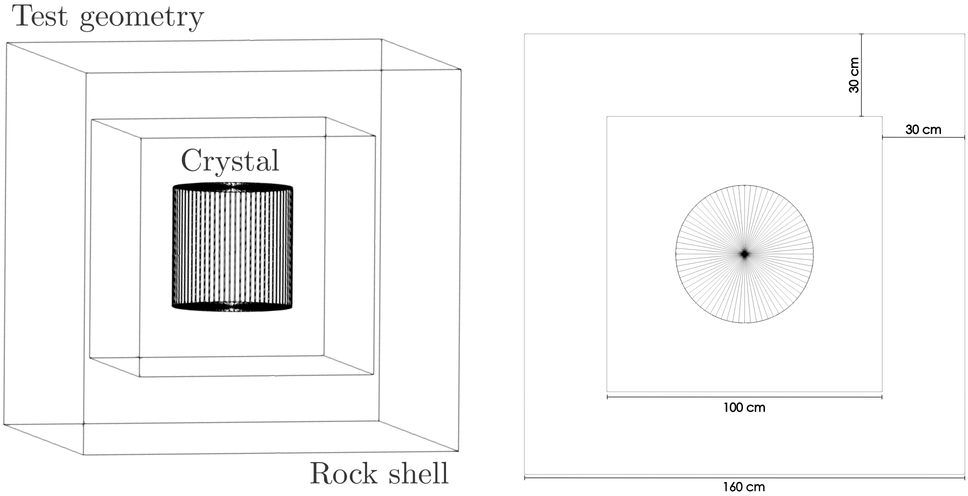

Figure 6.4.1: 3D and 2D (top-down) projections of the test rock model geometry viewed using *ParaView* [392], with key volumes and dimensions of the rock shell labelled.

centre of a small cubic rock shell volume. The shell is defined with uniform thickness of 30 cm and interior sides of length 1 m, resulting in a minimum distance of 25 cm between the edge of the crystal and the shell interior. Figure 6.4.1 shows a visualisation of the test geometry in 3D and 2D (top-down view) which was created using *ParaView* [392] software which can visualise GEANT4 VRML files.

Two simulations were conducted using this geometry: one to study alpha interactions in the rock, and one to study energy depositions in the sodium iodide crystal. Each set of simulations utilised the HTCondor batch farm system available on the Oxford HEP computing cluster [393]. The studies are summarised below:

1. **Rock study:** To study primordial decays in the rock itself, 1×10^6 radioactive decays of ^{238}U and ^{232}Th were simulated and recorded in the rock volume. Each decay chain has an activity of 1 Bq kg^{-1}.
2. **Sodium iodide study:** ^{238}U, ^{232}Th and ^{40}K decays are initialised in the rock volume with an activity of 1 Bq kg^{-1}, and particle track information and energy deposits are recorded for interactions in the sodium iodide volume only. For each isotope 5×10^7 primary decays were simulated.

Radioactive decays are simulated using GEANT4 data libraries from the Evaluated Nuclear Structure Data File (ENSDF) [394] and the Livermore Evaluated Atomic Data Library (EADL) [274] which describe nuclear decays and any subsequent atomic transitions, respectively.

^{238}U, ^{232}Th and ^{40}K decays are initiated within the 30 cm thick shell modelling the cavern environment. For the ^{238}U and ^{232}Th chains, the G4Decay event generator developed for use in LZ background simulations was used [256]. For each simulated event, this generator initiates decays with parent particles ^{238}U or ^{232}Th and ending at the respective stable Pb isotope. Therefore, α, β and γ-decays for the decay chain are generated with correct energies and branching ratios. Secular equilibrium is assumed for both decay chains, since any break in equilibrium is not expected to affect this analysis and the four prominent high-energy gamma lines are products of the late sub-chains.

6.4.2 ^{238}U and ^{232}Th decays in the rock

Assuming secular equilibrium, radioactive decays from ^{232}Th and ^{238}U produce 6 and 8 α particles, respectively. These α particles are highly energetic, and typically have energy on the order of a few MeV. The highest energy alpha in the ^{232}Th chain is $E_\alpha = 8785\,\text{keV}$ for ^{212}Po; for the ^{238}U chain the maximum energy is $E_\alpha = 7687\,\text{keV}$ for ^{214}Po [249, 355].

Analysis of the Geant4 track output for Th and U decays in Homestake rock and shotcrete was conducted to assess the proportion of α-captures and neutron captures observed due to alpha decays in the rock. An example of the resulting products from alpha and neutron interactions for ^{232}Th decays in Homestake rock are shown in Figure 6.4.2 by the gold and green bar charts. The total number of particle tracks associated with each creator process are shown by the grey horizontal bar chart. For 1×10^6 events of ^{232}Th decays in Homestake rock, 308 inelastic alpha processes and 11 neutron captures resulted in 1038 and 25 decay products, respectively. The number of neutron captures are subdominant in comparison of alpha inelastic processes and all 11 neutron capture events occur in events that also contain alpha inelastic processes.

Table 6.4.1: The number of events that contain `alphaInelastic` and `nCapture` tracks for ^{232}Th and ^{238}U decay chains for both the Homestake rock and shotcrete models from 10^6 simulated primary decays.

Geant4 Process	Homestake rock		Shotcrete	
	^{232}Th	^{238}U	^{232}Th	^{238}U
`alphaInelastic`	308	268	414	327
`nCapture`	11	5	0	3

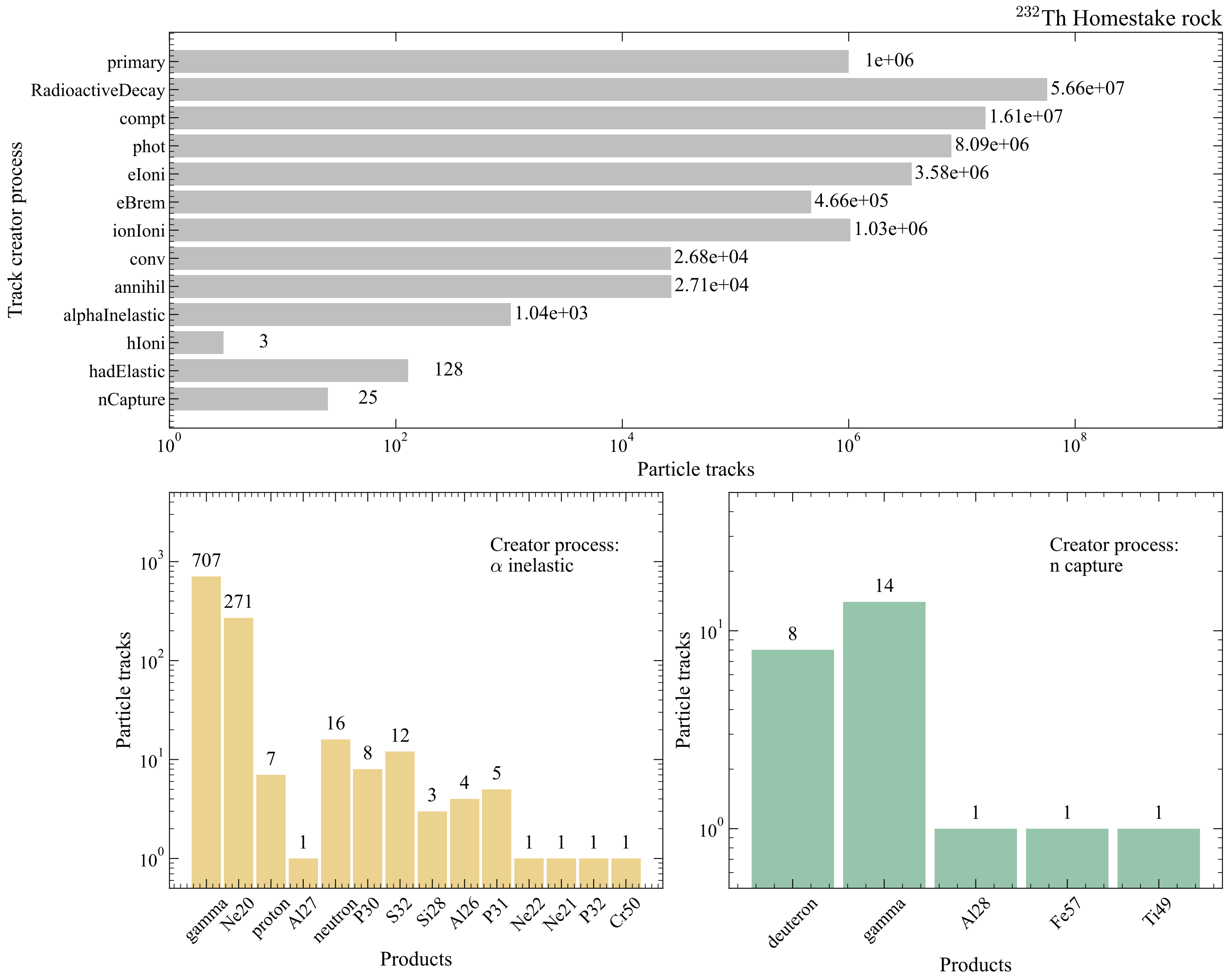

Figure 6.4.2: The number of tracks associated with GEANT4 track creator processes for ^{232}Th decays initiated in Homestake rock (grey bar chart). The products of `alphaInelastic` and `nCapture` events are shown by the gold and green bar charts, respectively.

The alpha interactions produce the final isotope in addition to a multitude of gamma particles by a gamma-ray cascade or proton and neutrons, e.g. by the reaction $\alpha + {}^{27}\text{Al} \rightarrow {}^{30}\text{P} + \text{n} + \gamma$. For this particular simulation dataset, the gold bar chart shows that ${}^{16}\text{O}(\alpha,\gamma){}^{20}\text{Ne}$ capture dominates the `alphaInelastic` processes with a total contribution approximately ×10 greater than other capture products listed. This dominant contribution from ^{20}Ne was also observed for U/Th decays in the shotcrete rock model. A summary of the number of `alphaInelastic` and `nCapture` events for ^{232}Th and ^{238}U decays in both Homestake rock and shotcrete is given in Table 6.4.1.

The intensity of the gamma-rays produced by `alphaInelastic` processes as a function of the kinetic energy of the gamma-ray are plotted in Figure 6.4.3. The majority of the gamma-rays are associated with ${}^{16}\text{O}(\alpha,\gamma){}^{20}\text{Ne}$ events, dominated by the 1633 keV γ-ray produced by the E2 transition from the first excited 2^+ to the 0^+ ground state of ^{20}Ne. Decays from higher excited nuclear states of ^{20}Ne result

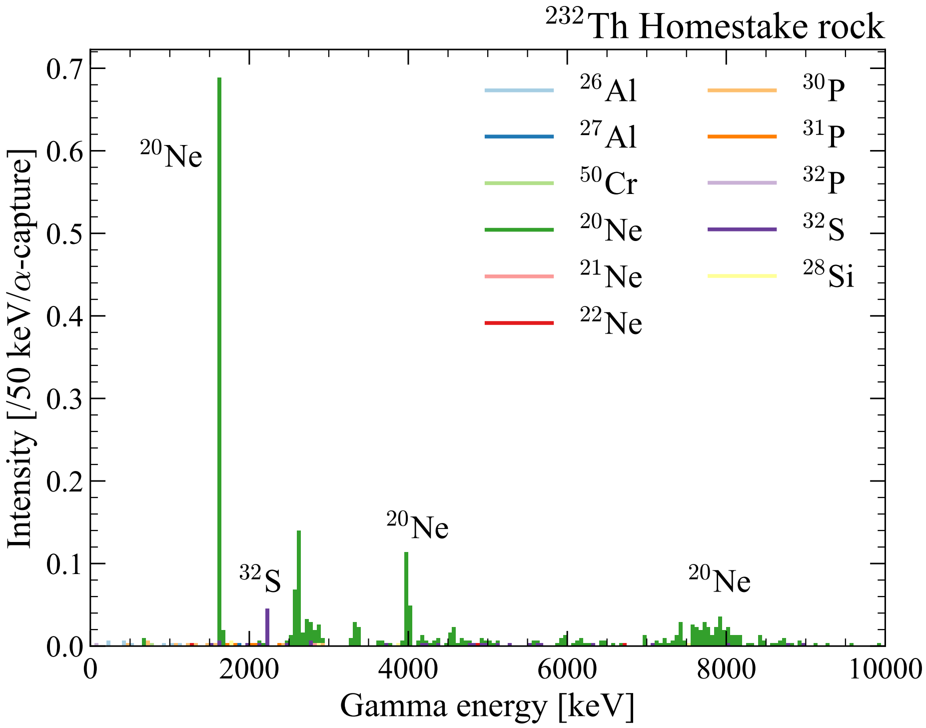

Figure 6.4.3: The γ-ray intensities for (α,γ) reactions in the Homestake rock for the ^{232}Th decay chain. The final products from the (α,γ) reactions are listed in the legend.

in populations of γ-rays at energies of 2613 keV, 3987 keV and 7831 keV [395]. The next prominent contribution is the 2230 keV gamma from the decay of ^{32}S produced by ^{28}Si(α,γ)^{32}S captures [396].

An increase in the proportion of `alphaInelastic` events was first reported when the BACCARAT simulation code upgraded from GEANT4 version 9.5.p02 to version 10.03.p02 [397]. This effect has yet to be fully explored and accounted for within the LZ simulations framework as it had minimal impact on background simulations for the main WIMP search. As the exposure of the LZ experiment increases, refinements to the accuracy of the BACCARAT simulation framework at energies above 2.6 MeV are becoming high priority tasks, with modelling sensitivity to high-ER physics in mind.

6.4.3 Cavern background recorded in sodium iodide

Products from the radioactive decays of ^{40}K, ^{232}Th and ^{238}U originating from the rock that deposit energy in the sodium iodide crystal volume are recorded. The raw output from the simulation of 1 Bq kg^{-1} for the Homestake rock model is shown in Figure 6.4.4. This shows the true energy spectra produced by separately simulating the ^{238}U and ^{232}Th decays chain in addition to decays of ^{40}K. The prominent photopeaks associated with each decay are labelled with the relative energies and branching ratios; where the ^{214}Bi and ^{208}Tl photopeaks from the U and Th chains are the most prominent, respectively. High-energy gammas beyond 2.6 MeV are visible in the U/Th energy spectra, contributing low statistics in the range 4–12 MeV. A coarse binning of 40 keV was chosen to highlight any populations present in the high-energy range. The inset included for the U/Th plots shows finer binning with counts per 10 keV in the energy range 3.5–11.5 MeV. No high-energy contribution is expected from ^{40}K.

The true energy spectra simulated for each material are shown in Figure 6.4.5. The relative activities of ^{238}U, ^{232}Th and ^{40}K have been scaled according to

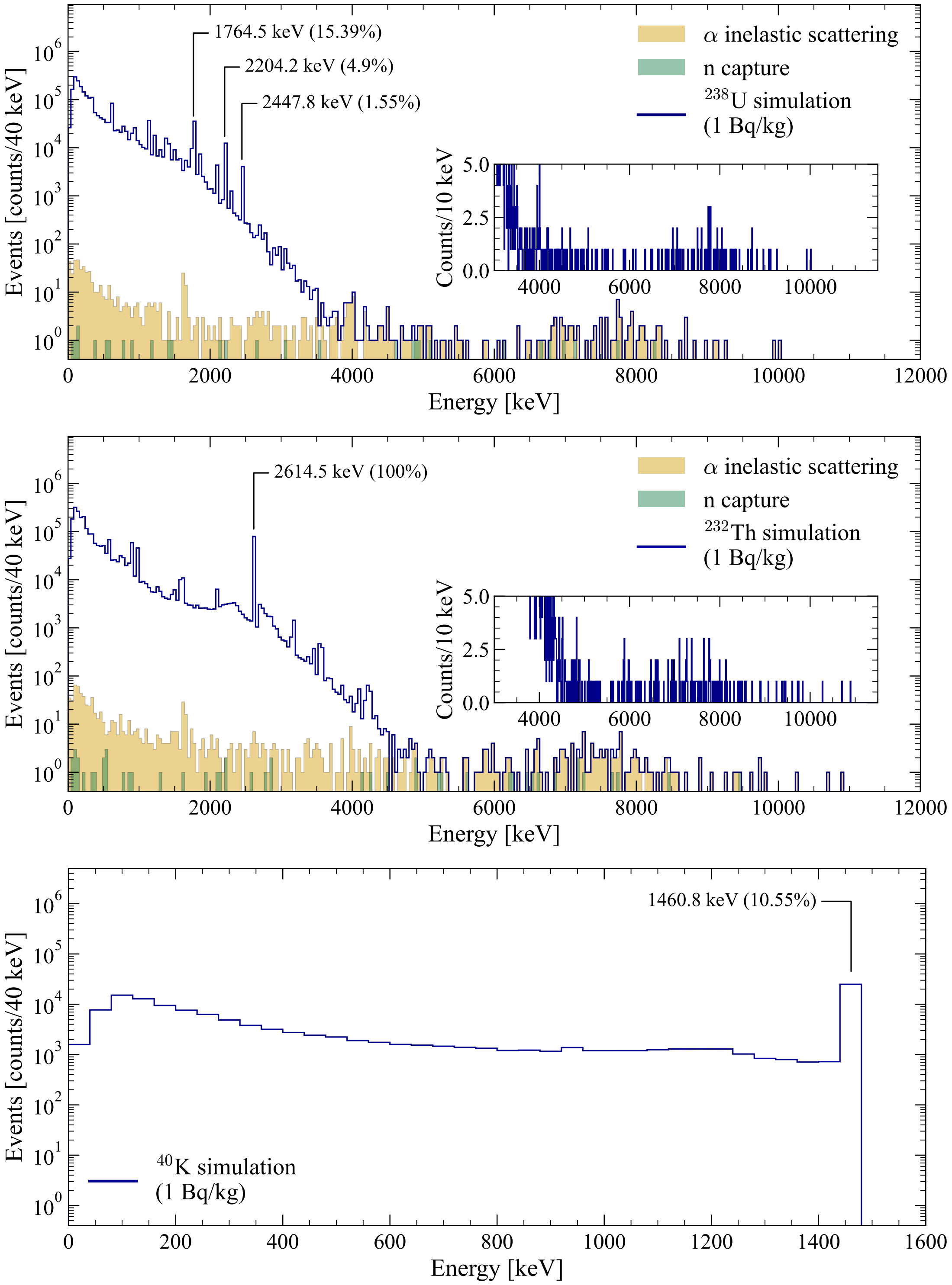

Figure 6.4.4: The simulated true energy spectra for ^{238}U, ^{232}Th and ^{40}K decays originating from the test Homestake rock volume recorded in the NaI crystal. Prominent photopeaks are labelled with the respective gamma-ray energy and branching ratios. ^{238}U and ^{232}Th are plotted in the energy range 0–12 MeV, whereas ^{40}K is shown up to 1.6 MeV.

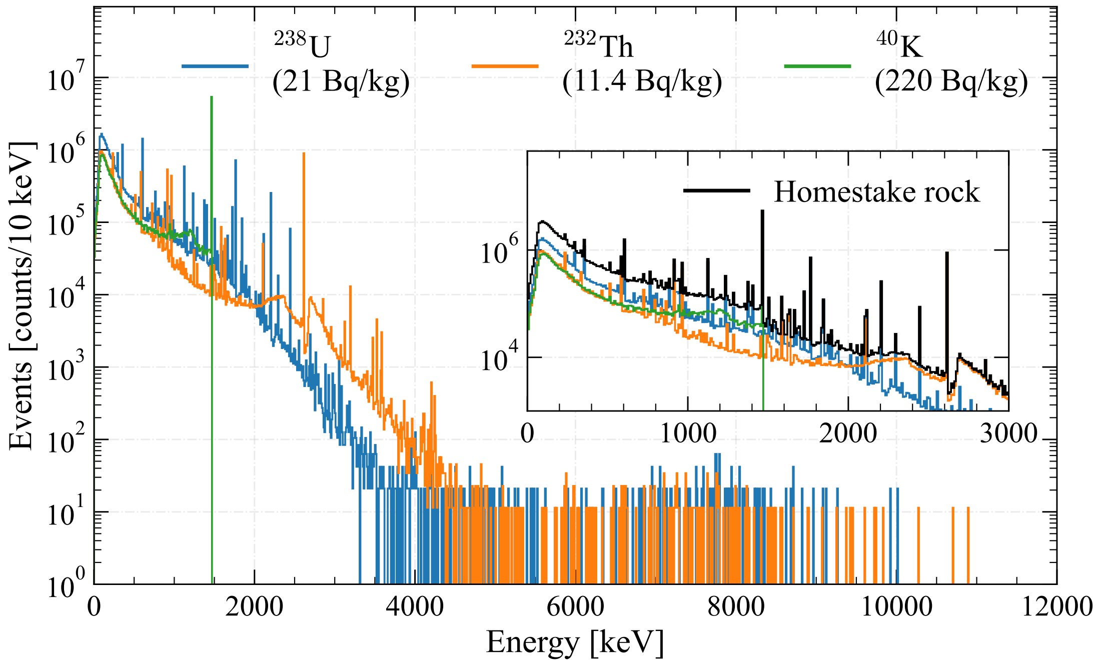

(a) Homestake rock model.

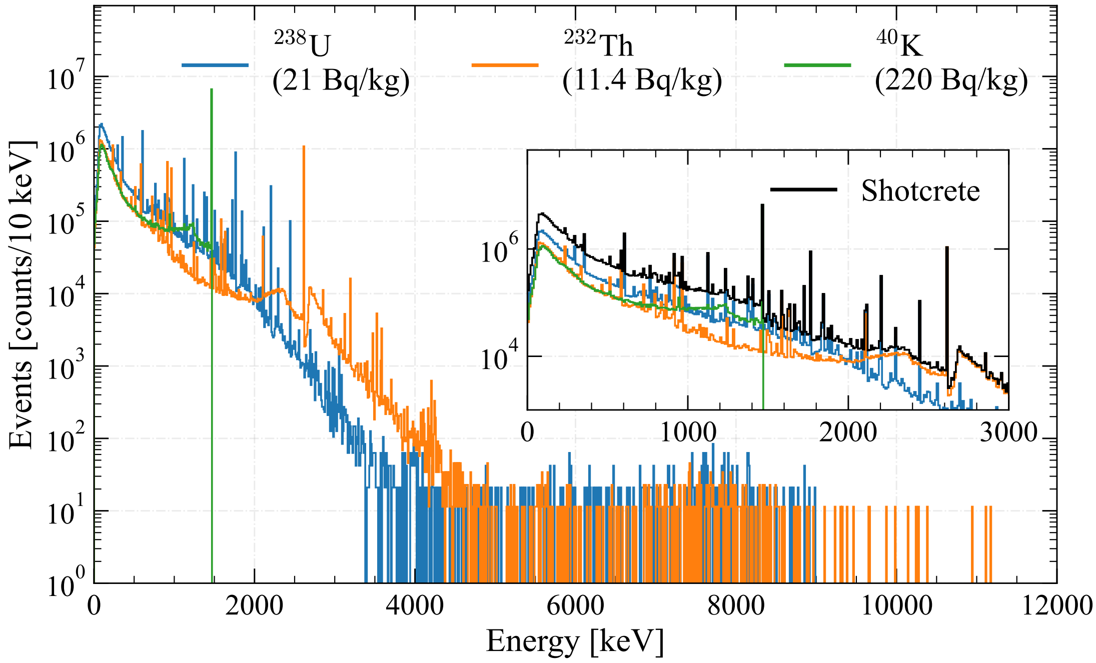

(b) Shotcrete model.

Figure 6.4.5: The simulated true energy spectra recorded in a generic sodium iodide volume from ^{238}U (blue), ^{232}Th (orange) and ^{40}K (green) decays from a surrounding rock volume. The two rock materials considered are: Homestake rock (a) and shotcrete (b). The overall energy range of 0–12 MeV is shown, with the inset focussing on the energy range 0–3 MeV where the solid black line shows the combined total model.

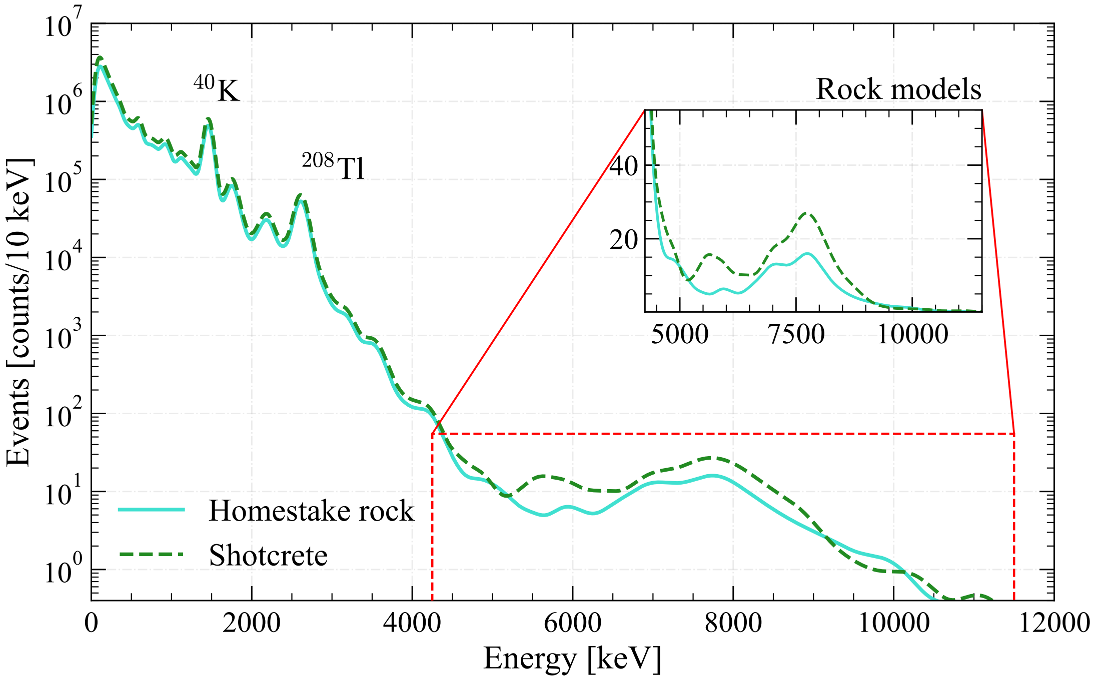

Figure 6.4.6: Simulated spectra of energy deposits in the sodium iodide from γ-rays produced by Homestake rock and shotcrete materials. The Homestake rock model is shown by the solid turquoise line and shotcrete model is shown by the dashed green line. The energy resolution model described in Equation 4.4.1 has been applied to the true energy spectra.

shotcrete assay values given in Table 3.2.1. Note that the binning has been refined from 40 keV to 10 keV width bins. The combined total spectrum shown via the black solid line is then smeared using the energy resolution model derived for the sodium iodide detector in Section 4.3.4 to account for limited energy resolution. The resultant energy spectra for Homestake rock and shotcrete models are presented in Figure 6.4.6.

A two-sample Kolmogorov-Smirnov (KS) test may be used to assess the underlying continuous distributions of the two rock models given a specific energy range [398]. The KS test statistic is defined as:

$$D_{n,m} = \sup_x |(F_{1,n}(x) - F_{2,m}(x)|, \tag{6.4.1}$$

where $F_{1,n}$ and $F_{2,m}$ are the empirical cumulative distribution functions (CDF) and sup is the supremum function and n and m are the sample sizes of each distribution, respectively. Therefore, $D_{n,m}$ is the maximum absolute difference between the CDFs and is bound to values in the range [0,1].

A CL of 95% is chosen, so that the null hypothesis is rejected for p–values below a threshold of 0.05. Performing the two-sample KS test in the range 0–5 MeV results in a reported p–value of 0.29. Therefore, the null hypothesis cannot be rejected and the two models are assumed to be consistent within this energy range. From Figure 6.4.6 it is evident that the two models begin to deviate beyond 5 MeV, where the high-energy gammas contribute from inelastic alpha processes. However, it is important to note that statistics in this high-energy range are limited in comparison to the primary gamma background and that some bins that originally contain one or two counts are now multiplied by the scaling factors applied ($\sim$ 10–20×).

6.5 Simulations of the Davis cavern

6.5.1 Construction of the Davis cavern geometry

A custom geometry of the Davis cavern, shown in Figure 6.5.1, was built featuring the following components:

- **Water tank:** The water tank is modelled as two concentric cylinders; one cylinder of water with dimensions ⌀ 7.62 m × 5.97 m, enclosed within a steel tank with thickness of 4.76 mm. The LZ detector is not included in these simulations.

- **Steel pyramid and steel plate:** The inverted steel pyramid is constructed of six octagonal plates of steel with thickness 5.08 cm located directly underneath the water tank. The pyramid is placed inside the cavern rock volume to model the gravel layer that surrounds the pyramid. A square 3-inch thick steel plate with dimensions 9 ’ × 9 ’ sits approximately 60 cm above the centre of the top of the water tank to provide additional shielding.

- **Cavern rock:** A 30 cm thick rock shell is simulated to model the internal cavern wall. Radioactive decays are generated in the shell volume and this is sufficient to produce 96% of the gamma flux without accounting for the underlying rock [399]. The inner dimensions of the rock in the simulation are 20 m × 14 m × 12 m and were chosen so that the surface area of the rock face is similar to that in reality, as the faces of the cavern walls are known to be uneven. The rock shell extends into a much larger volume of cavern rock, which is 5 m thick on both sides and bottom and 7 m thick on top. The outer dimensions of the cavern are 30 m × 24 m × 24 m.

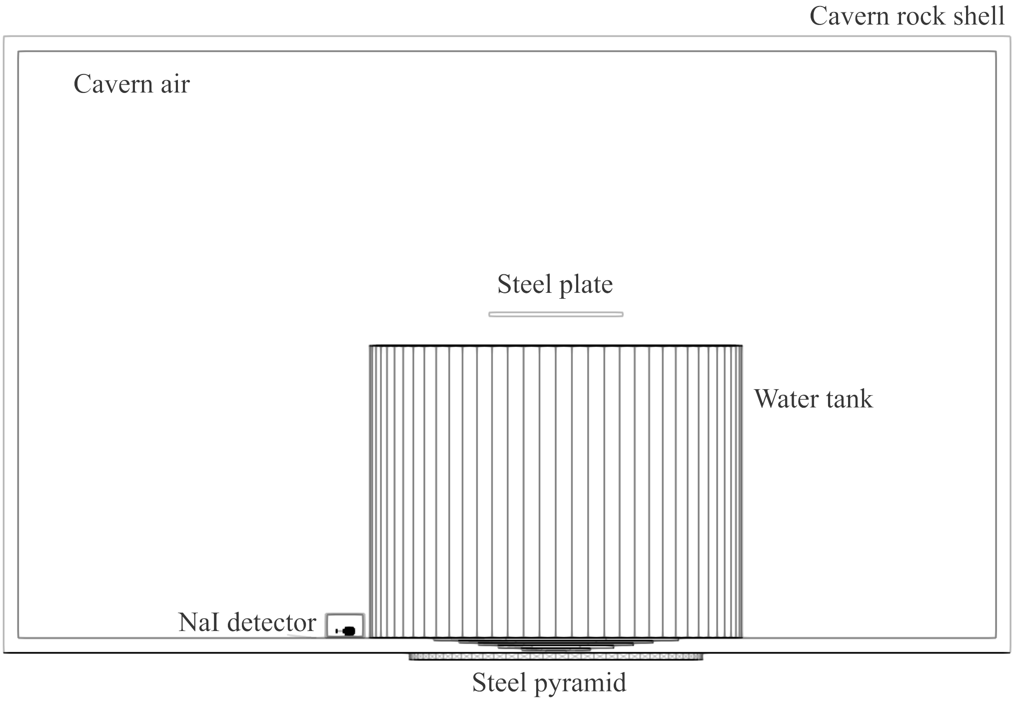

Figure 6.5.1: A 2D projection of the Baccarat geometry used to define the Davis cavern viewed using *ParaView* [392], with key volumes labelled.

Table 6.5.1: The number of expected decays in a one-year exposure for ^{40}K, ^{232}Th and ^{238}U using previously measured activity values, taken from Ref. [262].

Isotope	Activity, A [Bq kg^{-1}]	Decays in one year
^{40}K	220 ± 60	7.99×10^{15}
^{238}U	29 ± 15	1.05×10^{15}
^{232}Th	13 ± 3	4.72×10^{14}

6.5.2 CPU requirements

Before considering the production of Monte Carlo simulations that accurately model the gamma background from the cavern walls, it is prudent to assess the computing requirements needed. We must consider the number of primary particles to simulate in order to obtain events that deposit energy in the NaI crystal volume. The number of gammas originating from the rock surface for an isotope i is:

$$N_{\gamma,i} = N_{\gamma}^{\text{chain}} \times M \text{ [kg]} \times A_i \text{ [Bq kg}^{-1}\text{]}, \tag{6.5.1}$$

where A_i is the activity of isotope i in the rock, M is the mass of the rock volume from which the gammas are generated and $N_{\gamma}^{\text{chain}}$ is the number of γ-rays emitted per decay chain.

By considering the activity of U/Th/K decays reported by the previous studies mentioned previously in Section 3.4, and taking the mass of the rock volume to be $\sim 1.15 \times 10^6$ kg the number of decays for each isotope corresponding to one year of live time can be calculated. The measured activities and corresponding number of days for a one-year exposure are shown in Table 6.5.1. From these estimates, the number of initial events needed to simulate the equivalent of one year of exposure is on the order of $\mathcal{O}(10^{15})$.

Additionally, simulation tests performed with the full cavern geometry by initiating 10^7 events of each radioisotope uniformly distributed in the 30 cm rock shell results in an observed survival fraction of $\sim 2.5 \times 10^{-5}$ events that deposit energy in the NaI crystal volume. This is a result of gamma attenuation by transportation through additional volumes of shielding including the air in the cavern space, the water tank, the Pelican case housing and the rock shell volume itself coupled with a small target volume with respect to the cavern dimensions.

6.5.3 Future simulation efforts

From these estimates and tests it is evident that simulating $\mathcal{O}(10^{15})$ initial events and recording events that interact within the crystal volume with high-statistics is unfeasible with basic brute force simulation methods. This is due to the high computational expense of transporting the gamma-rays from the rock through the cavern geometry to the target volume. A solution to this problem is to divide the simulation into several stages. At each stage, the gammas can be propagated through a section of the geometry and those surviving can be saved and "boosted", i.e. re-propagated several times during the next stage of the simulation.

Event biasing is a technique that can be applied to aid simulation efforts [273]. A custom generator was developed for LZ background simulations of the Davis cavern due to the low probability of γ-rays surviving through the steel pyramid, the OD which contains water and liquid scintillator volumes, and skin layer of liquid xenon reaching the TPC [253, 256, 273]. This simulation technique can be tuned to our purposes of recording cavern gamma events in the NaI detector.

In the first stage, gammas are produced from the cavern rock by generating radioactive decays using BACCARAT macro commands, with the source generator, volume and activity set by the user. The gammas from these decays are simulated and transported through the cavern geometry and any that reach the surface of a cylinder defined enclosing the target detector are saved to a file.

In subsequent stages, the gamma-rays are re-propagated numerous times with the same initial position and momentum and are transported to the next shell

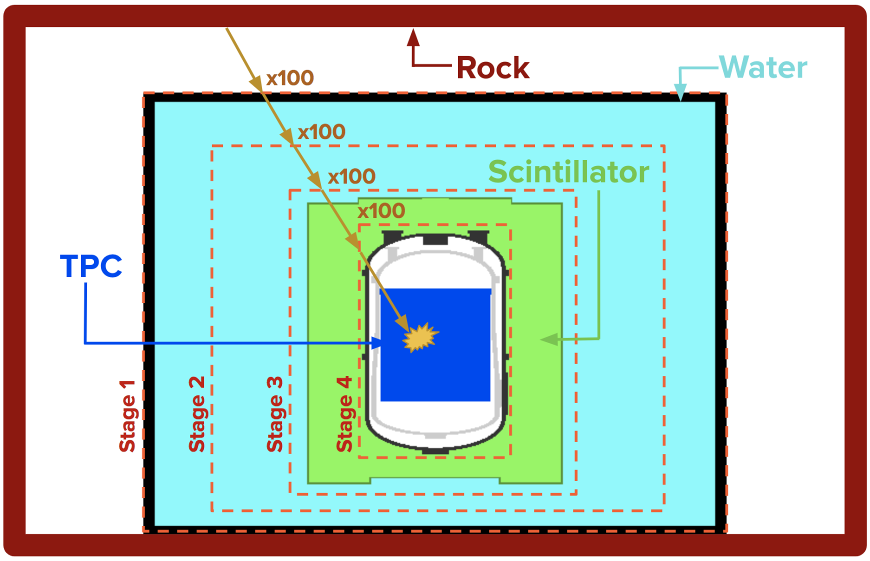

Figure 6.5.2: A schematic drawing of the event biasing method implemented into BACCARAT allowing the simulations of the cavern rock gamma-rays. The relative dimensions of the cavern, water tank, liquid scintillator veto and TPC are not to scale. Figure taken from Ref. [273].

boundary, with the surviving gammas undergoing re-propagation at the next stage. These boundaries are concentric cylindrical shells which are defined by the user at run-time. The boundaries defined for previous simulations of the cavern background in LZ are shown in Figure 6.5.2. This re-propagation method increases the initial number of decays by a total boosting factor:

$$f = \prod_{i=1}^{n} m_i, \tag{6.5.2}$$

where n is the number of stage boundaries and m_i is the stage multiplication factor [273].

Boundary surfaces are defined by implementing a parallel world in GEANT4 used to create artificial volumes. This is necessary due to the fact that physical volumes cannot overlap in GEANT4 geometries - the complex structure of the LZ geometry makes it difficult to avoid overlaps with existing detector volumes. Boundary surfaces are defined as cylindrical volumes that can be placed at a user-specified (x,y,z) position with respect to the global coordinates, along with radius and length variables in cm. This is an extension of the previous implementation, where only the z position was taken as input. Here the global coordinate origin is set to be at the centre of the bottom of the water tank. Cylinders are used as many of the detector volumes outside the TPC are approximately cylindrical (e.g. water tank, cryostat vessel), but in theory the shape of the boundary could be changed depending on the simulation needs.

The positioning of the boundary volumes is non-trivial; if there is significant shielding between surfaces for a stage of the simulation, only a small fraction of gammas may survive and as a result be incorrectly biased. Additionally, the artificial volumes should be defined just outside the physical volume to maximise the number of gammas boosted. The transportation of the gamma is then stopped once it crosses into the parallel volume, saved, and passed to the next stage.

The systematic uncertainty introduced by this biasing technique dominates the overall uncertainty in the final result when propagating the surviving gammas multiple times [253, 273]. The consistency of results has been tested by running simulations several times with different positions of surfaces at each stage, with the conclusion that the results are consistent within a 20% margin.

An example of boosting boundaries that may be used to simulate the cavern background in the NaI detector is illustrating in the schematic of Figure 6.5.3. Preliminary work has been carried out using the LZ simulation framework and it has become evident that fully understanding and ensuring the validity of the cavern background simulation is a major effort.

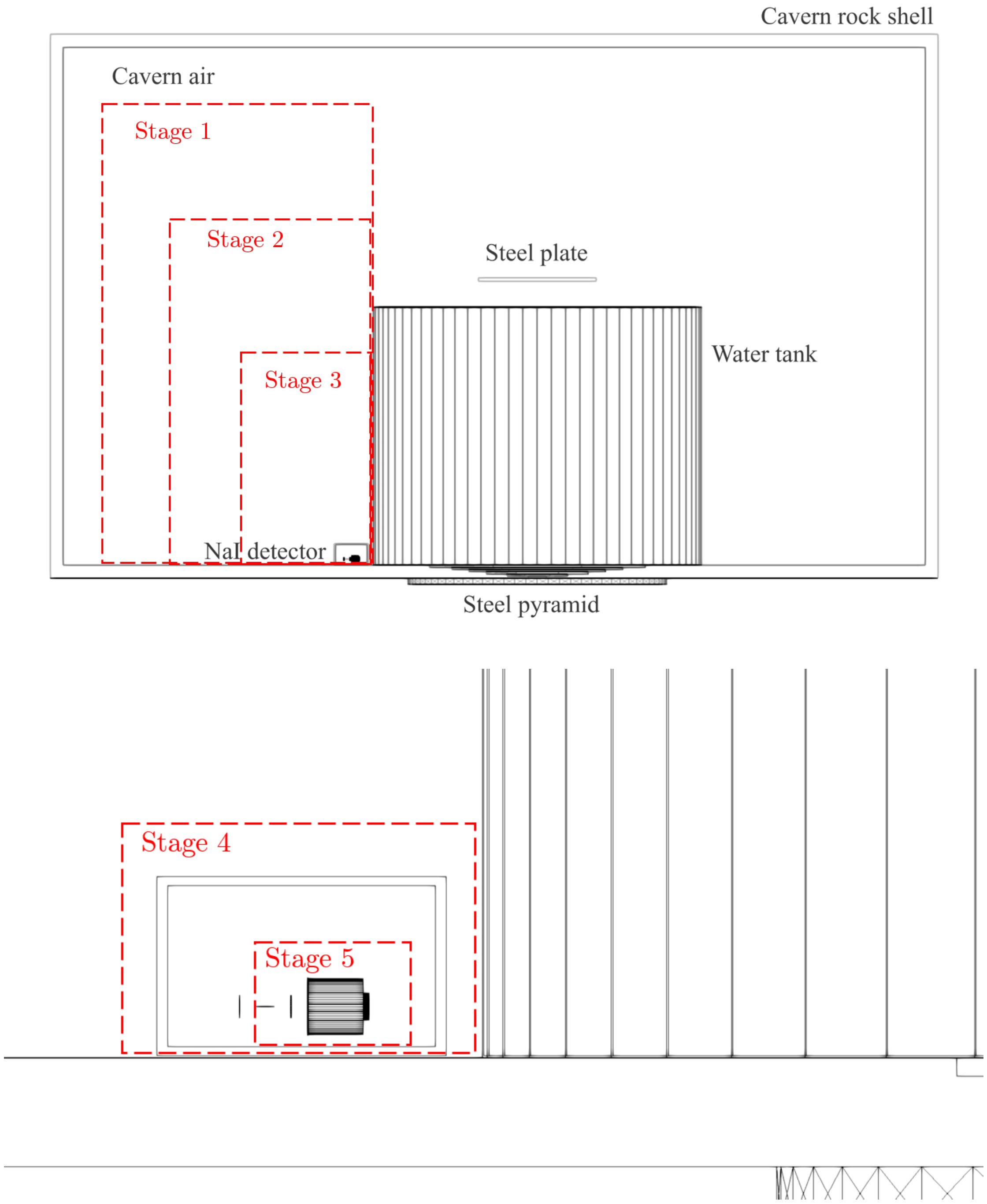

Figure 6.5.3: A schematic drawing of the potential boosting stage boundaries that would employ event biasing techniques to generate high-statistics recorded in the NaI detector. Here the five boundary volumes are represented with dashed red lines.

6.6 Conclusion

A comparison of cavern backgrounds considering two prominent materials present in the Davis cavern, Homestake rock and shotcrete, is presented. Specialist neutron yield code was employed to assess the yield from (α,n) reactions. A test geometry was constructed in BACCARAT to simulate radioactive decay chains inside rock volumes. The products of these decays were recorded in a NaI crystal volume.

The NeuCBOT code was used to calculate neutron yields from (α,n) reactions due to the series of α decays resulting from ^{232}Th and ^{238}U. The neutron yields are calculated considering the stopping power and (α,n) cross-sections for each α in the decay chain for isotopes within a material. The most significant contributions to the yields from both Homestake rock and shotcrete were from (α,n) interactions with ^{27}Al and ^{23}Na. The yield values for Homestake rock are in agreement with those previously calculated using the SOURCES4A code [256], which quoted $Y_{n,\mathrm{Th}} = 4.15 \times 10^{-6}$ n/decay and $Y_{n,\mathrm{U}} = 3.95 \times 10^{-6}$ n/decay for the combined contribution of ^{235}U and the early chain of ^{238}U. The highest overall yields were attributed to the shotcrete material, with yields for ^{232}Th and ^{238}U equal to $Y_{n,\mathrm{Th}} = 4.66 \times 10^{-6}$ n/decay and $Y_{n,\mathrm{U}} = 3.64 \times 10^{-6}$ n/decay, respectively.

Accurate simulations of high-energy ER backgrounds are increasingly important for LZ to aid physics searches such as for $0\nu\beta\beta$ of ^{136}Xe. The LZ simulation framework BACCARAT was updated to include material definitions of shotcrete material that coats the cavern walls based on analysis of samples. A test geometry was constructed in BACCARAT, comprising a cubic rock shell of thickness 30 cm with a generic NaI detector volume located at the centre. Analysis of these simulations indicated a high rate of alpha inelastic events occurring in the rock volume, with the ^{16}O(α,γ)^{22}Ne process dominating. This contribution is assumed to be overestimated, and further work is required to validate output from BACCARAT simulations.

In order to fully encapsulate the background originating from the Davis cavern walls, high-statistics on the order of $\mathcal{O}(10^{15})$ are needed. Therefore, novel simulation techniques are required. Future work discussing event biasing techniques is briefly introduced. This work will use methods previously used for assessing the contribution of cavern backgrounds in LZ, tailored towards boosting events recorded in the NaI crystal volume. This will offer further insight into the activity of ^{40}K, ^{232}Th and ^{238}U in the Davis cavern and secondary high-energy products, utilising the long-exposure gamma spectroscopy experiment currently operating on-site at SURF.

7 Conclusions and outlook

Dark matter remains undetected by direct detection, indirect detection and collider search experimental efforts. Substantial evidence for the existence of this non-luminous substance has been presented by astrophysical studies of galaxy dynamics, lensing observations and modelling of the large scale structure of the Universe. Numerous possible dark matter candidates exist spanning many orders of magnitude, from the wave-like regime up to the macroscopic Planck scale. The search for dark matter continues with many established global efforts using a wide range of novel technologies.

The LZ experiment has reported the world-leading limit on the spin-independent WIMP–nucleon cross-section sensitivity due to excellent event discrimination and rejection, fiducialisation, low-background environment and large target exposure. With 60 days of live time collected during the first science run, $\sim 6\%$ of the total live time goal of 1000 days, cross-sections above $9.2 \times 10^{-48}\,\mathrm{cm}^2$ are rejected for a WIMP mass of $36\,\mathrm{GeV}/c^2$ at 90% confidence level. LZ has also demonstrated broad science reach extending beyond the main WIMP search, including searches for low-energy electron recoil events such as from axions and ALPs, dark photons, low-threshold Migdal and S2-only searches.

LZ has achieved this low-background environment via passive shielding provided by locating the experiment at the 4850’ level of the Sandford Underground Research Facility. Active shielding of the liquid xenon target is provided by the LZ veto detectors: the Xe skin and OD. One of the key background sources to consider for the WIMP search and other high-energy physics searches is the background produced by naturally occurring radioactive material present in the cavern environment. This thesis presents the authors' contributions towards constraining the cavern background via both measurements and simulation for the LZ experiment.

Measurements from a long-exposure gamma-ray spectroscopy campaign conducted and led by the author in the lower Davis cavern are reported in Chapter 4. A ⌀ 6-inch × 6-inch NaI detector has been collecting measurements of the cavern gamma-ray background from February 2023. Calibrations using gamma-ray sources allowed for the characterisation of the detector energy response, resolution and efficiency. A total of six measurements of the ambient cavern background were analysed, amounting to a total live time of roughly 327 days. This long-exposure allows for excellent reconstruction of the NORM background contribution from ^{40}K and the ^{238}U and ^{232}Th decay chains in the surrounding cavern rock.

Additionally, this campaign also provided the first *in situ* observation of high-energy gamma-rays above 2.6 MeV which can be produced by (α,γ) and (n,γ) captures on light nuclei present in the rock. Peak structures in the reconstructed energy spectrum suggest recording of neutron capture on ^{16}O and ^{28}Si, which produced prominent gamma-rays at energies of 4.1 MeV and 4.6 MeV. The total integrate rate of events above 3.5 MeV for the combination of the six measurements is $(3.79 \pm 1.76) \times 10^{-5}$ Hz. Chapter 5 shows analysis of the high-energy (n,γ) background produced by DD neutron capture on the stainless steel water tank and surrounding cavern rock. The high rates of background were recorded during the H-reflector configuration, where a continuum spectrum out to 10 MeV was observed.

These measurements preface the integration of the NaI detector into a long-term environmental monitoring station, the LZ EMS. The authors' contribution to demonstrating the stable operation of a new long-exposure gamma-ray spectroscopy campaign on-site at SURF constitute a major success of this thesis. Similar environmental monitoring stations could be integrated into slow-control systems of future rare search experiments, such as XLZD, as quantifying environmental backgrounds will be vital. Measurements of the rate of gamma-ray, neutron and radon backgrounds will be taken into consideration when selecting potential locations for G3 experiments.

Simulation were utilised to compare background originating from the Homestake rock and shotcrete materials in Chapter 6. Using a neutron yield code, the dominant contribution to the (α,n) background was from decays of ^{232}Th in the shotcrete material. A test geometry was constructed in the LZ GEANT4 simulation framework BACCARAT to model the cavern gamma-ray background to confirm the detector response in simulation. A novel biasing technique is introduced in order to aid future high-statistics simulations modelling the full cavern geometry.

Future third generation direct detection experiments will push the sensitivity of established dual-phase TPC technologies down to the neutrino floor with multi-tonne target masses. The XLZD consortium is the combined effort of the XENON, LZ and DARWIN Collaborations to construct a G3 xenon observatory, utilising the knowledge and R&D successes from each individual experiment. The scale of this detector will offer sensitivity to multiple physics channels including dark matter searches, competitive neutrinoless double-beta decay sensitivity and neutrino physics studies. XLZD will have the capability to advance the study of fundamental science on a variety of fronts, namely particle physics, astrophysics and nuclear physics.

Bibliography

[1] J. C. Kapteyn and P. J. van Rhijn, “On the Distribution of the Stars in Space Especially in the High Galactic Latitudes”, The Astrophysical Journal **52**, 23 (1920).

[2] J. H. Jeans, “The Motions of Stars in a Kapteyn-Universe”, Monthly Notices of the Royal Astronomical Society **82**, 122–132 (1922).

[3] J. H. Oort, “The force exerted by the stellar system in the direction perpendicular to the galactic plane and some related problems”, Bulletin of the Astronomical Institutes of the Netherlands **6**, 249 (1932).

[4] G. Bertone and D. Hooper, “History of dark matter”, Reviews of Modern Physics **90**, 045002 (2018).

[5] F. Zwicky, “Die Rotverschiebung von extragalaktischen Nebeln”, Helv.Phys.Acta **6**, 110–127 (1933).

[6] E. Hubble and M. L. Humason, “The Velocity-Distance Relation among Extra-Galactic Nebulae”, The Astrophysical Journal **74**, 43 (1931).

[7] F. Zwicky, “On the Masses of Nebulae and of Clusters of Nebulae”, The Astrophysical Journal **86**, 217 (1937).

[8] S. Smith, “The Mass of the Virgo Cluster”, The Astrophysical Journal **83**, 23 (1936).

[9] K. G. Begeman et al., “Extended rotation curves of spiral galaxies: dark haloes and modified dynamics”, Monthly Notices of the Royal Astronomical Society **249**, 523–537 (1991).

[10] V. C. Rubin and J. Ford, W. Kent, “Rotation of the Andromeda Nebula from a Spectroscopic Survey of Emission Regions”, The Astrophysical Journal **159**, 379 (1970).

[11] D. H. Rogstad and G. S. Shostak, “Gross properties of five Scd galaxies as determined from 21-centimeter observations”, The Astrophysical Journal **176**, 315 (1972).

[12] M. S. Roberts and A. H. Rots, “Comparison of rotation curves of different galaxy types”, Astronomy and Astrophysics **26**, 483–485 (1973).

[13] M. S. Roberts and R. N. Whitehurst, “The rotation curve and geometry of M31 at large galactocentric distances”, The Astrophysical Journal **201**, 327 (1975).

[14] V. C. Rubin et al., “Extended rotation curves of high-luminosity spiral galaxies. IV - Systematic dynamical properties, SA through SC”, The Astrophysical Journal **225**, L107 (1978).

[15] M. Bartelmann and P. Schneider, “Weak gravitational lensing”, Physics Report **340**, 291–472 (2001).

[16] R. Lynds and V. Petrosian, “Luminous arcs in clusters of galaxies”, The Astrophysical Journal **336**, 1 (1989).

[17] D. Clowe et al., “A Direct Empirical Proof of the Existence of Dark Matter”, The Astrophysical Journal **648**, L109–L113 (2006).

[18] V. Springel et al., “The large-scale structure of the Universe”, Nature **440**, 1137–1144 (2006).

[19] R. A. Alpher et al., “The origin of chemical elements”, Physical Review **73**, 803–804 (1948).

[20] A. Einstein, “Cosmological Considerations in the General Theory of Relativity”, Sitzungsber.Preuss.Akad.Wiss.Berlin **1917**, 142–152 (1917).

[21] A. G. Riess et al., “Observational Evidence from Supernovae for an Accelerating Universe and a Cosmological Constant”, The Astronomical Journal **116**, 1009–1038 (1998).

[22] S. Perlmutter et al., “Measurements of Ω and Λ from 42 High-Redshift Supernovae”, The Astrophysical Journal **517**, 565–586 (1999).

[23] T. M. C. Abbott et al., “First Cosmology Results using Type Ia Supernovae from the Dark Energy Survey: Constraints on Cosmological Parameters”, The Astrophysical Journal Letters **872**, L30 (2019).

[24] A. A. Penzias and R. W. Wilson, “A Measurement of Excess Antenna Temperature at 4080 Mc/s.”, The Astrophysical Journal **142**, 419 (1965).

[25] D. J. Fixsen, “The temperature of the cosmic microwave background”, The Astronomical Journal **707**, 916–920 (2009).

[26] N. Aghanim et al., “Planck 2018 results: I. Overview and the cosmological legacy of Planck”, Astronomy and Astrophysics **641**, A1 (2020).

[27] N. Aghanim et al., “Planck 2018 results: VI. Cosmological parameters”, Astronomy and Astrophysics **641**, A6 (2020).

[28] W. Hu et al., “The physics of microwave background anisotropies”, Nature **386**, 37–43 (1997).

[29] M. Schumann, “Direct detection of WIMP dark matter: concepts and status”, Journal of Physics G: Nuclear and Particle Physics **46**, 103003 (2019).

[30] R. L. Workman et al., “Review of Particle Physics”, Progress of Theoretical and Experimental Physics **2022**, 1–878 (2022).

[31] D. H. Jones et al., “The 6dF Galaxy Survey: Final redshift release (DR3) and southern large-scale structures”, Monthly Notices of the Royal Astronomical Society **399**, 683–698 (2009).

[32] A. Almeida et al., “The Eighteenth Data Release of the Sloan Digital Sky Surveys: Targeting and First Spectra from SDSS-V”, The Astrophysical Journal Supplement Series **267**, 44 (2023).

[33] T. M. Abbott et al., “Dark Energy Survey Year 3 results: Cosmological constraints from galaxy clustering and weak lensing”, Physical Review D **105**, 30 (2022).

[34] A. G. Brown et al., “Gaia Early Data Release 3 - Summary of the contents and survey properties”, Astronomy and Astrophysics **649**, A1 (2021).

[35] J. P. Gardner et al., “The James Webb space telescope”, Space Science Reviews **123**, 485–606 (2006).

[36] R. Scaramella et al., “Euclid preparation: I. the Euclid Wide Survey”, Astronomy and Astrophysics **662**, A112 (2022).

[37] M. Lochner et al., “The Impact of Observing Strategy on Cosmological Constraints with LSST”, The Astrophysical Journal Supplement Series **259**, 58 (2022).

[38] V. Springel et al., “Simulations of the formation, evolution and clustering of galaxies and quasars”, Nature **435**, 629–636 (2005).

[39] J. Schaye et al., “The EAGLE project: Simulating the evolution and assembly of galaxies and their environments”, Monthly Notices of the Royal Astronomical Society **446**, 521–554 (2015).

[40] V. Springel et al., “First results from the IllustrisTNG simulations: Matter and galaxy clustering”, Monthly Notices of the Royal Astronomical Society **475**, 676–698 (2018).

[41] B. Famaey and S. S. McGaugh, “Modified newtonian dynamics (MOND): Observational phenomenology and relativistic extensions”, Living Reviews in Relativity **15**, 10 (2012).

[42] M Milgrom, “A modification of the Newtonian dynamics as a possible alternative to the hidden mass hypothesis”, The Astrophysical Journal **270**, 365 (1983).

[43] M. Milgrom, “A modification of the Newtonian dynamics - Implications for galaxies”, The Astrophysical Journal **270**, 371 (1983).

[44] M Milgrom, “A Modification of the Newtonian Dynamics - Implications for Galaxy Systems”, The Astrophysical Journal **270**, 384 (1983).

[45] R. B. Tully and J. R. Fisher, “A new method of determining distances to galaxies”, Astronomy and Astrophysics **54**, 661–673 (1977).

[46] S. D. McDermott et al., “Turning off the lights: How dark is dark matter?”, Physical Review D **83**, 063509 (2011).

[47] D. Budker et al., “Millicharged Dark Matter Detection with Ion Traps”, PRX Quantum **3**, 010330 (2022).

[48] B. Holdom, “Two U(1)’s and ϵ charge shifts”, Physics Letters B **166**, 196–198 (1986).

[49] D. Feldman et al., “Stueckelberg Z extension with kinetic mixing and millicharged dark matter from the hidden sector”, Physical Review D **75**, 115001 (2007).

[50] M. Markevitch et al., “Direct Constraints on the Dark Matter Self-Interaction Cross Section from the Merging Galaxy Cluster 1E 0657−56”, The Astrophysical Journal **606**, 819–824 (2004).

[51] D. A. Buote et al., “Chandra Evidence of a Flattened, Triaxial Dark Matter Halo in the Elliptical Galaxy NGC 720”, The Astrophysical Journal **577**, 183–196 (2002).

[52] B. Audren et al., “Strongest model-independent bound on the lifetime of Dark Matter”, Journal of Cosmology and Astroparticle Physics **2014**, 028 (2014).

[53] R. D. Peccei and H. R. Quinn, “CP conservation in the presence of pseudoparticles”, Physical Review Letters **38**, 1440–1443 (1977).

[54] C. B. Adams et al., “Axion Dark Matter”, `10.48550/arXiv.2203.14923` (2023).

[55] H. Primakoff, “Photo-production of neutral mesons in nuclear electric fields and the mean life of the neutral meson”, Physical Review **81**, 899 (1951).

[56] Y. K. Semertzidis and S. W. Youn, “Axion dark matter: How to see it?”, Science Advances **8**, eabm9928 (2022).

[57] P Sikivie, “Experimental tests of the “invisible” axion”, Physical Review Letters **51**, 1415–1417 (1983).

[58] N Du et al., “Search for Invisible Axion Dark Matter with the Axion Dark Matter Experiment”, Physical Review Letters **120**, 151301 (2018).

[59] T. Braine et al., “Extended Search for the Invisible Axion with the Axion Dark Matter Experiment”, Physical Review Letters **124**, 101303 (2020).

[60] V. Anastassopoulos et al., “New CAST limit on the axion-photon interaction”, Nature Physics **13**, 584–590 (2017).

[61] E. Armengaud et al., “Physics potential of the International Axion Observatory (IAXO)”, Journal of Cosmology and Astroparticle Physics **2019**, 047–047 (2019).

[62] L. Di Luzio et al., “The landscape of QCD axion models”, Physics Reports **870**, 1–117 (2020).

[63] C. O’Hare, *cajohare/AxionLimits: AxionLimits*, 2020.

[64] S. Dodelson and L. M. Widrow, “Sterile neutrinos as dark matter”, Physical Review Letters **72**, 17–20 (1994).

[65] B. Dasgupta et al., “Neutrino mass hierarchy and three-flavor spectral splits of supernova neutrinos”, Physical Review D **81**, 093008 (2010).

[66] P. Abratenko et al., “First Constraints on Light Sterile Neutrino Oscillations from Combined Appearance and Disappearance Searches with the MicroBooNE Detector”, Physical Review Letters **130**, 011801 (2023).

[67] CMS Collaboration, *Search for long-lived heavy neutral leptons decaying in the CMS muon detectors in proton-proton collisions at* $\sqrt{s} = 13 \sim$ TeV, tech. rep. (2023).

[68] H. Almazán et al., “STEREO neutrino spectrum of 235U fission rejects sterile neutrino hypothesis”, Nature **613**, 257–261 (2023).

[69] B. Carr et al., “Primordial black holes as dark matter”, Physical Review D **94**, 083504 (2016).

[70] A. M. Green and B. J. Kavanagh, “Primordial black holes as a dark matter candidate”, Journal of Physics G: Nuclear and Particle Physics **48**, 043001 (2021).

[71] Y. B. Zel’dovich et al., “The Hypothesis of Cores Retarded during Expansion and the Hot Cosmological Model”, Soviet Astronomy **10**, 602 (1967).

[72] S. Hawking, “Gravitationally Collapsed Objects of Very Low Mass”, Monthly Notices of the Royal Astronomical Society **152**, 75–78 (1971).

[73] B. Carr et al., “Constraints on primordial black holes”, Reports on Progress in Physics **84**, 116902 (2021).

[74] B. J. Kavanagh, *bradkav/PBHbounds: Release version*, 2019.

[75] P. Tisserand et al., “Limits on the Macho content of the Galactic Halo from the EROS-2 survey of the magellanic clouds”, Astronomy and Astrophysics **469**, 387–404 (2007).

[76] C. Alcock et al., “MACHO Project Limits on Black Hole Dark Matter in the 1-30 $M_\odot$ Range”, The Astrophysical Journal **550**, L169 (2001).

[77] H. Niikura et al., “Constraints on Earth-mass primordial black holes from OGLE 5-year microlensing events”, Physical Review D **99**, 083503 (2019).

[78] B. P. Abbott et al., “Observation of gravitational waves from a binary black hole merger”, Physical Review Letters **116**, 061102 (2016).

[79] B. P. Abbott et al., “Prospects for observing and localizing gravitational-wave transients with Advanced LIGO, Advanced Virgo and KAGRA”, Living Reviews in Relativity **23**, 1–69 (2020).

[80] R. Abbott et al., “GWTC-3: Compact Binary Coalescences Observed by LIGO and Virgo during the Second Part of the Third Observing Run”, Physical Review X **13**, 041039 (2023).

[81] S. Bird et al., “Did LIGO Detect Dark Matter?”, Physical Review Letters **116**, 201301 (2016).

[82] G. Franciolini et al., “Searching for a subpopulation of primordial black holes in LIGO-Virgo gravitational-wave data”, Physical Review D **105**, 083526 (2022).

[83] S. W. Hawking, “Particle creation by black holes”, Communications in Mathematical Physics **43**, 199–220 (1975).

[84] J. McEnery et al., “All-sky Medium Energy Gamma-ray Observatory: Exploring the Extreme Multimessenger Universe”, `10.48550/arXiv.1907.07558` (2019).

[85] A. Ray et al., “Near future MeV telescopes can discover asteroid-mass primordial black hole dark matter”, Physical Review D **104**, 023516 (2021).

[86] P. S. Bhupal Dev et al., “Constraining non-thermal and thermal properties of Dark Matter”, Frontiers in Physics **2**, 1–16 (2014).

[87] G. Jungman et al., “Supersymmetric dark matter”, Physics Report **267**, 195–373 (1996).

[88] J. Billard et al., *Direct detection of dark matter - APPEC committee report*, 2022.

[89] G. Steigman et al., “Precise relic WIMP abundance and its impact on searches for dark matter annihilation”, Physical Review D **86**, 023506 (2012).

[90] J. L. Feng, “Dark Matter Candidates from Particle Physics and Methods of Detection”, Annual Review of Astronomy and Astrophysics **48**, 495–545 (2010).

[91] H Haber and G. Kane, “The search for supersymmetry: Probing physics beyond the standard model”, Physics Reports **117**, 75–263 (1985).

[92] G. Bertone et al., “Particle dark matter: Evidence, candidates and constraints”, Physics Reports **405**, 279–390 (2005).

[93] L. Evans and P. Bryant, “LHC Machine”, Journal of Instrumentation **3**, S08001 (2008).

[94] K. Aamodt et al., “The ALICE experiment at the CERN LHC”, Journal of Instrumentation **3**, S08002 (2008).

[95] G. Aad et al., “The ATLAS Experiment at the CERN Large Hadron Collider”, Journal of Instrumentation **3**, S08003 (2008).

[96] S. Chatrchyan et al., “The CMS experiment at the CERN LHC”, Journal of Instrumentation **3**, S08004 (2008).

[97] A. Augusto Alves et al., “The LHCb Detector at the LHC”, Journal of Instrumentation **3**, S08005 (2008).

[98] The ATLAS Collaboration, *Dark matter summary plots for s-channel, 2HDM+a and Dark Higgs models*, tech. rep. (2023).

[99] B. Penning, “The pursuit of dark matter at colliders - an overview”, Journal of Physics G: Nuclear and Particle Physics **45**, 063001 (2018).

[100] A. Boveia and C. Doglioni, “Dark matter searches at colliders”, Annual Review of Nuclear and Particle Science **68**, 429–459 (2018).

[101] I Béjar et al., *High-Luminosity Large Hadron Collider (HL-LHC) Technical design report* (2020).

[102] K. Griest and M. Kamionkowski, “Unitarity limits on the mass and radius of dark-matter particles”, Physical Review Letters **64**, 615–618 (1990).

[103] J. Smirnov and J. F. Beacom, “Tev-scale thermal WIMPs: Unitarity and its consequences”, Physical Review D **100**, 043029 (2019).

[104] C. A. Argüelles et al., “Dark matter annihilation to neutrinos”, Reviews of Modern Physics **93**, 035007 (2021).

[105] C. Pérez de los Heros, “Status, Challenges and Directions in Indirect Dark Matter Searches”, Symmetry **12**, 1648 (2020).

[106] L. Goodenough and D. Hooper, “Possible Evidence For Dark Matter Annihilation In The Inner Milky Way From The Fermi Gamma Ray Space Telescope”, `10.48550/arXiv.0910.2998` (2009).

[107] D. Hooper and L. Goodenough, “Dark matter annihilation in the Galactic Center as seen by the Fermi Gamma Ray Space Telescope”, Physics Letters, Section B: Nuclear, Elementary Particle and High-Energy Physics **697**, 412–428 (2011).

[108] S. Murgia, “The Fermi –LAT Galactic Center Excess: Evidence of Annihilating Dark Matter?”, Annual Review of Nuclear and Particle Science **70**, 455–483 (2020).

[109] O. Adriani et al., “An anomalous positron abundance in cosmic rays with energies 1.5-100 GeV”, Nature **458**, 607–609 (2009).

[110] M Aguilar et al., “Electron and positron fluxes in primary cosmic rays measured with the alpha magnetic spectrometer on the international space station”, Physical Review Letters **113**, 41 (2014).

[111] M. Aguilar et al., “The Alpha Magnetic Spectrometer (AMS) on the international space station: Part II — Results from the first seven years”, Physics Reports **894**, 1–116 (2021).

[112] M Ackermann et al., “Searching for Dark Matter Annihilation from Milky Way Dwarf Spheroidal Galaxies with Six Years of Fermi Large Area Telescope Data”, Physical Review Letters **115**, 14 (2015).

[113] R Abbasi et al., “Search for GeV-scale dark matter annihilation in the Sun with IceCube DeepCore”, Physical Review D **105**, 062004 (2022).

[114] A Albert et al., “Search for dark matter towards the Galactic Centre with 11 years of ANTARES data”, Physics Letters, Section B: Nuclear, Elementary Particle and High-Energy Physics **805**, 135439 (2020).

[115] S. Adrián-Martínez et al., “Letter of intent for KM3NeT 2.0”, Journal of Physics G: Nuclear and Particle Physics **43**, 084001 (2016).

[116] A. Šaina et al., “Indirect Search for Dark Matter with the KM3NeT Neutrino Telescope”, Proceedings of 38th International Cosmic Ray Conference — PoS(ICRC2023) **444**, 1377 (2023).

[117] D. Baxter et al., “Recommended conventions for reporting results from direct dark matter searches”, The European Physical Journal C **81**, 907 (2021).

[118] J. Lewin and P. Smith, “Review of mathematics, numerical factors, and corrections for dark matter experiments based on elastic nuclear recoil”, Astroparticle Physics **6**, 87–112 (1996).

[119] J. Bland-Hawthorn and O. Gerhard, “The Galaxy in Context: Structural, Kinematic, and Integrated Properties”, Annual Review of Astronomy and Astrophysics **54**, 529–596 (2016).

[120] R. Abuter et al., “Improved GRAVITY astrometric accuracy from modeling optical aberrations”, Astronomy and Astrophysics **647**, A59 (2021).

[121] M. C. Smith et al., “The RAVE survey: Constraining the local Galactic escape speed”, Monthly Notices of the Royal Astronomical Society **379**, 755–772 (2007).

[122] N. W. Evans et al., “Refinement of the standard halo model for dark matter searches in light of the Gaia Sausage”, Physical Review D **99**, 023012 (2019).

[123] J. Aalbers et al., *JelleAalbers/wimprates: v0.5.0*, 2023.

[124] A. Ianni, “Considerations on Underground Laboratories”, Journal of Physics: Conference Series **1342**, 012003 (2020).

[125] J. A. Formaggio and C. J. Martoff, “Backgrounds to sensitive experiments underground”, Annual Review of Nuclear and Particle Science **54**, 361–412 (2004).

[126] A Bettini, “The world deep underground laboratories”, European Physical Journal Plus **127**, 11 (2012).

[127] M Robinson et al., “Measurements of muon flux at 1070 m vertical depth in the Boulby underground laboratory”, Nuclear Instruments and Methods in Physics Research, Section A: Accelerators, Spectrometers, Detectors and Associated Equipment **511**, 347–353 (2003).

[128] Z. Y. Guo et al., “Muon flux measurement at China Jinping Underground Laboratory”, Chinese Physics C **45**, 025001 (2021).

[129] D.-M. Mei and A Hime, “Muon-induced background study for underground laboratories”, Physical Review D **73**, 053004 (2006).

[130] K Eguchi et al., “First Results from KamLAND: Evidence for Reactor Antineutrino Disappearance”, Physical Review Letters **90**, 6 (2003).

[131] M. Agostini et al., “Modulations of the cosmic muon signal in ten years of Borexino data”, Journal of Cosmology and Astroparticle Physics **2019**, 046 (2019).

[132] B Schmidt et al., “Muon-induced background in the EDELWEISS dark matter search”, Astroparticle Physics **44**, 28–39 (2013).

[133] B Aharmim et al., “Measurement of the cosmic ray and neutrino-induced muon flux at the Sudbury neutrino observatory”, Physical Review D **80**, 012001 (2009).

[134] C Zhang and D. M. Mei, “Measuring muon-induced neutrons with liquid scintillation detector at Soudan mine”, Physical Review D **90**, 122003 (2014).

[135] N Abgrall et al., “Muon flux measurements at the Davis Campus of the Sanford Underground Research Facility with the MAJORANA DEMONSTRATOR veto system”, Astroparticle Physics **93**, 70–75 (2017).

[136] M. Adrover et al., “Cosmogenic background simulations for neutrinoless double beta decay with the DARWIN observatory at various underground sites”, European Physical Journal C **84**, 88 (2024).

[137] K Rielage et al., “Update on the MiniCLEAN Dark Matter Experiment”, Physics Procedia **61**, 144–152 (2015).

[138] R Ajaj et al., “Search for dark matter with a 231-day exposure of liquid argon using DEAP-3600 at SNOLAB”, Physical Review D **100**, 022004 (2019).

[139] K. Abe et al., “A direct dark matter search in XMASS-I”, Physics Letters B **789**, 45–53 (2019).

[140] C. Regenfus, “The argon dark matter experiment (ArDM)”, Journal of Physics: Conference Series **203**, 012024 (2010).

[141] P. Agnes et al., “First results from the DarkSide-50 dark matter experiment at Laboratori Nazionali del Gran Sasso”, Physics Letters, Section B: Nuclear, Elementary Particle and High-Energy Physics **743**, 456–466 (2015).

[142] P Agnes et al., “Search for Dark-Matter-Nucleon Interactions via Migdal Effect with DarkSide-50”, Physical Review Letters **130**, 101001 (2023).

[143] P. Agnes et al., “Search for low-mass dark matter WIMPs with 12 ton-day exposure of DarkSide-50”, Physical Review D **107**, 063001 (2023).

[144] C. E. Aalseth et al., “DarkSide-20k: A 20 tonne two-phase LAr TPC for direct dark matter detection at LNGS”, European Physical Journal Plus **133**, 1–129 (2018).

[145] D. S. Akerib et al., “Projected WIMP sensitivity of the LUX-ZEPLIN dark matter experiment”, Physical Review D **101**, 052002 (2020).

[146] J. Aalbers et al., “First Dark Matter Search Results from the LUX-ZEPLIN (LZ) Experiment”, Physical Review Letters **131**, 041002 (2023).

[147] E. Aprile et al., “Projected WIMP sensitivity of the XENONnT dark matter experiment”, Journal of Cosmology and Astroparticle Physics **2020**, 031 (2020).

[148] XENON Collaboration et al., “First Dark Matter Search with Nuclear Recoils from the XENONnT Experiment”, Physical Review Letters **131**, 041003 (2023).

[149] XENON Collaboration et al., “The XENONnT Dark Matter Experiment”, `10.48550/arXiv.2402.10446` (2024).

[150] Y. Meng et al., “Dark Matter Search Results from the PandaX-4T Commissioning Run”, Physical Review Letters **127**, 261802 (2021).

[151] C Amole et al., “Dark matter search results from the complete exposure of the PICO-60 C3 F8 bubble chamber”, Physical Review D **100**, 022001 (2019).

[152] M. Bressler et al., “A buffer-free concept bubble chamber for PICO dark matter searches”, Journal of Instrumentation **14**, P08019 (2019).

[153] C. B. Krauss, “PICO-60 Results and PICO-40L Status”, Journal of Physics: Conference Series **1468**, 012043 (2020).

[154] A. Aguilar-Arevalo et al., “Results on Low-Mass Weakly Interacting Massive Particles from an 11 kg d Target Exposure of DAMIC at SNOLAB”, Physical Review Letters **125**, 241803 (2020).

[155] I. J. Arnquist et al., “The DAMIC-M experiment: Status and first results”, SciPost Physics Proceedings **12**, 014 (2023).

[156] L. Barak et al., “SENSEI: Direct-Detection Results on sub-GeV Dark Matter from a New Skipper CCD”, Physical Review Letters **125**, 171802 (2020).

[157] A. Aguilar-Arevalo et al., “The Oscura Experiment”, `10.48550/arXiv.2202.10518` (2022).

[158] R. Agnese et al., “Results from the Super Cryogenic Dark Matter Search Experiment at Soudan”, Physical Review Letters **120**, 061802 (2018).

[159] R Agnese et al., “Projected sensitivity of the SuperCDMS SNOLAB experiment”, Physical Review D **95**, 082002 (2017).

[160] M. F. Albakry et al., “Investigating the sources of low-energy events in a SuperCDMS-HVeV detector”, Physical Review D **105**, 112006 (2022).

[161] E. Armengaud et al., “Performance of the EDELWEISS-III experiment for direct dark matter searches”, Journal of Instrumentation **12**, P08010–P08010 (2017).

[162] E Armengaud et al., “Search for sub-GeV dark matter via the Migdal effect with an EDELWEISS germanium detector with NbSi transition-edge sensors”, Physical Review D **106**, 062004 (2022).

[163] A. H. Abdelhameed et al., “First results from the CRESST-III low-mass dark matter program”, Physical Review D **100**, 102002 (2019).

[164] R. Bernabei et al., “First results from DAMA/LIBRA and the combined results with DAMA/NaI”, European Physical Journal C **56**, 333–355 (2008).

[165] G. Adhikari et al., “Search for a Dark Matter-Induced Annual Modulation Signal in NaI(Tl) with the COSINE-100 Experiment”, Physical Review Letters **123**, 031302 (2019).

[166] G. Adhikari et al., “Three-year annual modulation search with COSINE-100”, Physical Review D **106**, 052005 (2022).

[167] J Amaré et al., “Annual modulation results from three-year exposure of ANAIS-112”, Physical Review D **103**, 102005 (2021).

[168] R. Bernabei et al., “Dark Matter: DAMA/LIBRA and its perspectives”, SciPost Physics Proceedings, 025 (2023).

[169] F. Froborg, “SABRE: WIMP modulation detection in the northern and southern hemisphere”, Journal of Physics: Conference Series **718**, 042021 (2016).

[170] M. Antonello et al., “The SABRE project and the SABRE proof-of-principle”, European Physical Journal C **79**, 8 (2019).

[171] M. J. Zurowski, “Status of the SABRE South experiment at the Stawell underground physics laboratory”, Nuclear Instruments and Methods in Physics Research, Section A: Accelerators, Spectrometers, Detectors and Associated Equipment **1045**, 167585 (2023).

[172] G. Angloher et al., “Results from the first cryogenic NaI detector for the COSINUS project”, Journal of Instrumentation **12**, P11007 (2017).

[173] G Angloher et al., “First measurements of remoTES cryogenic calorimeters: Easy-to-fabricate particle detectors for a wide choice of target materials”, Nuclear Instruments and Methods in Physics Research, Section A: Accelerators, Spectrometers, Detectors and Associated Equipment **1045**, 167532 (2023).

[174] Q Arnaud et al., “First results from the NEWS-G direct dark matter search experiment at the LSM”, Astroparticle Physics **97**, 54–62 (2018).

[175] L. Balogh et al., “The NEWS-G detector at SNOLAB”, Journal of Instrumentation **18**, T02005 (2023).

[176] L Balogh et al., “Copper electroplating for background suppression in the NEWS-G experiment”, Nuclear Instruments and Methods in Physics Research, Section A: Accelerators, Spectrometers, Detectors and Associated Equipment **988**, 164844 (2021).

[177] L Balogh et al., “Exploring light dark matter with the DarkSPHERE spherical proportional counter electroformed underground at the Boulby Underground Laboratory”, Physical Review D **108**, 112006 (2023).

[178] M. Ibe et al., “Migdal effect in dark matter direct detection experiments”, Journal of High Energy Physics **2018**, 36 (2018).

[179] C. A. O’Hare, “New Definition of the Neutrino Floor for Direct Dark Matter Searches”, Physical Review Letters **127**, 251802 (2021).

[180] J Billard et al., “Implication of neutrino backgrounds on the reach of next generation dark matter direct detection experiments”, Physical Review D **89**, 023524 (2014).

[181] D. Akimov et al., “Observation of coherent elastic neutrino-nucleus scattering”, Science **357**, 1123–1126 (2017).

[182] A. S. Chou et al., “Snowmass Cosmic Frontier Report”, `10.48550/arXiv.2211.09978` (2022).

[183] J. Aalbers et al., “DARWIN: towards the ultimate dark matter detector”, Journal of Cosmology and Astroparticle Physics **2016**, 017–017 (2016).

[184] J. Aalbers et al., “A next-generation liquid xenon observatory for dark matter and neutrino physics”, Journal of Physics G: Nuclear and Particle Physics **50**, 013001 (2023).

[185] L. Baudis, “DARWIN/XLZD: A future xenon observatory for dark matter and other rare interactions”, Nuclear Physics B **1003**, 116473 (2024).

[186] B. J. Mount et al., *LUX-ZEPLIN (LZ) Technical Design Report*, tech. rep. (2017), p. 368.

[187] J Heise, "The Sanford Underground Research Facility at Homestake", Journal of Physics: Conference Series **606**, 012015 (2015).

[188] D. S. Akerib et al., "Projected sensitivities of the LUX-ZEPLIN experiment to new physics via low-energy electron recoils", Physical Review D **104**, 092009 (2021).

[189] J. Aalbers et al., "Search for new physics in low-energy electron recoils from the first LZ exposure", Physical Review D **108**, 072006 (2023).

[190] D. S. Akerib et al., "Enhancing the sensitivity of the LUX-ZEPLIN (LZ) dark matter experiment to low energy signals", `10.48550/arXiv.2101.08753` (2021).

[191] E. Aprile et al., "Observation of two-neutrino double electron capture in ^{124}Xe with XENON1T", Nature **568**, 532–535 (2019).

[192] D. S. Akerib et al., "Projected sensitivity of the LUX-ZEPLIN experiment to the two-neutrino and neutrinoless double β decays of ^{134}Xe", Physical Review C **104**, 57754–1700 (2021).

[193] D. S. Akerib et al., "Projected sensitivity of the LUX-ZEPLIN experiment to the $0\nu\beta\beta$ decay of ^{136}Xe", Physical Review C **102**, 014602 (2020).

[194] M. J. Berger et al., "XCOM: photon cross sections database", NIST Standard Reference Database 8 (XGAM) **8**, 87–3597 (1998).

[195] J. R. De Laeter et al., "Atomic weights of the elements: Review 2000 (IUPAC Technical Report)", Pure and Applied Chemistry **75**, 683–800 (2003).

[196] A. Minamino et al., "Self-shielding effect of a single phase liquid xenon detector for direct dark matter search", Astroparticle Physics **35**, 609–614 (2012).

[197] V. Chepel and H. Araújo, "Liquid noble gas detectors for low energy particle physics", Journal of Instrumentation **8**, R04001 (2013).

[198] J. Jortner et al., "Localized excitations in condensed Ne, Ar, Kr, and Xe", The Journal of Chemical Physics **42**, 4250–4253 (1965).

[199] S. Kubota et al., "Evidence for a triplet state of the self-trapped exciton states in liquid argon, krypton and xenon", Journal of Physics C: Solid State Physics **11**, 2645–2651 (1978).

[200] M. Piotter et al., "First time-resolved measurement of infrared scintillation light in gaseous xenon", European Physical Journal C **83**, 1–11 (2023).

[201] J. Mock et al., "Modeling pulse characteristics in Xenon with NEST", Journal of Instrumentation **9**, T04002 (2014).

[202] A. Hitachi et al., "Effect of ionization density on the time dependence of luminescence from liquid argon and xenon", Physical Review B **27**, 5279–5285 (1983).

[203] M. G. Boulay and A Hime, "Technique for direct detection of weakly interacting massive particles using scintillation time discrimination in liquid argon", Astroparticle Physics **25**, 179–182 (2006).

[204] K. Fujii et al., “High-accuracy measurement of the emission spectrum of liquid xenon in the vacuum ultraviolet region”, Nuclear Instruments and Methods in Physics Research, Section A: Accelerators, Spectrometers, Detectors and Associated Equipment **795**, 293–297 (2015).

[205] B. López Paredes et al., “Response of photomultiplier tubes to xenon scintillation light”, Astroparticle Physics **102**, 56–66 (2018).

[206] E. Aprile and T. Doke, “Liquid xenon detectors for particle physics and astrophysics”, Reviews of Modern Physics **82**, 2053–2097 (2010).

[207] D. R. Nygren, “Origin and development of the TPC idea”, Nuclear Instruments and Methods in Physics Research, Section A: Accelerators, Spectrometers, Detectors and Associated Equipment **907**, 22–30 (2018).

[208] L. Baudis, “Dual-phase xenon time projection chambers for rare-event searches”, Philosophical Transactions of the Royal Society A: Mathematical, Physical and Engineering Sciences **382**, 20230083 (2024).

[209] D. S. Akerib et al., “Signal yields, energy resolution, and recombination fluctuations in liquid xenon”, Physical Review D **95**, 012008 (2017).

[210] C. E. Dahl, “The physics of background discrimination in liquid xenon, and first results from XENON10 in the hunt for WIMP dark matter”, PhD thesis (Princeton University, 2009).

[211] G. Anton et al., “Measurement of the scintillation and ionization response of liquid xenon at MeV energies in the EXO-200 experiment”, Physical Review C **101**, 65501 (2020).

[212] L. Baudis et al., “A measurement of the mean electronic excitation energy of liquid xenon”, The European Physical Journal C **81**, 1060 (2021).

[213] J Lindhard et al., “Range concepts and heavy ion ranges (Notes on atomic collisions, II)”, Mat. Fys. Medd. Dan. Vid. Selsk **33**, 42 p. (1963).

[214] S. Farrell et al., *NESTCollaboration/nestpy: v2.0.0*, 2022.

[215] T. Doke et al., “Absolute scintillation yields in liquid argon and xenon for various particles”, Japanese Journal of Applied Physics, Part 1: Regular Papers and Short Notes and Review Papers **41**, 1538–1545 (2002).

[216] D. S. Akerib et al., “Calibration, event reconstruction, data analysis, and limit calculation for the LUX dark matter experiment”, Physical Review D **97**, 102008 (2018).

[217] M. Szydagis et al., “NEST: A comprehensive model for scintillation yield in liquid xenon”, Journal of Instrumentation **6**, P10002 (2011).

[218] M. Szydagis et al., “A review of basic energy reconstruction techniques in liquid xenon and argon detectors for dark matter and neutrino physics using NEST”, Instruments **5**, 13 (2021).

[219] P. Sorensen and C. E. Dahl, “Nuclear recoil energy scale in liquid xenon with application to the direct detection of dark matter”, Physical Review D **83**, 063501 (2011).

[220] D. S. Akerib et al., “Tritium calibration of the LUX dark matter experiment”, Physical Review D **93**, 072009 (2016).

[221] S. Nagy et al., “On the Q-value of the tritium β-decay”, Europhysics Letters **74**, 404–410 (2006).

[222] J. Vainionpaa et al., “Technology and Applications of Neutron Generators Developed by Adelphi Technology, Inc”, Physics Procedia **60**, 203–211 (2014).

[223] J. R. Verbus et al., “Proposed low-energy absolute calibration of nuclear recoils in a dual-phase noble element TPC using D-D neutron scattering kinematics”, Nuclear Instruments and Methods in Physics Research, Section A: Accelerators, Spectrometers, Detectors and Associated Equipment **851**, 68–81 (2017).

[224] LUX Collaboration et al., “Low-energy (0.7-74 keV) nuclear recoil calibration of the LUX dark matter experiment using D-D neutron scattering kinematics”, `10.48550/arXiv.1608.05381` (2016).

[225] D. S. Akerib et al., “The LUX-ZEPLIN (LZ) experiment”, Nuclear Instruments and Methods in Physics Research, Section A: Accelerators, Spectrometers, Detectors and Associated Equipment **953**, 163047 (2020).

[226] D. S. Akerib et al., “Identification of radiopure titanium for the LZ dark matter experiment and future rare event searches”, Astroparticle Physics **96**, 1–10 (2017).

[227] D. S. Akerib et al., “The LUX-ZEPLIN (LZ) radioactivity and cleanliness control programs”, The European Physical Journal C **80**, 1044 (2020).

[228] J. Aalbers et al., “Background determination for the LUX-ZEPLIN (LZ) dark matter experiment”, Physical Review D **108**, 012010 (2023).

[229] S. J. Haselschwardt et al., “A liquid scintillation detector for radioassay of gadolinium-loaded liquid scintillator for the LZ Outer Detector”, Nuclear Instruments and Methods in Physics Research, Section A: Accelerators, Spectrometers, Detectors and Associated Equipment **937**, 148–163 (2019).

[230] D. Y. Akimov et al., “Observation of light emission from Hamamatsu R11410-20 photomultiplier tubes”, Nuclear Instruments and Methods in Physics Research, Section A: Accelerators, Spectrometers, Detectors and Associated Equipment **794**, 1–2 (2015).

[231] C. H. Faham et al., “Measurements of wavelength-dependent double photoelectron emission from single photons in VUV-sensitive photomultiplier tubes”, Journal of Instrumentation **10**, P09010 (2015).

[232] S. Sobieski, “Ultraviolet response of semitransparent multialkali photocathodes”, Applied Optics **15**, 2298 (1976).

[233] R. Linehan et al., “Design and production of the high voltage electrode grids and electron extraction region for the LZ dual-phase xenon time projection chamber”, Nuclear Instruments and Methods in Physics Research, Section A: Accelerators, Spectrometers, Detectors and Associated Equipment **1031**, 165955 (2022).

[234] D. S. Akerib et al., “Discrimination of electronic recoils from nuclear recoils in two-phase xenon time projection chambers”, Physical Review D **102**, 112002 (2020).

[235] M Arthurs et al., “Performance study of charcoal-based radon reduction systems for ultraclean rare event detectors”, Journal of Instrumentation **16**, P07047 (2021).

[236] K Pushkin et al., “Study of radon reduction in gases for rare event search experiments”, Nuclear Instruments and Methods in Physics Research, Section A: Accelerators, Spectrometers, Detectors and Associated Equipment **903**, 267–276 (2018).

[237] T. Tanaka et al., “Gamma-ray spectra from thermal neutron capture on gadolinium-155 and natural gadolinium”, Progress of Theoretical and Experimental Physics **2020**, 043D02 (2020).

[238] W. Turner et al., “Optical calibration system for the LUX-ZEPLIN (LZ) outer detector”, Nuclear Instruments and Methods in Physics Research, Section A: Accelerators, Spectrometers, Detectors and Associated Equipment **1010**, 165551 (2021).

[239] Eckert & Ziegler, *Eckert & Ziegler Strahlen- und Medizintechnik AG: Isotope Products.*

[240] A. B. Sazzad et al., “Design and characterization of AmLi neutron sources for the LZ experiment”, Journal of Instrumentation **18**, P05006 (2023).

[241] H. Ito et al., “Analyzing the neutron and γ-ray emission properties of an americium-beryllium tagged neutron source”, `10.48550/arXiv.2304.12153` (2023).

[242] J. Xu et al., “Detection and Calibration of Low-Energy Nuclear Recoils for Dark Matter and Neutrino Scattering Experiments”, Annual Review of Nuclear and Particle Science **73**, 95–121 (2023).

[243] J. Aalbers et al., “The Design, Implementation, and Performance of the LZ Calibration Systems”, `10.48550/arXiv.2406.12874` (2024).

[244] N. Rupp, “Radon background in liquid xenon detectors”, Journal of Instrumentation **13**, C02001–C02001 (2018).

[245] S. Bruenner et al., “Radon daughter removal from PTFE surfaces and its application in liquid xenon detectors”, European Physical Journal C **81**, 1–10 (2021).

[246] H. Zou et al., “Quantifying the triboelectric series”, Nature Communications **10**, 1–9 (2019).

[247] J. B. Albert et al., "Measurements of the ion fraction and mobility of α- And β -decay products in liquid xenon using the EXO-200 detector", Physical Review C **92**, 45504 (2015).

[248] V. A. Kudryavtsev et al., "Neutron production in (α,n) reactions", Nuclear Instruments and Methods in Physics Research, Section A: Accelerators, Spectrometers, Detectors and Associated Equipment **972**, 164095 (2020).

[249] M.-M.Be et al., *Table of Radionuclides (Vol. 4 – A = 133 to 252)*, Vol. 4 (2008), p. 309.

[250] M.-M.Be et al., *Table of Radionuclides (Vol. 5 – A = 22 to 244)*, Vol. 5 (2010), p. 256.

[251] E. H. Miller et al., "Constraining radon backgrounds in LZ", AIP Conference Proceedings **1921**, 050003 (2018).

[252] D. S. Akerib et al., "Chromatographic separation of radioactive noble gases from xenon", Astroparticle Physics **97**, 80–87 (2018).

[253] A. Naylor, "Background studies for LUX and LZ: activation, gammas from rock and krypton removal", PhD thesis (University of Sheffield, 2022).

[254] D.-M. Mei et al., "Early results on radioactive background characterization for Sanford Laboratory and DUSEL experiments", Astroparticle Physics **34**, 33–39 (2010).

[255] V. A. Kudryavtsev, "Muon simulation codes MUSIC and MUSUN for underground physics", Computer Physics Communications **180**, 339–346 (2009).

[256] D. Woodward, "Simulations of cosmic muons and background radiations for muon tomography and underground experiments", PhD thesis (University of Sheffield, 2017).

[257] J Aalbers et al., "Cosmogenic production of ^{37}Ar in the context of the LUX-ZEPLIN experiment", Physical Review D **105**, 082004 (2022).

[258] S. Cebrián, "Cosmogenic activation of materials", International Journal of Modern Physics A **32**, 1743006 (2017).

[259] L. Baudis et al., "Cosmogenic activation of xenon and copper", European Physical Journal C **75**, 1–9 (2015).

[260] M.-M.Be et al., *Table of Radionuclides (Vol. 8 – A = 41 to 198)*, Vol. 8 (2016), p. 288.

[261] M.-M.Be et al., *Table of Radionuclides (Vol. 7 – A = 14 to 245)*, Vol. 7 (2013), p. 216.

[262] D. Akerib et al., "Measurement of the gamma ray background in the Davis cavern at the Sanford Underground Research Facility", Astroparticle Physics **116**, 102391 (2020).

[263] E Aprile et al., "Double-weak decays of ^{124}Xe and ^{136}Xe in the XENON1T and XENONnT experiments", Physical Review C **106**, 024328 (2022).

[264] A. Gando et al., "Measurement of the double-β decay half-life of ^{136}Xe with the KamLAND-Zen experiment", Physical Review C **85**, 45504 (2012).

[265] J. B. Albert et al., “Improved measurement of the $2\nu\beta\beta$ half-life of ^{136}Xe with the EXO-200 detector”, Physical Review C **89**, 015502 (2014).

[266] L. Si et al., “Determination of Double Beta Decay Half-Life of ^{136}Xe with the PandaX-4T Natural Xenon Detector”, Research **2022**, 9798721 (2022).

[267] M. Redshaw et al., “Mass and double-beta-decay Q value of ^{136}Xe”, Physical Review Letters **98**, 053003 (2007).

[268] S. J. Haselschwardt et al., “Improved calculations of β decay backgrounds to new physics in liquid xenon detectors”, Physical Review C **102**, 065501 (2020).

[269] J. N. Bahcall and C. Peña-Garay, “Solar models and solar neutrino oscillations”, New Journal of Physics **6**, 1–19 (2004).

[270] S. Agostinelli et al., “GEANT4 - A simulation toolkit”, Nuclear Instruments and Methods in Physics Research, Section A: Accelerators, Spectrometers, Detectors and Associated Equipment **506**, 250–303 (2003).

[271] J. Allison et al., “Geant4 developments and applications”, IEEE Transactions on Nuclear Science **53**, 270–278 (2006).

[272] J. Allison et al., “Recent developments in GEANT4”, Nuclear Instruments and Methods in Physics Research, Section A: Accelerators, Spectrometers, Detectors and Associated Equipment **835**, 186–225 (2016).

[273] D. S. Akerib et al., “Simulations of events for the LUX-ZEPLIN (LZ) dark matter experiment”, Astroparticle Physics **125**, 102480 (2021).

[274] S. Perkins et al., *Tables and graphs of electron-interaction cross sections from 10 eV to 100 GeV derived from the LLNL Evaluated Electron Data Library (EEDL), Z = 1–100*, tech. rep. (Lawrence Livermore National Laboratory (LLNL), Livermore, CA, 1991), p. 500.

[275] D. Cullen et al., *EPDL97: the evaluated photo data library ‘97 version*, tech. rep. (Lawrence Livermore National Laboratory (LLNL), Livermore, CA, 1997), pp. 1–35.

[276] F. Bečvář, “Simulation of γ cascades in complex nuclei with emphasis on assessment of uncertainties of cascade-related quantities”, Nuclear Instruments and Methods in Physics Research, Section A: Accelerators, Spectrometers, Detectors and Associated Equipment **417**, 434–449 (1998).

[277] I. Antcheva et al., “ROOT-A C++ framework for petabyte data storage, statistical analysis and visualization”, Computer Physics Communications **182**, 1384–1385 (2011).

[278] J. Pivarski et al., *Uproot*, 2023.

[279] V. N. Solovov et al., “Position reconstruction in a dual phase xenon scintillation detector”, IEEE Transactions on Nuclear Science **59**, 3286–3293 (2012).

[280] D. Akerib et al., “Radiogenic and muon-induced backgrounds in the LUX dark matter detector”, Astroparticle Physics **62**, 33–46 (2015).

[281] G. Cowan et al., “Asymptotic formulae for likelihood-based tests of new physics”, European Physical Journal C **71**, 1–19 (2011).

[282] R. James, “Signals, backgrounds and statistical inference for dark matter direct detection experiments”, PhD thesis (University College London, 2024).

[283] D. S. Akerib et al., “Results from a Search for Dark Matter in the Complete LUX Exposure”, Physical Review Letters **118**, 021303 (2017).

[284] E. Aprile et al., “Dark Matter Search Results from a One Ton-Year Exposure of XENON1T”, Physical Review Letters **121**, 111302 (2018).

[285] T. M. Undagoitia and L. Rauch, “Dark matter direct-detection experiments”, Journal of Physics G: Nuclear and Particle Physics **43**, 013001 (2016).

[286] S. W. Caddey et al., *The Homestake gold mine, an early Proterozoic iron-formation-hosted gold deposit, Lawrence County, South Dakota*, tech. rep. (1991).

[287] K Hart et al., “Topographic, geologic, and density distribution modeling in support of physics experiments at the Sanford Underground Research Facility (SURF)”, Proceedings of the South Dakota Academy of Science **93** (2014).

[288] N. Abgrall et al., “The MAJORANA DEMONSTRATOR Neutrinoless Double-Beta Decay Experiment”, Advances in High Energy Physics **2014**, 1–18 (2014).

[289] K. T. Lesko et al., “Deep Underground Science and Engineering Laboratory - Preliminary Design Report”, `10.48550/arXiv.1108.0959` (2011).

[290] J. Heise, “The Sanford Underground Research Facility”, `10.48550/arXiv.2203.08293` (2022).

[291] F. E. Gray et al., “Cosmic ray muon flux at the Sanford Underground Laboratory at Homestake”, Nuclear Instruments and Methods in Physics Research, Section A: Accelerators, Spectrometers, Detectors and Associated Equipment **638**, 63–66 (2011).

[292] A. Best et al., “Low energy neutron background in deep underground laboratories”, Nuclear Instruments and Methods in Physics Research, Section A: Accelerators, Spectrometers, Detectors and Associated Equipment **812**, 1–6 (2016).

[293] G. Pereira et al., “Energy resolution of the LZ detector for high-energy electronic recoils”, Journal of Instrumentation **18**, C04007 (2023).

[294] K. Thomas, *An estimate of the gamma flux in the East Counting Room of the Davis cavern*, tech. rep. (2014), p. 7.

[295] M. Haffke et al., “Background measurements in the Gran Sasso Underground Laboratory”, Nuclear Instruments and Methods in Physics Research, Section A: Accelerators, Spectrometers, Detectors and Associated Equipment **643**, 36–41 (2011).

[296] D. Malczewski et al., “Gamma background measurements in the Gran Sasso National Laboratory”, Journal of Radioanalytical and Nuclear Chemistry **295**, 749–754 (2013).

[297] H. Ohsumi et al., “Gamma-ray flux in the Fréjus underground laboratory measured with NaI detector”, Nuclear Instruments and Methods in Physics Research, Section A: Accelerators, Spectrometers, Detectors and Associated Equipment **482**, 832–839 (2002).

[298] D. Malczewski et al., “Gamma background measurements in the Laboratoire Souterrain de Modane”, Journal of Radioanalytical and Nuclear Chemistry **292**, 751–756 (2012).

[299] D. Malczewski et al., “Gamma background measurements in the Boulby Underground Laboratory”, Journal of Radioanalytical and Nuclear Chemistry **298**, 1483–1489 (2013).

[300] P. R. Scovell et al., “Low-background gamma spectroscopy at the Boulby Underground Laboratory”, Astroparticle Physics **97**, 160–173 (2018).

[301] M. Perillo Isaac et al., *High energy gamma-rays measurements in the SNO cavity Technical Report SNO-STR-97-009*, tech. rep. (1997).

[302] Z. Zeng et al., “Environmental gamma background measurements in China Jinping Underground Laboratory”, Journal of Radioanalytical and Nuclear Chemistry **301**, 443–450 (2014).

[303] P. Adhikari et al., “Understanding internal backgrounds in NaI(Tl) crystals toward a 200 kg array for the KIMS-NaI experiment”, European Physical Journal C **76**, 185 (2016).

[304] L. Baudis et al., “Performance of the Hamamatsu R11410 photomultiplier tube in cryogenic xenon environments”, Journal of Instrumentation **8**, P04026 (2013).

[305] D. S. Akerib et al., “An ultra-low background PMT for liquid xenon detectors”, Nuclear Instruments and Methods in Physics Research, Section A: Accelerators, Spectrometers, Detectors and Associated Equipment **703**, 1–6 (2013).

[306] S. Abe et al., “Search for Majorana Neutrinos with the Complete KamLAND-Zen Dataset”, `10.48550/arXiv.2406.11438` (2024).

[307] A. Pomansky, “Underground low background laboratories of the Baksan Neutrino Observatory”, Nuclear Instruments and Methods in Physics Research, Section B: Beam Interactions with Materials and Atoms **17**, 406–410 (1986).

[308] T. Florkowski et al., “Natural production of radionuclides in geological formations”, Nuclear Geophysics **2**, 1–14 (1988).

[309] R. Heaton et al., “Alpha-induced neutron activity in materials”, Nuclear Geophysics **4**, 499–510 (1990).

[310] R. Heaton et al., "α-particle induced high-energy γ-ray yields from light elements", Nuclear Instruments and Methods in Physics Research, Section A: Accelerators, Spectrometers, Detectors and Associated Equipment **364**, 317–327 (1995).

[311] R. K. Heaton et al., "α-particle induced γ-ray transitions in light elements", Physical Review C **56**, 922–937 (1997).

[312] A. Tiwari et al., "Observation of annual modulation induced by γ rays from (α,γ) reactions at the Soudan Underground Laboratory", Physical Review C **96**, 44609 (2017).

[313] R Heaton et al., "Neutron production from thick-target (α, n) reactions", Nuclear Instruments and Methods in Physics Research, Section A: Accelerators, Spectrometers, Detectors and Associated Equipment **276**, 529–538 (1989).

[314] D. M. Mei et al., "Evaluation of (α, n) induced neutrons as a background for dark matter experiments", Nuclear Instruments and Methods in Physics Research, Section A: Accelerators, Spectrometers, Detectors and Associated Equipment **606**, 651–660 (2009).

[315] G. F. Knoll, *Radiation Detection and Measurement, 4th Edition* (John Wiley and Sons, Hoboken, N.J., 2010).

[316] G. R. Gilmore, *Practical Gamma-Ray Spectrometry: Second Edition* (John Wiley and Sons, Chichester, England, 2008), pp. 1–387.

[317] R. Hofstadter, "The detection of gamma-rays with thallium-activated sodium iodide crystals", Physical Review **75**, 796–810 (1949).

[318] Saint Gobain Crystals, *Scintillation Products - Scintillation Materials and Assemblies*, tech. rep. (2004), p. 12.

[319] A Perez-Andujar and L Pibida, "Performance of CdTe, HPGe and NaI(Tl) detectors for radioactivity measurements", Applied Radiation and Isotopes **60**, 41–47 (2004).

[320] ORTEC, *ORTEC ® Experiment 3: Gamma-Ray Spectroscopy Using NaI(Tl)*, tech. rep. (2010).

[321] ORTEC, *MAESTRO Multichannel Analyzer Emulation Software*, 2022.

[322] Spectrum Techniques, *Spectrum Techniques, LLC.*

[323] M.-M.Be et al., *Table of Radionuclides (Vol. 3 – A = 3 to 244)*, Vol. 3 (2006), p. 210.

[324] D. Madland et al., *SOURCES 4A: A Code for Calculating (alpha,n), Spontaneous Fission, and Delayed Neutron Sources and Spectra*, tech. rep. (Los Alamos National Laboratory (LANL), Los Alamos, NM, 1999).

[325] M. Solmaz, "Search for annual and diurnal modulations in the LUX experiment and assembling a tagged neutron source for the LZ Outer Detector", PhD thesis (University of California, Santa Barbara, 2020).

[326] S. Croft, “The use of neutron intensity calibrated ^{9}Be(α, n) sources as 4438 keV gamma-ray reference standards”, Nuclear Instruments and Methods in Physics Research, Section A: Accelerators, Spectrometers, Detectors and Associated Equipment **281**, 103–116 (1989).

[327] Z. Liu et al., “The 4.438 MeV gamma to neutron ratio for the Am-Be neutron source”, Applied Radiation and Isotopes **65**, 1318–1321 (2007).

[328] F. P. An et al., “Measurement of electron antineutrino oscillation based on 1230 days of operation of the Daya Bay experiment”, Physical Review D **95**, 072006 (2017).

[329] Saint Gobain Crystals, *Efficiency Calculations for Selected Scintillators*, tech. rep. (2004), p. 14.

[330] COSINE Collaboration, *Private Communication*, 2023.

[331] Castle Game Engine, *view3dscene: Viewer for glTF, X3D, sprite sheets and other model formats*.

[332] J. B. Birks, “Scintillations from organic crystals: Specific fluorescence and relative response to different radiations”, Proceedings of the Physical Society. Section A **64**, 874–877 (1951).

[333] W. W. Moses et al., “Scintillator Non-Proportionality: Present Understanding and Future Challenges”, IEEE Transactions on Nuclear Science **55**, 1049–1053 (2008).

[334] S. A. Payne et al., “Nonproportionality of Scintillator Detectors: Theory and Experiment. II”, IEEE Transactions on Nuclear Science **58**, 3392–3402 (2011).

[335] Bertin Technologies S.A.S, *AlphaGUARD*, tech. rep. (2023), pp. 1–2.

[336] DUNE Collaboration et al., “The DUNE Far Detector Interim Design Report Volume 1: Physics, Technology and Strategies”, `10.48550/arXiv.1807.10334` (2018).

[337] K. W. Kim et al., “Tests on NaI(Tl) crystals for WIMP search at the Yangyang Underground Laboratory”, Astroparticle Physics **62**, 249–257 (2015).

[338] S. Mughabghab, *Thermal neutron capture cross sections resonance integrals and G-factors*, tech. rep. (2003), pp. 1–30.

[339] K. Lesko et al., *Private Communication*, 2023.

[340] T. Iida et al., “The energy calibration system for CANDLES using (n,γ) reaction”, Nuclear Instruments and Methods in Physics Research, Section A: Accelerators, Spectrometers, Detectors and Associated Equipment **986**, 164727 (2021).

[341] K Nakajima et al., “Background studies of high energy γ rays from (n,γ) reactions in the CANDLES experiment”, Astroparticle Physics **100**, 54–60 (2018).

[342] D. A. Brown et al., “ENDF/B-VIII.0: The 8th Major Release of the Nuclear Reaction Data Library with CIELO-project Cross Sections, New Standards and Thermal Scattering Data”, Nuclear Data Sheets **148**, 1–142 (2018).

[343] R. B. Firestone and Z. Revay, “Thermal neutron capture cross sections for ^{16,17,18}O and ^{2}H”, Physical Review C **93**, 044311 (2016).

[344] S Raman et al., “Thermal-neutron capture by silicon isotopes”, Physical Review C **46**, 972–983 (1992).

[345] R. B. Firestone et al., “Thermal neutron capture cross section for ^{56}Fe(n,γ)”, Physical Review C **95**, 014328 (2017).

[346] L. Venturini and B. Pecequilo, “Thermal neutron capture cross-section of ^{48}Ti, ^{51}V, ^{50,52,53}Cr and ^{58,60,62,64}Ni”, Applied Radiation and Isotopes **48**, 493–496 (1997).

[347] S Raman et al., “Thermal-neutron capture by ^{58}Ni, ^{59}Ni, and ^{60}Ni”, Physical Review C **70**, 044318 (2004).

[348] R Saldanha et al., “Cosmogenic activation of sodium iodide”, Physical Review D **107**, 022006 (2023).

[349] J. Amaré et al., “Cosmogenic radionuclide production in NaI(Tl) crystals”, Journal of Cosmology and Astroparticle Physics **2015**, 046 (2015).

[350] P. Villar et al., “Study of the cosmogenic activation in NaI(Tl) crystals within the ANAIS experiment”, International Journal of Modern Physics A **33**, 1843006 (2018).

[351] J. Amaré et al., “Analysis of backgrounds for the ANAIS-112 dark matter experiment”, European Physical Journal C **79**, 412 (2019).

[352] E. Barbosa de Souza et al., “Study of cosmogenic radionuclides in the COSINE-100 NaI(Tl) detectors”, Astroparticle Physics **115**, 102390 (2020).

[353] E. Barberio et al., “Simulation and background characterisation of the SABRE South experiment”, The European Physical Journal C **83**, 878 (2023).

[354] J Amaré et al., “Cosmogenic production of tritium in dark matter detectors”, Astroparticle Physics **97**, 96–105 (2018).

[355] M.-M.Be et al., *Table of Radionuclides (Vol. 2 – A = 151 to 242)*, Vol. 2 (2004), p. 307.

[356] D West, “The calculation of neutron yields in mixtures and compounds from the thick target (α,n) yields in the separate constituents”, Annals of Nuclear Energy **6**, 549–552 (1979).

[357] S. Andringa et al., “Snowmass 2021 Letter of Interest: Neutron yield in (α,n)-reactions in rare-event searches”, 1–5 (2021).

[358] D. Baxter et al., “Snowmass 2021 Cosmic Frontier White Paper: Calibrations and backgrounds for dark matter direct detection”, `10.48550/arXiv.2203.07623` (2022).

[359] Y. Feige et al., “Production rates of neutrons in soils due to natural radioactivity”, Journal of Geophysical Research **73**, 3135–3142 (1968).

[360] H. Liskien and A. Paulsen, “Neutron yields of light elements under α-bombardment”, Atomkernenergie **30**, 59–61 (1977).

[361] J. K. Bair and J. Gomez del Campo, “Neutron Yields from Alpha-Particle Bombardment”, Nuclear Science and Engineering **71**, 18–28 (1979).

[362] D West and A. C. Sherwood, “Measurements of thick-target (α, n) yields from light elements”, Annals of Nuclear Energy **9**, 551–577 (1982).

[363] N. A. Roughton et al., “Thick-target measurements and astrophysical thermonuclear reaction rates: Alpha-induced reactions”, Atomic Data and Nuclear Data Tables **28**, 341–353 (1983).

[364] V. V. Zerkin and B. Pritychenko, “The experimental nuclear reaction data (EXFOR): Extended computer database and Web retrieval system”, Nuclear Instruments and Methods in Physics Research, Section A: Accelerators, Spectrometers, Detectors and Associated Equipment **888**, 31–43 (2018).

[365] N. Otuka et al., “Towards a More Complete and Accurate Experimental Nuclear Reaction Data Library (EXFOR): International Collaboration Between Nuclear Reaction Data Centres (NRDC)”, Nuclear Data Sheets **120**, 272–276 (2014).

[366] M Febbraro et al., “New $^{13}\mathrm{C}(\alpha, n)^{16}\mathrm{O}$ Cross Section with Implications for Neutrino Mixing and Geoneutrino Measurements”, Physical Review Letters **125**, 062501 (2020).

[367] S Westerdale and P. D. Meyers, “Radiogenic neutron yield calculations for low-background experiments”, Nuclear Instruments and Methods in Physics Research, Section A: Accelerators, Spectrometers, Detectors and Associated Equipment **875**, 57–64 (2017).

[368] M. B. Gromov et al., “Calculation of Neutron and Gamma Yields of (α,n) and (α,$n\gamma$) Reactions by Means of a New Version of the NeuCBOT Program for low background Experiments”, Physics of Atomic Nuclei **86**, 181–187 (2023).

[369] G. N. Vlaskin et al., “Neutron Yield of the Reaction (α, n) on Thick Targets Comprised of Light Elements”, Atomic Energy **117**, 357–365 (2015).

[370] E. Mendoza et al., “Neutron production induced by α-decay with Geant4”, Nuclear Instruments and Methods in Physics Research, Section A: Accelerators, Spectrometers, Detectors and Associated Equipment **960**, 163659 (2020).

[371] V Pesudo et al., “SaG4n: Calculation of (α,n) yields for low background experiments using Geant4”, Journal of Physics: Conference Series **1468**, 012059 (2020).

[372] W. B. Wilson et al., “Sources: A code for calculating (alpha, n), spontaneous fission, and delayed neutron sources and spectra”, Progress in Nuclear Energy **51**, 608–613 (2009).

[373] J. F. Ziegler et al., “SRIM - The stopping and range of ions in matter (2010)”, Nuclear Instruments and Methods in Physics Research, Section B: Beam Interactions with Materials and Atoms **268**, 1818–1823 (2010).

[374] M. J. Berger et al., “ICRU Report 49: Stopping Powers and Ranges for Protons and Alpha Particles”, Journal of the ICRU **os-25** (1993).

[375] M. Herman et al., “EMPIRE: Nuclear Reaction Model Code System for Data Evaluation”, Nuclear Data Sheets **108**, 2655–2715 (2007).

[376] A. J. Koning and D. Rochman, “Modern Nuclear Data Evaluation with the TALYS Code System”, Nuclear Data Sheets **113**, 2841–2934 (2012).

[377] A. Koning et al., “TALYS: modeling of nuclear reactions”, European Physical Journal A **59**, 131 (2023).

[378] A. C. Fernandes et al., “Comparison of thick-target (alpha,n) yield calculation codes”, EPJ Web of Conferences **153**, 07021 (2017).

[379] J Cooley et al., “Input comparison of radiogenic neutron estimates for ultra-low background experiments”, Nuclear Instruments and Methods in Physics Research, Section A: Accelerators, Spectrometers, Detectors and Associated Equipment **888**, 110–118 (2018).

[380] A. Blokhin et al., “New version of neutron evaluated data library BROND-3.1”, Problems of Atomic Science and Technology. Series: Nuclear and Reactor Constants, 62–93 (2016).

[381] Z. Ge et al., “CENDL-3.2: The new version of Chinese general purpose evaluated nuclear data library”, EPJ Web of Conferences **239**, 09001 (2020).

[382] A. J. Plompen et al., “The joint evaluated fission and fusion nuclear data library, JEFF-3.3”, European Physical Journal A **56**, 1–108 (2020).

[383] O. Iwamoto et al., “Japanese evaluated nuclear data library version 5: JENDL-5”, Journal of Nuclear Science and Technology **60**, 1–60 (2023).

[384] A. J. Koning et al., “TENDL: Complete Nuclear Data Library for Innovative Nuclear Science and Technology”, Nuclear Data Sheets **155**, 1–55 (2019).

[385] D. A. Brown, *Collaborative International Evaluated Library Organization (CIELO) Pilot Project*, tech. rep. (Brookhaven National Laboratory (BNL), Upton, NY (United States), 2019).

[386] E. Mendoza et al., “A new physics model for the charged particle transport with Geant4”, Proceedings of the IEEE Symposium on Nuclear Science, 2242–2244 (2011).

[387] E. Mendoza et al., “New standard evaluated neutron cross section libraries for the GEANT4 code and first verification”, IEEE Transactions on Nuclear Science **61**, 2357–2364 (2014).

[388] T. Murata et al., *Evaluation of the (α, xn) reaction data for JENDL/AN-2005*, tech. rep. (2006).

[389] S. Westerdale, *GitHub - shawest/neucbot.*

[390] P. De Biévre and P. D. Taylor, "Table of the isotopic compositions of the elements", International Journal of Mass Spectrometry and Ion Processes **123**, 149–166 (1993).

[391] Brookhaven National Laboratory, *NuDat 3*, 2008.

[392] J. Ahrens et al., "ParaView: An end-user tool for large-data visualization", in *Visualization handbook* (Butterworth-Heinemann, 2005), pp. 717–731.

[393] D. Thain et al., "Distributed computing in practice: the Condor experience", Concurrency and Computation: Practice and Experience **17**, 323–356 (2005).

[394] J. K. Tuli, "Evaluated nuclear structure data file", Nuclear Instruments and Methods in Physics Research, Section A: Accelerators, Spectrometers, Detectors and Associated Equipment **369**, 506–510 (1996).

[395] D. R. Tilley et al., "Energy levels of light nuclei, A = 20", Nuclear Physics A **636**, 249–364 (1998).

[396] C. Ouellet and B. Singh, "Nuclear Data Sheets for A = 32", Nuclear Data Sheets **112**, 2199–2355 (2011).

[397] S. Shaw et al., *Private Communication*, 2023.

[398] J. L. Hodges, "The significance probability of the Smirnov two-sample test", Arkiv för Matematik **3**, 469–486 (1958).

[399] V Tomasello et al., "Radioactive background in a cryogenic dark matter experiment", Astroparticle Physics **34**, 70–79 (2010).

A Background summary

For the LZ projected WIMP sensitivity study, measured material radioactivity and estimated levels of dispersed and surface contamination are combined with Monte Carlo simulations and analysis criteria to determine rates of background in the detector [145]. Table A.0.1 presents the integrated background ER and NR counts for a 1000 live day exposure with a 5.6 t fiducial mass, using a cut-and-count analysis both before and after ER discrimination criteria are applied. The counts reported are relevant to the spectrum for a 40 GeV/c^2 WIMP, which corresponds to approximately 1.5–6.5 keV for ERs and 6–30 keV for NRs.

Background originating from the laboratory environment are the main focus of this thesis. Backgrounds from outside the water tank are dominated by the cavern walls. The gamma-ray flux has been measured at the 4850’ level of SURF at various locations in the Davis cavern (both in the 2017 campaign and the campaign presented in this work). Neutrons from the laboratory walls are attenuated efficiently by the water and GdLS surrounding the LZ cryostat. The minimum thickness of hydrogenous shielding is 70 cm, which results in a reduction of the neutron flux by more the 6 order of magnitude [399]. This results in a negligible contribution to LZ backgrounds. The total number of counts in the defined WIMP ROI from the rock walls is 4.6 ER events and 0 NR events, as stated in Table A.0.1.

Table A.0.1: Estimated backgrounds from all significant sources in the LZ 1000 day WIMP search exposure. Counts are for a region of interest relevant to a 40 GeV/c^2 WIMP: approximately 1.5–6.5 keV for ERs and 6–30 keV for NRs; and after application of the single scatter, skin and OD veto, and 5.6 tonne fiducial volume cuts. Mass-weighted average activities are shown for composite materials and the ^{238}U and ^{232}Th chains are split into contributions from early- and late-chain, with the latter defined as those coming from isotopes below and including ^{226}Ra and ^{224}Ra, respectively. Table taken from Ref. [145].

		^{238}U$_e$	^{238}U$_l$	^{232}Th$_e$	^{232}Th$_l$	^{60}Co	^{40}K			
Background Source	Mass [kg]	[mBq kg^{-1}]						n/yr	ER [cts]	NR [cts]
Detector Components										
PMT systems	308	31.2	5.20	2.32	2.29	1.46	18.6	248	2.82	0.027
TPC systems	373	3.28	1.01	0.84	0.76	2.58	7.80	79.9	4.33	0.022
Cryostat	2778	2.88	0.63	0.48	0.51	0.31	2.62	323	1.27	0.018
Outer detector (OD)	22950	6.13	4.74	3.78	3.71	0.33	13.8	8061	0.62	0.001
All else	358	3.61	1.25	0.55	0.65	1.31	2.64	39.1	0.11	0.003
								Subtotal	9	0.07
Surface Contamination										
Dust (intrinsic activity, 500 ng cm^{-2})									0.2	0.05
Plate-out (PTFE panels, 50 nBq cm^{-2})									...	0.05
^{210}Bi mobility (0.1 µBq kg^{-1} LXe)									40.0	...
Ion misreconstruction (50 nBq cm^{-2})									...	0.16
^{210}Pb (in bulk PTFE, 10 mBq kg^{-1} PTFE)									...	0.12
								Subtotal	40	0.39
Xenon contaminants										
^{222}Rn (1.8 µBq kg^{-1})									681	...
^{220}Rn (0.09 µBq kg^{-1})									111	...
$^{\text{nat}}$Kr (0.015 ppt g/g)									24.5	...
$^{\text{nat}}$Ar (0.45 ppb g/g)									2.5	...
								Subtotal	819	0
Laboratory and Cosmogenics										
Laboratory rock walls									4.6	0.00
Muon induced neutrons									...	0.06
Cosmogenic activation									0.2	...
								Subtotal	5	0.06
Physics										
^{136}Xe $2\nu\beta\beta$									67	...
Solar neutrinos: pp+^{7}Be+^{13}N, ^{8}B+hep									191	0*
Diffuse supernova neutrinos (DSNB)									...	0.05
Atmospheric neutrinos (Atm)									...	0.46
								Subtotal	258	0.51
Total									1131	1.03
Total (with 99.5% ER discrimination, 50% NR efficiency)									5.66	0.52
Sum of ER and NR counts in LZ for 1000 days, 5.6 tonne FV, with all analysis cuts									6.18	

*NR events from solar neutrinos will be concentrated at very low energies; we expect none above the 6 keV NR threshold used here.